UNIVERSITY OF CALIFORNIA
RIVERSIDE

Modeling Reionization From Small to Large Scales

A Dissertation submitted in partial satisfaction
of the requirements for the degree of

Doctor of Philosophy

in

Physics

by

Christopher L. Cain

September 2023

Dissertation Committee:

Dr. Anson D'Aloisio, Chairperson
Dr. George Becker
Dr. Laura Sales

The Dissertation of Christopher L. Cain is approved:

Committee Chairperson

University of California, Riverside

Acknowledgments

I am grateful to the many teachers, professors, and mentors who invested time and energy into helping me develop the skills that made this work possible. Most of all, I am grateful to my advisor, who dedicated many long hours and late nights to teaching me how to be a scientist.

This work is dedicated to my friends and family who supported me throughout my doctoral program and my life. I especially thank my parents for their tireless support. Most of all, “to God be the glory” - Romans 16:27.

ABSTRACT OF THE DISSERTATION

Modeling Reionization From Small to Large Scales

by

Christopher L. Cain

Doctor of Philosophy, Graduate Program in Physics
University of California, Riverside, September 2023
Dr. Anson D'Aloisio, Chairperson

The Epoch of Reionization (EoR) saw the Intergalactic Medium (IGM) transition from neutral to highly ionized. This took place during the first billion years after the Big Bang and was driven by the first generation of HI-ionizing sources, likely the first galaxies. Reionization is a complicated process involving a wide range of physical scales. The shapes and sizes of ionized regions during the EoR are driven by the clustering of galaxies on 100-Mpc scales, while the opacity of the intervening IGM is affected by kpc-scale density fluctuations and the processes regulating the escape of ionizing photons from galaxies take place on even smaller scales. Thus, reionization is challenging to solve from a theoretical perspective. I have developed a radiative transfer code optimized to solve reionization efficiently without sacrificing accuracy. My code uses a novel sub-grid prescription for the opacity of the ionized IGM built on high-resolution simulations that resolve the clumping and dynamics of intergalactic gas down to kpc scales. This work will describe the development and deployment of this code to address the implications of several key EoR observables.

Contents

List of Figures

List of Tables

Chapter 1

Introduction

The Epoch of Reionization (EoR) saw the intergalactic medium (IGM) transition from being neutral to highly ionized, a process driven by the first generation of ionizing photon sources. These sources are believed to have been the first galaxies, making the EoR a key source of insight into galaxy formation and evolution, and the underlying cosmology in which galaxies formed. The next decade will witness a considerable increase in the quantity and quality of observations probing this process. JWST is rapidly expanding our understanding of the properties of high-z galaxies, which were likely the sources that drove reionization. The Roman telescope will reveal how the source properties vary on large scales [25]. Radio experiments like HERA are closing in on a detection of the EoR 21 cm signal [26]. Forthcoming LAE surveys such as LAGER [27] will give insight into both the sources and the IGM surrounding them. Large telescopes such as TMT will provide more spectra of quasars at $z > 6$. Last but not least, CMB-S4 [28] and the Simons Observatory [29] will improve constraints on the electron optical depth and the patchy

kSZ effect from reionization. These complementary data channels will offer unprecedented insight into reionization and the sources responsible for it.

Constraining the properties of the first galaxies (and the underlying cosmology in which they live) from reionization observations is a chief goal of the field. Doing this requires a robust theoretical framework to help interpret observations. Any such framework, in addition to modeling the properties of galaxies themselves, must account for the physics of the IGM relevant for the reionization process. Recent measurements of the ionizing photon mean free path (MFP) at $5 < z < 6$ by [13], along with complementary measurements of the opacity of the Lyα forest [30], have highlighted a key piece of IGM physics. Dense gas structures with masses too small to form stars and act as sources nonetheless helped shape the reionization process by *absorbing* HI ionizing photons. These "sinks" set the opacity of the ionized IGM and may have profoundly affected both the reionization process and its observables.

Despite influencing features of reionization on hundred-Mpc scales, the sinks can be a few kpc or smaller during reionization. Including them in volumes large enough to capture the observables of reionization is a daunting challenge, and the role they play in reionization remains poorly understood. Such simulations are needed to help interpret a wealth of current and forthcoming observations from the EoR. These include Lyα Emitter (LAE) surveys[31, 32, 33, 34, 35], constraints from quasar absorption spectra [36, 37, 38, 30, 39], JWST observations [40, 41, 42], and intensity mapping surveys [43, 44] which include forthcoming measurements of the 21 cm signal and its fluctuations [45, 46, 47].

This thesis presents a body of work aimed at three major goals. The first is to develop better techniques for modeling the physical properties and dynamics of the sinks, and to better understand how their interplay with reionization. The second is to develop an efficient framework for modeling sinks in full radiative transfer simulations that capture the large-scale features of reionization, upon which most existing and forthcoming observations depend. The third is to use this framework to study the implications of several reionization observables and to address a wide range of outstanding questions in the field.

This thesis is organized as follows. Chapters 2-5 each constitute an individual work that has already been accepted for publication in one of several journals (ApJ, JCAP, and MNRAS). Each chapter covers a distinct research topic, but also represents a distinct stage in development of the modeling framework described earlier. Appendices A, B, and C constitute the published appendices for chapters 2, 4, and 5, respectively (chapter 3 has no appendices). Chapter 6 contains a collection of material that is relevant for the goals outlined earlier, but that either will not be or has not yet been published in a scientific journal. Some of this material will be included in the main text or appendices of subsequent publications, and some will not be published outside this thesis. We briefly conclude in Chapter 7.

Chapter 2

A Model-Insensitive Baryon Acoustic Oscillation Feature in the 21 cm Signal from Reionization

2.1 Introduction

The Epoch of Reionization (EoR) was the last major phase transition in the Universe, during which the first sources of ionizing photons re-ionized the IGM. In recent years, observational progress has been made towards constraining this epoch. The timing of Reionization has been constrained by Cosmic Microwave background (CMB) optical depth measurements ([1]). Additional constraints are provided by observations of high-redshift quasars (e.g. [36, 38, 48, 18, 49, 50, 51]) and the population of high-z Lyman-α (Lyα) emitters (e.g. [31, 33, 52, 34, 53, 54]). These observations have been effective at constrain-

ing timing of Reionization, but currently little is known in detail about the Reionization process. Forthcoming observations of the 21 cm spin-flip transition of neutral hydrogen promise a definitive window into the EoR (see e.g. [55] and references therein).

Following a first detection of the EoR 21 cm signal, early efforts will focus on characterizing its brightness temperature fluctuations with the power spectrum. In this paper, we will investigate whether baryon-dark matter relative velocities (or "streaming velocities", or just $v_{\rm bc}$; [56]; henceforth T10), which were sourced at recombination, were able to significantly impact the EoR 21 cm power spectrum. Though formally a second-order effect in perturbation theory, $v_{\rm bc}$ was several times the baryon sound speed at decoupling, so its effect on baryonic structure formation is important. Previous work has shown that $v_{\rm bc}$ impacts a number of astrophysical processes in the early universe, including star formation in low mass halos [57, 58, 59], gas content of halos [60], formation of direct-collapse black holes [61], the BAO feature in the galaxy correlation function [62], the Lyα forest [63, 64], and possibly the formation of globular clusters [65, 66]. Of particular relevance for the current paper, $v_{\rm bc}$ has been shown to modify the *pre-reionization* 21 cm signal at $z \sim 20$ through its impact on the properties of the first stars and galaxies (e.g. [67, 68, 69, 70, 71, 72]). These papers have demonstrated that $v_{\rm bc}$ can imprint distinct BAO features in the 21 cm power spectrum that could be detectable by future experiments.

Streaming velocities impacted the universe at two scales that are particularly important for our investigation: (1) near the baryon jeans scale $k_J \sim 10^2 - 10^3$ h/Mpc,

and (2) at the peak of the power spectrum of fluctuations in $v_{\rm bc}^2$, $P_{v^2}(k)$, which occurs at $k \sim 10^{-1}$ h/Mpc (T10, [73]). The former is roughly the minimum clumping scale of the pre-EoR gas. Recently, [74] (henceforth D20) showed that gas clumpiness on this scale contributes significantly to the ionizing photon budget required to reionize the IGM. The suppression of small-scale clumpiness caused by $v_{\rm bc}$, together with any impact $v_{\rm bc}$ has on ionizing photon sources, will therefore translate into fluctuations in the neutral fraction that trace $P_{v^2}(k)$. Moreover, near 10^{-1} h/Mpc, $P_{v^2}(k)$ is a factor of $\sim 10^2$ larger than the EoR linear matter power spectrum. These facts suggest that $v_{\rm bc}$ may have a pronounced effect on the EoR 21 cm power spectrum $P_{21}(k)$ at large scales if it can be written in the form

$$P_{21}(k) = b_{21,v^2}^2 P_{v^2}(k) + \text{ matter terms} \tag{2.1}$$

where b_{21,v^2}^2 is a linear bias factor coupling fluctuations in $v_{\rm bc}$ to fluctuations in the 21 cm signal. This $v_{\rm bc}$-sourced term may be detectable in measurements of P_{21} even if $b_{21,v^2}^2 < 10^{-2}$. Since P_{v^2} exhibits strong BAO features, its appearance in measurements of P_{21} could serve as a "smoking gun" signature of Reionization. Such a signature would be particularly helpful given the relatively featureless nature of the expected EoR 21-cm power spectrum, and the extreme difficulty of the measurement. Whereas previous studies have explored the coupling of P_{v^2} with P_{21} through the reionization sources [75, 71], the effect from gas clumpiness (or the "sinks") has not been quantified in detail before.

Employing a modified version of the code used in D20, we investigate with fully coupled radiative transfer and hydrodynamics simulations the impact of $v_{\rm bc}$ on the sinks. We will use our simulation results to quantify their contribution to b_{21,v^2}. We will also

assess the potential impact of $v_{\rm bc}$ on source properties during the EoR to see whether this effect may contribute at a similar level to sinks. As we will show, the contribution from the sinks is relatively insensitive to the details of reionization, being mostly fixed by the spectrum of cosmological density fluctuations and gas dynamics. This will allow us to more tightly bracket the coupling between P_{v^2} and P_{21} from the sinks, as opposed to the highly uncertain effect from the sources.

This paper is organized as follows. In § 2.2, we present the details of our simulation code and how we set up our initial conditions. In § 2.3, we present the results of our simulations and describe the impact of $v_{\rm bc}$ during reionization. In § 2.4, we model the contribution of sinks to P_{21} analytically and estimate the magnitude of this term using our simulation results. We also discuss potential contributions to b_{21,v^2} coming from $v_{\rm bc}$'s impact on source properties and assess the detectability of the $v_{\rm bc}$-sourced signal. We summarize in § 2.5. Throughout this work, we assume the following cosmological parameters: $\Omega_m = 0.305$, $\Omega_\Lambda = 1 - \Omega_m$ (flat universe), $\Omega_b = 0.048$, $\sigma_8 = 0.82$, $n_s = 0.9667$, and $h = 0.68$, consistent with the [1] results.

2.2 Numerical Simulations

We ran a suite of ray tracing radiative transfer simulations using the same code employed in D20, modified to include $v_{\rm bc}$. These are set up to track the response of a highly resolved patch of the IGM to ionizing radiation produced by external sources of constant intensity. Hence, we do not explicitly model galaxy formation in our simulations. This

approach allows us to assess the evolution of the sinks in a controlled manner, whereas it can be difficult to disentangle the physical effects at play in a full simulation of reionization that also models the sources. Our approach also allows us to achieve the required resolution for robustly modeling the clumpiness of the un-relaxed gas (see discussion in D20).

This section describes the code (2.2.1), initial conditions (2.2.2), and simulations included in this work (2.2.3).

2.2.1 The Code

We used a modified version of the Eulerian hydrodynamics code of [76] that includes the plane-parallel version of the ray-tracing radiative transfer from [77]. Our simulations were run on one large node of the Bridges supercomputer [78] and ran for $200 - 400$ wall clock hours per simulation. We assume a gas of primordial composition with H mass fraction $X = 0.7547$ and He fraction $Y = 1 - X$. The number of hydro cells, RT cells, and DM mass elements are all equal to N^3 (with $N = 1024$ in our fiducial runs), and our fiducial box length is $L = 1.024$ Mpc/h, for a cell length of 1 h^{-1}kpc. The radiation is handled via plane-parallel ray tracing with an adaptive reduced speed-of-light approximation. Following D20, the radiation sources lie on the boundaries of cubical "sub-domains" of side length $L_{\rm dom} = 32\ h^{-1}$kpc. The sub-domain structure of our boxes allows us to ionize all the gas at approximately the same redshift ($z_{\rm re}$) and to maintain a nearly constant photo-ionization rate throughout the box, which simplifies interpretation of the gas evolution. We use a power law spectrum with intensity $\propto \nu^{-1.5}$ and 5 frequency bins between 1 and 4 Ryd, roughly typical of the expected energy spectrum of reionization-era galaxies. All the important heating/cooling processes relevant to primordial gas are tracked by the code after

the radiation turns on (see [79]). In addition, we keep track of Compton scattering off the CMB at $z > z_{\rm re}$ (which is important for $z > 150$) using an approximate analytical fit to the RECFAST free electron fraction[1]. For a more detailed description of the setup of our simulations, we refer the reader to §3.1 of D20.

2.2.2 Initial Conditions

We generated Gaussian random field initial conditions at Recombination ($z = 1080$), the time $v_{\rm bc}$ was sourced, using CAMB[2] transfer functions (TFs). We did this to capture the cumulative effect of $v_{\rm bc}$ self-consistently rather than starting from linear theory solutions at lower redshift (as was done in [73] and [80]). Following those works, we used separate TFs for Baryons and DM to compute density and velocity growth factors. The initial density and velocity fields were generated using the Zel'dovich approximation (see [81] for a description). We modeled $v_{\rm bc}$ by adding a constant velocity to the gas along the x direction at the initial redshift. This approximation is appropriate on scales $<$ several h^{-1}Mpc because $v_{\rm bc}$ is coherent on those scales (T10). We tested the accuracy of our initial conditions prescription by showing that the matter power spectrum produced by our simulations agrees with the linear theory prediction at redshifts when it should (see Appendix A.2). We also compared our results to simulations initialized at a lower redshift to see whether starting from such a high redshift produced spurious shot noise. We found (as did [63]) that this was not a significant effect.

[1]For $z > z_{\rm re}$, we set $x_e(z) = 0.5\tanh((z-1272)/180.6) + 9.309\times10^{-5}\times\theta(600-z)\times z^{0.25} + 0.5$ (where θ is the heaviside function) was a good fit to the RECFAST free electron fraction.

[2]http://camb.info/

2.2.3 Simulations

Our simulations are run with only hydrodynamics until $z_{\rm re}$. At this time, the box is rapidly filled with radiation and all the gas that cannot self-shield is ionized within a few times steps. The hydrogen photo-ionization rate Γ_{-12} (in units of 10^{-12} s^{-1}) at the boundaries of the sub-domains is a free parameter. We note that Γ_{-12} is nearly constant throughout the box due to our sub-domain method. We ran simulations with $\Gamma_{-12} = 0.3$ and 3.0, $z_{\rm re} = 6$, 8, and 12, $v_{\rm bc} = 20$, 41, and 65 km/s. We used the simulations from D20 with these values of Γ_{-12} and $z_{\rm re}$ to allow for comparison to the no-$v_{\rm bc}$ case. Note that D20 also considered box-scale density fluctuations by adding a constant background overdensity to some of their simulations. We do not do this here because it would make the parameter space unmanageable given the computational cost of our simulations. In addition, simulating over-dense regions with non-zero v_{bc} requires a more complex treatment of the initial conditions (see [82, 80]). Simulations with $v_{\rm bc}$ were run down to $z_{\rm stop} = 5$, 5.5, and 8 for $z_{\rm re} = 6$, 8, and 12, respectively, while the simulations taken from D20 are all run to z = 5. Note that throughout this work, the quoted $v_{\rm bc}$ values are those at $z = 1080$, after which $v_{\rm bc}(z) \propto (1 + z)$. The values of $v_{\rm bc}$ used here were chosen to facilitate evaluation of integrals of the form

$$\langle X \rangle_{v_{\rm bc}} = \int_0^\infty dv_{\rm bc} X(v_{\rm bc}) \mathcal{P}_{v_{\rm bc}} \tag{2.2}$$

where $X(v_{\rm bc})$ is any quantity of interest and $\mathcal{P}_{v_{\rm bc}}$ is the probability distribution of $v_{\rm bc}$ in the universe, given by [83, 84].

$$\mathcal{P}_{v_{\rm bc}} = \left(\frac{3}{2\pi\sigma_{bc}^2}\right)^{\frac{3}{2}} \times 4\pi v_{\rm bc}^2 e^{-\frac{3v_{\rm bc}^2}{2\sigma_{bc}^2}} \tag{2.3}$$

where $\sigma_{bc} = 30$ km/s is the RMS value. Equation 2.2 is the average of quantity X over the distribution of $v_{\rm bc}$ in the universe. Assuming $X(v_{\rm bc})$ can be well-approximated by an order ≤ 5 polynomial in $v_{\rm bc}$, Equation 2.2 can be evaluated exactly via Gaussian Quadrature with only the three $v_{\rm bc}$ values used here.

Our goal is to capture the impact of $v_{\rm bc}$ on the formation of gas structures at high redshift and quantify how important this effect is once the gas becomes ionized. Our simulation setup is well-suited to achieve this goal. Our simulations have resolution high enough to capture the impact of $v_{\rm bc}$ on the gas at $k \geq 10^2\ h^{-1}$Mpc, while being large enough to include structures on mass scales of $10^7 - 10^8\ M_\odot$, which should be relatively unaffected [67]. Hence, it is unlikely that our simulations will significantly under or over-estimate $v_{\rm bc}$'s effect on the gas distribution (see Appendix A.3 for some convergence tests). Second, our numerical setup allows us to isolate the effects of $v_{\rm bc}$ on the sinks independently of its effect on sources, allowing for a straightforward interpretation of our results. Finally, our use of fully coupled hydro/RT will provide a realistic picture of how $v_{\rm bc}$ ties into the reionization process. By modeling the response of the sinks to reionization as in D20, we can make a physically realistic assessment of how important $v_{\rm bc}$ is to their evolution.

2.3 Results

2.3.1 Visualization of the IGM gas structure

We begin by visualizing the gas structure in runs with different $v_{\rm bc}$. Figure 2.1 shows 2D slices through the gas density field at redshifts of 7.9, 7.5, and 6.5 (left to right)

for $v_{\rm bc} = 0$, 41, and 65 km/s (top to bottom) for $(z_{\rm re}, \Gamma_{-12}) = (8, 0.3)$. After the radiation turns on at $z_{\rm re}$, the gas ionizes quickly, reaching high temperatures. This rapidly increases the pressure in the high density gas filaments, which respond by expanding ("relaxing") out of their DM potential wells, smoothing the gas density field considerably (see D20 for a detailed discussion). At redshift 7.9, most of the gas is still tightly bound in these filaments, but by $z = 6.5$ it has reached the "relaxed limit" in which nearly all the small-scale filamentary structure has been erased. The relaxation process considerably reduces the clumpiness of the IGM, and with it, the recombination rate. This important effect is missed in simulations that do not account for the coupling between hydrodynamics and RT.

At z = 7.9, the impact of $v_{\rm bc}$ is still visible, reflecting the integrated history of the un-relaxed gas. However, the differences largely disappear after the gas has relaxed. Even by $z = 7.5$, it is difficult to detect by eye any difference between the three runs, and in the relaxed limit at $z = 6.5$ there is no visible difference. This result is reasonable, since $v_{\rm bc}$ affects the gas distribution the most on small scales, and it is precisely these scales that are smoothed by the gas relaxation. Thus, the majority of the $v_{\rm bc}$ effect does not survive the relaxation process. All this suggests that shortly after the gas is ionized, the recombination rate should be appreciably modulated by $v_{\rm bc}$ because of its impact on small-scale structure. However, after some time passes the differences should largely disappear owing to the smoothing effect of the relaxation process.

For further clarity, in Figure 2.2 we show a 80×80 kpc^2 zoom-in of the gas density field at the same redshifts shown in Figure 2.1. This figure directly compares the

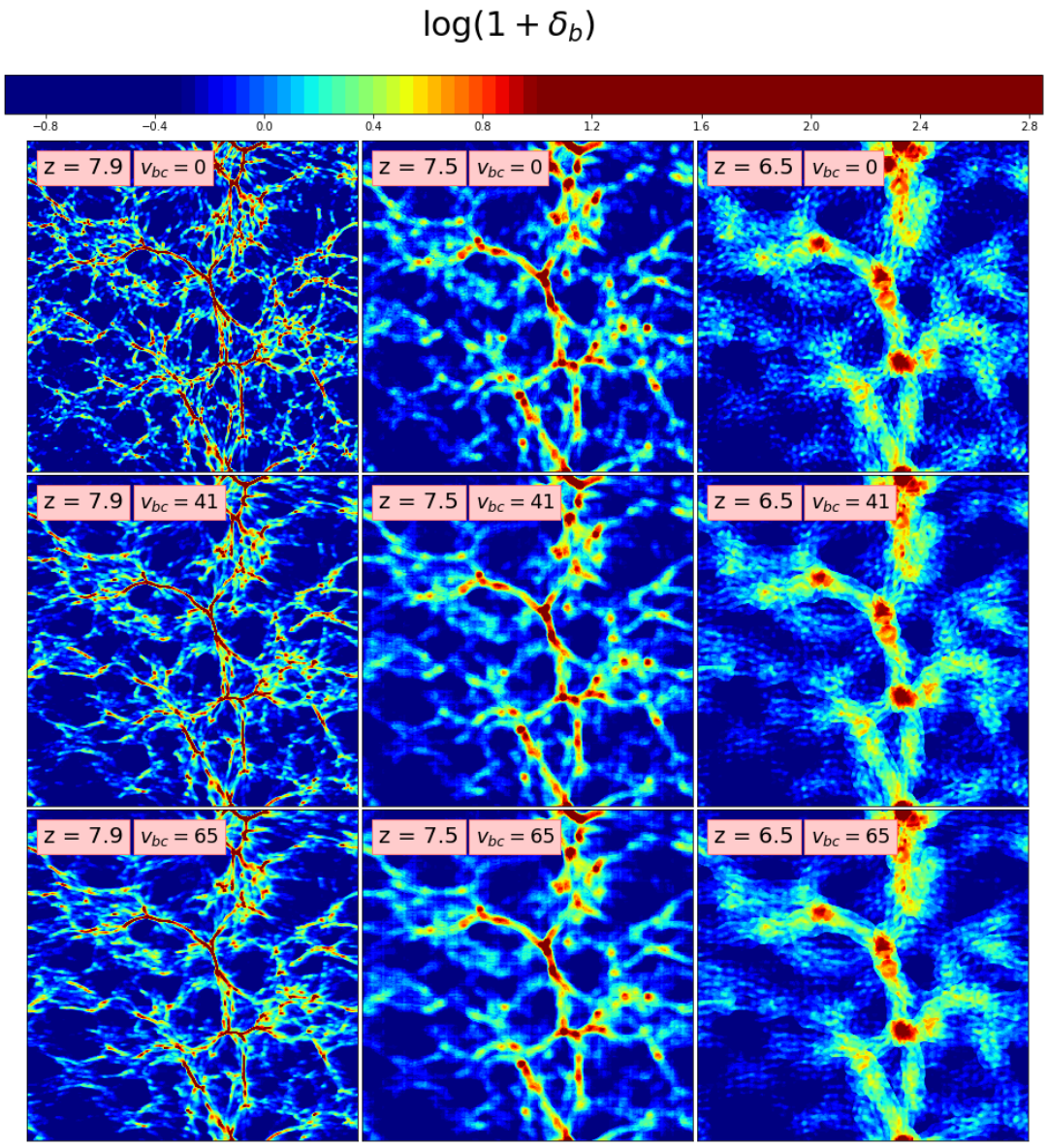

Figure 2.1: 2D slices through the gas density field for redshifts 7.9, 7.5, and 6.5, (left to right) and $v_{\rm bc}$ of 0, 41, and 65 km/s (top to bottom). The relaxation of the gas is seen going from left to right. At $z = 7.9$ reduction of small-scale structure by $v_{\rm bc}$ is visible, but after the gas relaxes the differences are too small to easily detect by eye. We show the results for $z_{\rm re} = 8$ and $\Gamma_{-12} = 0.3$ here; we have checked that they are qualitatively the same for the other combinations of these parameters.

initial and relaxed state of the gas. At $z = 7.9$, the structures are much more diffuse in the high-$v_{\rm bc}$ runs, and the missing gas fills in some of the voids between structures. The effect is less prominent at $z = 7.5$, and almost absent by $z = 6.5$. Note also that the structures themselves are different in the relaxed plot. This highlights the fact that the relaxation process effectively erases the initial conditions of the un-relaxed gas on small scales, including the $v_{\rm bc}$ effect. This relaxation process makes it unlikely that any integrated high-redshift effect that affects only small scales will survive Reionization.

2.3.2 Clumping Factor & Mean Free Path

Based on these results, we expect the recombination rate in a patch of the IGM to be substantially affected by $v_{\rm bc}$ only relatively soon after $z_{\rm re}$. Here, we quantify the recombination rate by the clumping factor $C_{\rm R}$, defined to be the ratio of the true recombination rate to that in a uniform-density IGM with constant temperature $T_{\rm ref}$,

$$C_{\rm R} \equiv \frac{\langle \alpha_B n_e n_{\rm HII} \rangle}{\alpha_B(T_{\rm ref}) \langle n_e \rangle \langle n_{\rm HII} \rangle} \tag{2.4}$$

where α_B is the case B recombination rate for hydrogen, n_e is the free electron density, $n_{\rm HII}$ is the HII number density, and $T_{\rm ref} = 10^4$ K. Since all of our simulations have mean densities equal to the global mean and the hydrogen is almost completely ionized after $z_{\rm re}$, we approximate $\langle n_{\rm HII} \rangle \approx n_{\rm H}(z)$ and $\langle n_e \rangle \approx n_{\rm H}(z)(1 + n_{\rm He}(z)/n_{\rm H}(z))$, i.e. assuming singly ionized helium, where $n_{\rm H}(z)$ and $n_{\rm He}$ are the cosmological average number densities of H and He, respectively.

We plot $C_{\rm R}$ vs. cosmic time (Δt) since $z_{\rm re}$ in the left panels of Figure 2.3 for $z_{\rm re} = 12$ (top), 8 (middle) and 6 (bottom) and $\Gamma_{-12} = 0.3$ (dashed) and 3.0 (dotted). The

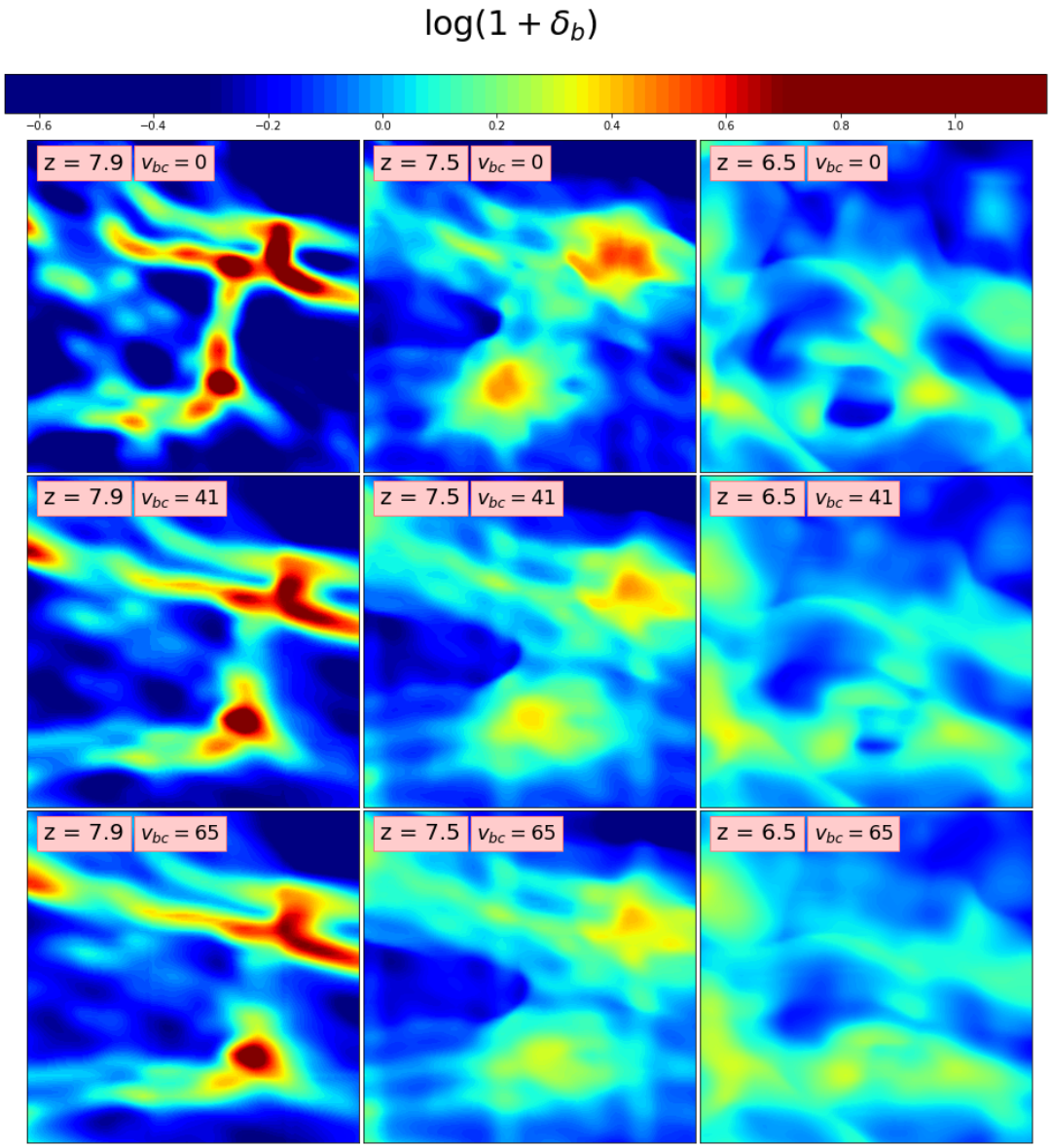

Figure 2.2: Zoom-in on an 80×80 kpc^2 region in Figure 2.1. From left to right, the $v_{\rm bc}$ values are 0, 41, and 65 km/s. The top row shows a marked reduction in structure moving from smaller to higher $v_{\rm bc}$ (left to right). At the lower redshift, there is much less of a difference

right panels show the ratio $C_{\rm R}(v_{\rm bc})/C_{\rm R}(v_{\rm bc}=0)$ i.e. $C_{\rm R}$ as a fraction of the no-$v_{\rm bc}$ case. We see that the percentage difference between the different $v_{\rm bc}$ values is largest $\approx 5-10$ Myr after $z_{\rm re}$, the time at which $C_{\rm R}$ is also at a maximum. At this time, the ionizing radiation has penetrated deep into the most overdense regions, but the gas has not yet had time to dynamically relax. So, the recombination rate is set by the clumpiness of the initial density field, which is significantly modulated between patches with different $v_{\rm bc}$. After ~ 200 Myr, the gas has had time to relax and the fluctuations in $C_{\rm R}$ sourced by $v_{\rm bc}$ have largely disappeared [3]. We emphasize that if our code did not capture the relaxation process, we would significantly over-estimate how much $v_{\rm bc}$ reduces the recombination rate. Still, the effect on recently ionized gas is not insignificant, reaching $\sim 15-20\%$ for $z_{\rm re}=12$ and $\sim 10\%$ for $z_{\rm re}=6$ for $v_{\rm bc}=41$ km/s. Because of the patchy nature of Reionization, at any time there will always be some regions in the IGM that were ionized recently and haven't had time to relax. In these regions, the recombination rate will depend non-negligibly on $v_{\rm bc}$, potentially leading to detectable fluctuations in the IGM neutral fraction (see the next section).

It has been shown that X-ray heating prior to Reionization also reduces the clumpiness of the gas. D20 ran a simulation in which they set the pre-Reionization temperature to a uniform 1000 K to gauge the maximum effect of X-ray pre-heating. They found that $C_{\rm R}$ was suppressed in a fashion similar to what we find here due to $v_{\rm bc}$. This occurs because X-ray pre-heating raises the pre-EoR Jeans mass, which eliminates structure on

[3]Note that for $\Delta t > 100$ Myr, the clumping factor is actually larger for the $v_{\rm bc}=41$ case than for $v_{\rm bc}=0$, particularly in the $z_{re}=6$ case. We believe this offset is due to the difference in starting redshift between the $v_{\rm bc}=0$ simulations and the others. We tested this by running a set of small box simulations starting at different redshifts, and found that starting at $z=300$ produces a $\sim 2\%$ suppression in C_R relative to starting at $z=1080$. This difference is not large enough to impact our results.

the smallest scales. In the event that pre-heating is significant, we expect the importance of $v_{\rm bc}$ to be reduced somewhat as the two processes affect structure at the same mass scales.

Another important quantity during the EoR is the MFP of ionizing photons, which quantifies the typical distance an ionizing photon can travel before being absorbed. We calculated the MFP from our simulations using the approach of [85] (see D20 for details). Figure 2.4 shows the MFP from the same simulations as in Figure 2.3. We find that $v_{\rm bc}$ modulates the MFP by roughly the same percentage that it does the clumping factor, but in the opposite direction. This result is consistent with Figure 2.3 because a less clumpy IGM should allow ionizing photons to travel further on average before being absorbed. The behavior with time is also qualitatively the same as for $C_{\rm R}$; early on, the MFP is modulated by $10-20\%$, but as the gas relaxes the difference disappears. Note that the MFP for the $v_{\rm bc}$ runs starts out slightly below the $v_{\rm bc}=0$ case. This is likely because the first regions in the box to ionize are the under-dense ones, which are slightly less dense in the $v_{\rm bc}=0$ case because more of the gas is locked up in small, dense structures. Unlike for $C_{\rm R}$, the percentage difference in the MFP from $v_{\rm bc}$ is small compared to the difference between the runs with high and low Γ_{-12}. Thus, spatial variations in MFP sourced by $v_{\rm bc}$ should be subdominant to those coming from fluctuations in the photo-ionization rate.

We conclude from these results the IGM recombination rate and MFP are impacted by $v_{\rm bc}$ at the $10-20\%$ level in patches of the universe that have reionized recently. After the gas has had time to relax, the effect we observe is largely erased. During Reionization, there

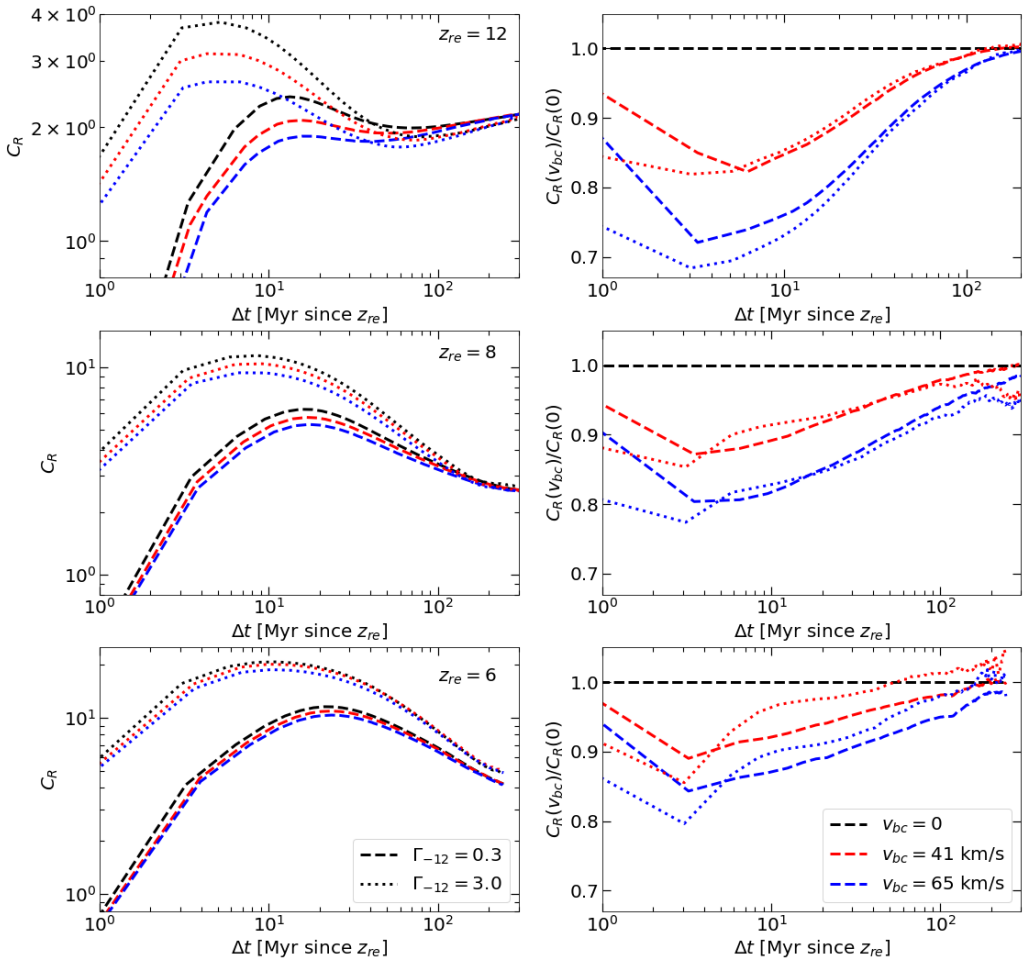

Figure 2.3: Left: Clumping factor vs. cosmic time since $z_{\rm re} = 12$ (top), 8 (middle), and 6 (bottom) for $\Gamma_{-12} = 3.0$ (dotted) and 0.3 (dashed) for all values of $v_{\rm bc}$. The difference in $C_{\rm R}$ is largest shortly after the radiation turns on, but attenuates as the gas relaxes. Right: Ratio of $C_{\rm R}$ to $C_{\rm R}(v_{\rm bc} = 0)$ for both values of Γ_{-12}. The difference peaks $5 - 10$ Myr after $z_{\rm re}$ and steadily declines thereafter, reaching $\sim$ a few percent 200 Myr after $z_{\rm re}$. We note that the kinks in the right panels are due to the sparse time-stepping at small Δt.

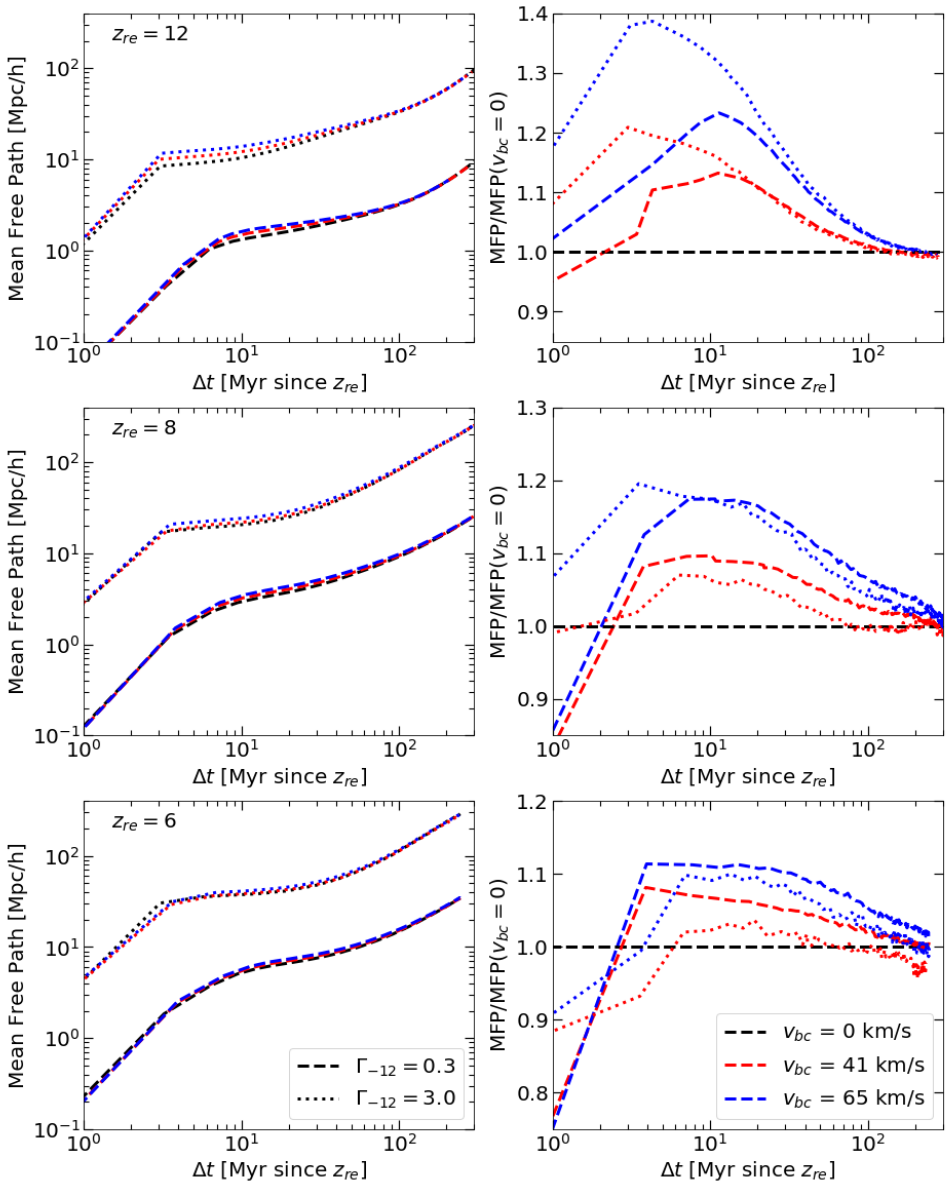

Figure 2.4: Same as Figure 2.3, but for the MFP of ionizing photons. The effect of $v_{\rm bc}$ on the MFP is roughly equal and opposite to its effect on the clumping factor. After $\sim 5-10$ Myr, the difference reaches 25% in the most extreme case, but has largely disappeared after ~ 200 Myr. This is much less than the factor of ~ 10 difference between the runs with high and low Γ_{-12}.

will always be a small percentage of the IGM that was ionized recently, and will therefore display a moderate variation in $C_{\rm R}$ and MFP due to $v_{\rm bc}$. These patches will consume fewer ionizing photons due to recombinations than they would in the absence of $v_{\rm bc}$ because of the reduced clumpiness, which will speed up the local Reionization process. Patches with different values of $v_{\rm bc}$ will be affected differently, leading to fluctuations in the local ionized fraction that trace fluctuations in $v_{\rm bc}$. Granted, these fluctuations should be small, but we also argued in §1 that even a tiny coupling between P_{v^2} and P_{21} could result in a detectable BAO feature in the latter. Exploring this possibility is the subject of the next section.

2.4 Impact of $v_{\rm bc}$ on the 21 cm Signal

In this section, we model the impact of $v_{\rm bc}$ on the EoR 21 cm signal and estimate its detectability. We begin with some preliminaries in §2.4.1. In §2.4.2, we adapt the perturbative model for the signal provided by [86] (henceforth MQ18) to include a $v_{\rm bc}$-dependent term. Using this model, we quantify how large the bias factor b_{21,v^2} must be to produce a detectable imprint on P_{21}. In §2.4.3 and §2.4.4, we assess the contributions to b_{21,v^2} from ionizing photon sinks (§2.4.3) and sources (§2.4.4). Finally, in §2.4.5, we assess the detectability of the predicted signal using current and future 21 cm experiments.

2.4.1 The EoR 21 cm Signal

The EoR 21 cm signal is produced by neutral patches of the IGM that have yet to ionize, so its spatial fluctuations set by those of the neutral fraction and the density

field [55, 87]. For simplicity, we neglect redshift-space distortions[4] [88, 89] and adopt the typical assumption that Lyα coupling and the first X-ray sources drove the 21 cm spin temperature to be $T_s >> T_{\rm CMB}$ by the time reionization largely begins [90, 91, 92]. Under these assumptions, the 21 cm brightness temperature T_{21} can be written

$$T_{21}(\boldsymbol{r}, z) = \hat{T}_{21}(z) x_{\rm HI}(\boldsymbol{r})(1 + \delta_\rho(\boldsymbol{r})) \tag{2.5}$$

where δ_ρ is the (nonlinear) matter overdensity, $x_{\rm HI}$ is the neutral hydrogen fraction, and $\hat{T}_{21}$ depends only on cosmological parameters and redshift. To first order in over-densities, fluctuations in T_{21} are proportional to $\delta_{\rm HI} + \delta_\rho$, where $\delta_{\rm HI}$ is the overdensity in the neutral hydrogen fraction. Because the highest-density regions ionized first, $\delta_{\rm HI}$ and δ_ρ will generally have opposite signs early in the EoR (e.g. [93]). For a given wavenumber k, the signal will reach a local minimum when $\tilde{\delta}_\rho(k) = -\tilde{\delta}_{\rm HI}(k)$ where the tildes denote the Fourier Transform (FT). At this time, the dominant density and ionization terms will cancel out and the signal will be sourced entirely by higher-order terms, one of which should be the $v_{\rm bc}$ term in Equation 2.1. The signal will later reach a local maximum before disappearing entirely when there is no more neutral hydrogen.

2.4.2 21 cm Fluctuations

Forthcoming surveys will characterize the EoR brightness temperature fluctuations with the power spectrum, defined as $P_{21}(k) \equiv \langle \tilde{\delta}_{21}(k) \tilde{\delta}_{21}(k) \rangle$ where $\delta_{21} \equiv x_{\rm HI}(1 + \delta_\rho)$. While modelling the signal is quite complicated and requires numerical simulations (see e.g.[94, 95, 96] for a general discussion), MQ18 showed that on large scales the power

[4]Note that redshift-space distortions have been shown to distort the 21 cm power spectrum at the scales we consider in what follows. Our conclusions are somewhat dependent on these effects being small.

spectrum can be described surprisingly well with perturbation theory. They modeled the 21 cm signal using a multi-parameter bias expansion, keeping the minimum number of terms that produced a reasonable fit to the signal in numerical simulations of Reionization. At large scales and early times, they obtained a good fit using a model with only three parameters; their "minimal model" is given by

$$\tilde{\delta}_{21} = b_1 \left(1 - \frac{1}{3} R_{\rm eff}^2 k^2\right) \tilde{\delta_\rho} + b_2 \tilde{\delta_\rho^2} \tag{2.6}$$

where $\tilde{\delta_\rho}$ is the FT of the total matter over-density, and b_1, b_2 and $R_{\rm eff}$ are time-dependent but scale-independent bias factors. In what follows, we will approximate $\delta_\rho \approx \delta_1$ in Equation 2.6, where δ_1 is the linear matter over-density; this approximation is valid at the redshifts and scales considered here. $R_{\rm eff}$ roughly characterizes the size of ionized bubbles, which should be small compared to $1/k$ at times and scales considered here, so we will drop it.

We will build upon this model by adding a term proportional to the $v_{\rm bc}^2$ "overdensity", $\delta_{v^2} \equiv [v_{\rm bc}^2 - \sigma_{bc}^2]/\sigma_{bc}^2$. First, we write $x_{\rm HI}$ as

$$x_{\rm HI} \equiv \langle x_{\rm HI} \rangle (1 + \delta_{\rm HI}) \tag{2.7}$$

where the angle brackets denote an average over the whole IGM. Next, we assume that $\delta_{\rm HI}$ is a biased tracer of δ_1, δ_1^2, and δ_{v^2} and that δ_ρ traces δ_{v^2}. Then we have

$$\delta_{\rm HI} = b_{\rm HI,1}\delta_1 + b_{\rm HI,2}\delta_1^2 + b_{\rm HI,v^2}\delta_{\rm v^2} \qquad \delta_\rho = \delta_1 + b_{\rho,{\rm v}^2}\delta_{\rm v^2} \tag{2.8}$$

where the coefficients are bias parameters. Combining Equations 2.7 and 2.8 with the

definition of δ_{21} and dropping all terms 3rd order or higher yields

$$\delta_{21} = \langle x_{\rm HI} \rangle (1 + [1 + b_{\rm HI,1}]\delta_1 + b_{\rm HI,2}\delta_1^2 + [b_{\rm HI,v^2} + b_{\rho,v^2}]\delta_{v^2}) \tag{2.9}$$

Comparing this to Equation 2.6, we identify $b_1 = \langle x_{\rm HI} \rangle (1 + b_{\rm HI,1})$ and $b_2 = \langle x_{\rm HI} \rangle b_{\rm HI,2}$ in the case with no δ_{v^2} term, so we can substitute accordingly to get

$$\delta_{21} = \langle x_{HI} \rangle + b_1\delta_1 + b_2\delta_1^2 + b_{21,v^2}\delta_{v^2} \tag{2.10}$$

where $b_{21,v^2} \equiv \langle x_{HI} \rangle [b_{\rm HI,v^2} + b_{\rho,v^2}]$. Taking the Fourier transform of both sides of Equation 2.10 and squaring gives[5], assuming cross-terms are negligible,

$$P_{21}(k) = b_{21,v^2}^2 P_{v^2}(k) + b_1^2 P_1(k) + b_2^2 P_2(k) \tag{2.11}$$

where P_1 and $P_2 \propto P_1 \star P_1$ are the first and second order total matter power spectra, respectively, and $P_{v^2}(k)$ is the Fourier transform of $\langle \delta_{v^2}(\boldsymbol{x}) \delta_{v^2}(\boldsymbol{x} + \boldsymbol{r}) \rangle$. [70] found that the linear and quadratic density fields are uncorrelated on all scales because δ_1 $(\delta_1)^2$ have odd (even) dependence on v_{bc}. By the same reasoning, δ_1 and δ_{v^2} should be uncorrelated as well. Thus our assumption of negligible cross-terms is exact for the terms involving δ_1. As long as the cross-term between the quadratic terms is sub-dominant to $b_2^2 P_2(k)$, we may safely ignore it when comparing the v_{bc} term to the contribution from the density terms, as we will do shortly[6]. Figure 2.5 plots the dimensionless power spectra ($\Delta^2 \equiv k^3 P(k)/2\pi^2$) for δ_1, δ_1^2, and $v_{\rm bc}^2$ at redshifts 5.8, 8, and 10 (note that P_{v^2} is independent of redshift). For all times shown here, $P_{v^2} > P_1 > P_2$ for $k < 5 \times 10^{-1}$ hMpc^{-1}, with the differences growing larger

[5]Note that the zeroth-order term becomes a delta function at $k = 0$ in Fourier space and thus does not contribute.

[6]The neglected cross term will either be featureless and can therefore be absorbed into the δ^2 term or will have BAO features, in which case it may contribute to the signal we are studying. In either case, we can ignore it as long as it is small.

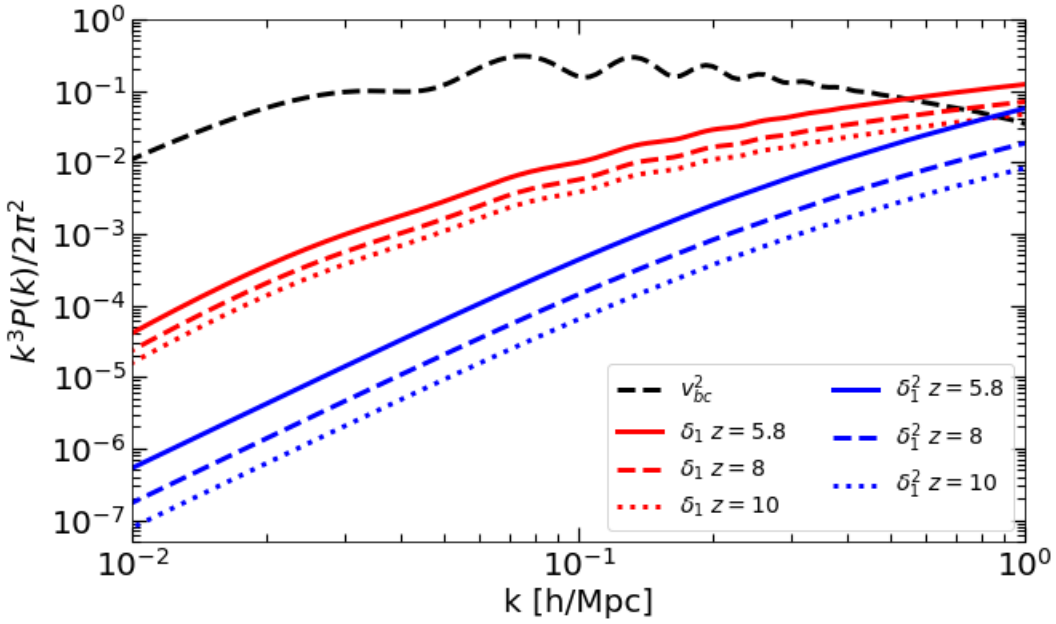

Figure 2.5: Comparison of the power spectra entering Equation 2.11 at redshifts 5.8 (solid curves), 8.0 (dashed curves), and 10 (dotted curves). P_{v^2} (black dashed curve) is the same at all three redshifts. At scales $k < 5 \times 10^{-1}$ h^{-1}Mpc, P_{v^2} dominates over the matter terms.

for with increasing redshift and decreasing k. Moreover, P_{v^2} shows strong baryon acoustic oscillation (BAO) features, suggesting that it's appearance in P_{21} would be distinct even if it only contributes to the total signal at the $\sim 10\%$ level.

Figure 7 of MQ18 shows how b_1 and b_2 evolve with time for three idealized models of Reionization. t. The signal reaches a maximum amplitude when b_1^2 is largest (since the P_1 term dominates). Depending on the model, the maximum value of b_1^2 is between 0.5^2 and 2^2, at which time $b_2^2 \sim 0 - 3^2$. As discussed in 2.4.1, there is a time early in Reionization when $b_1^2 = 0$, and the amplitude of P_{21} is dominated by the second order term, with $b_2^2 \sim 1 - 2^2$. In Figure 2.6, we show how the $v_{\rm bc}$ term impacts P_{21} in two representative

cases for several values of b^2_{21,v^2}. In the top left panel, we plot the signal at $z = 8$ assuming $b_1^2 = b_2^2 = 1$, representative of the P_{21} maximum, with $b^2_{21,v^2} \in \{0, 10^{-4}, 10^{-3}, 10^{-2}, 10^{-1}\}$. The top right panel shows the same plot at $z = 10$, $b_1^2 = 0$, and $b_2^2 = 1$, representative of the P_{21} minimum, with $b_{21,v^2} \in \{0, 10^{-6}, 10^{-5}, 10^{-4}, 10^{-3}\}$. The bottom panels show the range of $b^2_{21,v^2} P_{v^2}$ as a fraction of the total signal without $v_{\rm bc}$ for the bias parameters considered in the top panel. At the P_{21} maximum, $b^2_{21,v^2} > 10^{-3}$ is required to produce a $\sim 10\%$ effect on the signal at 10^{-1} Mpc/h, whereas at the P_{21} minimum the same effect is achieved with $b^2_{21,v^2} > 10^{-4}$. The takeaway here is that $v_{\rm bc}$ has its largest fractional effect at the P_{21} minimum, where the linear contributions from density and ionization cancel, and P_{21} is set by higher order terms in the bias expansion.

We emphasize that the results shown in Figure 2.6 are entirely agnostic about the *cause* of b_{21,v^2}. In general, we can write

$$b_{21,v^2} = \langle x_{HI} \rangle \left[b_{\rho,v^2} + b^{\rm sink}_{HI,v^2} + b^{\rm source}_{HI,v^2} \right] \tag{2.12}$$

where the second and third terms come from $v_{\rm bc}$'s impact on the sink and source properties, respectively. In what follows, we will make the assumption that b_{ρ,v^2} is essentially 0, since $v_{\rm bc}$ does not affect the shape of the linear matter power spectrum at scales near 10^{-1} hMpc^{-1} (T10). In the next two subsections, we will derive a rigorous model for the contribution to b_{21,v^2} from ionizing photon sinks informed by our simulation results in § 2.3, and assess analytically the potential contribution from sources.

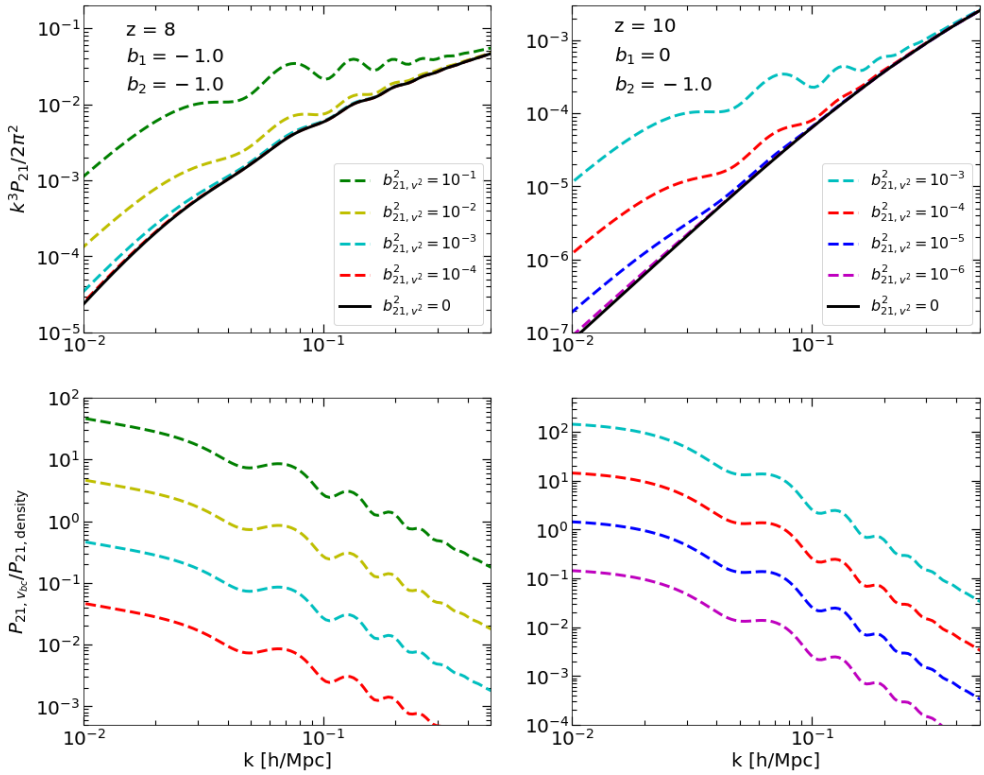

Figure 2.6: Top Left: Dimensionless 21 cm power spectrum at $z = 8$ for $b_1^2 = b_2^2 = (-1.0)^2$ for $b_{21,v^2}^2 = 0$ (solid black), 10^{-4} (red), 10^{-3} (cyan), 10^{-2} (yellow), and 10^{-1} (green). This plot shows a conservative estimate of P_{21} near its maximum. Top Right: The same at $z = 10$ for $b_1^2 = 0$, $b_2^2 = 1$, and $b_{21,v^2}^2 = 0$ (solid black), 10^{-6} (magenta), 10^{-5} (blue), 10^{-4} (red), and 10^{-3} (cyan). This plot shows an estimate of P_{21} at its minimum. The bottom panels show the $v_{\rm bc}$-sourced component as a fraction of the signal without $v_{\rm bc}$ for each of the bias factors.

2.4.3 A Model for b_{21,v^2} from Sinks

In this section, we present our model for the contribution to b_{21,v^2} from the sinks, which we can evaluate using the simulation results presented in § 2.3. Our approach is to relate fluctuations in $v_{\rm bc}^2$ to fluctuations in the ionized fraction x_i via the effect on the

clumping factors that we measure from our simulations. From this relationship, we will derive an expression for the sinks bias $b^{\rm sink}_{\rm HI,v^2}$ and relate this to the corresponding 21 cm sinks bias $b^{\rm sink}_{21,v^2}$.

We begin with the reionization "accounting equation", given by [97],

$$\dot{x}_i = \frac{\epsilon}{n_{\rm H}} - \langle C_{\rm R}\rangle \alpha_B n_e x_i \tag{2.13}$$

where $\langle C_{\rm R}\rangle$ is given by

$$\langle C_{\rm R}\rangle(t) = \int_{z_0}^{z(t)} dz_{\rm re} \mathcal{P}_{z_{\rm re}}(x_i(t)) \int_0^\infty dv_{\rm bc} \mathcal{P}_{v_{\rm bc}} C_{\rm R}(z_{\rm re}, v_{\rm bc}, t) \tag{2.14}$$

Here, ϵ is the emissivity of ionizing photons, x_i is the ionized fraction, and n_e, $n_{\rm HII}$, and $n_{\rm H}$ are the mean free electron density, HII number density, and H number density, respectively. The integral runs from the start of Reionization at z_0 to redshift $z(t)$. The clumping factor, $C_{\rm R}(z_{\rm re}, v_{\rm bc}, t)$, which depends on the local values of $v_{\rm bc}$ and $z_{\rm re}$, is extracted directly from our simulations. Equation 2.3 gives $\mathcal{P}_{v_{\rm bc}}$, and $\mathcal{P}_{z_{\rm re}}(x_i(t))$ is the probability distribution of $z_{\rm re}$,

$$\mathcal{P}_{z_{\rm re}}(x_i(t)) = \frac{dx_i/dz_{\rm re}}{x_i(t) - x_i(z_0)} \tag{2.15}$$

Note that $\langle C_{\rm R}\rangle$ depends on the ionization history $x_i(t)$ through $\mathcal{P}_{z_{\rm re}}(x_i(t))$; this is how our model accounts for the "patchiness" of Reionization. However, there are two important dependencies missing from Equation 2.14: Γ_{-12} and the local over-density. Because Reionization proceeds "inside-out" i.e. moves from higher to lower density regions [98, 99, 100] over-dense regions are more likely to ionized at higher z. Because these regions have a higher density of sources, they will also have higher-than average Γ_{-12}, and the impact of

v_{bc} will be different from what we measure here at mean density. The top right panel of Figure 2.3 shows that the relative v_{bc} effect is slightly larger for higher Γ_{-12} at $z_{\rm re} = 12$, with the difference disappearing at lower $z_{\rm re}$. Density fluctuation on scales larger than our simulation boxes (so-called "DC modes", see [101]) can be accounted for by re-scaling the local redshift (as was done in D20). The effect of increasing the box-scale overdensity should thus be similar to that of lowering $z_{\rm re}$, so we expect a modestly reduced v_{bc} effect in these patches based on Figure 2.3. We therefore suggest that the effect early in Reionization should be similar to what we calculate here for the mean density case, since higher Γ_{-12} and higher density the first patches to ionize drive the effect in opposite directions. We also note that X-Ray pre-heating could reduce the effect studied here, since it reduces clumping on the same scales as the stream velocity (see § 2.3.2). If X-rays and v_{bc} impact the same physical scales (i.e. the Jeans scale), the v_{bc} effect might be substantially reduced by X-rays. However, D20 found that pre-heating by X-rays impacts clumping by a factor of 2 as an upper limit, suggesting that the effect on the sinks bias is likely not much more than this. A factor of 2 reduction in the sinks bias would result in a factor of 4 reduction in the stream velocity contribution to the 21 cm power spectrum.

We perturb Equation 2.13 by assuming it holds for a spherical patch of the IGM of radius r with mean ionized fraction $x_i^r \equiv \langle x_i \rangle (1 + \delta_{x_i}^r)$ and clumping factor $C_{\rm R}^r = \langle C_{\rm R} \rangle (1 + \delta_{C_{\rm R}}^r)$. In doing so, we take Equation 2.13 to be locally true within the patch. This is only strictly true if the MFP of ionizing photons is $<< r$. Since we are primarily interested in the range 10^{-2} hMpc$^{-1} < k < 10^{-1}$ hMpc^{-1}, we will take 60 h^{-1}Mpc $< r <$ 600

h^{-1}Mpc for the perturbation scale. Figure 11 of D20 shows how the MFP in ionized regions evolves with time for our assumed ionization history (their solid red curve). For $\Gamma_{-12} = 0.3$, MFP $<<$ 60 h^{-1}Mpc at $z = 10$ and at $z = 8$ it is still an order of magnitude smaller. In the $\Gamma_{-12} = 3.0$ case, the MFP is only a factor of ~ 5 less at $z = 10$ and is comparable to 60 h^{-1}Mpc at $z = 8$. However, since this is the MFP for *ionized* regions only, the MFP with neutral regions included will be considerably smaller, especially early in Reionization. Moreover, typical values for Γ_{-12} extracted from the Lyα forest are in the range $0.3 - 0.5$ with spatial variations by a factor of a few around this value [102, 79, 103]. We therefore expect that Equation 2.13 holds locally on the perturbation scales we consider during the majority of the EoR.

Since Equation 2.13 is also satisfied by the IGM mean values $\langle x_i \rangle$ and $\langle C_{\rm R} \rangle$, we can solve for the perturbation $\delta^r_{x_i}(t)$ (see Appendix A.1 for details). Assuming $\mathcal{P}_{z_{\rm re}}(x_i(t))$ is roughly scale-independent, we may write

$$\delta^r_{x_i}(t) = b_{x_i,v^2}(t)\delta^r_{v^2} \tag{2.16}$$

where $\delta^r_{v^2}$ is time-independent and $b_{x_i,v^2}(t)$ is scale-independent. An expression for $b_{x_i,v^2}(t)$ can be obtained by Taylor-expanding $\delta^r_{C_{\rm R}}$ to first order in $\delta^r_{v^2}$. Since $b_{{\rm HI},v^2} = -\langle x_i \rangle / \langle x_{\rm HI} \rangle b_{x_i,v^2}$ and $b_{21,v^2} = \langle x_{\rm HI} \rangle b_{{\rm HI},v^2}$, we have

$$b^{\rm sink}_{21,v^2} = -\langle x_i \rangle b_{x_i,v^2} \tag{2.17}$$

Hence, we obtain a model for the $v_{\rm bc}$ term in Equation 2.11. The assumption of a scale-independent $\mathcal{P}_{z_{\rm re}}(x_i(t))$ is valid provided that spatial fluctuations in $\mathcal{P}_{z_{\rm re}}(x_i(t))$ on the per-

turbation scale are small compared to the global mean (given by plugging $\langle x_i \rangle$ into Equation 2.15) at each redshift. This is not immediately obvious because $\delta^r_{x_i}$ implicitly contains not only the $v_{\rm bc}$ perturbation term, but also matter terms analogous to those in Equation 2.10. So, it is important to check that $\mathcal{P}_{z_{\rm re}}(x_i(t))$ is roughly homogeneous on the scales considered here. Figure 3 of [104] plots the distribution of $z_{\rm re}$ for three different models of Reionization. In these plots, the distribution of $z_{\rm re}$ appears to be roughly homogeneous at scales $r > 60\ h^{-1}$Mpc, justifying our approximation of a scale-independent bias factor.

To compute $b^{\rm sink}_{21,v^2}$ from our simulations, we must first solve Equation 2.13 for $\langle x_i \rangle$ and $\langle C_{\rm R} \rangle$ by plugging in our simulation results for $C_{\rm R}(z_{\rm re}, v_{\rm bc}, t)$ in Equation 2.14. The integral over $v_{\rm bc}$ in this equation can be done via Gaussian Quadrature as discussed in 2.2.3. Integrating over $z_{\rm re}$ requires interpolating in two dimensions between the $z_{\rm re} = 12$, 8, and 6 $C_{\rm R}$ data as was done in D20 (see their Figure 11). To solve Equation 2.13, we assume the uniform emissivity function from [105] for ϵ and that n_e and $n_{\rm H}$ assume their cosmological mean values at each redshift. Once we have the global history, we can compute the bias (see Appendix A.1). Figure 2.7 shows the results of this exercise for several Reionization histories. The left panel plots $|b^{\rm sink}_{21,v^2}|^2$ vs. x_i for each history and the right panel plots x_i vs. redshift. Our fiducial history (red solid curve) starts Reionization at redshift $z_0 = 12$ and uses the $C_{\rm R}(z_{\rm re}, v_{\rm bc}, t)$ from our simulations with $\Gamma_{-12} = 0.3$. We also include histories using $C_{\rm R}(z_{\rm re}, v_{\rm bc}, t)$ from our $\Gamma_{-12} = 3.0$ simulations ("High Γ_{-12}", solid cyan), $z_0 = 10$ (Late Start, magenta dashed), an emissivity that is 50% higher ("High Emissivity", blue dashed). Lastly, we include a "Best Case" model (green dashed, discussed below) in which

the first $\sim 10\%$ of the IGM is ionized almost instantly, and we take $C_{\rm R}(z_{\rm re}, v_{\rm bc}, t)$ from our $\Gamma_{-12} = 3.0$ simulations.

The bias squared varies in the range $10^{-6} - 10^{-5}$ depending on ionization history near $x_i = 0.1$, but approaches a few times 10^{-5} in all histories by $x_i = 0.5$. The bias factor is only modestly sensitive to the pace at which Reionization proceeds. Our fiducial and high Γ_{-12} models have the same emissivity function, so they proceed at the same pace early, the latter ending slightly later due to increased recombinations. Re-ionization proceeds more quickly in the other three models, ending at the same time as the fiducial model except for the high emissivity case. However, the late start and high emissivity models have bias factors that evolve similarly with ionized fraction to the fiducial model.

The Best-Case model, by construction, provides a rough upper limit on $b_{21,v^2}^{\rm sink}$ at an ionized fraction of $10 - 15\%$, which is around the value of x_i for which P_{21} reaches a minimum, where $v_{\rm bc}$ has its largest fractional effect. This is because the "flash-ionized" patches reach the time at which the $v_{\rm bc}$ effect is largest coherently, so they contribute maximally to $b_{21,v^2}^{\rm sink}$ all at once. However, even in this case the bias squared is only a factor of ~ 2 larger than the physically realistic history with the higher Γ_{-12} value. We therefore do not expect the pace and duration of Reionization to significantly impact the sinks bias (although note that we do not consider histories here that begin earlier than z = 12). This highlights the relative insensitivity of the sinks bias to details of the Reionization history and the properties of the ionizing sources that drove it.

To get a 1% level effect in $P_{21}(z = 8)$ at $k = 10^{-1}$ h/Mpc would require $|b^{\rm sink}_{21,v^2}|^2 \sim 10^{-4}$ (see Figure 2.6), so for any of these histories the effect would be sub-percent level at the epoch of maximum P_{21}. Even at $k \sim 10^{-2}$ Mpc/h, where the difference between P_{v^2} and the linear terms is much larger, the effect would still only be a few percent for the bias factors measured here. However, at the epoch of minimum P_{21} the results are more promising. The Best Case model gives $|b^{\rm sink}_{21,v^2}|^2 \approx 10^{-5}$ at this time, which is enough to change the signal by a few percent at 10^{-1} h/Mpc and by $\sim 100\%$ at 10^{-2} h/Mpc. The other histories (which are physically realistic) give a $\sim 1\%$ effect at 10^{-1} h/Mpc and tens of percent at 10^{-2} h/Mpc. Note that the curves in the left panel of Figure 2.7 are very similar (even at low ionized fraction) despite the significant differences in the ionization histories in the right panel. This suggests that the sinks bias is constrained to be $|b_{21,v^2}|^2 \sim 10^{-6} - 10^{-5}$ regardless of the details of Reionization, e.g. the nature of the source population. As we will see in the next section, this is not true of the $v_{\rm bc}$ term coming from the sources themselves.

2.4.4 Contributions to b_{21,v^2} from Sources

Here, we discuss possible contributions to the source bias, $b^{\rm source}_{21,v^2}$. Since our simulations do not model the sources, we will proceed analytically and use results from the literature where appropriate. Previous work has demonstrated that $v_{\rm bc}$ has an important effect on the star formation rate in "minihalos," with masses $10^6 - 10^8$ $M_\odot$, within which it is believed the first stars (Pop III) formed ([67, 69, 68, 72], to name a few). Primarily, $v_{\rm bc}$ raises the minimum halo mass able to form stars, thereby modulating the radiation backgrounds produced. As a result, $v_{\rm bc}$ could modulate the 21 cm spin temperature T_s

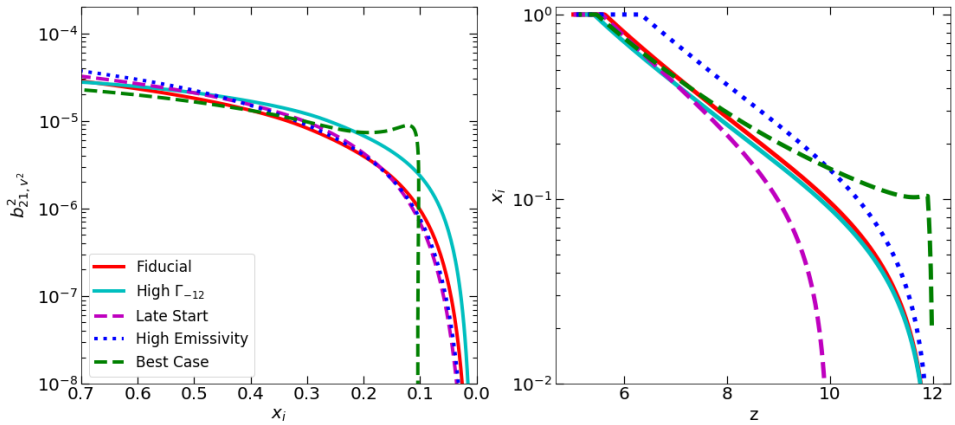

Figure 2.7: Left: $|b^{\rm sink}_{21,v^2}|^2$ vs. ionized fraction for each of the EoR histories discussed in the text. At low ionized fractions, the bias varies in the range $10^{-6} - 10^{-5}$ between the different models, but settles down to a few $\times 10^{-5}$ for all the models late in Reionization. None of these models produce bias factors large enough to produce a detectable signal at the epoch of 21 cm maximum (see Figure 2.6). At the 21 cm minimum near $x_i = 0.13$, the Best-Case model gives $|b^{\rm sink}_{21,v^2}|^2 \approx 10^{-5}$, which would alter the minimum signal by a few percent at $k = 10^{-1}$ hMpc^{-1} and by a factor of 2 at $k = 10^{-2}$ hMpc^{-1}. Among the physically realistic histories, the one with high Γ_{-12} gives the largest bias. Right: The ionized fraction as a function of redshift for each history. Note that Γ_{-12} changes the ionization history very little early on, but raises $|b^{\rm sink}_{21,v^2}|^2$ by a factor of $\sim 2 - 3$ for low ionized fractions.

near the start of Reionization. This could change the signal significantly if the assumption $T_s >> T_{\rm CMB}$ is not valid near the start of Reionization, which would introduce an extra factor of $1 - T_{\rm CMB}/T_s$ in Equation 2.5. Additionally, the suppression of ionizing photon production by $v_{\rm bc}$ would work opposite the direction of the sinks by slowing down Reionization locally, thereby increasing the 21 cm signal in patches with higher $v_{\rm bc}$. Although it is widely believed that halos more massive than 10^8 $M_\odot$ (which are less affected by $v_{\rm bc}$) drove Reionization, the degree to which Pop III star formation in minihalos contributed to its early phases is highly uncertain. In this section we continue to assume $T_s \gg T_{\rm CMB}$ and we attempt to quantify the coupling of P_{v^2} with P_{21} through the source bias, $b_{21,v^2}^{\rm source}$.

To estimate the impact of $v_{\rm bc}$ on halos, we begin with a general expression for the star formation rate density (SFRD) during Reionization ([106, 9]).

$$\dot{\rho}_{\rm SFRD} = \int_{M_{\rm c}(v_{\rm bc})}^{\infty} dM n(M) f_\star(M) \dot{M} \frac{\Omega_b}{\Omega_m} \tag{2.18}$$

where $n(M)$ is the halo mass function, $\dot{M}$ is the halo accretion rate, and $f_\star(M)$ is the mass-dependent star formation efficiency. This integral contains contributions from both Population II and III stars, with the mass cutoff at $M_{\rm atom} \equiv M_{\rm vir}(T_{\rm vir} = 10^4 \text{ K})$, is the atomic cooling threshold, given by inverting Eq. 26 of [107]. For the lower limit $M_{\rm c}(v_{\rm bc})$, we assume

$$M_c(v_{\rm bc}, z) = M_{\rm vir}(500 \text{ K}, z) \times \left(\frac{V_{\rm cool}(z, v_{\rm bc}, J_{\rm LW} = 0)}{V_{\rm cool}(z, v_{\rm bc} = 0, J_{\rm LW} = 0)} \right)^3 \times [1 + B(4\pi J_{\rm LW})^\beta] \tag{2.19}$$

where $J_{\rm LW}$ is the specific intensity of the Lyman-Werner (LW) background in units of 10^{-21}erg/s/cm^2/Hz/sr, $(B, \beta) = (7, 0.47)$ for the regular feedback model in [72], and

$V_{\rm cool}(z, v_{\rm bc}, J_{\rm LW} = 0)$ is the minimum circular velocity for star formation in the absence of LW feedback, derived from simulations by [68] (their Eq. 2). To obtain $J_{\rm LW}$, we combine Eq. 8 of [108] with Eq. 6 of [69] and include the LW opacity correction from [9] to obtain

$$J_{\rm LW} = \frac{7.28}{4\pi} \times \frac{(1+z)^3}{H(z)} e^{-\tau_{\rm LW}} (N_{\rm LW}^{\rm II} \dot{\rho}_{\rm SFR}^{\rm II} + N_{\rm LW}^{\rm III} \dot{\rho}_{\rm SFR}^{\rm III}) \tag{2.20}$$

where we take $N_{\rm LW}^{\rm II} = 9690$, $N_{\rm LW}^{\rm III} = 10^5$, nd $e^{-\tau_{\rm LW}} = 0.5$ following [9] and the units of $H(z)$ and SFRD are km/s/Mpc and $\rm M_\odot/yr/Mpc^3$, respectively. For $f_\star(M)$, we used the form in [109] for Pop III stars (their Eq. 2) and the form in [110] for Pop II stars (their Eq. 10), where we have tuned the parameters of the latter to give Pop II SFRDs that agree well with the results of [111]. The Pop III star formation efficiency at $M_{\rm atom}$, $f_\star^0$, is a free parameter in our model. To evaluate Equation 2.18, we use the Sheth-Torman mass function and the halo accretion rate given by [112] (their Eq. 11) which is calibrated from high-redshift simulations. Since $J_{\rm LW}$ and $\dot{\rho}_{\rm SFR}$ are interdependent, we use an iterative scheme to simultaneously solve for them given a value of $f_\star^0$.

Following the same formalism as [67] (see their section 2 for details), it can be shown that

$$\dot{\rho}_{\rm SFR} = \langle \dot{\rho}_{\rm SFR} \rangle (1 + b_{\rm SFR,v^2} \delta_{v^2}) \tag{2.21}$$

where

$$b_{\rm SFR,v^2} = -1 + \frac{\langle v_{\rm bc}^2 \dot{\rho}_{\rm SFR} \rangle}{\sigma_{bc}^2 \langle \dot{\rho}_{\rm SFR} \rangle} \tag{2.22}$$

and the averages are over $\mathcal{P}_{v_{\rm bc}}$. Depending on the magnitude of $J_{\rm LW}$, M_c may be larger or smaller than this cutoff, so we will include contributions from both populations of stars to the bias. From here, we can work out an expression for $b_{21,v^2}^{\rm source}$ using the same strategy

as in §2.4.3, but this time by perturbing the emissivity term in Equation 2.13. Using the emissivity model in [9], we can write these fluctuations as

$$\frac{\langle\epsilon\rangle}{n_{\rm H}}\delta_\epsilon = A_{He}N_{\rm ion}^{\rm III}f_{\rm esc}^{\rm III}\langle\rho_m^{-1}\dot{\rho}_{\rm SFR}^{\rm III}\rangle b_{{\rm SFR,v}^2}^{\rm III}\delta_{v^2} \equiv b_{\epsilon,v^2}^{\rm III}\delta_{v^2} \tag{2.23}$$

where $A_{\rm He} = 1.22$, $N_{\rm ion}$ is the number of ionizing photons produced per stellar baryon, $f_{\rm esc}$ is the escape fraction, and $\rho_m = \Omega_m\rho_{\rm crit}(z=0)$ is the present-day matter density of the universe. For Pop III stars we assume $f_{\rm esc} = 0.5$ and $N_{\rm ion} = 40000$. We do not include a contribution from Pop II stars to the bias because these stars are expected to form in atomic cooling halos that are unaffected by LW feedback [68]. We therefore do not expect $v_{\rm bc}$ by itself to raise the minimum circular velocity for star formation in these halos above the threshold set by the atomic cooling limit. If we ignore the recombination term in Equation 2.13, the 21 cm bias $b_{21,v^2}^{\rm source}$ is simply the time integral over $b_{\epsilon,v^2}^{\rm III}$. We start this integral at $z = 30$, which is early enough to account for the full cumulative impact of Pop III stars on the signal (see [72]). Note that this bias factor has the opposite sign of the sinks bias because $v_{\rm bc}$ *reduces* the number of ionizing photons being produced.

The left panel of Figure 2.8 shows the result of this exercise for $f_\star^0 = 10^{-3}$ (cyan-dashed) and a range of $f_\star^0$ going from 10^{-4} to 10^{-2} (pink shaded band). This range brackets the values generally considered in the literature (e.g. [113, 114, 9, 111]) as well as other sources of uncertainty (see below). At $z = 10$ for $f_\star^0 = 10^{-3}$, the source bias is comparable to the sinks bias ($\sim$ a few times 10^{-6}) and spans a range of about 2 orders of magnitude above and below this (since $|b_{21,v^2}^{\rm source}|^2 \propto |f_\star^0|^2$). The right panel shows the average SFRD for both populations of stars, with the range given for Pop III corresponding to the range of

bias factors in the left panel. The Pop III SFRDs in our model agree reasonably well with those in [111] for the same Pop III star formation efficiencies[7]. Note that the bias shown in Figure 2.8 is formally an upper limit because we neglected the recombination term in Equation 2.13. It is therefore likely that the source bias is less important than the sinks bias early in the EoR[8]. However, the result above depends strongly on the assumed values of $f_\star^0$, as well as on how the critical mass M_c is modeled, the assumed accretion rate $\dot{M}$, and the exact relationship between star formation rate and $J_{\rm LW}$. For example, weaker LW feedback will result in a larger bias, and a smaller minimum Pop III star formation mass (in the absence of $v_{\rm bc}$ or $J_{\rm LW}$) will increase the bias as Pop III stars will play a larger role in Reionization. In light of these large uncertainties, we cannot draw definitive conclusions about the magnitude of the EoR source bias. Note that these uncertainties highlight the relative precision of our model for the sinks bias.

The case in which $T_s \gg T_{\rm CMB}$ does not hold is even more difficult to assess. In this work, we employed the common assumption (e.g. [73, 115, 116, 93]) that by the time Reionization starts, T_s has been coupled to the gas temperature T_K such that $T_s >> T_{\rm CMB}$, as assumed in Equation 2.5. However, some recent models (e.g. [117, 118, 119]) suggest that this assumption may not hold at the start of Reionization. This could be either because Lyα photons are inefficient at coupling T_s to the gas temperature, or because heating by

[7]That work assumed a constant Pop III $f_\star$, but because ours depends rather weakly on mass, their $f_{\rm III}$ corresponds closely with our $f_\star^0$

[8]Note that [72] finds much larger effective bias factors at $z \sim 20$ than we show in Figure 2.8. However, in that work, the main source of coupling between v_{bc} and P_{21} was the coupling between spin temperature and gas temperature rather than between emissivity and ionized fraction. We briefly address the possibility of spin temperature fluctuations below.

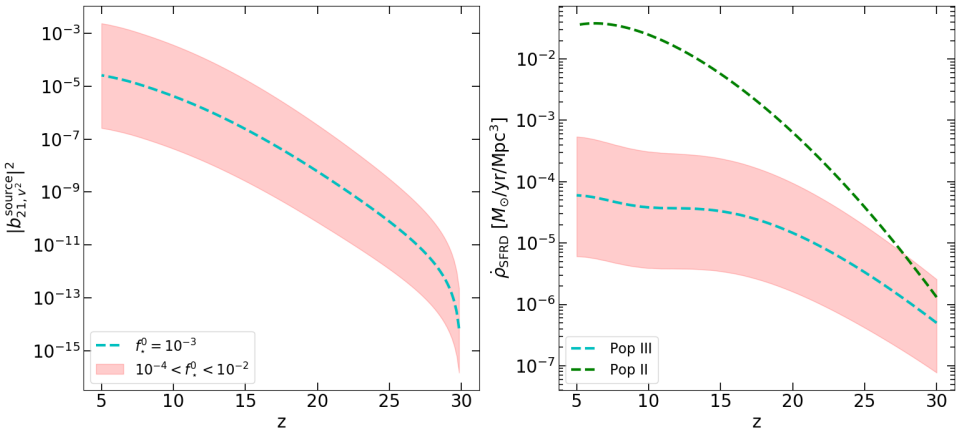

Figure 2.8: Left: source bias squared for $f_\star^0 = 10^{-3}$ (cyan), and the range $10^{-4} < f_\star^0 < 10^{-2}$ (red band). The bias grows with increasing $f_\star^0$, and spans 4 orders of magnitude over the range we consider here for that parameter. Right: SFRD for pop III and II stars in our model for the same range of $f_\star^0$ shown in the left panel. For that choice of $f_\star^0$, our star formation efficiency parameters for both populations are similar to the fiducial values used in that work.

X-rays is not efficient enough to raise the gas temperature well above $T_{\rm CMB}$ (see [115] for a detailed study). In either scenario, to first order Equation 2.5 would be multiplied by a factor $1 - \frac{T_{\rm CMB}}{\langle T_s \rangle} + \frac{T_{\rm CMB}}{\langle T_s \rangle}\delta_{T_s}$. The fluctuation δ_{T_s} would occur because higher $v_{\rm bc}$ would reduce the production of X-Rays and Lyα photons by Pop III stars[9]. This bias would work in the same direction as the sinks bias because it would reduce the amplitude of the 21 cm signal in regions with higher $v_{\rm bc}$. For reionization models in which $T_{\rm CMB} = \langle T_s \rangle$ occurs early in reionization, the signal at that time would be dominated to linear order by the δ_{T_s} term, which may trace δ_{v^2}. This may offer another window of time during Reionization at which $v_{\rm bc}$ could be detectable. Estimating the magnitude of this effect is beyond the scope of this paper, so we leave it to future research.

[9]We note that previous work (e.g. [69, 72]) has studied this effect at $15 < z < 30$, but not during Reionization.

2.4.5 Detectability of $v_{\rm bc}$

Here we briefly discuss the detectability of the expected signal near the EoR 21 cm minimum (where the fractional effect of $v_{\rm bc}$ is likely to be largest). Cosmological 21 cm experiments like the Square Kilometer Array (SKA, [120]) and the Hydrogen Epoch Reionization Array (HERA, [121]) are expected to be able to probe the scales discussed here with much higher sensitivity than current experiments, which are struggling to detect the EoR signal at its maximum (EDGES, LOFAR, etc.). [122] show, in their Figure 1, the levels of noise in the dimensionless 21 cm brightness power spectrum Δ_b^2 expected for several 21 cm experiments at $z = 8.5$ assuming 1000 hours of integration, including SKA and HERA. In the best-case scenario of thermal noise only, they find uncertainties of $\approx 2 \times 10^{-2}$ (1×10^{-2}) mK^2 for SKA (HERA) at the smallest wavenumber that both experiments can detect, $k = 0.06\ h\mathrm{Mpc}^{-1}$. Assuming the thermal noise power spectrum scales as $\nu^{-2\alpha}$ where $\alpha = 2.55$ [123], the thermal noise will be larger by a factor of ~ 2.1 at $z = 10$ than at $z = 8.5$. The resulting uncertainties are a factor of $\sim 2(4)$ larger than the density term for SKA (HERA) at this wavenumber; this ratio is roughly the same at $k = 0.1\ h\mathrm{Mpc}^{-1}$. This suggests that the signal near the 21 cm minimum is marginally below the current detection limit of SKA and HERA, assuming these modes are not inaccessible due to foregrounds (see [124] for a discussion of foreground contamination). We therefore suggest that future versions of these experiments may be able to detect the EoR 21 cm minimum signal at these wave-numbers if foregrounds can be removed.

Figure 2.9 illustrates the possible contribution of the $v_{\rm bc}$ sourced signal to the total at the EoR 21 cm minimum. The black-dashed line denotes the second-order density term

in Equation 2.11 with $b_2^2 = 1$ at $z = 10$. The blue (red) shaded regions denote the range of signal contributions from the sinks (sources) that we compute in § 2.4.3 (2.4.4). The blue solid line denotes $k = 0.06$ h/Mpc and the dotted magenta (green) lines roughly denote the thermal noise limits of SKA (HERA) at and above that wavenumber. At k = 0.06 h/Mpc, the sinks term contributes $3 - 17\%$ of the signal for an ionized fraction of 13% depending on the Reionization history and assumed value of Γ_{-12}. The lower end of this range comes from physically realistic histories with $\Gamma_{-12} = 0.3$, and the high end comes from our Best Case scenario and should be treated as an upper limit. A physically realistic history with $\Gamma_{-12} = 3.0$ gives a 7% effect. Figure 1 of [71] shows that this epoch of minimum power (which occurs in the range $8 < z < 14$ in that paper) should have a duration of at least several tenths of a redshift, which should be a long enough time interval to see the signal if it is detectable. As mentioned earlier, a more realistic model would take variations in the photo-ionization rate and local over-density with $z_{\rm re}$ into account, although it is likely that such an improved model would give the same order of magnitude effect (see discussion in § 2.4.3).

Despite these uncertainties, we suggest that a $\sim 5\%$ contribution to the signal from the sinks term is not unrealistic for $k = 0.06$ h/Mpc, provided the linear order term in Equation 2.10 is close to 0. At $k = 0.1$ h/Mpc, the relative contribution of the sinks term is a factor of ~ 5 lower than at 0.06 h/Mpc, so we expect a $\sim 1\%$ contribution at this wavenumber. Note that the range of percentages we find for the sinks term varies by only a factor of a few, whereas the source term varies by 4 orders of magnitude for the range of $f_\star^0$ we consider. We therefore interpret the sinks term as a lower bound on the $v_{\rm bc}$-sourced

signal, except in the very unlikely case that the source and sinks terms happen to exactly cancel each other. In addition to the these terms, there will be additional higher-order terms that will achieve their maximum influence at this time as well. MQ18 obtained a modestly improved fit to the 21 cm power spectrum using a 7 parameter perturbative model that includes all terms contributing to the power spectrum at 1-loop order (see their Eq. 3.4). However, these terms are quite featureless, so although they may contribute to the amplitude of the signal they are unlikely the mask the unique features in the stream velocity term. Additional cross terms between the stream velocity term and the higher order matter terms are likely to be much smaller than the stream velocity term. Even if these terms are important, they would likely be either featureless (like the matter terms) or contain the same BAO features as the targeted signal (see [125] for a detailed treatment of similar cross-terms in the context of the low-redshift galaxy power spectrum).

2.5 Summary

In this work, we studied the impact of baryon-dark matter relative velocities on the small-scale clumpiness of the IGM during reionization, and how this effect impacts the EoR 21 cm signal. Although the streaming velocities were small (~ 0.3 km/s) by the start of reionization, their cumulative effect from earlier times suppressed gas clumpiness, especially in regions where $v_{\rm bc}$ was previously large relative to the sound speed. To quantify these effects, we used high-resolution radiation hydrodynamics simulations that tracked the hydrodynamic response of the IGM to reionization. We found that the peak suppression of the clumpiness occurs within the first 5-10 Myr after the gas becomes mostly ionized, before

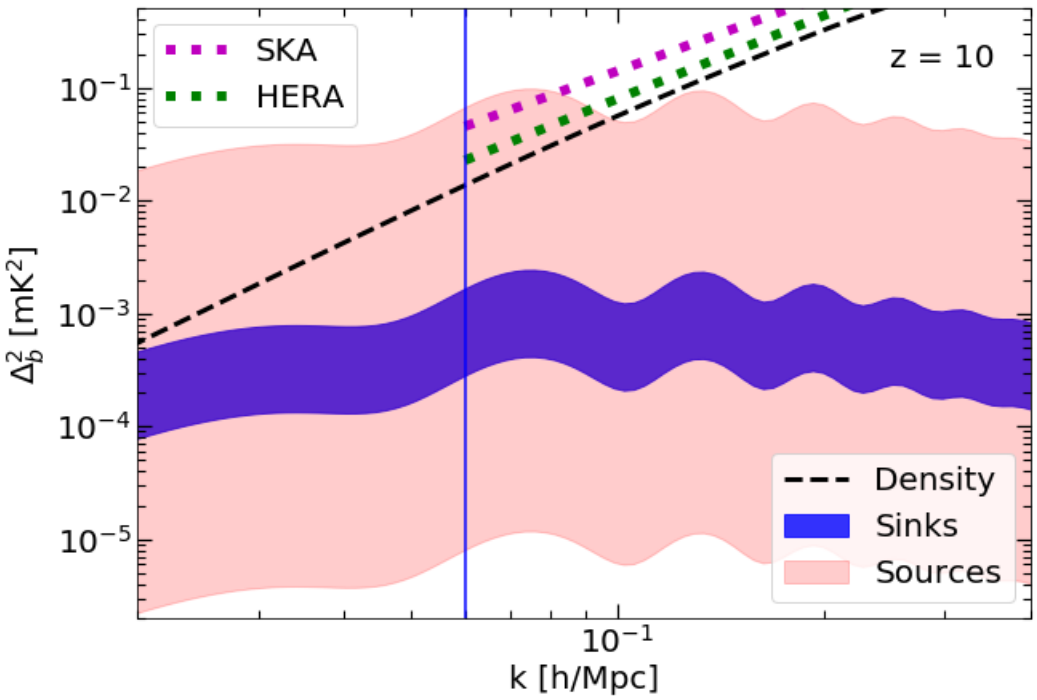

Figure 2.9: Components of the 21 cm brightness power spectrum at $z = 10$ when the signal is at its minimum during the EoR, using the same density bias parameters as in the upper right panel of Figure 2.6. We show the contribution from the second-order density term in Equation 2.11 with $b_2^2 = 1$ at $z = 10$ (black dashed). The blue (red) shaded region denotes the range of possible contributions from the sinks (sources) term discussed above at z = 10. The blue vertical line denotes $k = 6 \times 10^{-2}$ h/Mpc, and the magenta (green) dashed lines approximately denote the thermal noise limits of SKA (HERA) at and above that wavenumber.

the small-scale structure is erased by Jeans pressure smoothing of the gas. The clumping factor of ionized gas shows a peak suppression of $5-10\%$ in regions that had streaming velocities of 30 km/s at recombination (approximately the RMS value). Differences between regions with and without $v_{\rm bc}$ fall to the percent level by $\Delta t = 300$ Myr, after the gas has had sufficient time to relax in response to the photo-heating from reionization.

To quantify the impact of $v_{\rm bc}$ on the EoR 21 cm power spectrum, we constructed a model for the signal that includes a term coupling P_{21} to fluctuations in $v_{\rm bc}$ through a corresponding bias parameter. We modelled contributions to this parameter from ionizing photon sinks and sources. Using our simulation results for the former, we found that the contribution from sinks is relatively insensitive to the details of Reionization, as it is set mainly by the spectrum of primordial density fluctuations and pressure smoothing of the gas. We found that the characteristic BAO feature imprinted on P_{21} through coupling with the sinks is likely to appear at only the sub-percent level when P_{21} is at its maximum, roughly halfway through reionization. The feature is most pronounced at $\approx 10\%$ ionization, when P_{21} is at a minimum. At this time, the near cancellation of fluctuations in density and ionization allows power from higher-order terms (i.e. from $v_{\rm bc}$) to contribute more significantly. At the epoch of minimum P_{21}, we expect the BAO feature to appear at the 1% (5%) level at $k \sim 0.1$ (0.06) h/Mpc due to modulation of the sinks. The signal due to sources may be larger than this, but it is subject to a large uncertainty because it depends on poorly-constrained source properties like the star formation efficiency. At these wave numbers, the minimum P_{21} that we estimate is close to the thermal noise sensitivity limits

of 21 cm experiments like SKA and HERA, so the prospect of detecting the signal in the near future seems low. However, it may well be within the capability of the next generation of 21 cm instruments.

Chapter 3

A short mean free path at $z = 6$ favors late and rapid reionization by faint galaxies

There are several lines of evidence that reionization ended around $z = 6$, or perhaps later. The large Lyα forest opacity fluctuations at $z \geq 5.5$ have been attributed to neutral islands below $z = 6$ [38, 49, 50, 126, 127, 104, 128]. Other independent constraints from high-z Lyα emitter (LAE) surveys and quasar damping wing analyses also suggest a significantly neutral IGM at $z \sim 7$ [18, 21, 31, 33, 52, 32]. The reionization models invoked to explain these observations are consistent with the low value of Cosmic Microwave Background optical depth reported by Planck, $\tau_{\rm CMB} = 0.054 \pm 0.007$ [1]. Given large uncertainties in these measurements, however, it is unclear whether reionization was rapid or more extended in duration (e.g. [129]). In this letter, we argue that recent measurements of the mean free path at $5 < z \leq 6$ point to a reionization process that was both late and rapid.

The new evidence considered here was reported by [13] (hereafter B21). They extended direct measurements of the mean free path (MFP; $\lambda_{912}^{\rm mfp}$) to $z = 6$ and found a rather low value of $\lambda_{912}^{\rm mfp}(z = 6) = 3.57^{+3.09}_{-2.14}$ cMpc/h. This disfavors at the 97% level even the low MFP predicted by the "Low $\tau_{\rm CMB}$" model of [130], in which the IGM was still 20% neutral at $z = 6$ and reionization ended at $z \approx 5.3$. The B21 result suggests that ionizing photon sinks played a larger role than previous models have captured, and/or that the IGM was even more neutral at $z = 6$.

Recent theoretical work has demonstrated that modeling the sinks is complicated by the interplay between self-shielding and the hydrodynamic response of the IGM to photoheating [131, 74]. Before reionization, the gas clumps down to its Jeans scale, which in the ΛCDM cosmology can be as low as ~ 1 kpc. After ionization fronts (I-fronts) sweep through, the local density structure "relaxes" by Jeans smoothing and photoevaporative processes, evolving to a less clumpy state over a timescale $\Delta t \sim 200$ Myr. State-of-the-art radiative hydrodynamics (RHD) simulations have yet to fully bridge the scale gap between the sinks and the > 100 Mpc boxes necessary to converge on reionization observables [132]. In addition, the largest dynamic ranges have been achieved with moment-based radiative transfer (RT) methods, which may be numerically inaccurate in the sinks [133].

A key addition of this work is that we have developed a new sub-grid model for the sinks based on the study of ([74], hereafter D20). We have incorporated this into a new ray tracing RT code, giving our reionization simulations a formal dynamic range of over 5 orders of magnitude in scale. In this letter, we present first results from this new simulation framework and we use them to interpret the B21 measurements.

This letter is organized as follows. In § 3.1, we describe our numerical methods. In § 3.2 we present our results and we conclude in § 3.3.

3.1 Numerical Methodology

We ran RT simulations of reionization in a $(200h^{-1}$ cMpc$)^3$ volume using our new ray tracing code, which we will describe in detail elsewhere (Cain & D'Aloisio in prep.). We use a coarse-grained uniform RT grid with $N = 200^3$. The premise is to use a pre-run suite of highly resolved (small volume) RHD simulations to model the opacity evolution in each $(1h^{-1}$ Mpc$)^3$ RT cell during reionization.

3.1.1 Coarse-grained RT

Our monochromatic RT algorithm traces rays from source cells using an adaptive splitting and merging scheme based on [134] and similar to the procedure of [77]. We track 48 directions (HEALPix level 1) and use the full speed of light because the commonly adopted reduced-speed approximation leads to inaccuracies near the end of reionization. We propagate sub-grid "moving-screen" I-fronts across the coarse cells with speed $v_{\rm IF} = \frac{F}{(1+\chi)n_{\rm H}}$, where F is the incident ionizing flux, $n_{\rm H}$ is the proper H density, and $\chi = n_{\rm He}/n_{\rm H} \approx 0.082$ accounts for singly ionized helium. We assume that ray j intersecting cell i contributes photoionizations over a path length $x^i_{\rm ion}\Delta s^{ij}$, where $x^i_{\rm ion}$ is the cell ionized fraction and Δs^{ij} is the total path length of the ray through the cell. We further assume that the MFP in the ionized part of the cell takes a locally uniform value, $\overline{\lambda}^i$. The mean H photoionization rate there is

$$\Gamma^i_{\rm HI} = \sum_{j=1}^{N_{\rm rays}} \frac{N^{ij}_{\gamma,0}[1-\exp(-x^i_{\rm ion}\Delta s^{ij}/\overline{\lambda}^i)]\ /\ \Delta t}{x^i_{\rm ion}V_{\rm cell}\ /\ \overline{\sigma}_{\rm HI}\overline{\lambda}^i}, \tag{3.1}$$

where $N^{ij}_{\gamma,0}$ is the number of photons incident on the cell in a time Δt from ray j, $V_{\rm cell}$ is the cell volume, and $\overline{\sigma}_{\rm HI}$ is the H photoionization cross-section. The over-bars denote frequency averages. To compute these quantities, we assume a specific intensity of $J_\nu \propto \nu^{-1.5}$ between 1 and 4 Ry, consistent with models of young metal-poor stellar populations (e.g. [135]). The numerator of eq. 3.1 counts H ionizations per unit time. The denominator gives the number of HI atoms in ionized gas since $(\overline{\sigma}_{\rm HI}\overline{\lambda}^i)^{-1}$ is the $\Gamma_{\rm HI}$-weighted mean $n_{\rm HI}$. We tested this moving-screen framework against simulations of plane-parallel I-fronts similar to those in D20 (but with one domain) and found good agreement in the photon budget. For comparison against Lyα forest measurements, we track temperatures on the RT grid using the approximate method of [135]. We adopt their fit for the post I-front temperature, $T_{\rm reion}$, and the subsequent thermal evolution is modeled using their Eq. 6.

3.1.2 Sub-grid model for $\overline{\lambda}$

We extract $\overline{\lambda}$ from the RHD simulations of D20, which use $N_{\rm dm} = N_{\rm gas} = N_{\rm rt} = 1024^3$ dark matter particles and gas/RT cells in a $(1h^{-1}\ {\rm Mpc})^3$ box. These simulations are parameterized by three environmental quantities: the reionization redshift, $z_{\rm re}$, the impinging $\Gamma_{\rm HI}$, which quantifies the strength of the external ionizing background, and the box-scale linear over-density over its standard deviation, δ/σ. We have expanded the D20 suite to include all combinations of $\Gamma_{-12} \equiv \Gamma_{\rm HI}/10^{-12}{\rm s}^{-1} \in \{0.03, 0.3, 3.0\}$, $z_{\rm re} \in \{12, 8, 6\}$, and $\delta/\sigma \in \{-\sqrt{3}, 0, \sqrt{3}\}$. For cells reionized below $z_{\rm re} = 6$, we extrapolate logarithmically

in cosmic time. We tested our extrapolation against a simulation with $z_{\rm re} = 5.2$ and found good agreement. The frequency-averaged MFP is obtained using $\overline{\lambda^{-1}} = \langle n_{\rm HI}\Gamma_{\rm HI}\rangle_V / F$, where $\langle \ldots \rangle_V$ is a volume average.

The D20 simulations track the self-shielding and hydrodynamic response of the IGM in the wake of I-fronts sourced by a steady background (constant $\Gamma_{\rm HI}$). However, $\Gamma_{\rm HI}$ can evolve considerably in realistic environments. Using D20-style simulations with time-varying $\Gamma_{\rm HI}$, we have developed an empirical model for the evolution of $\overline{\lambda}$,

$$\frac{d\overline{\lambda}}{dt} = \frac{\partial\overline{\lambda}}{\partial t}\Big|_{\Gamma_{\rm HI}} + \frac{\partial\overline{\lambda}}{\partial\Gamma_{\rm HI}}\Big|_t \frac{d\Gamma_{\rm HI}}{dt} - \frac{\overline{\lambda} - \overline{\lambda}_{\rm eq}}{t_{\rm relax}}. \tag{3.2}$$

The first term on the right is the quantity measured from the D20 simulations – the evolution of $\overline{\lambda}$ at fixed $\Gamma_{\rm HI}$. The second term captures the instantaneous change in $\overline{\lambda}$ with $\Gamma_{\rm HI}$. The last term implements a relaxation timescale $t_{\rm relax}$ over which $\overline{\lambda}$ evolves towards an equilibrium value $\overline{\lambda}_{\rm eq}$ in response to a sudden increase in $\Gamma_{\rm HI}$. The $\frac{\partial\overline{\lambda}}{\partial t}\Big|_{\Gamma_{\rm HI}}$ term and $\overline{\lambda}_{\rm eq}$ are interpolated from the expanded D20 suite. When interpolating over $z_{\rm re}$, we correct for the I-front crossing time of the cell by averaging the opacity in the least and most recently ionized gas. For $\frac{\partial\overline{\lambda}}{\partial\Gamma_{\rm HI}}\Big|_t$, we assume a power law $\overline{\lambda} \propto \Gamma_{\rm HI}^{\xi}$, where $\xi = 2/3$. This form is motivated by [136], the constraints of B21, as well as our D20-style calibration simulations. Eq. 3.2 is integrated in fully ionized cells with $\Gamma_{-12} \geq 0.03$. In partially ionized cells or those with $\Gamma_{-12} < 0.03$, we set $\overline{\lambda} = \overline{\lambda}_{\rm eq}$. Since $\overline{\lambda}$ depends on Γ_{-12}, we iterate Eqs. 3.1-3.2 until convergence. The D20-style simulations that we used to calibrate Eq. 3.2 included up to $\times 100$ impulsive increases in Γ_{-12} as well as more realistic cases with gradual evolution. Eq. (3.2) captures $\overline{\lambda}(t)$ in the gradually time-varying-Γ simulations to better than a few percent, while a straight interpolation over-estimates it by 10-15%. Our impulsive tests

yielded similar levels of improvement. Consistent with the results of these tests, we use $t_{\rm relax} = 100$ Myr.

3.1.3 Density fields and source models

The RT sims were run on a coarse-grained version of the $(200h^{-1}$ Mpc$)^3$ hydrodynamics simulation in [79], which employed a modified version of the code of [76]. Density fields and halo catalogs were saved at time intervals of 10 Myr from $z = 12 - 4.5$. The halo mass functions are converged down to 2×10^{10} h^{-1}M$_\odot$, more massive than the smallest halos believed to have contributed to reionization. We extended our sources by generating sub-resolution halos down to $M_{\rm min} = 10^9$ h^{-1}M$_\odot$ using the nonlinear biasing method of [137], applied with the halo mass function of [112]. (As discused below, we have also run tests with $M_{\rm min} = 10^8$ h^{-1}M$_\odot$.) We used two models for the ionizing photon production rate of each halo: $\dot{n}_\gamma$ = constant (dependent only on z) and $\dot{n}_\gamma \propto$ UV luminosity ($L_{\rm UV}$), where $\dot{n}_\gamma$ is the number of photons per unit time produced by a halo. The former is our fiducial model, which assigns more weight to low-mass galaxies in the ionizing photon budget. As we will see, the motivation for this choice is that the short value of $\lambda_{912}^{\rm mfp}$(z=6) favors models in which reionization is driven by faint, less-biased sources. For the $L_{\rm UV}$ model, we abundance matched to the UV luminosity function of [129]. In both cases we chose the overall normalization of $\dot{n}_\gamma$ at each redshift to set the global emissivity history, $\dot{N}_\gamma(z)$. We varied $\dot{N}_\gamma(z)$ by trial and error to find reionization models consistent with the Planck $\tau_{\rm CMB}$ constraints and the mean free path measurements.

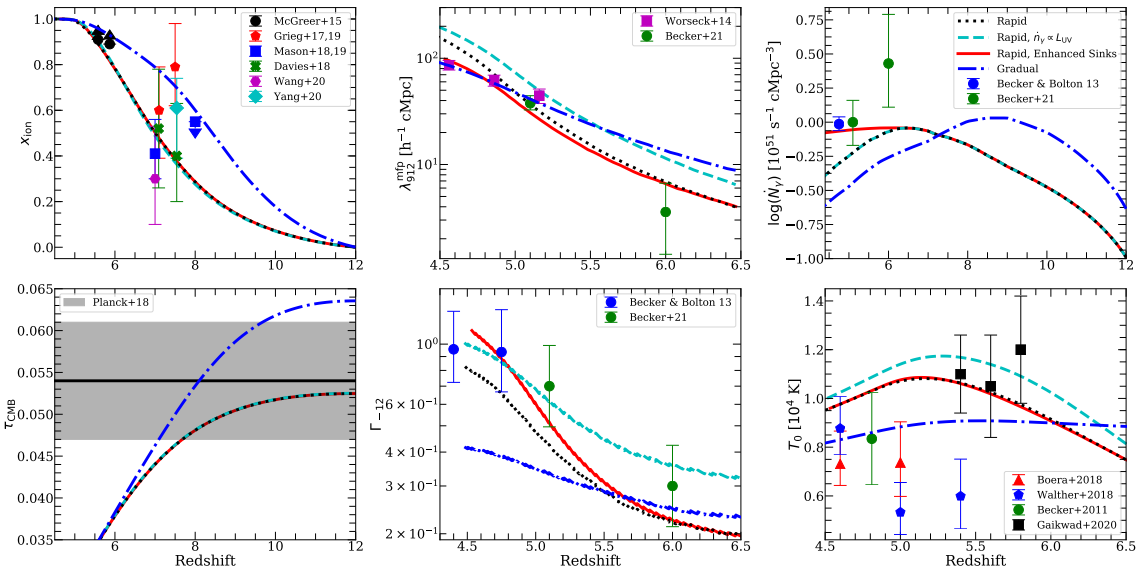

Figure 3.1: Reionization observables in our models. In clockwise order, starting from the top left, we show the ionized fraction, comoving MFP at 1 Ry, source comoving emissivity, IGM temperature at the cosmic mean density, H photoionization rate, and CMB optical depth. We compare against a selection of recent observational constraints with 1σ error bars.

3.2 Results

In Fig. 3.1 we show 4 models chosen to illustrate our conclusions. In clock-wise order, starting at the top left, the panels show the volume-weighted mean ionized fraction, co-moving MFP at 1 Ry ($\lambda_{912}^{\rm mfp}$), co-moving ionizing emissivity ($\dot{N}_\gamma$), temperature at the cosmic mean density (T_0), volume-weighted mean Γ_{-12} in ionized gas, and the cumulative CMB optical depth. We compare against an assortment of existing constraints [15, 16, 17, 18, 19, 20, 12, 1, 138, 139, 140, 141, 142, 21, 22]. To calculate $\lambda_{912}^{\rm mfp}$, we traced 50,000 sight lines from random locations, created mock quasar absorption spectra, and fit to the model of [143] and [12].[1]

[1]Our sight lines do not start on QSOs, thus are not affected by biases from the proximity effect [79, 13]. When we anchored sight lines on massive halos, we found that the model of [143] did not provide a good

All models in Fig. 3.1 end reionization at $z = 5.1$ and formally have the same duration of 780 Myr ($x_{\rm ion} = 1 - 99\%$). The key distinction between the rapid and gradual scenarios is how quickly $x_{\rm ion}$ evolves in the last half of reionization. In the rapid model (black/dotted), the emissivity peaks at $z \approx 6.5$ and reionization proceeds rapidly after its $z = 7.1$ midpoint. As a result, Γ_{-12} and $\lambda_{912}^{\rm mfp}$ grow rapidly between $z = 6$ and 5.2, consistent with the measurements at those redshifts. The cyan/dashed curve shows a model with the same emissivity, but with $\dot{n_\gamma} \propto L_{\rm UV}$. In this case reionization is driven by rarer, brighter galaxies[2] which, on average, produce larger Γ_{-12} in ionized bubbles. This results in $\lambda_{912}^{\rm mfp}$ being too long across all redshifts.

A principal conclusion from our modeling is that the short $\lambda_{912}^{\rm mfp}(z = 6)$ measured by B21 prefers faint, less-biased sources as the main drivers of reionization. We have run a set of models with a lower $M_{\rm min}$ of $10^8 h^{-1} M_\odot$. Adopting the same $\dot{N}_\gamma$ as in our rapid model, we find $\Gamma_{-12} = 0.2$ and $\lambda_{912}^{\rm mfp} = 5 h^{-1}$Mpc at $z = 6$. The dependence of $\lambda_{912}^{\rm mfp}$ on $M_{\rm min}$ can be understood in terms of halo bias. Sources are less clustered in models with lower $M_{\rm min}$, which leads to ionized bubbles being smaller, on average. Large-scale fluctuations in $\Gamma_{\rm HI}$ are also reduced. In contrast, for models with highly clustered sources, the intense ionizing radiation in over-dense regions quickly clears away the local sinks, allowing this radiation to penetrate much further into the IGM bulk.

fit at rest-frame 900Å $< \lambda <$ 912Å, owing to the local clustering of sources and the back-reaction of $\Gamma_{\rm HI}$ on $\lambda_{912}^{\rm mfp}$. Excluding these wavelengths in the fit gave the un-biased $\lambda_{912}^{\rm mfp}$. In this work, we assume that the observations represent the un-biased $\lambda_{912}^{\rm mfp}$. For reference, the biased $\lambda_{912}^{\rm mfp}(z = 6)$ is 9.3, 15.8, 15.1, 9.1 h^{-1}Mpc in the rapid, gradual, $\dot{n}_\gamma \propto L_{\rm UV}$, and enhanced sinks models, respectively.

[2]For the $\dot{n}_\gamma \propto L_{\rm UV}$ model, half the ionizing photons are produced by halos with $M < M_{1/2} = (0.39, 1.8, 3.4) \times 10^{10} h^{-1} {\rm M}_\odot$ at $z = (9, 6, 5)$. For the model with $\dot{n}_\gamma$ independent of $L_{\rm UV}$, production is peaked around $M_{\rm min}$; we find $M_{1/2} = (1.6, 1.8, 1.8) \times 10^9 h^{-1} {\rm M}_\odot$.

In the gradual model (blue/dot-dashed), reionization proceeds more gradually after its $z = 8.5$ midpoint. By $z = 6$, more of the gas has relaxed in response to photoheating. This, combined with the larger $x_{\rm ion}$, results in a factor of 1.5 longer $\lambda_{912}^{\rm mfp}$ at $z = 6$ compared to the rapid model. The evolution in Γ_{-12} is flatter but it undershoots by a factor of ~ 2 the measurements of [138] at $z < 5$. Generally, models in which most of the IGM was reionized well before $z = 6$ are difficult to reconcile with a short $\lambda_{912}^{\rm mfp}(z = 6)$. We have confirmed this with other runs as well, including those with $M_{\rm min} = 10^8 h^{-1}{\rm M}_\odot$. The problem is that the local $\lambda_{912}^{\rm mfp}$ grow with time after $z_{\rm re}$ owing to relaxation and photoevaporation. In gas that was reionized at higher redshift, the only way to obtain low $\lambda_{912}^{\rm mfp}$ is to lower Γ_{-12}. But the slow evolution results in undershooting the Lyα forest measurements of Γ_{-12} at $z \sim 5$. Hence, another principal conclusion from our modeling is that a rapidly evolving $x_{\rm ion}$ is required to recover both the short value of $\lambda_{912}^{\rm mfp}$ at $z = 6$ and its rapid evolution to $z = 5.2$. However, we note that the rapid models are in 2-3σ tension with the [15] constraints on $x_{\rm ion}$ (top-left of Fig. 3.1). Updating these constraints with more QSO sight lines will provide a critical test of our assertion.

There are two more obvious deficits of the rapid model (black/dashed): (1) The quick growth in $\lambda_{912}^{\rm mfp}$ continues below $z = 5.2$, which is incompatible with measurements; (2) Relatedly, to control the growth of Γ_{-12} and $\lambda_{912}^{\rm mfp}$ at $z < 5.5$, $\dot{N}_\gamma$ must fall by $> 40\%$ in the 240 Myr between $z = 6$ and 5, a rapid evolution in the galaxy population (see however [144]). We emphasize that $\dot{N}_\gamma(z)$ is an input to our simulations; the decline is not the result of any feedback prescription. D20 found that their $\lambda_{912}^{\rm mfp}$ are converged in resolution at the 10 % (factor of ~ 2) level in relaxed (un-relaxed gas), respectively. Moreover, up to

$\Delta t \approx 10$ Myr after $z_{\rm re}$, D20 found $\lambda_{912}^{\rm mfp}$ similar to the unheated simulations of [85]. This argues against numerical convergence being the sole culprit.

One plausible explanation for the behavior of $\dot{N}_\gamma$ is that our sub-grid model over-estimates $\lambda_{912}^{\rm mfp}$ in over-dense cells, e.g. by inadequately sampling massive sinks near the end of reionization. To illustrate that we can obtain milder evolution in $\dot{N}_\gamma$ through sinks, we crudely scale down $\lambda_{912}^{\rm mfp}$ in all over-dense cells after $z = 6.5$ by a factor of $[(1+z)/(1+6.5)]^{3.5}$, such that $\lambda_{912}^{\rm mfp}$ is a factor of 2 shorter in those cells by $z = 5.2$. The result is the rapid+enhanced sinks model (red/solid), for which $\dot{N}_\gamma$ levels off after $z = 6.5$. In this case, the enhanced sinks regulate the growth of Γ_{-12} and $\lambda_{912}^{\rm mfp}$ so they do not outpace the measurements below $z = 5.2$. This obviates the need for a rapid decline in $\dot{N}_\gamma$, illustrating an approximate degeneracy between the emissivity and the sinks.[3]

The thick curves in the top panel of Fig. 3.2 show the cumulative number of photons per hydrogen atom absorbed. The thin curves show the cumulative recombinations.[4] For reference, the vertical line corresponds to reionization's end. All our models require ≈ 3 photons/H atom to complete reionization. This is a factor of $1.5 - 2$ more than in recent models of the ionizing emissivity.[5] Although more photons are absorbed earlier in the gradual model, the cumulative number is similar to the rapid models because much of the gas remains un-relaxed in the latter.

[3] We have also run an enhanced sinks version of the gradual model. While it is in better agreement with the $z < 5$ Γ_{-12} measurements – reconciling a major deficiency of the model – we find $\lambda_{912}^{\rm mfp}(z = 6) = 14h^{-1}$ Mpc. This is still much larger than the measurement, suggesting that an even larger boost to the sinks at $z \sim 6$ would be required in this scenario.

[4] The number of recombinations is given by the total number of absorptions minus the net number of ionizations.

[5] We find 1.5 and 1.8 photons/H atom in the models of [105] and [129], respectively.

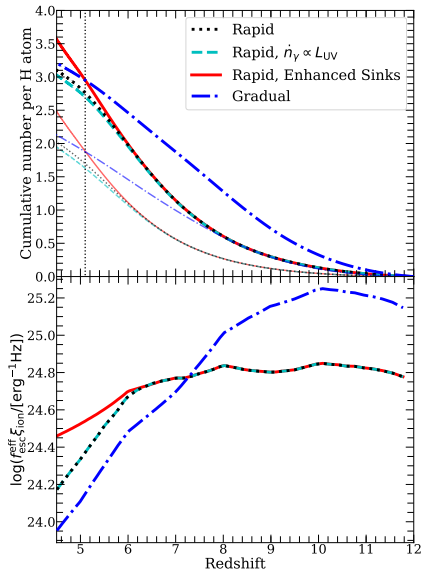

Figure 3.2: Top: Cumulative number of absorptions (thick curves) and recombinations (thin faded curves) per H atom for our models. The vertical line corresponds to the end of reionization. Bottom: Product of the effective LyC escape fraction and ionizing efficiency for each of our models. The rapid models are broadly consistent with observational constraints on $\xi_{\rm ion}$ provided that $f_{\rm esc}^{\rm eff} = 10 - 40\%$ (see text).

In a paper submitted concurrently with this work, [145] quantify in detail the implications of the B21 measurement of $\lambda_{912}^{\rm mfp}(z = 6)$ for high-z galaxies. Considering also the dark pixel fraction constraints on $x_{\rm ion}(z = 5.9)$, they find that $6.1^{+11.1}_{-2.4}$ photons per baryon are required to bring reionization to 90% completion. Although this appears considerably larger than our budget, we note that $\lambda_{912}^{\rm mfp}(z = 6)$ in our rapid models are 1σ longer than the central value of B21, and the neutral fractions are $x_{\rm HI} = 20\%$. Adjusting for the former would bring down their budget to 3.7 photons per baryon. Adjusting for latter would bring us further into agreement. Moreover, we have rerun the rapid simulation, but with a uniform 3.8× (2.5×) boost to the clumping (emissivity). This yields $x_{\rm ion}(z = 5.9) = 88\%$ and $\lambda_{912}^{\rm mfp} = 3.65h^{-1}$, closer to the B21 central value of $3.57h^{-1}$ Mpc. It requires 5.2 photons/H atom by $z = 5.9$.

The emissivity is commonly modeled as $\dot{N}_\gamma = f_{\rm esc}^{\rm eff}\xi_{\rm ion}\rho_{\rm UV}$, where $f_{\rm esc}^{\rm eff}$ is an effective escape fraction, $\xi_{\rm ion}$ is the ionizing efficiency, and $\rho_{\rm UV}$ is the UV luminosity density. The bottom panel of Fig.3.2 shows the product, $f_{\rm esc}^{\rm eff}\xi_{\rm ion}$, obtained by applying this relation to our $\dot{N}_\gamma$ and integrating the UV luminosity function of [129] for $\rho_{\rm UV}$. Previous studies have assumed $\log(\xi_{\rm ion}/[{\rm erg}^{-1}{\rm Hz}]) = 25.2 - 25.3$, consistent with the constraints of [146] for $4 < z < 5$ galaxies. There is evidence that the bluest galaxies at higher redshift exhibit higher efficiencies, $\log(\xi_{\rm ion}/[{\rm erg}^{-1}{\rm Hz}]) = 25.6 - 25.9$ [146, 147, 148]. For the rapid models to be consistent with values of 25.8(25.3) requires $f_{\rm esc}^{\rm eff} = 11(35)\%$. The gradual model requires a more extreme $f_{\rm esc}^{\rm eff} = 28(89)\%$ at its peak of $z = 10$. However, if we let $M_{\rm min} = 10^8 h^{-1}{\rm M}_\odot$, we find $f_{\rm esc}^{\rm eff} = 10(32)\%$, indicating that such an early peak in emissivity would likely require efficient star formation in galaxies with $M < 10^9 h^{-1}{\rm M}_\odot$ (see e.g. [129]). Our $f_{\rm esc}^{\rm eff}$ are similar to those reported by [145]. That our rapid models require $f_{\rm esc}^{\rm eff} = 10 - 40\%$ supports the conclusion that faint $z > 6$ galaxies must have been prolific leakers of LyC radiation, if reionization was driven by stellar emissions.

The top and bottom sets of panels in Fig. 3.3 show light cones through our rapid+enhanced sinks and gradual models, respectively. In each set, the top(bottom) panel shows $\Gamma_{-12}(\lambda_{912}^{\rm mfp})$. The neutral islands down to $z \approx 5.5$ likely make both models compatible with the large opacity fluctuations observed in the Lyα forest [126, 104]. The Lyα forest mean flux evolution, however, may already disfavor the gradual model (c.f. bottom-middle of Fig. 3.1). Another contrasting feature is the existence of large ($R \sim$ 10s Mpc) ionized bubbles out to $z \sim 9$ in the gradual model, which is of interest for recent observations of

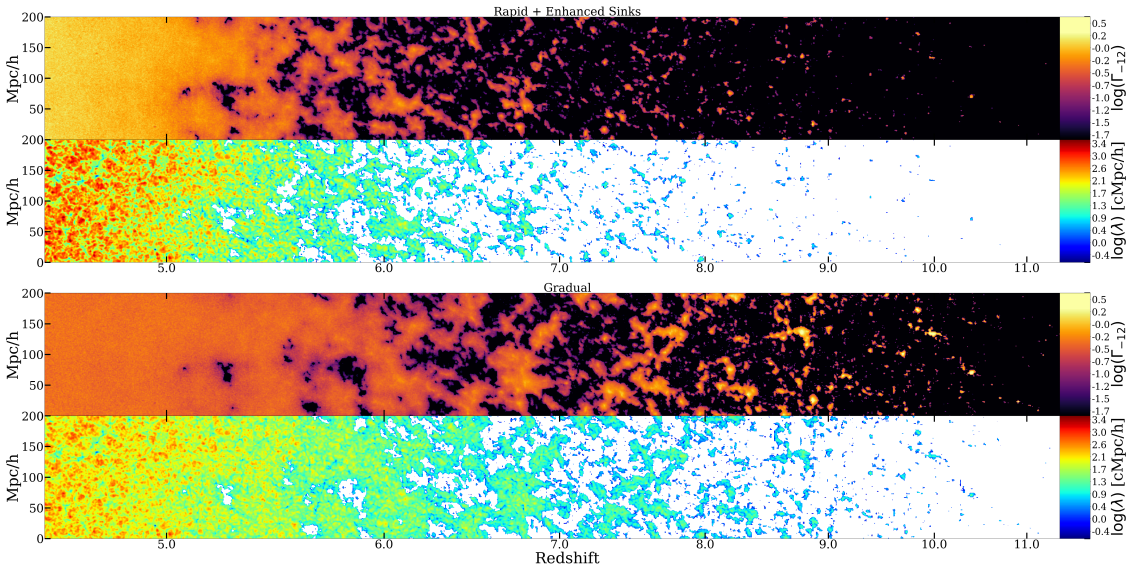

Figure 3.3: Light-cone slices (1 Mpc/h thick) of Γ_{-12} and $\lambda_{912}^{\rm mfp}$ from our rapid+enhanced sinks (top) and gradual (bottom) models. In the rapid model, $\lambda_{912}^{\rm mfp}$ evolves quickly at $z < 6$ as the gas relaxes and neutral islands disappear. After reionization is finished, $\lambda_{912}^{\rm mfp}$ is limited by sinks in over-dense regions. In the gradual model most gas is relaxed by $z \sim 6$ and there is less neutral gas, resulting in a longer $\lambda_{912}^{\rm mfp}$.

bright LAE over-densities at $z > 7$ [149, 150, 148]. The different global $x_{\rm ion}$ and morphologies may be testable by forthcoming 21cm surveys.

3.3 Conclusion

We have explored the implications of the B21 MFP measurements for reionization. Taken together with constraints on the intensity of the metagalactic ionizing background, we have argued that the rapid evolution from $\lambda_{\rm mfp}^{912}(z = 6) = 3.57^{+3.09}_{-2.14}$ cMpc/h to $\lambda_{\rm mfp}^{912}(z = 5.1) = 37.71^{+6.72}_{-5.06}$ cMpc/h favors a rapid and late reionization process. We have also argued that the short value of $\lambda_{\rm mfp}^{912}(z = 6)$ is evidence that reionization was driven primarily by the faintest, least biased galaxies among its sources. In our preferred models, ≈ 3

ionizing photons/H atom are required to complete reionization. Half of them come from galaxies with $M \sim 10^9 h^{-1}$ $M_\odot$, or lower. At $z = 6(8)$, this corresponds to UV magnitudes $M_{1600} > -12.9(-14.0)$. In addition to confirming the low value of $\lambda_{\rm mfp}^{912}(z = 6)$, other avenues forward include updating the Lyα forest dark pixel limits on $x_{\rm ion}$ and constraining the IGM temperature at $z \sim 5.5$. Our analysis highlights the complementary channels for constraining reionization with QSO absorption spectra.

Chapter 4

Small-scale clumping of dark matter and the mean free path of ionizing photons at $z = 6$

4.1 Introduction

Small-scale power is a defining feature of cold collisionless dark matter (CDM), manifested in halo formation down to perhaps Earth-mass scales [151, 152, 153, 154]. Figure 4.1 summarizes some recent constraints on the linear matter power spectrum, $P_{\rm lin}(k)$, across the range of scales currently accessible to observations. The top horizontal axis shows the Larangian mass scale corresponding to wavenumber k, $M = \frac{4\pi}{3}\rho_m(z=0)R^3$, where $R = 2\pi/k$ and ρ_m is the cosmological matter density. The Lyman-α forest flux power spectrum is sensitive to $P_{\rm lin}(k)$ up to wavenumber $k \approx 50\ h{\rm Mpc}^{-1}$, with the most

recent measurements placing tight limits on the parameter space of CDM alternatives [155, 156, 8, 157, 158, 159, 5][1]. Probing $P_{\rm lin}(k)$ on smaller scales, flux ratio measurements in strong gravitational lenses are currently sensitive to perturbations by halos with masses $M > 2 \times 10^7\ h^{-1}{\rm M}_\odot$, corresponding to $k \approx 160\ h{\rm Mpc}^{-1}$ [160, 7, 161]. Future observations by the James Webb Space Telescope (JWST) aim to extend this sensitivity to $M \sim 2 \times 10^6\ h^{-1}{\rm M}_\odot$, or $k \approx 340\ h{\rm Mpc}^{-1}$ (JWST GO-02046; PI Nierenberg). Developing methods to measure power on even smaller scales is of great interest, given its status as an inevitable but largely untested feature of CDM, and for its potential in probing inflationary physics.

Observations of the abundance and properties of Milky Way satellites can in principle constrain $P_{\rm lin}(k)$ down to the scales of the smallest observable galaxies – a program termed near-field cosmology. In theory, halos with masses much below 10^8 M$_\odot$ are thought to be extremely inefficient at forming stars because they lack a robust cooling channel to kickstart star formation[2]. They also struggle to accrete/retain gas against feedback and heating by the extragalactic ionizing background [164, 165, 166, 167, 168, 169]. According to simulations, dense remnants of at least a significant fraction of these barren halos are expected to survive to the present day, even after they are incorporated into larger halos (e.g. [170]). Strong gravitational lensing magnifications are uniquely sensitive to such dark matter-dominated structures. Together with near-field cosmology, the forthcoming expansion of strong lensing observations will play a chief role in nailing down the small-scale $P_{\rm lin}(k)$ [171]. However, inverting these observations still requires an accurate model connecting the

[1]We emphasize that the gold and gray shaded regions in Fig. 4.1 correspond to *model dependent* constraints on $P_{\rm lin}(k)$.

[2]See however Refs [162, 163].

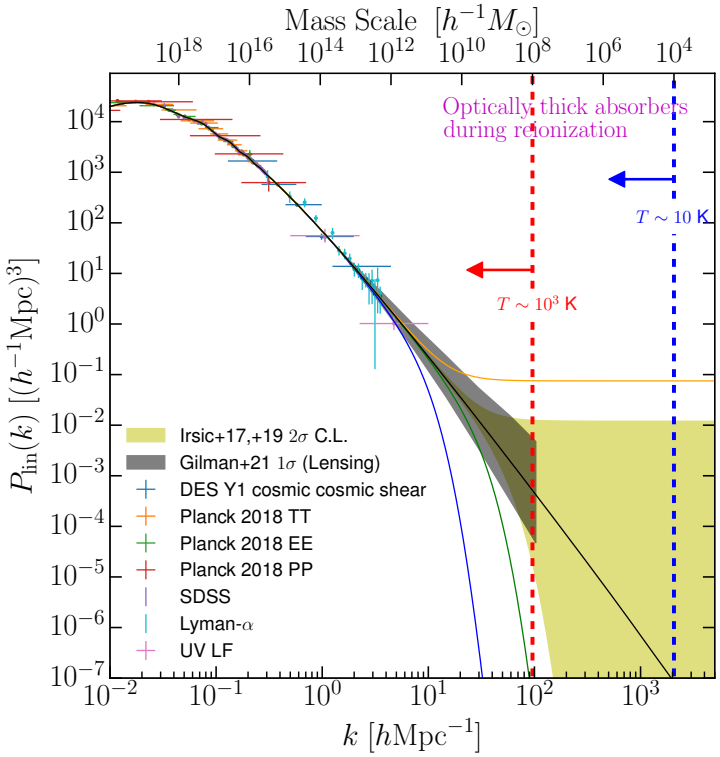

Figure 4.1: Summary of constraints on the linearly extrapolated matter power spectrum. Power on the largest scales is constrained by Planck CMB measurements [1] and galaxy clustering in the Sloan Digital Sky Survey (SDSS) [2]. On intermediate scales, constraints come from cosmic shear measurements in the Dark Energy Survey (DES) [3], the Lyman-α forest 1D flux power spectrum [4, 5], and the UV luminosity function of high-z galaxies [6]. The thin curves show the different DM models considered in this work. The black curve is the concordance CDM power spectrum. The yellow, green and blue curves show an axion-like cosmology with enhanced small scale power, and thermal relic WDM scenarios with masses $m_X = 3$ and 1 keV, respectively. The gray shaded region denotes the 1σ constraints from [7], derived from flux ratios and positions of strongly lensed quasars. The yellow-shaded region denotes the range spanned by the 2σ lower limits on the thermal relic WDM particle mass from [8] and the 2σ upper limits on the isocurvature fraction in the ultra-light axion scenario from [9]. Although much of the constraining power from the Lyα forest and lensing comes from mass scales as small as $M = 10^8\ h^{-1}{\rm M}_\odot$, on smaller scales (right of the red dashed line) the constraints from Refs [8, 9] are extrapolations of the assumed DM cosmology and are thus strongly model-dependent. As such these scales are effectively unconstrained. The thick vertical dashed lines denote rough lower limits on the range of mass scales expected to contribute to the opacity of the IGM during reionization for two different minimum pre-reionization gas temperatures. The IGM opacity during and shortly after ($\Delta t \sim 300$ Myr) reionization might have been sensitive to power on scales yet unconstrained. The possibility of exploiting this to constrain DM models is the topic of this paper.

abundance and properties of surviving halos to $P_{\rm lin}(k)$ – an extremely formidable challenge. It is therefore important to explore complimentary probes moving forward.

Reionization-era observations could, at least in principle, give insights into $P_{\rm lin}(k)$ from a much earlier time in the hierarchical assembly process. In fact, a census of reionization-era galaxies has already been applied to constrain $P_{\rm lin}(k)$ up to $k \sim 10\ h{\rm Mpc}^{-1}$ (see Fig. 4.1), albeit with large uncertainty [6]. Another window, as of yet unexploited, comes from the fact that reionization was also shaped by the small-scale structure of the IGM. In the cold pre-reionization IGM, the Jeans filtering scale was much smaller than it is today, somewhere in the range of $M \sim 10^4 - 10^8\ h^{-1}{\rm M}_\odot$, corresponding to characteristic temperatures of $T \sim 10 - 1,000$ K. These scales are denoted by the vertical dashed lines in Fig. 4.1. The quoted filtering scales bracket roughly the range of existing models for heating of the IGM by the first X-ray sources, preceding reionization [172, 173].

It has long been recognized that the "minihalos" with masses above the filtering scale, but below the minimum mass-scale for efficient galaxy formation, may have contributed significantly to the Lyman-continuum (LyC) opacity of the IGM during reionization [174, 175]. Absorptions by these halos raised the ionizing photon budget required to complete and maintain reionization, and possibly set the shapes and sizes of ionized bubbles [176, 177]. The minihalos did not retain their gas content indefinitely, however. They were evacuated over a timescale of $\Delta t \sim 10$ to a few hundred Myr as ionization fronts (I-fronts) eventually penetrated inward, driving evaporative winds into the IGM. Especially in the earlier stages of reionization, a significant number of absorptions likely occurred outside of halos as well, owing to the higher cosmic densities and weaker ionizing background [178].[3]

[3]In fact, the results of [178] suggest that the diffuse inter-halo gas contributed a LyC opacity roughly

After I-fronts passed through a region, pressure smoothing caused the inter-halo gas, e.g. within filaments, to expand outward and relax to a more diffuse configuration within a few hundred Myr. Simulating these dynamic processes requires hydrodynamics coupled with radiative transfer to capture the interplay between self-shielding and the response of the gas to photoheating [131, 74]. But the physics is comparatively simpler than the highly uncertain processes that shaped the properties of star-forming galaxies and their subhalos. Assuming that the gas structure of the IGM was not significantly spoiled by feedback from the star formation activity of halos, the sinks of reionization could potentially become a useful test for the existence of small-scale power.

Measuring the LyC mean free path of the IGM during reionization is the most direct way to probe the sinks. The highest redshift constraints to date were reported recently by Refs [13] and [14] using quasar absorption spectra at $z \approx 6$. According to recent models which place the end of reionization at around $z = 5.2$ [126, 127, 104], the measurement of [13] might be the first direct measurement of the mean free path during reionization, at a time when the global neutral fraction was $\approx 10\%$. Their measurement of $\lambda_{912}^{\rm mfp}(z = 6) = 3.57^{+3.09}_{-2.14}\ h^{-1}$cMpc came as somewhat of a surprise, though, because it is significantly shorter than predictions from the contemporaneous simulations of reionization. Shortly afterward, Ref [10] was able to recover values of $\lambda_{912}^{\rm mfp}(z = 6)$ compatible with the measurement. Crucially, their simulations included a sub-grid model of the sinks based on the highly resolved radiative hydrodynamics simulations of [74]. Thus, Ref [10] was able to incorporate the effects of small-scale power down to $\sim 10h^{-1}$ckpc scales in reionization simulations with box size $L = 200h^{-1}$cMpc. The key point is that the highly resolved

equal to that of the minihalos before the latter were photoevaporated.

simulations upon which their sub-grid model is based contain tiny gaseous structures close to the lower limit of filtering scales quoted above, $\sim 10^4$ $M_\odot$ (see [178] for a detailed discussion).[4] The apparent necessity of including such small structures to reproduce the short value of $\lambda_{912}^{\rm mfp}(z=6)$, if correct, suggests a potential broader implication for cosmology. Might the small-scale power predicted in the CDM paradigm be necessary to explain the LyC opacity of the reionizing IGM? This is among the central questions that we attempt to address here.

In this paper, we examine the connection between the small-scale clumping of the underlying dark matter model and the observed mean free path of the IGM at $z > 5$. We employ hydrodynamic simulations in warm dark matter (WDM) cosmologies to quantify the mean free path in models with a small-scale cutoff in $P_{\rm lin}(k)$. We also use a semi-analytic approach to explore scenarios with enhanced small-scale power relative to CDM. This is motivated by models receiving increased interest in recent years, e.g. ultralight axion-like particles [179, 180, 181, 9, 182, 183] and primordial black holes [184, 185, 186, 187, 188], and by the fact that the observed $\lambda_{912}^{\rm mfp}(z=6) = 3.57^{+3.09}_{-2.14}$ h^{-1}cMpc lies on the shorter side of expectation in the standard CDM picture [13, 10, 145]. The impetus for this exploration was the possibility that high-z mean free path measurements could become a kind of "no-go" test for all dark matter models lacking in small scale power. Unfortunately, as we will show, the situation turns out to be more complicated because of substantial uncertainties in the reionization process, the extragalactic ionizing background, and thermal history of the IGM.

[4] This owes to the fact that the simulations did not include any pre-heating by X-ray sources ahead of reionization.

This work is organized as follows. §4.2 describes our modeling methods. §4.3 discusses the mean free path in WDM models. §4.4 presents our axion-like scenario with enhanced small-scale power. In §4.5 we offer concluding remarks. Throughout this work, we assume the following cosmological parameters: $\Omega_m = 0.305$, $\Omega_\Lambda = 1 - \Omega_m$, $\Omega_b = 0.048$, $h = 0.68$, $n_s = 0.9667$ and $\sigma_8 = 0.82$, consistent with the latest constraints [1].

4.2 Numerical Methods

4.2.1 Hydrodynamic simulations of the sinks

We ran high-resolution hydrodynamic simulations of the IGM in CDM and WDM scenarios. (We will describe our semi-analytic approach for modeling enhanced power scenarios in §4.4.) We used a modified version of the RadHydro code [76] in boxes with $L = 2h^{-1}$Mpc, initialized at $z = 300$ using transfer functions generated with CAMB [189]. WDM cosmologies were implemented using the standard approach of Refs [190, 191]. We consider thermal relic WDM with particle masses of $m_X = 1$ and 3 keV.[5] The former was chosen to be an extreme case which is already ruled out observationally, while the latter is representative of models marginally allowed by recent Lyα forest analyses [8]. The blue and green curves in Figure 4.1 show the corresponding linear matter power spectra extrapolated to $z = 0$. Structure is suppressed below the free-streaming scale, which is (for thermal relic WDM) $k_F \sim 15$ and 45 hMpc^{-1} for $m_X = 1$ and 3 keV, respectively (Eq. 8 of Ref [191]).

As described in §4.1, pressure smoothing is a key ingredient for modeling the sinks [131, 74, 178]. To incorporate these effects, we ran simulations with and without a uniform

[5] When quoting DM particle masses, we will use the standard convention of setting $c = 1$.

ionizing background applied. For the former, the ionizing background was switched on at $z = 12$, with intensity fixed to a hydrogen photoionization rate of $\Gamma_{-12} \equiv \Gamma_{\rm HI}/10^{-12}$ s^{-1} = 0.3 at $z > 6$. For $z < 6$, $\Gamma_{\rm HI}$ evolves to approximately match observational measurements from the Lyα forest. The evolution of $\Gamma_{\rm HI}$ in our simulations is plotted, along with recent forest constraints, in §4.3.2. We account for self-shielding with a model calibrated to the fully coupled radiative hydrodynamics simulations of [74, 178]. Details are described in Appendix B.1. In summary, we use a modified version of the fitting function of [192] for the photoionization rate as a function of the local hydrogen density. We modified the functional form and fitting parameters to match the median $\Gamma_{\rm HI}(n_H)$ reported by [178] (see their Fig. 1). The intensity of the ionizing background declines steeply within density peaks, mimicking the effects of self-shielding observed in radiative hydrodynamics simulations. Note that our basic simulation setup and code is the same as that of [74], the main differences being the implementation of WDM, the use of a self-shielding prescription in lieu of full RT, and the evolution of $\Gamma_{\rm HI}$ in the relaxed runs.

With this setup, the gas in the runs that apply an ionizing background is almost instantaneously heated to $T \sim 20,000$ K at $z = 12$. The purpose of this early, impulsive heating is to achieve a limiting case in which photoionization heating has had sufficient time ($\Delta t > 300$ Myr) to smooth the density structure of the IGM by $z = 6$. We will refer to this smoothing process as "relaxation," and label the corresponding runs as "relaxed." For a fixed ionizing background intensity ($\Gamma_{\rm HI}$), most of the relaxation and photo-evaporation occurs within a time $\Delta t \sim 300$ Myr since I-front passage, after which the local density field possess essentially no memory of when it was reionized. Hence the density structures

at $z < 6$ in our relaxed runs are representative of IGM patches that were ionized/heated during the first half of reionization (up to differences in the local $\Gamma_{\rm HI}$, which we will address below). In the opposite limit, no ionizing background was applied, such that the cold gas clumps down to its pre-reionization Jeans filtering scale, more representative of very recently reionized patches (see e.g. [85]). We refer to these runs as "un-relaxed." We will use a simple model for the evolution connecting these two limiting configurations, described in §4.2.2.

In Appendix B.2, we show that numerical convergence can be achieved with a smaller number of DM particles ($N_{\rm dm}$) and gas cells ($N_{\rm gas}$) in the relaxed runs, compared to the un-relaxed ones. This finding reflects the different filtering scales, or minimum sizes of gaseous structures to form, in the relaxed and un-relaxed runs. A similar effect applies to the free streaming scale; the lighter the WDM particle, the less stringent the resolution requirements. We adopted $N \equiv N_{\rm dm} = N_{\rm gas} = 2048^3$ for the CDM and $m_X = 3$ keV un-relaxed runs, and $N = 1024^3$ for the corresponding relaxed runs. We used $N = 1024^3$ for both the un-relaxed and relaxed runs with $m_X = 1$ keV. In Appendix B.2, we justify the use of a lower resolution for the relaxed and $m_X = 1$ keV runs. We also show that, in the un-relaxed limit, the WDM runs are better converged than the CDM runs, owing to the intrinsic lack of small-scale power in the former. As a result, we likely underestimate the differences in opacities between our WDM and CDM models in the un-relaxed limit. Note, however, that our simulations do not include the effects of pre-heating by the first X-ray sources. The pre-heating would act in the opposite direction, smoothing out the smallest gaseous structures present in the CDM cosmology, and therefore diminishing differences.

Our box sizes are small in order to capture the clumpiness of the cold, pre-reionization gas, at the cost of missing large-scale power. We correct for this using the DC mode approach of [101], which allows us to model the effects of large-scale power. We refer the reader to [74] for a detailed description of our approach. In summary, we ran additional simulations with positive and negative box-scale overdensities applied to the cosmic mean density. Quantities of interest (e.g. the LyC opacity) were obtained by integrating over the distribution of densities smoothed on the box scale. We parameterize the box-scale over-density with δ/σ, the linearly extrapolated density contrast in units of its standard deviation, smoothed on 2 h^{-1}Mpc scales. In addition to our standard cosmic mean runs ($\delta/\sigma = 0$), we ran simulations with $\delta/\sigma = \pm\sqrt{3}$. We get the mean LyC opacity by averaging over the distribution of densities from a cosmological N-body simulation (described in § 4.2.3), assuming the opacity follows a power law in density between and outside our simulated values (see description of Eq. 4.4).[6]

Figure 4.2 shows slices through the gas density field from our mean-density ($\delta/\sigma = 0$) simulations at $z = 6$. The top and bottom rows show the un-relaxed and relaxed limits respectively. The columns show, from left to right, CDM, WDM with $m_X = 3$ keV, and with $m_X = 1$ keV. Note the vast differences between CDM and the WDM cosmologies in the un-relaxed (cold, pre-reionization) limit; CDM initially clumps down to much smaller scales. Comparing now the bottom panels, relaxation smooths the gas in CDM to a state not so dissimilar to that seen in the WDM run with $m_X = 3$ keV. Note also that the WDM structures evolve less during relaxation because they lack the small-scale power from the

[6]These values were originally chosen to apply the method of Gauss-Hermite Quadrature for the integration over the Gaussian distribution of linearly-extrapolated densities (see Appendix B of Ref [74]).

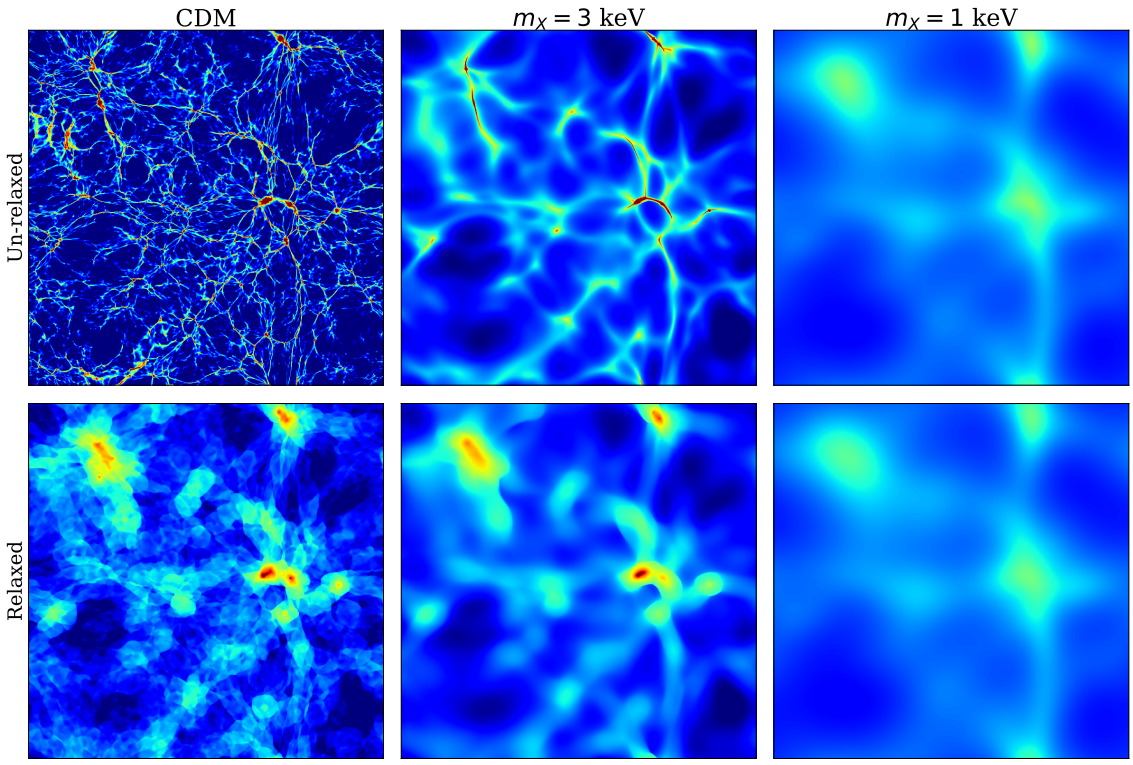

Figure 4.2: Visualization of the density field at $z = 6$ for CDM (left), and WDM with $m_X = 3$ keV (middle) and $m_X = 1$ keV (right). We show the un-relaxed runs in the top row and the relaxed runs in the bottom row. In the un-relaxed limit, the CDM case differs dramatically from the WDM runs, with the gas clumping down to much smaller scales, resulting in a shorter mean free path. However, in the relaxed limit, pressure smoothing and photoevaporation has mostly erased this extra structure, such that the mean free paths in the CDM and $m_X = 3$ keV density fields are similar. In the WDM models, especially the $m_X = 1$ keV case, the density fields evolve considerably less than in CDM because small structures are largely missing to being with. The lack of this small-scale structure in the $m_X = 1$ keV simulation results in a longer mean free path at all times.

start. This is especially evident in the $m_X = 1$ keV run, for which the un-relaxed and relaxed limits are nearly indistinguishable by eye.

4.2.2 Modeling the LyC opacity in ionized regions

We model the LyC opacity of the reionizing IGM as arising from two contributions: (1) Ionized gas within H II regions, including the self-shielding structures such as minihalos; (2) The neutral IGM that has yet to be reionized. At $z < 6$, when the global neutral fraction is $< 10\%$, these last remaining neutral regions are mainly relegated to structures of size $R \sim 10h^{-1}$Mpc that we will call "neutral islands" (see §4.2.3). The current section describes our procedure for modeling the opacity in ionized regions.

We calculate the MFP at 912Å in ionized gas directly from our simulations using the definition employed in [193],

$$\lambda_{912}^{\rm mfp} = -\left\langle \frac{\int x df}{\int df} \right\rangle = -\left\langle \int_1^0 x df \right\rangle \tag{4.1}$$

where x is the distance along a sightline and $f = \exp(-\tau(x))$ is the factor by which ionizing photon flux would be attenuated along the sightline. The second equality assumes that f is negligible at the end of the sightline. We evaluate Eq. 4.1 directly by computing the integral for 10,000 randomly positioned and oriented sight lines and averaging the results.[7] The gas fields in our un-relaxed runs are cold and fully neutral (because no ionizing background was applied). To obtain the MFP in the limit of short Δt after I-front passage, we post-processed the un-relaxed runs under the assumption of photoionization equilibrium assuming the case A recombination rate, applying also the self-shielding model discussed in the last section.

[7] We have checked that (1) the MFP as given by Eq. 4.1 agrees well with the definition used in Ref [74] and (2) 10,000 sightlines is sufficient for convergence of Eq. 4.1.

Applying the equilibrium assumption is motivated by the short photoionization time scale of $t_{\rm PI} \sim 1/\Gamma_{\rm HI} \sim 100,000$ yr, relative to the tens to hundreds of Myr over which the relaxation process occurs. We also set the temperature of the gas to a uniform $T_{\rm re} = 20,000$ K, which is representative of temperatures in the wake of recently passed I-fronts [194, 135, 195].

It is instructive the compare MFPs among our CDM and WDM simulations. In Figure 4.3 we show such a comparison using the same runs from Figure 4.2. To isolate differences arising from the different DM cosmologies (i.e. the gas density structures), we re-scale the photoionization rate in all of the simulations to a constant $\Gamma_{-12} = 0.3$, and we set the temperature to a uniform value of $T = 10^4$ K. In this case, evolution in the MFP is driven entirely by the density field. The solid and dashed curves show the un-relaxed and relaxed limits, respectively. In the un-relaxed limit, the MFP increases substantially as the WDM particle mass decreases and the free-streaming scale increases. The relaxed limits are much more similar, with the CDM and $m_X = 3$ keV models being nearly identical at all redshifts. This similarity between CDM and the $m_X = 3$ keV case follows intuitively from the similarity in the density strucure of the IGM seen in the bottom-left and bottom-middle panels of Fig. 4.2. The comparison also highlights that photoevaporation and pressure smoothing affect structures of the same mass scales that drive differences in the un-relaxed CDM and $m_X = 3$ keV runs.

Reionization is spatially patchy such that, at any given time during the process, different locations within the ionized phase of the IGM are at different stages of relaxation. We will denote the redshift at which some patch of the IGM was reionized with $z_{\rm re}$. The results of Figure 4.3 suggest that the *local* MFP in a recently reionized patch ($z \sim z_{\rm re}$)

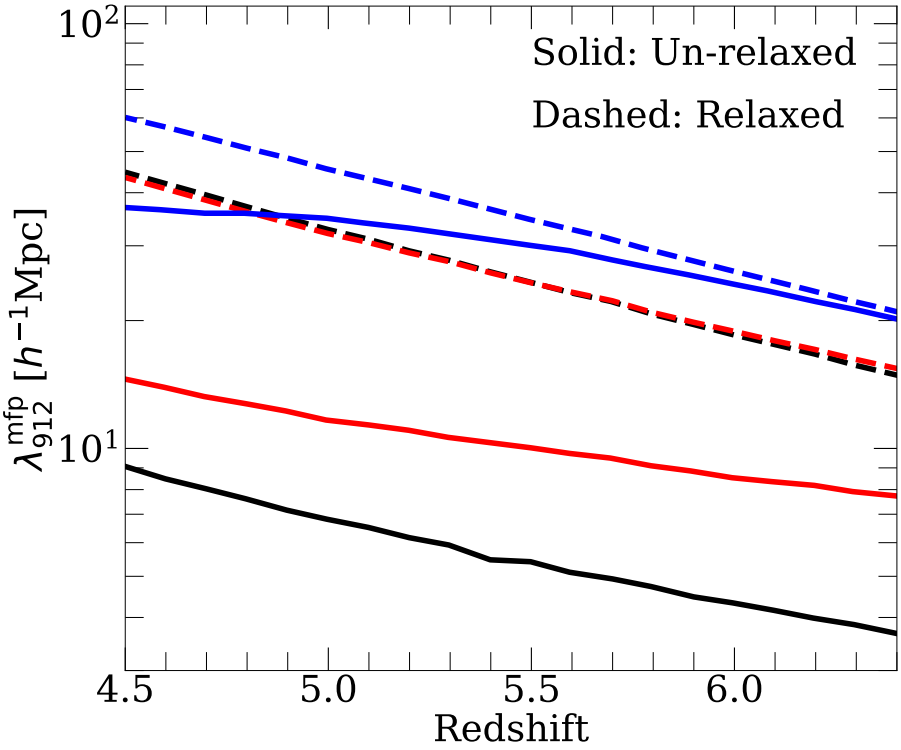

Figure 4.3: Mean free path for a simple test case in which we post-processed our mean-density runs assuming a constant $\Gamma_{-12} = 0.3$ and $T = 10^4$ K for CDM (black), $m_X = 3$ keV (red) and $m_X = 1$ keV (blue), in the un-relaxed (solid) and relaxed (dashed) limits. Holding $\Gamma_{\rm HI}$ and T constant ensures that the evolution in the MFP reflects only changes in the density field. There are considerable differences between the three DM models in the un-relaxed limit owing to the dramatic difference in the amount of small-scale structure shown in Figure 4.2. However in the relaxed limit the CDM and $m_X = 3$ keV cases are nearly identical and the relative difference with the $m_X = 1$ keV run decreases, again reflecting the trends in Figure 4.2. The similarity of the relaxed CDM and $m_X = 3$ keV cases highlights the fact that free-streaming and pressure smoothing affect the same mass scales in these models.

of the IGM differs substantially between the DM models considered here. However, the differences begin to disappear as the gas relaxes and small-scale power is erased. Clearly, the sensitivity of the global MFP to the free streaming scale depends on the fraction of IGM that is still relaxing ($\Delta t < 300$ Myr since ionization). The larger this fraction is, the more sensitive the global MFP will be to differences in small-scale power.

Modeling the global mean free path at a given z requires averaging over the distribution of local reionization redshifts, $z_{\rm re}$, in the ionized phase of the IGM. Given a global reionization history, $x_{\rm ion}(z)$, this distribution at redshift z can be written as

$$\frac{dP}{dz_{\rm re}}(z, z_{\rm re}) = \frac{1}{x_{\rm ion}(z)} \frac{dx_{\rm ion}}{dz_{\rm re}}\Big|_{z_{\rm re} \geq z} \tag{4.2}$$

Our simulations provide models for the opacity of the ionized IGM in the un-relaxed and relaxed limits. Denoting the local absorption coefficient at some location in the IGM as $\kappa(\Delta t, z_{\rm re})$, where Δt is the cosmic time that has elapsed since $z_{\rm re}$, we model the evolution between the two limits with a simple relaxation ansatz,

$$\kappa(\Delta t, z_{\rm re}) = \kappa_{\rm u} + [\kappa_{\rm r} - \kappa_{\rm u}] \left[1 - \exp\left(-\frac{\Delta t}{t_{\rm relax}}\right)\right]. \tag{4.3}$$

Here, $\kappa_{\rm u}$ and $\kappa_{\rm r}$ denote the un-relaxed and relaxed absorption coefficients, respectively, which are taken from our simulation runs (computed using Eq. 4.1 with $\kappa \equiv 1/\lambda_{912}^{\rm mfp}$), and $t_{\rm relax}$ is the relaxation time scale. Note that $\kappa_{\rm u}$ and $\kappa_{\rm r}$ are the opacities averaged over simulation box-scale densities (DC modes), given by

$$\kappa_{\rm X}(\Delta t, z_{\rm re}) = \int \kappa_{\rm X}(\Delta t, z_{\rm re}, \Delta_{\rm box}) \frac{dP}{d\Delta_{\rm box}} d\Delta_{\rm box} \tag{4.4}$$

where $X \in \{{\rm u}, {\rm r}\}$, $\Delta_{\rm box}$ is the matter density smoothed on the box scale $L = 2\ h^{-1}$Mpc,

$\kappa_{\rm X}(\Delta t, z_{\rm re}, \Delta_{\rm box}) = 1/\lambda_{912}^{\rm mfp}$ is the absorption coefficient in the simulation box with box-scale density $\Delta_{\rm box}$, and $\frac{dP}{d\Delta_{\rm box}}$ is the PDF of $\Delta_{\rm box}$, which is obtained from the cosmological N-body simulation described in the next section. We interpolated $\log\kappa$ linearly in $\log\Delta_{\rm box}$, effectively assuming a power law relation between κ and $\Delta_{\rm box}$. [8]

In what follows, we adopt a fiducial value of $t_{\rm relax} = 150$ Myr unless otherwise noted. This choice is consistent with the radiative hydrodynamics simulations of [74], in which relaxation is observed to be completed by $\Delta t \sim 300$ Myr.[9] Note that $t_{\rm relax}$ essentially sets the relative importance of un-relaxed gas in our model. Larger values result in more un-relaxed gas contributing to the opacity, which, in turn, amplifies differences between the DM cosmologies. We will explore how different choices of $t_{\rm relax}$ affect our main results in §4.3.2. In Appendix B.3, we test our relaxation ansatz against the opacity evolution in a simulation run with $z_{\rm re} = 6.5$. We find 10% or better agreement with the simulation at $4.5 < z < 6.5$, confirming both the accuracy of the ansatz and our fiducial choice of $t_{\rm relax}$.

Finally, the average absorption coefficient in ionized gas is

$$\langle\kappa_{\rm ion}\rangle(z) = \int_{z_{\rm init}}^{z} dz_{\rm re}\kappa(z, z_{\rm re})\frac{dP}{dz_{\rm re}}(z, z_{\rm re}), \tag{4.5}$$

where $z_{\rm init}$ is the starting point of reionization, which we take to be $z = 12$.[10] We note that the $\kappa(z, z_{\rm re})$ appearing in (4.5) is already averaged over DC modes (Eq. 4.4), hence Equation 4.5 neglects the correlation between density and $z_{\rm re}$ due to inside-out reionization. This may mean that we over-estimate the impact of un-relaxed gas, since at the end

[8] To convert between δ/σ and the nonlinear density $\Delta_{\rm box}$, we use Eq. 18 of Ref [196].

[9] Since $t_{\rm relax}$ is an e-folding timescale, relaxation will be $\sim 90\%$ complete after $2t_{\rm relax} = 300$ Myr in our fiducial model.

[10] Note that specifying z and $z_{\rm re}$ is equivalent to specifying Δt and $z_{\rm re}$.

of reionization recently ionized gas is expected to be under-dense on average. However, this effect is degenerate with uncertainties in $t_{\rm relax}$, since both affect the relative importance of un-relaxed gas, and hence should not impact our broad conclusions. We also note that our analysis does not account for spatial fluctuations in $\Gamma_{\rm HI}$ in ionized gas, which may persist on large scales near the end of and after reionization [197, 79]. This effect is also likely degenerate with $t_{\rm relax}$ to some extent, since un-relaxed gas in voids is likely to also have the lowest $\Gamma_{\rm HI}$. The absorption coefficient in ionized gas is added to a contribution coming from neutral islands, which we discuss in the next section. The global reionization histories from which $\frac{dP}{dz_{\rm re}}$ are obtained (see Eq. 4.2) come from radiative transfer simulations of reionization, which we also describe in the next section.

4.2.3 Opacity from Neutral Islands

We modeled the opacity from neutral islands using ionization fields from simulations of reionization. These were run with the radiative transfer code of [10] in a box with $L = 300h^{-1}$Mpc and $N = 300^3$ RT cells. The halo catalogs and density fields for the RT simulation were obtained from a cosmological DM-only simulation run with MP-Gadget [198], with $N = 2048^3$ DM particles. Halos were identified on-the-fly with a friends-of-friends algorithm down to a minimum mass of $M_{\rm min}^{\rm halo} = 8.5 \times 10^9\ h^{-1}{\rm M}_\odot$, which corresponds to 32 DM particles.[11] Models suggest that halos below this mass could have hosted galaxies that contributed significantly to reionization. Thus, we extended the RT source halos down to

[11] We checked that the halo mass function in our simulation agrees well with published mass functions down to this limit.

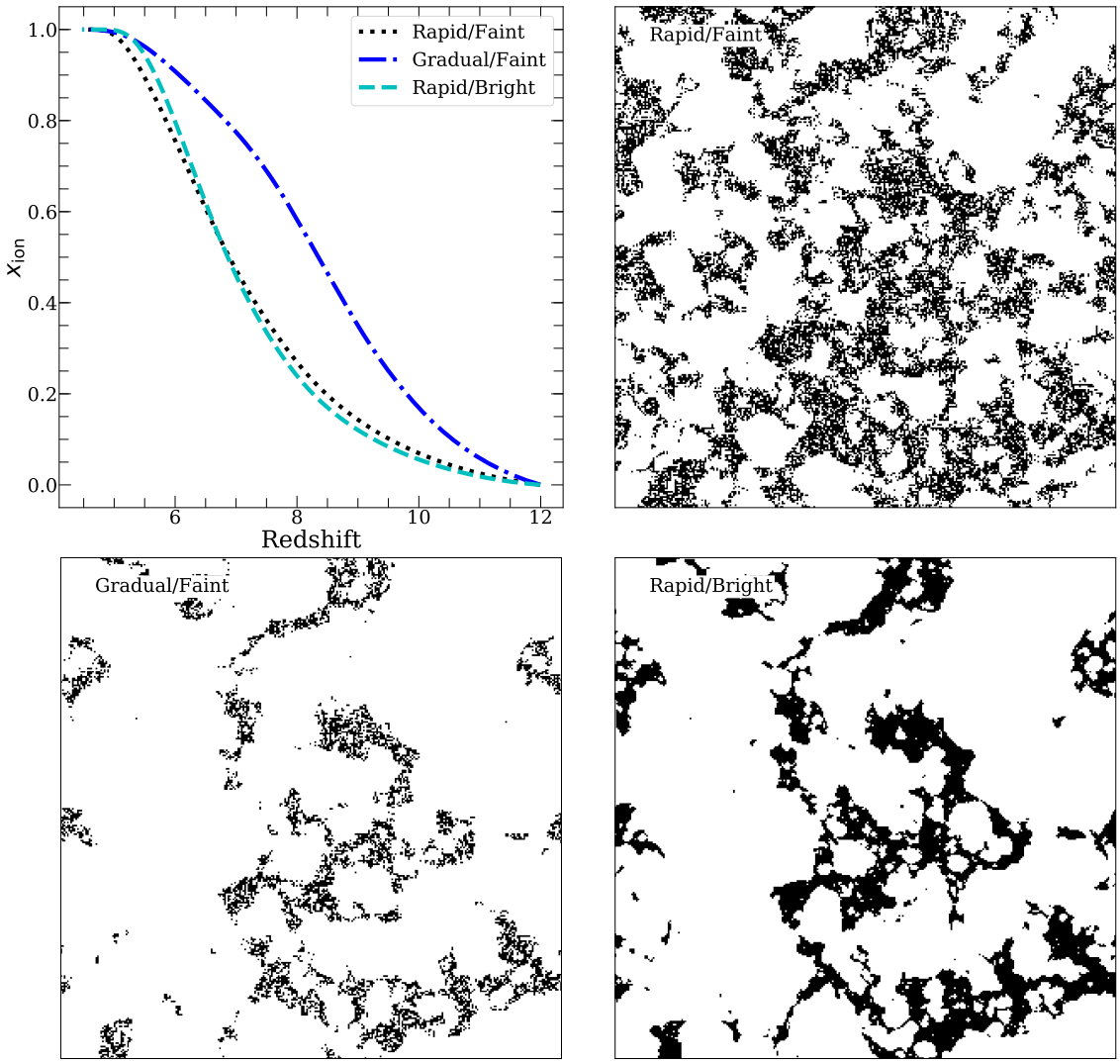

Figure 4.4: Reionization simulations employed in this study. **Upper left**: volume-weighted mean ionized fraction vs. redshift for the three reionization histories considered in this work. **Other panels**: slices through the ionization fields at $z = 6$ in a $(300\ h^{-1}\mathrm{Mpc})^3$ volume for each scenario. Black denotes cells with HI fractions ≥ 0.5. We consider rapid reionization models in which reionization is driven by faint and bright sources (upper right and lower right respectively) and a gradual model in which reionization is nearly over at $z = 6$ (lower left). The neutral islands are the smallest in the gradual case because the neutral fraction is smallest. In the case where bright sources dominate, the neutral island are less porous and hence take up a smaller effective volume (at approximately fixed global neutral fraction). These simulations were run with the radiative transfer code of [10]. We use them to model the distribution of reionization redshifts, $\frac{dP}{dz_{\rm re}}$ (see eqs. 4.2 and 4.5), as well as the contribution to the LyC opacity from neutral islands.

a minimum mass of $10^9 h^{-1} M_\odot$ using a sub-grid algorithm based on the non-linear biasing approach of [137] (see also [10]).[12]

Several recent works have studied how the reionization source population differs in WDM cosmologies, compared to CDM (e.g. [200, 201, 202]). In models with a larger free-streaming scale, reionization tends to start later and is driven by brighter sources owing to the suppression of the halo mass function at lower masses. In what follows, we do not model the effects of the underlying DM cosmology on the reionization history, with the rationale that any differences in the ionizing emissivity of the sources are mostly degenerate with uncertain astrophysical parameters such as the star formation efficiency or escape fraction. We assume that we could always tune these source parameters to achieve approximately the same global neutral fraction among the DM cosmologies. Our main aim here is to quantify how small-scale power in the ionized IGM changes the mean free path, so we will compare different cosmologies *at a fixed global neutral fraction*. We note that our approach neglects potential differences in the neutral island morphology among the cosmologies.

To explore how different reionization histories/morphologies come into play with the observed mean free path, we employed three models for the ionizing photon output of the sources. The first is the fiducial rapid reionization model from [10], in which reionization has a late midpoint ($z \sim 7.1$) and in which every halo down to with a minimum mass of $M_{\rm min}^{\rm halo} = 10^9\ h^{-1} M_\odot$ has the same ionizing photon emissivity. The latter condition means that the faintest, lowest-mass halos produce the bulk of the ionizing photons. We refer to this scenario as the "Rapid/Faint" model. Our second model has a more gradual

[12]To populate the sub-grid halos, we drew from the mass function of [199], which agrees well with the resolved mass function in our simulation.

reionization history with an earlier midpoint ($z \sim 8.5$), and also assigns the same emissivity to every halo - we refer to this as the "Gradual/Faint" model. Our third model has a similar reionization history as the Rapid/Faint case, but has a minimum mass of $8.5 \times 10^9\ h^{-1} M_\odot$ and assumes the emissivity of each halo is proportional to its UV luminosity, obtained by abundance matching to the UV luminosity function of [129]. In this case, reionization is dominated by bright, highly biased sources - we refer to this as the "Rapid/Bright" model. What is important for our purposes is that the structure of the neutral regions in these models are significantly different, as shown visually in Figure 4.4. The top-left panel shows the global reionization histories in the three models, while the other panels show slices through the ionization fields at $z = 6$. Neutral gas is depicted in black. Comparing the top- and bottom-right panels, the two rapid models have approximately the same global neutral fraction of $x_{\rm HI} \approx 25\%$ at $z = 6$. The model with brighter sources (bottom), however, exhibits less porous neutral islands and larger ionized regions compared to the model with fainter sources (top). The neutral islands are much smaller in the gradual model because reionization is closer to completion, with $x_{\rm HI}(z = 6) \approx 10\%$.

In Figure 4.5, we show the ionized bubble and neutral island size distributions (IBSD and NISD, left and right panels, respectively) in our simulations at $z = 6$. We define these sizes using the ray-tracing method described in Ref [11] and implemented in the publicly available package *tools21cm* [203]. The Rapid/Faint model has the smallest ionized bubbles, as is clearly seen in Fig. 4.4, and thus the highest opacity due to neutral gas. In the right panel the Rapid/Bright model stands out with the largest (least fragmented) neutral islands owing to the sparse and highly biased distribution of its ionizing sources. Note that

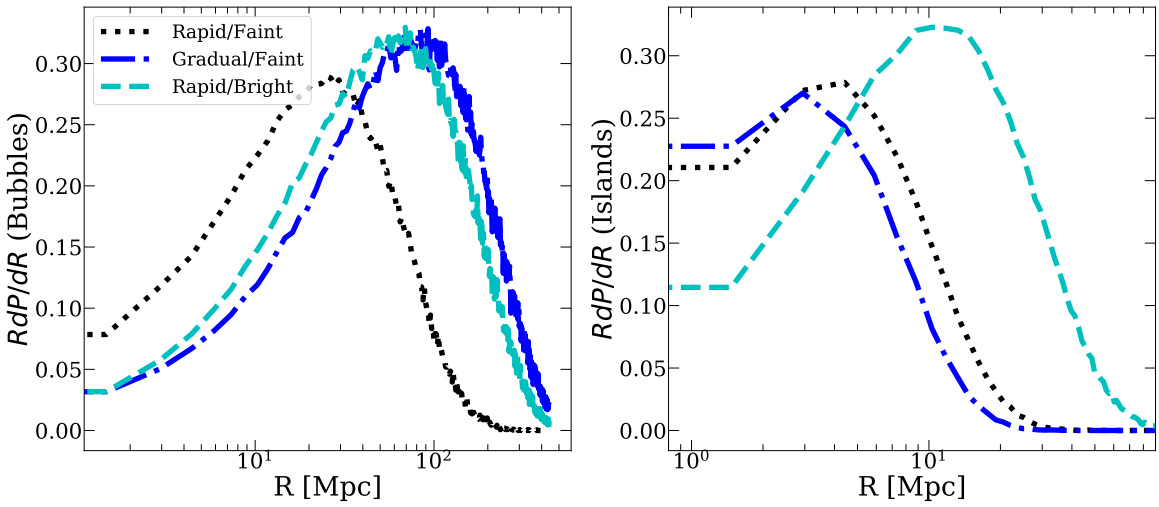

Figure 4.5: Distribution of ionized bubble (left) and neutral island (right) sizes in our reionization simulations at $z = 6$. Both use the ray tracing method of [11] for quantifying the region size. The Rapid/Faint case has the smallest ionized bubbles and hence the highest opacity due to neutral islands, while the other two models have similar bubble sizes. The Rapid/Bright model has the largest (least fragmented) neutral islands owing to the sparsity and bias of sources in that model, while the other two models have smaller islands sizes.

the x axis is in Mpc here rather than h^{-1}Mpc to aid comparison with the NISD results of Refs [93, 204].[13] WDM scenarios with lighter m_X have fewer low-mass halos (see left panel of Fig. 4.10 in §4.4) and thus we expect them to have morphologies more toward our Rapid/Bright case. As we will discuss below, the degree to which neutral islands affect the measured MFP is uncertain, potentially in a way degenerate with morphology differences between WDM models. Given these uncertainties, for simplicity we proceed by comparing different cosmologies with the neutral island morphologies fixed.

[13] On average our islands are somewhat smaller than found by [93] at 25% and 10% neutral (left and middle panels of their Fig. 9) while our Rapid/Bright model is similar to the models in [204] at 16% neutral (left panel of their Fig. 6). Our islands may be smaller than theirs in part because of our threshold of $x_{\rm HI} > 0.5$ for a cell to be part of an island, which ignores many partially ionized cells, especially in the models with faint sources. Still, the spread *between* our models is similar to the range found in [93] and larger than that in [204], giving us confidence that our range of scenarios is representative.

We used the 3-dimensional ionization fields to calculate the contribution from neutral islands to the mean absorption coefficient. Following [10], we traced 50,000 sight lines from random positions to create mock quasar absorption spectra, and then extracted the absorption coefficient by fitting a stack of these spectra to the model of [143]. This stacking/fitting procedure mimics the method by which the mean free path is measured observationally. When we fit the stacked absorption spectra following [143], we allow the normalization of the flux to float in the fit, as is done in [13]. Importantly, this prevents sightlines that start in neutral islands from contributing to $\langle\kappa_{\rm neutral}\rangle$, since they contribute zero flux to the stack at all wavelengths. In contrast, fixing the normalization of the stack to be 1 at 912Å effectively includes these sight lines (inappropriately) and yields a somewhat higher $\langle\kappa_{\rm neutral}\rangle$ (lower MFP). For the Rapid/Faint, Gradual/Faint, and Rapid/Bright models respectively, our fiducial procedure yields a neutral island MFP that is 43%, 16%, and 29% larger than obtained by fixing the stack normalizations to 1. To isolate the contribution from neutral islands, we set the opacity to zero in cells where the local ionized fraction is $x_{\rm ion} > 0.5$. Denoting the absorption coefficient from neutral islands with $\langle\kappa_{\rm neutral}\rangle$, we write the total absorption as $\kappa_{\rm global} = \langle\kappa_{\rm ion}\rangle + \langle\kappa_{\rm neutral}\rangle$, and then take the "measured" mean free path to be $\lambda_{912}^{\rm mfp} = 1/\kappa_{\rm global}$. We caution, however, that our estimate of $\lambda_{912}^{\rm mfp}$ likely does not provide an exact apples-to-apples comparison to the measurements of Refs [13, 14] at $z = 6$. We will return to this point in the next section.

4.3 DM models with suppressed small-scale power (WDM)

4.3.1 Results

Figure 4.6 shows the redshift evolution of the MFP in the CDM and two WDM models considered here. For this comparison, we use the Rapid/Faint reionization scenario described above, but we will explore the other scenarios below. The data points show the observational measurements and limits of Refs [12], [13] and [14]. The left panel shows our full models, including opacity from ionized gas and neutral islands, while the right panel considers only the opacity from ionized gas. The thin gray curve in the left panel corresponds to the opacity from neutral islands, i.e. $1/\langle\kappa_{\rm neutral}\rangle$ as defined in §4.2.3. As expected, the MFP generally increases with the free streaming scale. The differences are rather modest, however, in the left panel. At $z = 6$, the model with $m_X = 3$ (1) keV differs from the CDM case by 19 (45) %. By $z = 4.55$, the difference is 5 (43) %.

The differences between the DM cosmologies are smaller than we might naively expect, particularly at $z > 6$, where the prevalence of un-relaxed/clumpy gas should drive larger differences between CDM and WDM. To understand why, consider the MFP neglecting the contribution from neutral islands (right panel). There, the differences are indeed larger at higher redshift, when a larger fraction of the gas is un-relaxed. However, comparing to the left panel, the opacity from neutral islands contributes more at these redshifts. Most importantly, *at fixed global neutral fraction*, the neutral islands contribute a larger share of the opacity as the free streaming scale is increased. Thus, when they are accounted for, the neutral islands obscure differences arising from the free streaming scale. This effect would be even larger if the free streaming scale also suppressed the source population. For

example, one could imagine a scenario in which reionization is delayed in the model with $m_X = 1$ keV. In this case, the neutral islands would play an even larger role in setting the opacity at $z = 6$, perhaps bringing $\lambda_{912}^{\rm mfp}$ closer to the CDM result.

On the other hand, by $z \sim 4.5$, most of the small-scale structure in the CDM model has been erased by smoothing/photo-evaporation. We thus see the CDM and $m_x = 3$ keV models converging. Visually, this is consistent with the bottom- left and -middle panels of Fig. 4.2. We are led to conclude that the marked lack of difference seen in the left panel owes to two effects: (1) neutral island opacity at higher redshift ($z > 6$); (2) relaxation at lower redshift ($z < 5$). Both the CDM and $m_X = 3$ keV results agree reasonably well with MFP measurements at $z \leq 5$, while the $m_X = 1$ keV case overshoots by a factor of ~ 1.5. This suggests that it may be difficult to reconcile the $m_X = 1$ keV model with the measurements unless reionization ends even later than in our fiducial model, for which $x_{\rm ion} \approx 20\%$ at $z = 6$.

Figure 4.7 shows what happens if we vary the underlying reionization model. The left panel compares our Gradual/Faint (solid) and Rapid/Faint (dashed) reionization scenarios. The global neutral fractions at $z = 6$ are $x_{\rm HI} \approx 10\%$ and 20%, respectively. Overall, the MFP at $z = 6$ is significantly longer in the Gradual/Faint model for two reasons: (1) A smaller contribution from neutral islands owing to the smaller $x_{\rm HI}$; (2) A larger fraction of relaxed gas in the ionized regions, since much of the IGM is reionized earlier in the Gradual/Faint model (see top-left panel of Fig. 4.4). Neutral islands contribute less to the opacity at $z = 6$ in the gradual model, which would act to enhance differences between the WDM and CDM models. This effect is muted, however, because the ionized gas is, on

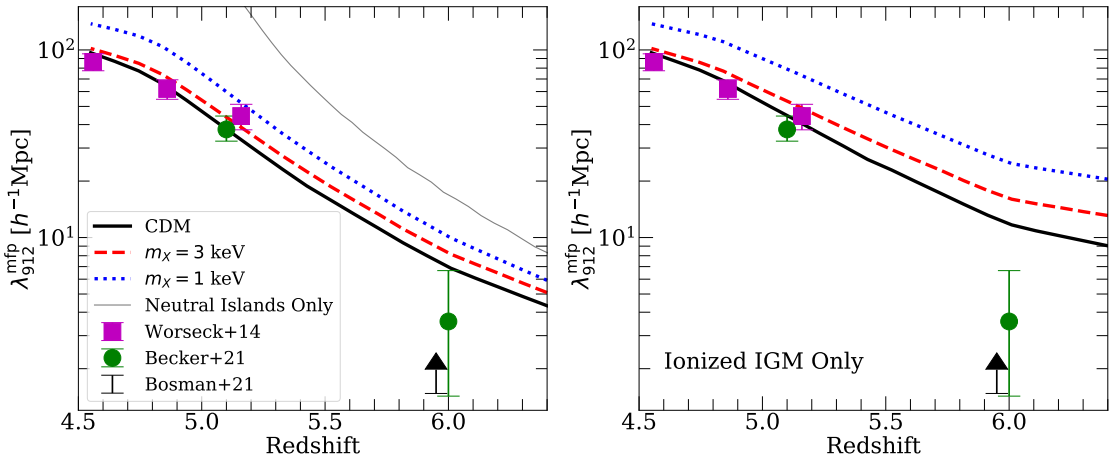

Figure 4.6: Mean free path for CDM and two WDM models with different particle masses. **Left**: Mean free path evolution for CDM (solid black), $m_X = 3$ keV (dashed red) and $m_X = 1$ keV (dotted blue) in our faint sources/rapid reionization scenario. The thin grey line shows the MFP due to netural islands alone ($1/\langle\kappa_{\rm neutral}\rangle$, see §4.2.3). The results shown here represent our full model of the IGM opacity, including contributions from ionized regions and neutral islands. We show the observational measurements of Refs [12, 13, 14] (the lower limit from Ref [14] at $z = 6$ has been shifted slightly to the left for clarity). **Right**: the MFP for the same three models but with the neutral island contribution omitted. Differences between the DM cosmologies are suppressed by two effects: (1) at lower redshift ($z < 5.5$), Jeans pressure smoothing and photo-evaporation erases much of the small-scale power that would otherwise distinguish these models; (2) At higher redshift $z > 6$, neutral islands contribute increasingly to the IGM opacity. Hence, at fixed global neutral fraction, the MFPs become more similar between the models when the effects of neutral islands are included (compare left and right panels).

average, more relaxed. Hence there is less small-scale structure to drive a difference between the CDM and WDM $\lambda_{912}^{\rm mfp}$.

The curves in the right panel correspond to our Rapid/Faint and Rapid/Bright scenarios. These have nearly identical reionization histories, so there is no significant difference in the relaxation state of the gas. Rather, the differences in the MFP at $z = 6$ are driven entirely by the structure of the neutral islands. In the Rapid/Bright scenario, there are fewer neutral islands and they are larger, on average, resulting in a significantly lower opacity contribution from neutral islands. Hence, the WDM results differ more from the CDM case at $z = 6$, with the MFP being 30% and 80% larger for $m_X = 3$ and 1 keV, respectively. These results highlight a key point for interpreting the measurement of $\lambda_{912}^{\rm mfp}(z = 6)$ by [13]. Constraining the global neutral fraction at $z = 6$ is of utmost importance for gaining insight into the sinks from the MFP measurement.

Indeed, it would be helpful to know whether *any* of the opacity comes from neutral islands. As mentioned in the previous section, our estimate of $\lambda_{912}^{\rm mfp}$ near $z = 6$ may not be directly comparable to the measurements of [13, 14], mainly because it is unclear to what extent neutral islands, if they are present at $z = 6$, affect those measurements. Most of the quasar spectra used in these works do not show evidence of neutral islands near the quasar, as is to be expected for the highly biased regions in which these quasars likely reside [205]. As such, their measurements may more closely reflect $\lambda_{912}^{\rm mfp}$ in the ionized component of the IGM (see right panel of Fig. 4.6).

Table 4.1 brackets the range of possibilities for the effect of neutral islands on our results. The middle column shows percentage differences in the MFP between WDM models

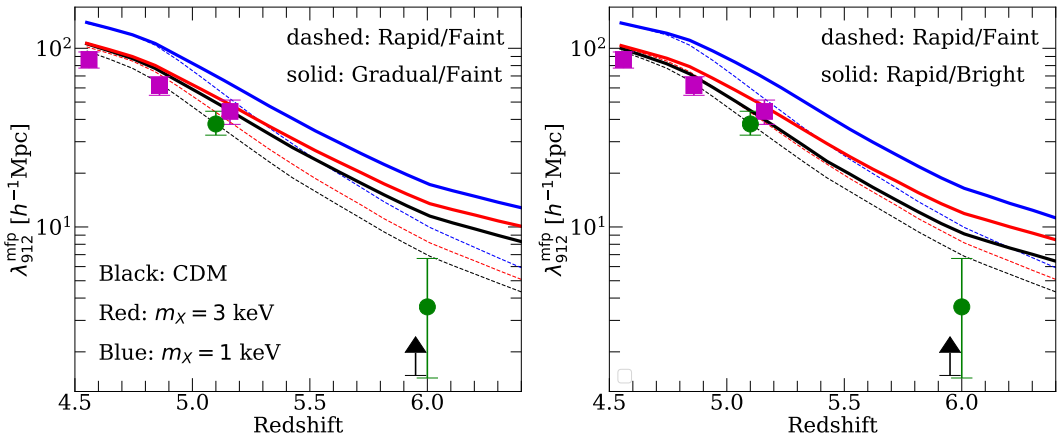

Figure 4.7: Interplay between the DM cosmology and features of the reionization model. **Left**: Comparing our Gradual/Faint (solid) and Rapid/Faint (dashed) reionization scenarios. Both models here assume our fiducial source model, which is driven by faint galaxies (see main text, and Fig. 4.4). In the Gradual/Faint case the MFP is longer at $z = 6$ owing to the reduced opacity from neutral islands, and to the dearth of clumpy, un-relaxed gas in the ionized regions. The latter also suppresses differences between the DM cosmologies. **Right**: Comparing our Rapid/Faint and Rapid/Bright scenarios. These models have the same global reionization histories, but vary the brightness and bias of the sources. The MFP is longer in the Rapid/Bright model because the neutral islands are more anti-biased, so they contribute less to the total IGM opacity. In this case, the relative differences between DM models are enhanced because the small-scale structure in ionized regions contributes a larger fraction of the total opacity.

% Diff. at $z = 6$ for $m_X = 3$ (1) keV	Ionized Only	Fiducial Prescription
Rapid/Faint	37 (112)%	19 (45)%
Gradual/Faint	22 (69)%	17 (50)%
Rapid/Bright	40 (121)%	30 (80)%

Table 4.1: Percentage differences between the $m_X = 3$ (1) scenarios and CDM at $z = 6$ for all three of our reionization histories under different assumptions about the contribution of neutral islands to the measured MFP. We bracket the range of possibility by assuming that either neutral islands do not contribute at all to the measured opacity ("Ionized Only"), or that they contribute as predicted by our fiducial stacking/fitting procedure ("Fiducial Prescription"). Although the differences between DM cosmologies are larger in the Ionized Only scenario, the truth is likely somewhere between these two limiting cases.

and CDM for the scenario in which neutral islands do not contribute at all to the opacity. The right column shows the same but adopting our fiducial prescription for the neutral island opacity. As mentioned previously, the differences between the cosmologies are larger if the quasar stacks effectively measure the opacity of only the reionized phase of the IGM. The truth is likely somewhere between these two cases. This discussion highlights the need for further work on how neutral islands affect the measured MFP during reionization.

4.3.2 Effects of modeling assumptions

In this section, we will examine the effects of several assumptions made in our modeling. We adopt our Rapid/Faint model in the ensuing comparisons. In Figure 4.8, we show the effect of varying the gas relaxation timescale in our model, $t_{\rm relax}$. Recall that lengthening (shortening) this timescale enhances (reduces) the contribution of un-relaxed gas to the opacity, which acts to increase (decrease) differences in $\lambda_{912}^{\rm mfp}$ between the WDM and CDM models. The left panel assumes $t_{\rm relax} = 50$ Myr, while the right panel assumes $t_{\rm relax} = 500$ Myr. These values were chosen to be somewhat extreme examples to highlight the effect of this parameter. (Our fiducial value is $t_{\rm relax} = 150$ Myr, which is motivated by recent results from radiative hydrodynamics simulations [131, 74].) We see that the difference between the DM models is generally greater when the relaxation time scale is longer, i.e. when a large fraction of the IGM is un-relaxed. For example, relative to the CDM $\lambda_{912}^{\rm mfp}$ at $z = 6$, the models with $m_X = 3$ (1) keV have a 37 (90) % longer $\lambda_{912}^{\rm mfp}$ for $t_{\rm relax} = 500$ Myr. For $t_{\rm relax} = 50$ Myr, the difference reduces to 7 (20) %. The CDM results with $t_{\rm relax} = 500$ Myr are more consistent with the short MFP at $z = 6$, but they under-shoot the $z \leq 5$ measurements. We note, however, that a value of $t_{\rm relax} = 500$ Myr

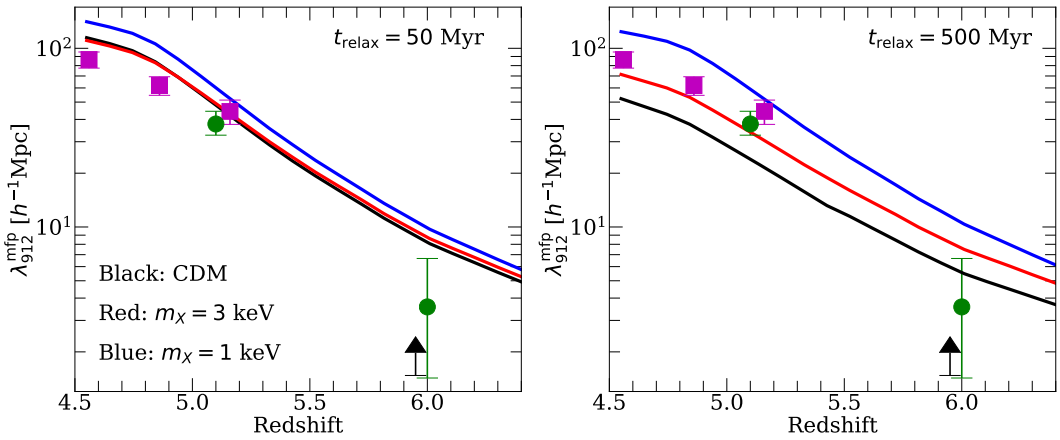

Figure 4.8: Effect of the relaxation timescale on the MFP. **Left**: MFP for each of our DM models assuming a relaxation timescale of $t_{\rm relax} = 50$ Myr. **Right**: same, but for $t_{\rm relax} = 500$ Myr. We see that shorter (longer) relaxation timescales result in longer (shorter) $\lambda_{912}^{\rm mfp}$ and a reduced (increased) difference between the different DM scenarios. All these trends owe to the increased contribution to the opacity from un-relaxed gas in the scenario with larger $t_{\rm relax}$.

is a much longer time scale than is observed in the simulations of [74]. Figure 4.8 mainly highlights that the sensitivity of the MFP to small-scale power relies on how much of the ionized IGM is un-relaxed.

Next we consider how the intensity of the extragalactic ionizing background factors into our calculations. The data points in the left panel of Figure 4.9 show Lyα forest measurements of the hydrogen photoionization rate, which scales with the intensity of the ionizing background. Clearly there is still considerable uncertainty in Γ_{-12} at $z > 4.5$. The solid/black curve shows the evolution of Γ_{-12} in our hydrodynamic simulations of the sinks. Here we explore what happens to our results if we vary Γ_{-12}. We bracketed the uncertainties in the measurements with two histories in Γ_{-12}, shown as the upper and lower bounds of the blue shading in Figure 4.9. We then re-scaled the neutral hydrogen densities in our simulations under the assumption of photoionization equilibrium, and recomputed

the MFPs in our models. The right panel of Figure 4.9 shows the result of this exercise. For each DM model, the shaded region corresponds to the ratio of the MFP from the high and low $\Gamma_{\rm HI}$ histories with the fiducial one. The solid curves denote the ratio of the MFP with CDM for each of the DM models assuming the fiducial $\Gamma_{\rm HI}$ history (that is, of the solid curves in Fig. 4.6). The range spanned by the shaded regions is similar to the difference between CDM and $m_X = 1$ keV at $z > 5.5$ (a factor of ~ 1.4), and becomes significantly larger at $z < 5.5$ (a factor of ~ 2.5 vs. ~ 1.5). These results suggest that the considerable uncertainties in Γ_{-12} alone make it difficult to rule out convincingly with MFP measurements even the $m_X = 1$ keV model, which has already been ruled out by Lyα forest flux power spectrum measurements [8].

Lastly, we comment on the assumed thermal history of the IGM in our models. Consider first the thermal history of a gas parcel starting with the impulsive heating by I-fronts at redshift $z_{\rm re}$ (we will discuss the history prior to this below). At $z \leq z_{\rm re}$, the thermal history of the gas affects the evolution of its Jeans filtering scale as well as its equilibrium HI fraction through the temperature dependence of the recombination rate. The simple relaxation ansatz employed here (eq. 4.3) implicitly models these effects by evolving the opacity in hot, un-relaxed gas (assumed to be at $T_{\rm re} = 20,000$ K), towards a cooler, relaxed limit with $T \sim 8,000$ K, the temperature to which the gas relaxes in our hydrodynamic simulations. Variation in the thermal history at $z \leq z_{\rm re}$ can come in two forms: (1) variation in the impulsive heat injection by I-fronts as they sweep through, encapsulated in the reionization temperature, $T_{\rm re}$; (2) variation in the photoionization equilibrium heating rate of the highly ionized gas, well after I-front passage. The latter depends only on the

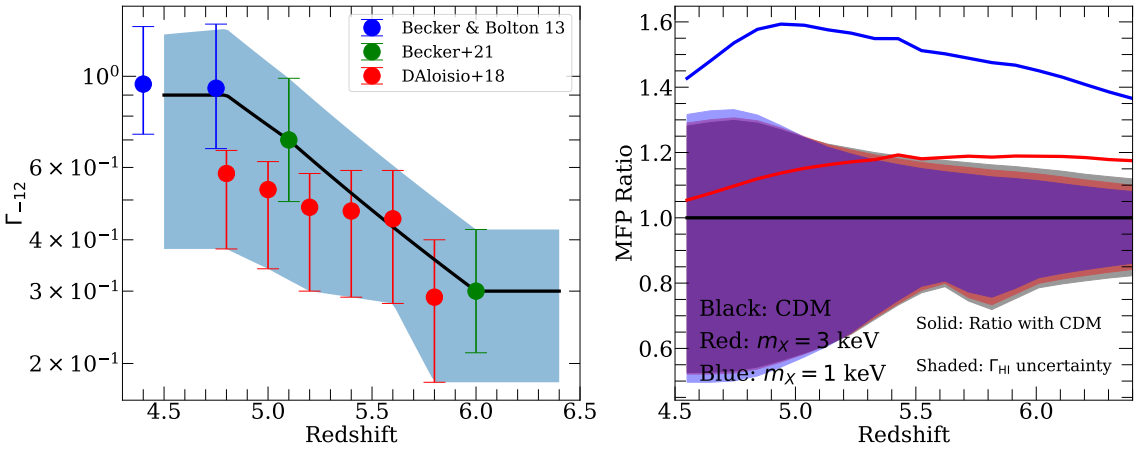

Figure 4.9: Effect of different $\Gamma_{\rm HI}$ histories on the MFP. **Left**: range of $\Gamma_{\rm HI}$ histories considered in our analysis (shaded region) compared to three sets of measurements from the literature. The solid black line denotes our fiducial history for $\Gamma_{\rm HI}$. **Right**: Comparison of the uncertainty in the MFP from DM models vs. $\Gamma_{\rm HI}$. The solid lines denote the ratio of the MFP with CDM for the different DM models assuming the fiducial $\Gamma_{\rm HI}$ history, and the shaded regions denote the range spanned by the different $\Gamma_{\rm HI}$ histories for each model. At $z > 5$ the size of the spread due to $\Gamma_{\rm HI}$ is similar to the difference between CDM and $m_X = 1$ keV, and at $z < 5$ the former is significantly larger. The shaded regions all roughly overlap, highlighting the insensitivity of the $\Gamma_{\rm HI}$ uncertainty to the assumed DM cosmology. We see that uncertainty in the history of $\Gamma_{\rm HI}$ would considerably complicate any effort to distinguish even the CDM and $m_X = 1$ keV scenarios, the latter of which has been ruled out already by the Lyα forest.

spectrum of the extragalactic ionizing background, which maintains the ionization state of the gas. While this spectrum is highly uncertain, a realistic variation in the spectral shape leads to only $\sim 30\%$ changes in the IGM temperature [206, 135], and a smaller change in the opacity/MFP. Variations in $T_{\rm re}$ could lead to factor of 2 changes in the thermal history if reionization is still ongoing at $z < 6$ (see e.g. Fig. 1 of [135]). Using radiative transfer simulations of I-fronts, Ref [135] found that reionization temperatures are likely in the range $T_{\rm re} \approx 17,000 - 30,000$ K. We note that the upper limit of this range, $T_{\rm re} = 30,000$ K, is 50% hotter than our assumed value. Since the amount of heat dumped into the IGM at $z_{\rm re}$ is $\sim k_B T_{\rm re}$, we expect no more than a $\sim 50\%$ effect on our results for a realistic variation $T_{\rm re}$. Note also that variations at this level are much smaller than the factor of $20 - 1,000$ jump in temperature that occurs when an I-front sweeps through a cold, neutral region.

Variation in the thermal history of the gas *before* $z_{\rm re}$, however, could have a larger effect on our results because it alters the Jeans filtering scale of the un-relaxed gas, which is the driver of differences in $\lambda_{912}^{\rm mfp}$ between CDM and WDM. Our hydrodynamic simulations assume that the gas was cooling adiabatically after kinematic decoupling from the CMB. As a result, the gas can get as cold as ~ 10 K before the impulsive heating to $T_{\rm re}$. If, for example, the first X-ray sources were extremely efficient at pre-heating the gas, then the IGM could have started out with far less small-scale structure on $\sim 10^4 - 10^6$ $M_\odot$ scales, perhaps lengthening the predicted MFP at $z = 6$. To quantify roughly the maximum effect of this pre-heating on IGM clumping, Ref [74] considered an extreme scenario among their radiative hydrodynamic simulations, in which the gas was not allowed to cool below $T = 1,000$ K below $z = 20$. They found a suppression in the IGM clumping factor of ~ 1.9

within the first $\sim$ 10 Myr of $z_{\rm re}$, which translates to a lengthening of $\lambda_{912}^{\rm mfp}$ by the same factor. Although this assessment likely overestimates the effect considerably, the thermal history of the gas prior to reionization is an important uncertainty further obscuring the cosmological interpretation of high-z MFP measurements.

We conclude this section by discussing briefly how uncertainties from modeling assumptions affect the feasibility of constraining WDM with MFP measurements. In a fully ionized IGM, the main factor limiting constraints is $\Gamma_{\rm HI}$. Figure 4.9 shows that given current measurements, $\Gamma_{\rm HI}$ produces factor of ~ 2 uncertainty in the MFP at $z < 5.2$. Under very optimistic assumptions assumptions about the longevity of un-relaxed gas (right panel of Figure 4.8, $t_{\rm relax} = 500$ Myr), the difference between CDM and $m_X = 3$ (1) keV is a factor of $\sim$ 1.4 (2) shortly after reionization ends. Assuming $\lambda_{912}^{\rm mfp} \propto \Gamma_{\rm HI}^{2/3}$, which holds approximately in our calculations, the uncertainty in $\Gamma_{\rm HI}$ should be reduced by at least a factor of $\sim$ 1.7 to produce a spread similar to the difference between CDM and $m_X = 3$ keV. More realistic values of $t_{\rm relax}$ suggest that this factor would be even larger.[14]

At $z > 5.2$, there is only one measurement ($z = 6$), which has large error bars. Even if future efforts can populate $5.2 < z < 6$ with measurements of similar fidelity to those at $z < 5.2$ (a challenging task), getting constraints would be complicated by uncertainties in the reionization history and morphology. As Figure 4.7 illustrates, the possible scenarios are sufficiently diverse that even if the detailed redshift evolution of the MFP were known, breaking the degeneracy with a poorly constrained reionization history could be challenging. So to obtain constraints from this range of redshifts, even with high-

[14]We note also that if the IGM was still undergoing reionization at $5 < z < 6$, it is unclear how to interpret existing measurements of $\Gamma_{\rm HI}$. These measurements generally rely on models/simulations to map the measured forest transmission to $\Gamma_{\rm HI}$. The models employed to date do not include neutral islands and fluctuations from reionization (see however Ref [79] for a discussion of the latter).

quality MFP measurements, some constraints on the global neutral fraction and a better understanding of how neutral islands contribute to the *measured* LyC opacity would be required.

In summary, the predicted difference in $\lambda_{912}^{\rm mfp}$ between CDM and WDM cosmologies depends critically on how much gas is in an un-relaxed (still clumpy) state, which, in turn, depends on the uncertain reionization history and time scale for relaxation. Furthermore, large uncertainties in the intensity of the extragalactic ionizing background, and in the thermal history of the gas prior to reionization, would further weaken cosmological inferences from high-z MFP measurements. Based on these considerations, we conclude that the observed short value of $\lambda_{912}^{\rm mfp}(z=6)$ is unlikely in the near future to be a useful no-go test of DM models with small-scale power cutoffs.

4.4 Models with enhanced small-scale power

Some alternatives to standard CDM, such as ultra-light axions [9, 183], or primordial black holes [188], predict a shot noise-like enhancement in the small-scale matter power spectrum. This class of scenarios is of interest for the current paper owing to the shortness of the measured $\lambda_{912}^{\rm mfp}(z=6)$. Indeed, the measurements of [13] are pushing models toward a very late and rapid reionization process, and it is unclear at present whether this picture can be reconciled in a physically consistent way with the evolution of the Lyα forest flux evolution and its spatial fluctuations [10, 207, 208]. This motivates exploring the role that additional small-scale power could have in producing short values of $\lambda_{912}^{\rm mfp}$, a task that we take up here.

As a representative example, we use the ultra-light axion DM scenario considered in Ref [9] in which there is a white noise contribution to the power spectrum from isocurvature fluctuations. We adopt their $f_{\rm iso} = 0.01$ model, which corresponds to a significant enhancement in halo abundance on $< 10^8 M_\odot$ scales, the mass range of interest for this study. The orange curve in Figure 4.1 shows the linearly extrapolated power spectrum in this model. In contrast to the previous section, we did not run hydrodynamic simulations in the ultra-light axion cosmology. Instead, we use a simplistic model to estimate the effect of the enhanced power on the opacity of un-relaxed gas. In the picture adopted here, the halos are treated as dense, optically thick "billiard ball" absorbers, with aggregate absorption coefficient

$$\kappa_{\rm halo} = \int_{M_{\rm min}}^{\infty} dM \sigma_h(M) \frac{dn}{dM}. \tag{4.6}$$

Here, dn/dM is the halo mass function and $\sigma_h(M)$ is the physical cross-section of a halo with mass M, which we approximate to be

$$\sigma_{\rm h}(M) = \pi R_{200}^2(M), \tag{4.7}$$

where $R_{200}(M) = [3M/(4\pi \times 200 \rho_c(z))]^{1/3}$ is the halo virial radius and $\rho_{\rm c}(z)$ is the critical density. The parameter $M_{\rm min}$ is the mass of the smallest *gaseous* halo to form, which roughly corresponds to the Jeans filtering scale of the gas. In the un-relaxed limit, we take $M_{\rm min} = 10^4\ h^{-1}{\rm M}_\odot$, the Jeans scale of the adiabatic hydrodynamic simulations that we use to model the un-relaxed IGM. To evaluate equation 4.6 we use the halo mass function from Ref [209], which is calibrated using the same definition of the virial radius (R_{200}) that we employ here. The left panel of Figure 4.10 compares the mass function in the axion-like model to CDM and the two WDM models of the last section. The axion-like model exhibits

enhanced halo formation on small-scales, but is nearly indistinguishable from CDM above $\sim 10^{10}$ $M_\odot$.

If we assume that the halos provide all the opacity to ionizing photons, the relative difference between the CDM and axion-like scenarios can be evaluated directly from the above expressions. This assumption is closest to true in the un-relaxed limit where most of the opacity is sourced by dense, self-shielding absorption systems in the mass range $\sim 10^4 - 10^8$ $M_\odot$ [178]. As more time elapses since $z_{\rm re}$, photoevaporation and relaxation of the small-scale power will drive the $\lambda_{912}^{\rm mfp}$ in the two models closer, as we have already seen in the previous section. We proceed here by assuming that the ratio $\kappa_{\rm halo}^{f_{\rm iso}=0.01}/\kappa_{\rm halo}^{\rm CDM}$ captures the enhancement over CDM in the un-relaxed limit, and that the relaxed limit of the two models are the same. To implement this in our relaxation model, we simply re-scale the κ_u for CDM in equation (4.3) by the ratio $\kappa_{\rm halo}^{f_{\rm iso}=0.01}/\kappa_{\rm halo}^{\rm CDM}$, while leaving κ_r the same as before. The results of this procedure are shown as the magenta dot-dashed curve in the right panel of Figure 4.10, alongside our CDM and WDM models, all assuming the Rapid/Faint reionization scenario. The green dot-dashed curve corresponds to the same $f_{\rm iso} = 0.01$ model, but adopting a shorter relaxation timescale of $t_{\rm relax} = 70$ Myr. Raising $M_{\rm min}$ to a value of 10^6 $h^{-1}M_\odot$ changes $\kappa_{\rm halo}^{f_{\rm iso}=0.01}/\kappa_{\rm halo}^{\rm CDM}$ very little across all redshifts, although the individual values of $\kappa_{\rm halo}$ change by nearly an order of magnitude.

The enhanced small-scale power in the axion-like model produces significantly better agreement with the central value of the $z = 6$ MFP for our fiducial $\Gamma_{\rm HI}$ and reionization histories. However, at least for our fiducial choice of $t_{\rm relax} = 150$ Myr, the agreement at $z < 5$ is considerably worse than for CDM and WDM with $m_X = 3$ keV. The reason is that

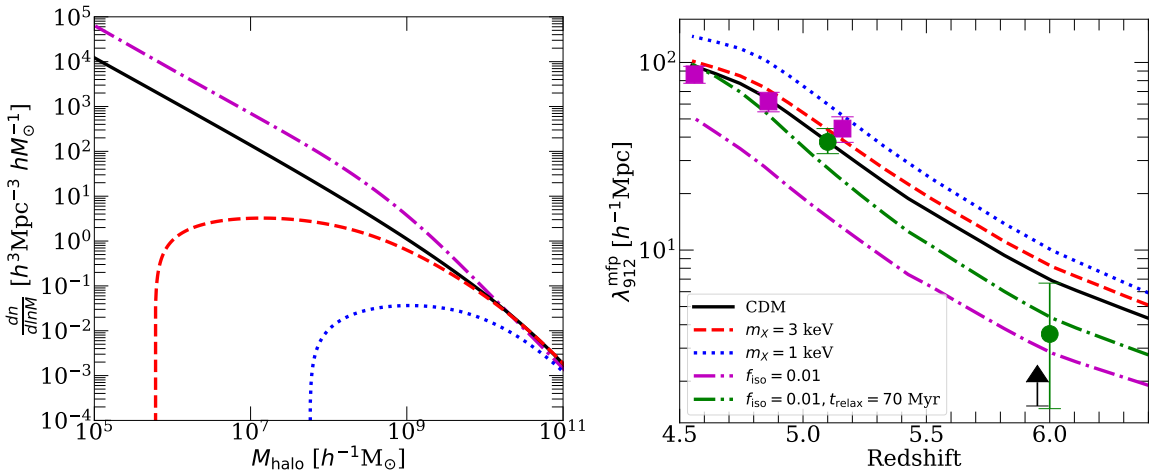

Figure 4.10: MFP evolution in DM cosmologies with enhanced small-scale power. As an illustrative model, we use the axion-like scenario considered in [9]. **Left**: halo mass function for the CDM case (black solid curve) compared against the axion-like scenario (dot-dashed magenta) and the thermal relic WDM models with $m_X = 3$ and 1 keV (dashed red and dotted blue). **Right**: the MFP for the axion-like case compared to the other DM models assuming $M_{\rm min} = 10^4\ h^{-1}M_\odot$ in equation 4.6, all assuming the Rapid/Faint reionization scenario. The enhanced power scenario has a factor of ~ 7 more halos at masses $\leq 10^8$ $h^{-1}M_\odot$ than the CDM case, which contribute significant additional opacity in the unrelaxed limit. The resulting MFP at $z = 6$ is in better agreement with the central value of the measurement, but under-shoots the measurements at lower redshifts considerably. This discrepancy can be ameliorated by modifying the reionization history or adopting a shorter relaxation timescale. The green dot-dashed curve shows an example of the latter, with $t_{\rm relax} = 70$ Myr (compared to our fiducial value of $t_{\rm relax} = 150$ Myr).

the extremely clumpy un-relaxed gas in the axion-like model that brings the MFP down at $z = 6$ stays un-relaxed for too long and drives the MFP too low at $z \leq 5$. This effect can be ameliorated to some degree by modifying the reionization history to give the gas more time to relax and/or by invoking a shorter relaxation timescale. The latter is illustrated by the green dot-dashed curve, with $t_{\rm relax} = 70$ Myr. In the axion-like model, the relaxation timescale could in fact be shorter than our fiducial choice of $t_{\rm relax} = 150$ Myr (which was motivated by radiative hydrodynamic simulations in a CDM cosmology), if the opacity is dominated by very small clumps/halos that are quickly photo-evaporated.

We conclude by noting that better agreement with the $z = 6$ MFP could also be achieved within CDM given the large uncertainties in astrophysical parameters discussed previously. For example, if $\Gamma_{\rm HI}(z = 6)$ were a factor of ~ 2 lower than our fiducial value (see e.g. Ref [208]) our CDM prediction would fall closer to the measured central value of the MFP, without compromising the agreement at lower redshift. Given this consideration as well as large uncertainties in the MFP measurements themselves, we caution against over-interpreting Figure 4.10 at this time. These results mainly serve to quantify the potential role of cosmology in setting the intergalactic LyC opacity.

4.5 Conclusion

Ref [13] recently presented a measurement of the mean free path of ionizing photons at $z = 6$. At face value, the short value reported by them can be interpreted as evidence that the IGM clumps on scales $M < 10^8$ $M_\odot$, raising the possibility of using $\lambda_{912}^{\rm mfp}(z = 6)$ to rule out DM models lacking small-scale power. Motivated by this, we have studied the

role that the underlying DM cosmology plays in setting the $z > 5$ mean free path. We considered thermal relic WDM as an example of models with a cutoff in small-scale power, and an ultralight axion candidate as an example with enhanced power. We compared these models against CDM predictions. The main takeaways from this study can be summarized as follows:

- Many viable DM candidates exhibit stark differences with CDM on mass scales $10^4 < M/[M_\odot] < 10^8$. Gaseous halos in this range contribute much of the IGM opacity to ionizing photons immediately after a region has been reionized. These structures are erased over a timescale ~ 300 Myr by photoevaporation and pressure smoothing. We therefore expect DM cosmologies to exhibit the largest differences in $\lambda_{912}^{\rm mfp}$ during or shortly after reionization. Recent models place the end of reionization around $z = 5.2$, making $z > 5$ $\lambda_{912}^{\rm mfp}$ measurements a potential window into the underlying DM model.

- In our thermal relic WDM scenarios with particle mass $m_{\rm X} = 3$ (1) keV, the $z = 6$ $\lambda_{912}^{\rm mfp}$ in *ionized gas* is 37 (112) % longer than in CDM. However, at fixed global neutral fraction, the contribution to $\lambda_{912}^{\rm mfp}$ from neutral islands acts to obscure these differences. For example, in our fiducial reionization model with neutral fraction $\approx 20\%$ at $z = 6$, we found more modest differences of 19 (45) % in $\lambda_{912}^{\rm mfp}$ when the contribution from neutral islands is included. Hence, without knowing the global neutral fraction, it is difficult to rule out DM models with a small-scale power cutoff.

- Scenarios is which reionization ends earlier exhibit smaller differences in $\lambda_{912}^{\rm mfp}$ between DM cosmologies. This owes to photoevaporation/pressure smoothing having more time to erase the small-scale structure that distinguishes these cosmologies.

- At fixed global neutral fraction, scenarios in which the neutral islands are larger, more clustered, and fewer in number lead to larger differences in $\lambda_{912}^{\rm mfp}$ between DM cosmologies. In these cases, the neutral islands contribute comparatively less to the IGM opacity, such that small-scale power in ionized regions plays a bigger role in setting $\lambda_{912}^{\rm mfp}$.

- The enhanced small-scale power in the axion-like model lowers the predicted MFP at $z = 6$, bringing it into better agreement with the central value measured by Ref [13] compared to CDM at fixed $\Gamma_{\rm HI}$ and global neutral fraction.

- Among the key uncertainties precluding a robust conclusion on cosmology are the intensity of the extragalactic ionizing background and the thermal history of the IGM prior to reionization. The former sets the densities which self-shield. The latter sets the smallest gaseous structures that can form, the Jeans filtering scale. Variations in these quantities within plausible models produce differences in $\lambda_{912}^{\rm mfp}$ similar to those observed among the DM cosmologies considered here.

Our results illustrate the role that small-scale power plays in setting the MFP during reionization. A key consideration that arises from our analysis is the relative importance of neutral islands in setting $\lambda_{912}^{\rm mfp}$ at $z = 6$. The less neutral islands contribute, the more opacity must come from small-scale power in ionized regions. This question may be addressable with existing quasar absorption spectra and obviously has important implications for reionization itself. Another more basic question is whether our model of IGM opacity arising entirely from cosmological fluctuations is fundamentally correct. If processes related to high-z galaxy formation affect the physical state of intergalactic gas at

large, then our models may be missing important physics shaping the sinks. This question can be imminently addressed with more detailed hydrodynamic simulations.

Chapter 5

The Morphology of Reionization in a Dynamically Clumpy Universe

5.1 Introduction

The past decade has seen an increase in the number and quality of observational constraints on the Epoch of Reionization (EoR). Planck's measurement of the cosmic microwave background (CMB) Thomson scattering optical depth ($\tau_{\rm es}$) have revised the midpoint of reionization to $z \approx 7.5$, driving the field toward late reionization models [1]. Meanwhile, studies of damping wings in high-z quasar spectra [37, 16, 18] and Lyman Alpha Emitter (LAE) surveys [31, 32, 33, 52, 34, 35, 210] have also suggested a significantly neutral intergalactic medium (IGM) at $z \sim 7$. At $z < 6$, quasar absorption spectra measurements may also be consistent with an ongoing reionization process down to $z \sim 5$ (e.g. [38, 126, 211, 30, 39]). Future observations with the James Webb Space Telescope (JWST),

the extremely large telescopes, 21 cm signal experiments – e.g. SKA [45] and HERA [47, 46] – and other line intensity mapping surveys (e.g. SPHEREx; [212]), promise to vastly expand our understanding of the EoR. This wealth of forthcoming data motivates theoretical studies to predict and interpret reionization observables with greater accuracy.

All reionization observables, with the exception of $\tau_{\rm es}$, are sensitive to the spatial structure of ionized regions, broadly termed morphology. Reionization's morphology is known to be sensitive to the nature of its sources as well as the LyC opacity of the IGM [213, 214, 177, 215, 216, 145]. During reionization, gaseous halos with masses $< 10^8 M_\odot$, which are too small to form stars, act as sinks of ionizing photons and play a role in setting the IGM opacity [174, 214]. The sinks can be as small as $10^4 M_\odot$ before reionization, roughly the Jeans filtering scale in the cold IGM [217, 218, 85]. Once the IGM surrounding these structures ionizes, their gas is photo-evaporated and pressure-smoothed over a timescale of a few hundred Myr [175, 131, 74, 178]. We refer to this process as relaxation. Modeling relaxation in simulations requires high ($\sim$ kpc) spatial resolution to resolve the sinks [85] and radiative transfer (RT) coupled to the hydrodynamics to capture the interplay between self-shielding and pressure smoothing [131, 74].

In RT simulations that are big enough to capture the large-scale structure of patchy reionization ($>$ 200-300 Mpc, [132, 219], resolving the sinks presents an extreme computational challenging owing to the $>$ 5 orders of magnitude in spatial scales that are required. RT simulations that come close (e.g. [220, 221, 222]) are too expensive to run more than a handful of times. On the other hand, the semi-numerical methods of approximating RT that have been employed for parameter space studies either ignore the

effect of the sinks or model them in an approximate manner (e.g. [223, 224, 145]). It is unclear, however, which approximation schemes for the sinks are accurate. Simulations that ignore the unresolved sinks implicitly assume that their effects are fully degenerate with the parameters that characterize the sources [214]. Other studies have attempted to model unresolved sinks with a sub-grid clumping factor [177, 225], by adding extra opacity to their cells [226, 227], or by specifying the mean free path as an input [197, 204, 228, 229]. These implementations vary in complexity and often disagree on what role the sinks play. As a result, currently there is no consensus on how much of an effect the sinks have on reionization and, relatedly, how important they are for interpreting observables. This paper aims to further address these questions.

Another motivation for the current study is the recent measurement of the Lyman-Limit mean free path at $z = 6$ by [13] (see also [14] for complementary constraints). They reported a value of $\lambda_{912}^{\rm mfp} = 3.57^{+3.09}_{-2.14}\ h^{-1}$cMpc, which is considerably shorter than extrapolations from measurements at lower redshift [12]. In addition to suggesting that the IGM may have still been significantly neutral at $z = 6$ [10, 230, 208], their measurement – if confirmed – may indicate that absorptions in ionized gas consumed a majority of the reionization photon budget [145]; in which case, accounting for the effect of sinks in simulations would be critical.

The main goal of this work is to assess how important the sinks are for modeling reionization's morphology. Towards this end, we use a new ray-tracing RT code that was first applied in [10]. The code has been developed for flexibility and low computational cost, mainly by the use of large cell sizes and adjustable angular resolution in the RT calculation.

For our fiducial simulations, we employ the [10] sub-grid model based on a suite of high-resolution, fully coupled hydro/RT simulations, which track how the LyC opacity of the IGM evolves in different environments after I-fronts sweep through (an expanded version of the numerical experiments in [74]). However, one of the main features of our RT code is that any sub-grid model of IGM opacity can be straightforwardly implemented. We exploit this feature to compare the reionization morphologies in our detailed fiducial simulations against sink models constructed to mimic the various assumptions made previously in the literature.

Another goal of this work is to explore the relationship between reionization sources and sinks. The large uncertainty in the nature of the LyC sources necessitates exploring the sinks in different source models. Although it is widely believed that galaxies were the main drivers of reionization, it remains unclear which galaxies sourced the LyC background (see for example [105, 129, 231, 232]). A number of studies have looked at the impact of different models for the sources and sinks separately; to our knowledge none have directly addressed the interplay between the two.

This work is organized as follows. In §5.2, we describe our numerical methods. In §5.3 we study the morphology of reionization in different sinks models. In §5.4, we extend our analysis to include different models for the sources. We summarize our results and conclude in §5.5. Throughout this work, we assume the following cosmological parameters: $\Omega_m = 0.305$, $\Omega_\Lambda = 1 - \Omega_m$, $\Omega_b = 0.048$, $h = 0.68$, $n_s = 0.9667$ and $\sigma_8 = 0.82$, consistent with the [1] results. All distances are quoted in comoving units unless otherwise specified.

5.2 Numerical Methods

5.2.1 Large-Scale Radiative Transfer

We ran our reionization simulations using the new RT code of [10]. Here we describe the features of the code relevant for this work, leaving a more detailed presentation to a future paper.

The code inputs are a time-series of halo catalogs and coarse-grained density fields from a cosmological N-body simulation. Halos are assigned ionizing photon emissivities and binned to their nearest grid points on the RT grid. Rays are cast from the centers of source cells at each time step. As rays travel, the optical depth through each cell is computed and photons are deposited accordingly. Rays are deleted when they contain $< 10^{-10}\times$ the average number of photons per ray. We use the full speed of light to maintain accuracy at the end of reionization.

As the rays propagate, they adaptively split to maintain a minimum angular resolution around the source cell. When rays from many sources intersect the same cell, the ones with the fewest photons are merged to a fixed level of angular resolution. Splitting and merging is handled with the HealPix formalism [233] following a procedure similar to the one described in [134] and implemented in [77].[1] The parameters for this are adjustable, allowing the user to trade accuracy for computational time. In Appendix C.1, we describe these parameters and show that our choices for them are converged in terms of morphology.

To maximize flexibility, our RT algorithm does not explicitly solve for the ionization state of each cell to determine its absorption coefficient, $\overline{\kappa}$. Instead, $\overline{\kappa}$ can be an

[1] In fact, we have tested our code against that of [77] and found excellent agreement in the shapes and sizes of ionized and neutral regions.

arbitrary function of density, photo-ionization rate, ionization redshift, and time. Moreover, since our RT cells are large enough to require many RT steps to ionize (1 h^{-1}Mpc in this work), we track the I-fronts within cells using a "moving screen" approximation. That is, I-fronts are infinitely sharp and the gas behind them is highly ionized. The photo-ionization rate in ionized gas is given by

$$\Gamma^i_{\rm HI} = \sum_{j=1}^{N_{\rm rays}} \frac{N^{ij}_{\gamma,0}\overline{\sigma}_{\rm HI}\overline{\lambda}^i[1-\exp(-x^i_{\rm ion}\Delta s^{ij}/\overline{\lambda}^i)]}{x^i_{\rm ion}V^i_{\rm cell}\Delta t}, \tag{5.1}$$

where the number of photons in ray j traveling a distance Δs_{ij} through cell i is $N^{ij}_{\gamma,0}$, $\overline{\lambda}^i \equiv 1/\overline{\kappa}^i$ is the mean free path, $x^i_{\rm ion}$ is the ionized fraction, $V_{\rm cell}$ is the cell volume, and the sum is over all rays crossing cell i during the time step Δt. The cross-section $\overline{\sigma}_{\rm HI}$ is averaged over the assumed spectrum of $J_\nu \propto \nu^{-1.5}$ from $1-4$ Ryd (as in [74], motivated by the scaling anticipated in stellar population synthesis models). In partially ionized cells, I-fronts move at a speed $v_{\rm IF} = F_\gamma/[(1+\chi)n_{\rm H}]$, where $\chi = 0.082$ accounts for HeI and F_γ is the leftover photon flux after attenuation by the ionized part of the cell. In Appendix C.2 we show explicitly that Eq. 5.1 is valid for arbitrary $\overline{\kappa}$.

5.2.2 Sub-grid model for $\overline{\lambda}$

In standard RT, Eq. 5.1 would be closed by an ionization balance equation (perhaps including a sub-grid clumping factor) and $\overline{\lambda}$ computed from the HI fraction. Our fiducial setup instead uses a prescription for $\overline{\lambda}$ based on an extended suite of the small-volume hydro plus ray-tracing RT simulations first presented in [74]. These were run with a modified version of the RadHydro code [76, 77] in 1 (Mpc/h)^3 volumes with $N = 1024^3$ DM particles, gas and RT cells. We ionize the whole volume at $z = z_{\rm reion}$ by sending I-fronts from the

boundaries of $L_{\rm dom} = 32\,h^{-1}$kpc domains. This setup avoids complicating the interpretation of our results with uncertain galaxy physics by treating the gas as if it were reionized by external sources. The photo-ionization rate $\Gamma_{-12} \equiv \Gamma_{\rm HI}/(10^{-12}\ {\rm s}^{-1})$ is constant in optically thin gas. (We emphasize, however, that our simulations explicitly include self-shielding systems and associated RT effects.) We simulated over-dense and under-dense regions by using the method of [101] to account for box-scale density fluctuations. These are parameterized by δ/σ, the linearly extrapolated over-density in units of its standard deviation. We refer the reader to [74] for more details[2].

We estimate $\overline{\lambda}$ in our RadHydro simulations using

$$\overline{\lambda}^{-1} \equiv \overline{\kappa} = \frac{\langle \Gamma_{\rm HI} n_{\rm HI} \rangle_{\rm V}}{F_\gamma}, \tag{5.2}$$

where F_γ is the ionizing photon flux in each domain. In Appendix C.3 we show that the right-hand side of Eq. 5.2 is equal to the volume-averaged absorption coefficient and is the relevant quantity for evaluating Eq. 5.1. Note that this definition of $\overline{\lambda}$ accounts for non-equilibrium absorptions by self-shielded systems (e.g. mini-halos), an effect that cannot be accurately captured with a clumping factor (as noted by [177, 226]).

Our RadHydro simulations give us $\overline{\lambda}$ versus time in a range of environments parameterized by $(z_{\rm reion}, \Gamma_{\rm HI}, \delta/\sigma)$. While we could simply interpolate over these parameters to get $\overline{\lambda}^i$ in Eq. 5.1, doing so would neglect the sensitivity of $\overline{\lambda}$ to the time-evolution of $\Gamma_{\rm HI}$, since $\Gamma_{\rm HI}$ does not evolve in the small-volume simulations. This sensitivity arises from the dependence of the relaxation process on the self-shielding properties of the gas, which

[2]Our expansion of the suite in [74] includes all combinations of $z_{\rm reion} \in \{6, 8, 12\}$, $\Gamma_{-12} \in \{0.03, 0.3.3.0\}$ and $\delta/\sigma \in \{-\sqrt{3}, 0, \sqrt{3}\}$. Due to computational limitations, not all of our small-volume simulations are run to when reionization ends ($5 < z < 6$). In these cases we extrapolate the results to lower redshifts by fitting $\overline{\lambda}$ to a power law in cosmic time over the last 50 Myr of the run.

are set by largely by $\Gamma_{\rm HI}$ (see Figs. 5 and 6 of [74]). We incorporated this $\Gamma_{\rm HI}$-dependence using an empirically-motivated model for the full time-evolution of $\overline{\lambda}$,

$$\frac{d\overline{\lambda}}{dt} = \frac{\partial\overline{\lambda}}{\partial t}\Big|_{\Gamma_{\rm HI}} + \frac{\partial\overline{\lambda}}{\partial\Gamma_{\rm HI}}\Big|_{t}\frac{d\Gamma_{\rm HI}}{dt} - \frac{\overline{\lambda}-\overline{\lambda}_0}{t_{\rm relax}}, \tag{5.3}$$

where the first term captures the time-dependence of $\overline{\lambda}$ at fixed $\Gamma_{\rm HI}$, and the second the instantaneous change in $\overline{\lambda}$ with $\Gamma_{\rm HI}$. The former is interpolated from our small-volume simulation suite, and for the latter we assume a power law $\overline{\lambda} \propto \Gamma_{\rm HI}^{2/3}$, consistent with the scaling found in simulations (e.g. [136]). The last term captures the evolution of $\overline{\lambda}$ towards the constant-$\Gamma_{\rm HI}$ limit $\overline{\lambda}_0$ (also interpolated from our small-volume suite). Here $t_{\rm relax}$ is the timescale over which the gas loses memory of its previous $\Gamma_{\rm HI}$ history, which we take to be 100 Myr. In Appendix C.4, we show that Eq. 5.3 compares well against small-volume simulations with evolving $\Gamma_{\rm HI}$. Since $\overline{\lambda}$ is a function of $\Gamma_{\rm HI}$, Eqs. 5.1 and 5.3 are iterated five times for each time step, which we find sufficient for convergence (Appendix C.1).

5.2.3 Caveats

Here we will briefly discuss two caveats to our sub-grid model. The first is that our small-volume simulations should under-produce massive halos, which can act as sinks. This may be true even in our over-dense DC mode runs, which sample biased regions of the IGM where these halos are more common. This would be most problematic at the lowest redshifts when rare, massive sinks contribute significantly to the IGM opacity [178][3].

The second concerns our treatment of self-shielded gas. Eq. 5.2 for $\overline{\lambda}$ accounts for absorptions by self-shielded gas clumps that remain neutral some time after I-front

[3] In [10], this issue partially motivated the enhanced sinks model, which appealed to missing rare sinks to help explain the mild evolution of the mean free path at $z < 5$.

passage [178]. The gas in these systems can be a significant fraction of the gas in the cell within 50 Myr of ionization when $\Gamma_{\rm HI}$ is low ($< 10^{-13}$ s^{-1}). In principle, this gas should be excised from our moving-screen I-front calculation, which counts 1 absorption per neutral atom during I-front passage. As such, gas that remains neutral for more than a few Myr after I-front passage is effectively treated as if it were ionized twice. We have run a conservative test in which we derive $\overline{\lambda}$ in the small-volume simulations using the recombination clumping factor C_R (Eq. 5 of [74]) under the assumption of photo-ionizational equilibrium. This approach ignores the fact that some of the neutral gas is ionized after I-front passage and counts only recombination-balanced absorptions (see §5.3.2 in the next section for more details). Thus using C_R likely under-estimates the photon budget and brackets the magnitude of the double-counting effect. We found that the difference between the number of absorptions in ionized gas between using C_R and our fiducial model can be as high as a factor of 2 when low-$\Gamma_{\rm HI}$ gas dominates the absorption rate. Thus the photon budget predicted by our fiducial sinks model is almost certainly too high, although which model is closer to the truth is unclear. Fortunately, the impact on our results is minimal because, as we will see, the sinks probably do not shape morphology substantially under most circumstances. Even so, our results using this model should be interpreted as an upper limit on the expected effect of un-relaxed gas. In what follows we will make note whenever this point becomes relevant.

5.2.4 Density Fields & Sources

The density and source fields for our large-volume RT simulations are taken from a cosmological N-body DM-only simulation in a 300 h^{-1}Mpc box run using MP-Gadget [198].

The run used $N = 2048^3$ DM particles, for a mass resolution of $2.5 \times 10^8\ h^{-1}\mathrm{M}_\odot$ and a minimum halo mass of $8.5 \times 10^9\ h^{-1}\mathrm{M}_\odot$ (corresponding to 32 DM particles). The DM particles were smoothed onto a grid with 1 h^{-1}Mpc cells to get the density fields for the RT calculation. Density and halo fields are updated every 10 Myr from $z = 12$ to 4.5, for a total of 99 snapshots. The RT time-step is equal to the light-crossing time of the RT cells, and varies from ≈ 0.4 to ≈ 0.8 Myr during the simulation. When the density field is updated, we keep the same ionized fractions in all cells - thus we neglect the advection of ionized/neutral gas between snapshots. This should be a reasonable approximation since bulk velocities on $\geq 1\ h^{-1}$Mpc scales are typically slower than the speed of ionization fronts (a few hundred vs. $10^3 - 10^4$ km/s). We assigned UV luminosities to halos by abundance matching to the UV luminosity function of [129].

Halos with masses well below $8.5 \times 10^9\ h^{-1}\mathrm{M}_\odot$ likely formed stars via atomic cooling, and so may have contributed significantly to reionization. We thus extended the halo mass function (HMF) of our simulation using a modified version of the non-linear biasing method of [137]. These "sub-resolved" halos follow the HMF of [199] (which agrees with our resolved HMF) and are spatially distributed following the extended Press-Schechter (EPS) formalism. The number of added halos in each cell and mass bin is drawn randomly from a Poisson distribution with mean equal to the halo abundance predicted by EPS. We found that the clustering of the halos predicted by this formalism was systematically higher than that in the SCORCH simulations [112]. Specifically, the halo bias produced by the EPS method was a factor of 1.4 $(1.32, 1.18)$ too high compared to SCORCH at $z = 10$ $(8, 6)$.

We therefore added an empirically derived bias correction to the model to approximately reproduce the clustering of SCORCH halos in the mass range of interest.

We extended the HMF in our simulations to a minimum mass of $M_{\rm min} = 10^9$ $h^{-1}M_{\odot}$. Emissivities were assigned to halos assuming that the emissivity of each halo follows a power law in UV luminosity, $\dot{n}_{\gamma} \propto L_{\rm UV}^{\beta}$. Smaller $M_{\rm min}$ and β correspond to reionization driven by fainter, less biased sources. Our fiducial model has $M_{\rm min} = 10^9$ $h^{-1}M_{\odot}$ and $\beta = 1$, which corresponds to assuming a single value of the escape fraction $f_{\rm esc}$ and ionizing efficiency $\xi_{\rm ion}$ for the entire source population at each redshift. We chose this as our fiducial model for two reasons: (1) it imposes minimal assumptions about the dependence of $f_{\rm esc}$ and $\xi_{\rm ion}$ on halo mass and (2) of the models we will consider, it is the most similar to models commonly used in reionization simulations (e.g. $n_{\gamma} \propto M$ as in [127] and [225]). In §5.4 we study what happens when $M_{\rm min}$ and β are varied. In all simulations, the global emissivity (summed over all halos) as a function of redshift is an input chosen to produce the desired reionization history. Our models all use re-scaled versions of the fiducial late-ending rapid model of [10], as shown in the middle panel of Figure 5.1.

One caveat of this method is that the sub-resolution halos (with $M < 8.5 \times 10^9$ h^{-1} $\rm M_{\odot}$) that are added, being randomly drawn at each 10 Myr time-step, are not causally connected – i.e. halos jump around between time steps. This is an insignificant effect in over-dense regions containing many halos, where the "shot noise" is small, but can be pronounced in under-dense regions containing very few halos. We have run a series of tests against idealized scenarios in which the halos are held in fixed locations throughout reionization. We find that the noise introduced by the random drawing tends to wash out

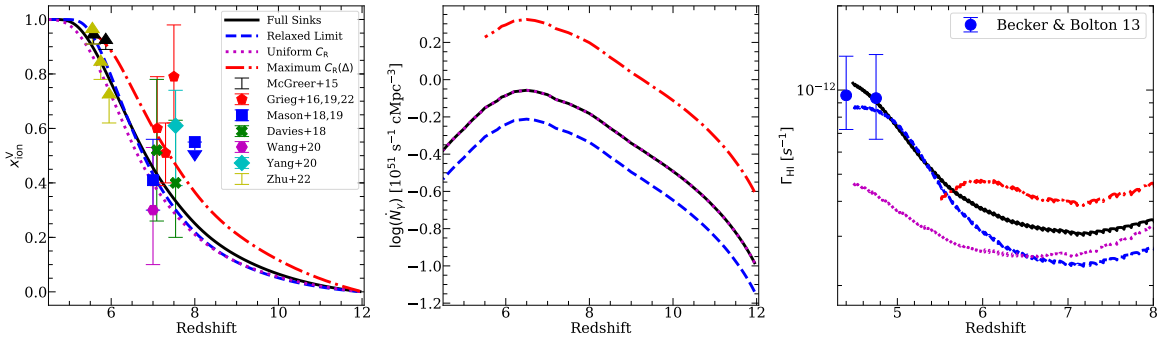

Figure 5.1: Volume-averaged ionized fraction (left), co-moving total ionizing emissivity (middle), and average photo-ionization rate in fully ionized cells (right) for each sinks model. All results shown here adopt our fiducial source scenario. We include measurements from the literature in the left panel [15, 16, 17, 18, 19, 20, 21, 22, 23, 24]. All the reionization histories are similar except the Maximum $C_R(\Delta)$ case. In the ensuing discussion, we show that the Full Sinks and Uniform C_R models have nearly indistinguishable morphologies assuming our fiducial source model. Notably, although these models have the same reionization and emissivity histories, they have significantly different photo-ionization rates. Hence they may be distinguishable by observables that are sensitive to Γ_{HI}, e.g. the mean free path and the Lyα forest.

the smallest structures in the ionization field, but that on the larger scales of interest the effects are modest. In general, we found slightly *less* power in the ionization field on large scales ($k < 0.5$ hMpc^{-1}) in our "fixed sources" tests. We find that the effect is never large enough to affect any of our forthcoming results at the qualitative level. We will discuss quantitative details of these tests in the results sections when they become relevant.

5.3 The Effect of Sinks on Reionization's Morphology

5.3.1 Sinks Models

In this section, we discuss the effect of sinks on the morphology of reionization. We compare our new sinks model to several representative alternatives. We assume our fiducial source model throughout (in §5.4 we will explore others.) We compare the following:

- **Full Sinks**: Our fiducial sinks model is based on the suite of RadHydro simulations as described in § 5.2.2. The evolution of $\overline{\lambda}$ in each cell includes the dynamical effects of pressure smoothing and photoevaporation, as well as the impact of sub-resolved self-shielding on the IGM opacity.

- **Relaxed Limit**: For this model, we extrapolate the low-redshift $\overline{\lambda}$ from our $z_{\rm reion} = 12$ RadHydro simulations to higher redshifts, assuming a power law in cosmic time, and directly interpolate $\overline{\lambda}$ instead of using Eq. 5.3. Thus, the gas is treated in the limit that it was ionized long ago and has reached a pressure-smoothed equilibrium. This model effectively removes the contribution of opacity from the initial clumpiness that is eventually erased during the relaxation process.

- **Sub-grid Clumping Factor**: Here we assume that all gas in ionized regions is in photo-ionization equilibrium at a constant $T = T_{\rm ref} \equiv 10^4$ K, which yields

$$\overline{\lambda} = \frac{\Gamma_{\rm HI}}{\overline{\sigma}_{\rm HI} C_{\rm R} \alpha_{\rm B}(T_{\rm ref})(1+\chi) n_{\rm H}^2} \tag{5.4}$$

  where $\alpha_{\rm B}$ is the case B recombination coefficient of ionized hydrogen. We adopt two prescriptions for $C_{\rm R}$:

  1. **Uniform $\mathbf{C_R}$** : We set $C_{\rm R} = 5$ everywhere at all times, which reproduces a reionization history and photon budget similar to the Full Sinks model. This case serves as a basis for comparison to assess the importance of the dynamics and spatial in-homogeneity of the sinks predicted by the Full Sinks model. We emphasize that $C_{\rm R}$ is a sub-grid clumping factor, not a global one.

2. **Maximum $\mathbf{C_R(\Delta)}$**: We use the density-dependent sub-grid clumping factor of [225].[4] This model is based on dark-matter-only N-body simulations and predicts $C_{\rm R} \approx 10-15$ in cells with $\Delta \geq 1$ at $z \leq 8$. Since this model neglects pressure smoothing effects, it represents an upper limit on the amount of clumping in the standard cosmology.

The left-most panel in Figure 5.1 shows the volume-averaged ionized fraction for each sinks model alongside measurements from the literature. The middle panel shows the global ionizing emissivity. The emissivity histories are all re-scaled versions of the "rapid" model from [10]. For comparison, the emissivities of the Full Sinks, Relaxed Limit, and Uniform $\rm C_R$ models have been tuned to yield very similar reionization histories and ionizing photon budgets, ending reionization late at $z = 5 - 5.5$. The Maximum $\rm C_R(\Delta)$ emissivity was tuned to end reionization somewhat earlier because the clumping factor fits from [225] do not extend below $z \sim 6.5$[5]. However, the ensuing morphology comparisons will be performed at fixed global ionized fraction, which should minimize any differences originating from the different reionization histories. Note that the Full Sinks and Uniform $\rm C_R$ models have the same emissivity, while the Relaxed Limit (Maximum $\rm C_R(\Delta)$) emissivity is a factor of 0.7 (2.4) smaller (larger) than the other two. We note that due to the over-counting issue discussed in §5.2.3, the emissivity in the Full Sinks and Uniform $\rm C_R$ models are likely higher than they should be. A lower photon budget would mean a smaller $C_{\rm R}$ in the latter to match the Full Sinks case; thus the value of $C_{\rm R} = 5$ is probably too high. In the ensuing

[4]Note that the large-volume simulations in [225] have smaller cells than ours, so their clumping factors are a slight under-estimate for our application. Still, this model serves the purpose of illustrating how the morphology evolves in an extremely clumpy IGM, which is our goal.

[5]We extrapolate the [225] fitting parameters to slightly lower redshifts by assuming their a_0 parameter evolves linearly in redshift, while a_1 and a_2 retain their $z = 6.5$ values (see their Eq. 17 and appendix B.)

discussion we will see that our main conclusions on morphology are not significantly affected by this issue.

The right-most panel of Figure 5.1 shows $\Gamma_{\rm HI}$ averaged over fully ionized cells for each model, compared to measurements from [138]. Here we omit $z > 5$ measurements (e.g. [234, 235, 79, 13]) for clarity, and also because it is unclear how to compare these measurements against our $\Gamma_{\rm HI}$ in simulations where reionization is still ongoing at $z = 5-6$. A number of reionization observables are explicitly sensitive to $\Gamma_{\rm HI}$, including the mean free path, Lyα forest statistics, and LAE visibility. In the ensuing discussion we will show that the Full Sinks and Uniform $C_{\rm R}$ models exhibit essentially identical morphologies in our fiducial source model. A key takeaway from Figure 5.1 is that sink models tuned to yield similar morphologies, e.g. the Full Sinks and Uniform $C_{\rm R}$ models, may nonetheless exhibit considerable differences in observables that are sensitive to $\Gamma_{\rm HI}$. So while these models may appear nearly identical in their predictions for the 21cm power spectrum, they will yield different predictions for e.g. Lyα forest statistics.

5.3.2 Visualization of the IGM Opacity

To aid in visualizing the dynamics and spatial morphology of the sinks, we define the "effective clumping factor" for cell i to be

$$C^i_{\rm eff} = \frac{(1/\overline{\lambda}^i)}{\overline{\sigma}_{\rm HI}\alpha_B(T_{\rm ref})(1+\chi){n^i_{\rm H}}^2/\Gamma^i_{\rm HI}}, \tag{5.5}$$

where $T_{\rm ref} = 10^4$ K and $\Gamma^i_{\rm HI}$, $\overline{\lambda}^i$, and $n^i_{\rm H}$ are the photo-ionization rate, mean free path, and H number density, respectively. The numerator is simply the absorption coefficient κ, and the denominator is what κ would be if the gas had a constant temperature $T_{\rm ref}$, was in

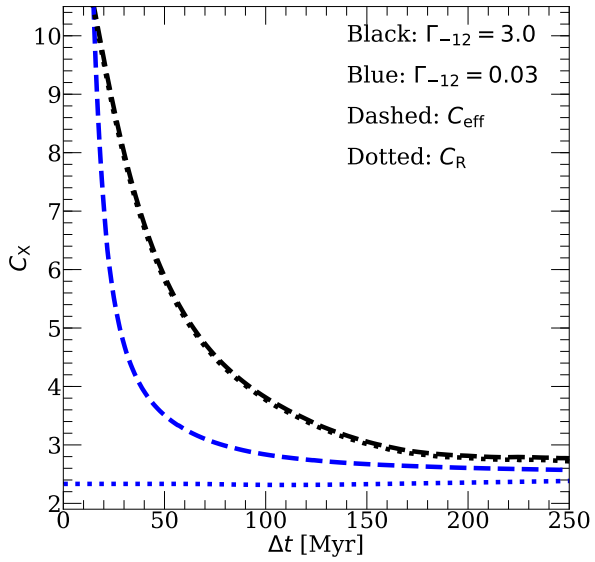

Figure 5.2: Examples of $C_{\rm eff}$ (dashed) compared to C_R (dotted) for small-volume simulations with high and low values of Γ_{-12} (3.0 and 0.03). In the former, the two quantities are similar owing to the scarcity of self-shielded gas. However for $\Gamma_{-12} = 0.03$, systems remain self-shielded and out of equilibrium for longer, producing a large difference between $C_{\rm eff}$ and C_R since the former reflects the total number of absorptions but the latter only those balanced by recombinations.

photo-ionizational equilibrium, and had no sub-resolved density fluctuations. $C_{\rm eff}$ quantifies the impact of sub-grid sink physics and large-scale temperature fluctuations on the opacity. In the limit of photo-ionizational equilibrium, Eq. 5.5 is equivalent to the recombination clumping factor C_R (see § 5.2.3). Differences between $C_{\rm eff}$ and C_R indicate the presence of sub-resolved self-shielded systems that are not in photo-ionizational equilibrium. Note that unlike in [74], the density in the denominator of our clumping factors is the *cell-wise* density rather than the cosmic mean density. Thus, density fluctuations influence $C_{\rm eff}$ only indirectly through their impact on the sub-resolved clumpiness of the gas and its self-shielding properties.

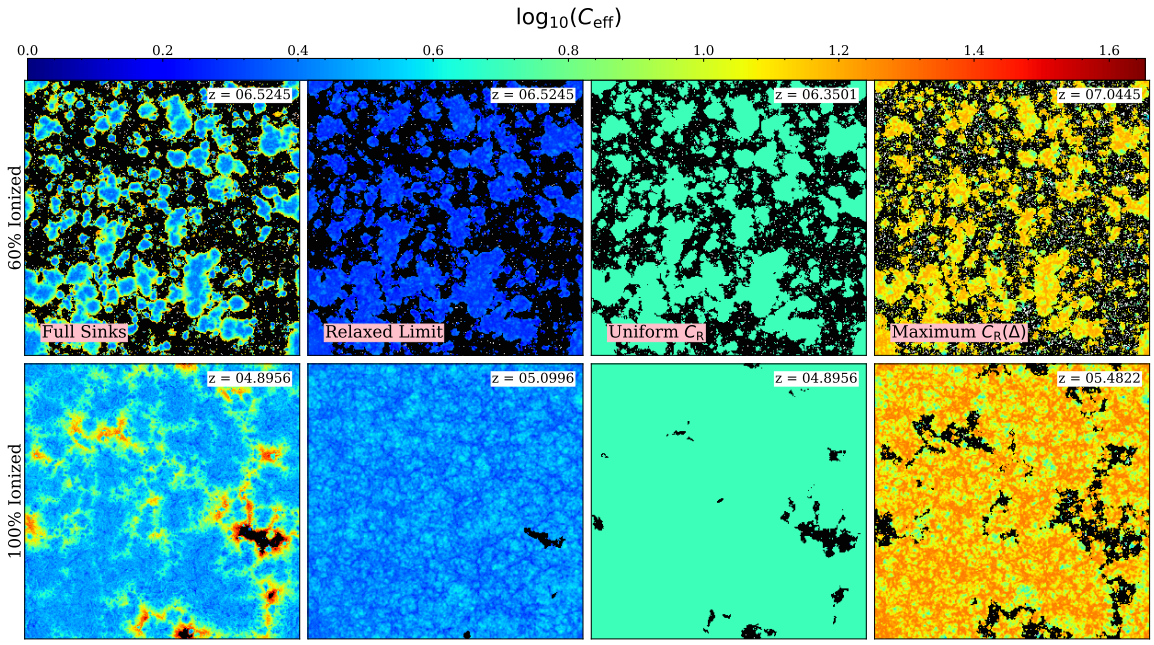

Figure 5.3: Visualization of the sink physics in each of our models. The redshifts are notated in the upper right of each panel. We show $\log_{10}(C_{\rm eff})$ at 60% volume ionized fraction (top) and 50 Myr after reionization ends ($x_{\rm ion}^{\rm V} < 0.01$, bottom row). The black regions denote cells that are at least 50% (10%) neutral in the top (bottom) panels. In the Full Sinks case, the opacity is boosted near I-fronts (top) and in under-dense voids that have yet to relax after reionization ends (bottom). The large scale fluctuations in $C_{\rm eff}$ are weaker in the other models. In the Uniform $\rm C_R$ case, $C_{\rm eff}$ is the same everywhere, and in the Maximum $\rm C_R(\Delta)$ models, $C_{\rm eff}$ is lower (higher) than average in voids (over-densities) after reionization, in contrast to the Full Sinks case. These visualizations illustrate the dynamical effects of pressure smoothing and photoevaporation in our Full Sinks model.

For intuition on $C_{\rm eff}$, Figure 5.2 shows its evolution (dashed curves) compared to that of C_R (dotted curves) vs. time since ionization for two of our mean density, $z_{\rm reion} = 8$ small-volume RadHydro simulations. One has $\Gamma_{-12} = 3.0$ (black), and the other 0.03 (blue). In the first case, $C_{\rm eff}$ and C_R are close together; both start above 10 and approach ~ 3 as the gas relaxes. Their similarity owes to the high intensity of the background, which leaves little gas self-shielded. In the $\Gamma_{-12} = 0.03$ case, there is significant self-shielding in high-density gas. This lowers C_R (which counts only recombination-balanced absorptions), while $C_{\rm eff}$ remains elevated, since it is affected by non-equilibrium absorptions taking place as the self-shielded gas is ionized. At later times, $C_{\rm eff}$ and C_R agree better as more self-shielded systems evaporate.

Figure 5.3 shows slices of $\log(C_{\rm eff})$ from large-volume simulations for each of our sinks models (assuming our fiducial source model). We show the Full Sinks (left-most), Relaxed Limit (middle left), Uniform $\rm C_R$ (middle right) and Maximum $\rm C_R(\Delta)$ (right-most) models at 60% volume ionized in the top row, and 50 Myr after reionization has finished ($x_{\rm ion}^{\rm V} = 0.01$) in the bottom row. The redshifts are given in the upper right of each panel. In the top (bottom) row, black regions denote cells that are at least 50% (10%) neutral (note that a small number of cells are still partially neutral even after $x_{\rm ion}^{\rm V} < 0.01$ in the bottom row). In the Full Sinks model, $C_{\rm eff}$ is highest near I-fronts where gas was most recently ionized. After reionization ends, patches of enhanced opacity with $C_{\rm eff} \sim 10 - 20$ (and even higher in the most recently ionized cells) persist in the voids, which ionized last and quickly, so have yet to relax. In regions re-ionized earlier, $C_{\rm eff}$ is $\sim 2 - 5$ at all redshifts, similar to the Relaxed Limit. The opacity is higher in the Uniform $\rm C_R$ case than in the Relaxed

Limit because it has been calibrated to match the photon budget of the Full Sinks model. The Maximum $C_R(\Delta)$ model has the highest opacity, with $C_{\rm eff} \sim 10 - 20$ everywhere after reionization.

A comparison between the top-left and the two top-right panels in Fig. 5.3 reveals that the opacity in over-dense regions hosting the earliest ionized bubbles is significantly lower in our Full Sinks model compared to the Uniform C_R and Maximum $C_R(\Delta)$ models. This results from the dynamics in our Full Sinks model, and may arise from two effects working in tandem: (1) $\Gamma_{\rm HI}$ is generally larger near the highly clustered sources, which leads to a quicker relaxation/evaporation of the sinks nearby ; (2) The structures that form in these regions may have a shorter relaxation time owing to their larger densities (see e.g. Eq. 4 of [74]). Together, these effects in our Full Sinks model work towards favoring the growth of larger bubbles compared to the Uniform C_R and Maximum $C_R(\Delta)$ models. Conversely, the opacity is elevated in recently ionized regions at lower redshifts near the end of reionization, despite these regions being under-dense on average.

In the other three models, $C_{\rm eff}$ is affected mainly by density fluctuations, which are most noticeable in the Maximum $C_R(\Delta)$ model (and absent by construction in the Uniform C_R case). In the Uniform C_R model all parts of the IGM have the same C_R, while in the Maximum $C_R(\Delta)$ model the over(under) dense regions have the highest (lowest) C_R, opposite the Full Sinks case. We emphasize that the contrasting $C_{\rm eff}$ topologies will affect any observables that are explicitly sensitive to $\Gamma_{\rm HI}$ and the opacity structure of the IGM, such as the Lyα forest and the mean free path (see discussion of Fig. 5.1). However, in the ensuing discussion we will see that they are probably not very important for morphology.

5.3.3 Ionized Bubbles

Visualization of Ionized Region Morphology

Figure 5.4 shows the ionization field (darker = more neutral) for each of our sinks models (top to bottom, see labels) at 20, 50, and 80% volume ionized fraction (left to right). At fixed ionized fraction, the Maximum $C_R(\Delta)$ model exhibits the smallest ionized bubbles. This is indicated by the red shading, which denote regions that are neutral in the Maximum $C_R(\Delta)$ (and Uniform C_R) model, but not the Full Sinks case. The other models are visually similar to the Full Sinks case - the Uniform $C_R$model having slight smaller bubbles and the Relaxed Limit model having slightly larger ones (as indicated by the cyan shading in that row). The largest bubbles are smaller in the Maximum $C_R(\Delta)$ model because the sources driving their growth are "taxed" disproportionately by recombinations compared to those in smaller bubbles [213].[6] Since large bubbles form in over-densities and start growing the earliest, their growth is slowed by recombinations sooner than their later-forming counterparts inhabiting lower densities. Thus the sinks act to reduce the average bubble size at fixed ionized fraction (as found by e.g. [213, 177, 215, 225, 236]).

Comparing the Full Sinks (top row) and Maximum $C_R(\Delta)$ (bottom row) models, the ionized bubbles generally appear larger in the former at fixed ionized fraction. As described in the previous section, this is a direct result of the dynamics in our sub-grid sinks model. In the earliest bubbles to form around highly clustered sources, the sinks relax/evaporate quickly, allowing the bubbles to grow more easily. By contrast, the smaller bubbles that start growing around less biased sources generally encounter a clumpier IGM

[6] This has been termed "taxing the rich" by [213].

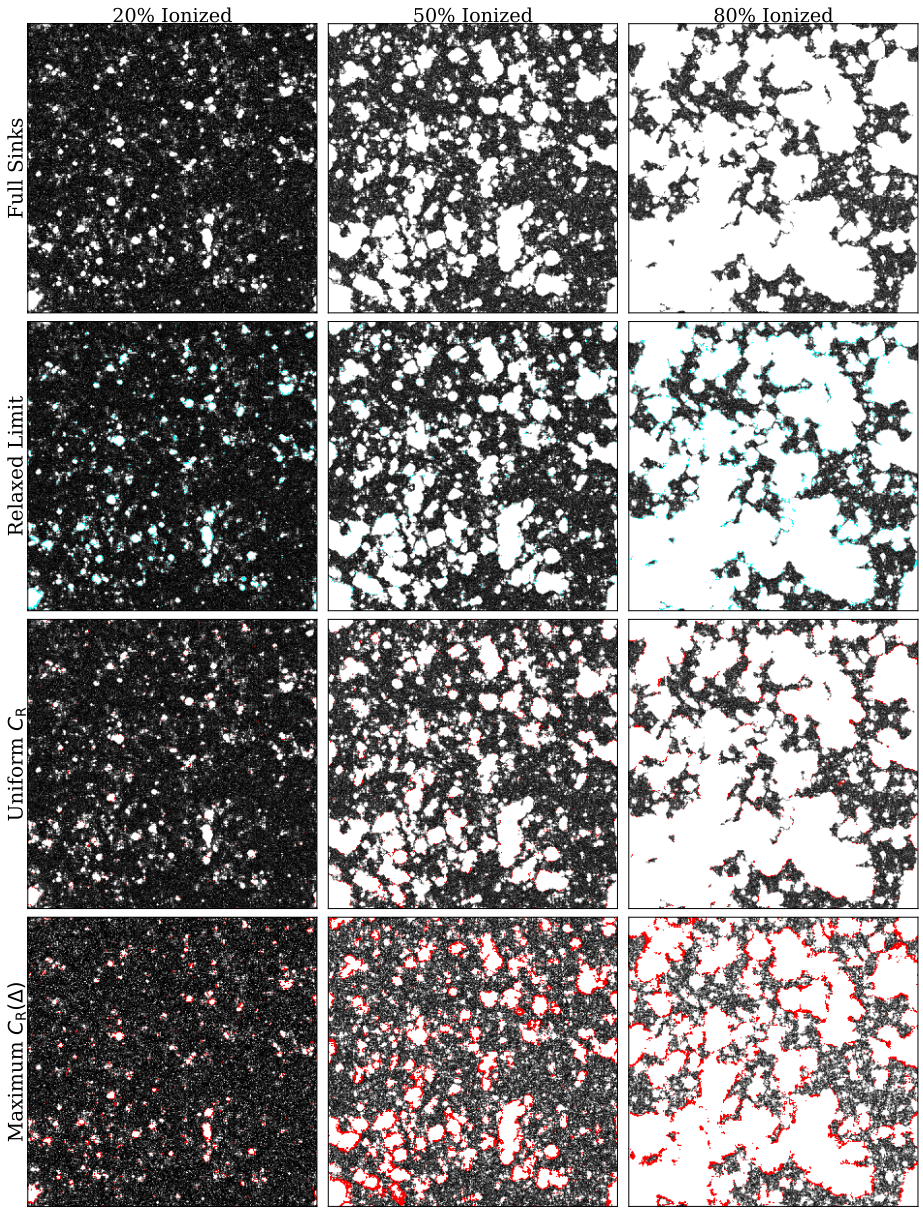

Figure 5.4: Visualization of the ionization field for our sinks models. All results here correspond to our fiducial source model with $\dot{n}_\gamma \propto L_{\rm UV}$, i.e. assuming the same escape fraction and ionizing efficiency for all sources. The columns show different volume ionized fractions (20, 50, and 80%, left to right) and the rows show different sinks models. In the second row, the cyan shading indicates bubbles that are slightly larger than in the Full Sinks model, while the red shading indicates the opposite in the other two rows. The ionized bubbles are smallest in the Maximum $C_R(\Delta)$ model at all ionized fractions. The Relaxed Limit model has slightly larger bubbles than the Full Sinks and Uniform C_R models, but these three models are visually very similar.

for longer periods of time. Together, these effects work toward favoring the growth of large bubbles and partially cancel the "taxing the rich" effect described in the previous paragraph. The Maximum $C_R(\Delta)$ model instead has higher clumping factors at higher densities, which slows the growth of the largest bubbles more. In other words, our Full Sinks model taxes the rich *less* than the Maximum $C_R(\Delta)$ model, which does not include any dynamical effects.

Interestingly, in Figure 5.4 we see a striking degree of similarity between the Full Sinks and Uniform C_R models at all ionized fractions. In fact, these models do not even differ significantly from the Relaxed Limit except near the beginning of reionization. The visual similarity leads us to one of our key conclusions, which we will hash out quantitatively in the ensuing sections. Accounting for the pressure-smoothing of the IGM by reionization is crucial for modeling morphology accurately. However, as long as this effect is accounted for "on average," e.g. in the simplest case with a uniform sub-grid clumping factor, the detailed dynamics and spatial in-homogeneity of the sinks are likely not very important for morphology. We emphasize, however, that this conclusion holds only for source models in which bright galaxies contribute significantly to the ionizing photon budget, as in our fiducial source model. In §5.4, we will see scenarios for which the details of the sink modeling *do* become quite important.

Bubble Size Distribution

Next, we study morphology more quantitatively using the ionized bubble size distribution (IBSD). We compute the IBSD using the ray-tracing definition proposed in [11] and implemented in the publicly available package *tools21cm* [203]. The IBSD defined this

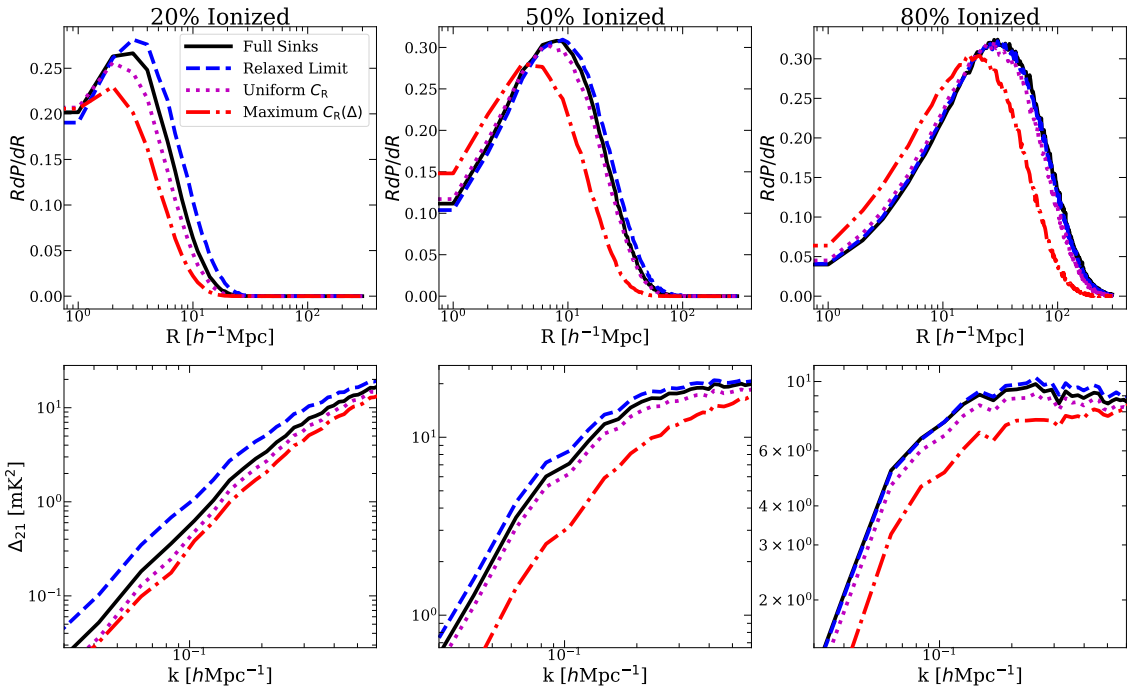

Figure 5.5: **Top**: Ionized Bubble Size Distribution (IBSD) for our sinks models (see legend) at 20%, 50%, and 80% volume ionized fractions (left to right). The Full Sinks and Uniform C_R models have strikingly similar IBSDs despite their very different clumping topologies. **Bottom**: 21 cm power (Δ_{21}) vs. wavenumber for the same models and ionized fractions. At 20% ionized, the Maximum $C_R(\Delta)$ model is well below the Relaxed Limit, with the other two models in between, but closer to the Maximum $C_R(\Delta)$ result. At later times, the Full Sinks and Uniform C_R models (which are always very similar to each other) move close to the Relaxed Limit. All results shown here adopt our fiducial source model with $\dot{n}_\gamma \propto L_{UV}$.

Mean Bubble Size [h^{-1}**Mpc**]	20%	50%	80%
Full Sinks	1.94	7.30	30.08
Relaxed Limit	2.45	8.10	29.26
Uniform C_R	1.66	6.84	26.86
Maximum $C_R(\Delta)$	1.21	4.41	18.18

Table 5.1: Mean ionized bubble size at 20%, 50%, and 80% ionized for each of the sinks models in this section.

way captures the distribution of distances to neutral gas along random rays starting in ionized regions, and thus quantifies bubble sizes well even after ionized regions overlap. To exclude un-resolved bubbles from the BSD, we do not count a cell as part of an ionized bubble unless it is $\geq 99\%$ ionized. We caution that our simulations likely have too few resolved small bubbles - those with sizes $\sim$ a few h^{-1}Mpc - both due to our limited spatial resolution and our implementation of sub-resolved sources (see §5.2.4).

Figure 5.5 (top row) shows the IBSD at 20%, 50%, and 80% (left to right) for our sinks models. The IBSD confirms that the Maximum $C_R(\Delta)$ has the smallest bubbles at all times, and that the other three models have similar bubble sizes. The average bubble size is given at 20%, 50%, and 80% ionized for each model in Table 5.1. The mean values are mainly intended to illustrate the relative differences between our models. At 20% and 50% ionized the Relaxed Limit model has slightly larger bubbles, but at 80% ionized is indistinguishable from the Full Sinks model. The bubble sizes for the Uniform C_R model are slightly smaller than for the Full Sinks model, but are within $10-15\%$ at all times. We see from the Relaxed Limit comparison that even assuming a fully pressure-smoothed IGM at all times is a reasonable approximation for morphology, especially late in reionization.

5.3.4 21 cm Power Spectrum

The 21 cm power spectrum, which probes the H I fluctuations in the IGM, is being targeted by PAPER [237], MWA [238], LOFAR [239], HERA [121, 46, 47], and forthcoming experiments such as SKA [120]. Ignoring redshift-space distortions and assuming the spin temperature of the 21 cm transition T_S is much greater than the CMB temperature, we can write the 21 cm brightness temperature at position $\vec{x}$ as

$$T_{21}(\vec{x}) = \overline{T_{21}} x_{\rm HI}(\vec{x})(1+\delta(\vec{x})) \tag{5.6}$$

where $\overline{T_{21}}$ is T_{21} at mean density in neutral gas, which depends on redshift and cosmology only[7], $x_{\rm HI}$ is the HI fraction, and $1+\delta$ is the gas density. The dimensionless 21 cm power spectrum is $\Delta_{21} = k^3/2\pi^2 P_{21}(k)$, where $P_{21}(k)$ is the power spectrum of T_{21}. Since Δ_{21} depends on $x_{\rm HI}$, it is sensitive to the differences in morphology between our sinks models.

Figure 5.5 (bottom row) shows Δ_{21} vs. wavenumber k for our sinks models at 20%, 50%, and 80% ionized fractions (left to right). In all cases we see familiar qualitative features. Early on, Δ_{21} is steep in k and its amplitude on large scales reaches a local minimum - a result of inside-out reionization [86, 93]. Later, Δ_{21} flattens out and its amplitude at $k \leq 0.2\ h^{-1}$Mpc has increased by $1-2$ orders of magnitude by an ionized fraction of 80%. (Note the different y axes on different panels.) This happens because the ionization field, which fluctuates on scales characteristic of the largest ionized bubbles ($10-30\ h^{-1}$Mpc), takes over for the density field as the main driver of Δ_{21} at small k.

[7]Specifically, $\overline{T_{21}}^2 \propto 1+z$. Since our Maximum $C_{\rm R}(\Delta)$ model has a somewhat earlier re-ionization history, when comparing to that model we re-scale $\overline{T_{21}}$ to bring it to the same redshift as the other models. Thus our comparisons reflect only differences sourced by $x_{\rm HI}$.

Note that in this and in subsequent sections, we only show Δ_{21} for $k \leq 0.6\ h\mathrm{Mpc}^{-1}$, due to the caveat regarding the effects of sub-resolved halos discussed in §5.2.4.

The main effect of sinks is to reduce Δ_{21} on large scales ($k \leq 0.6$ hMpc^{-1}) by decreasing the sizes of large ionized bubbles. At 20% ionized, Δ_{21} at $k = 0.1h\mathrm{Mpc}^{-1}$ for the (Relaxed Limit, Maximum $\mathrm{C_R}(\Delta)$) model is (1.75, 0.59) times its Full Sinks model value. At 50% ionized these numbers become (1.16, 0.43), and at 80% ionized, they are (1.0, 0.69). In all panels the Full Sinks and Uniform $\mathrm{C_R}$ models are always within a few percent of each other. We see that the Maximum $\mathrm{C_R}(\Delta)$ model, which neglects the effects of pressure smoothing, under-estimates the large-scale Δ_{21} by $\approx 30 - 60\%$ relative to the Full Sinks case during much of reionization. The Relaxed Limit over-estimates the power substantially only at 20% ionized, and becomes an increasingly better approximation as reionization progresses.

The Maximum $\mathrm{C_R}(\Delta)$ model illustrates that neglecting pressure smoothing can lead to a significant under-estimate of the large-scale power, owing to that model's smaller ionized bubbles. On the other hand, assuming a fully relaxed IGM likely over-estimates the power early on, but becomes a reasonable approximation in the last half of reionization. Finally the similarity of the Full Sinks and Uniform $\mathrm{C_R}$ models suggests that Δ_{21} is unlikely to be sensitive to the details of how sinks are modeled, as long as the dynamics of the sinks can be accounted for in an average fashion via a uniform sub-grid clumping factor. We caution, however, that all of these conclusions are sensitive to the properties of the sources, and we have employed only our fiducial source model so far. As we will see in §5.4.2,

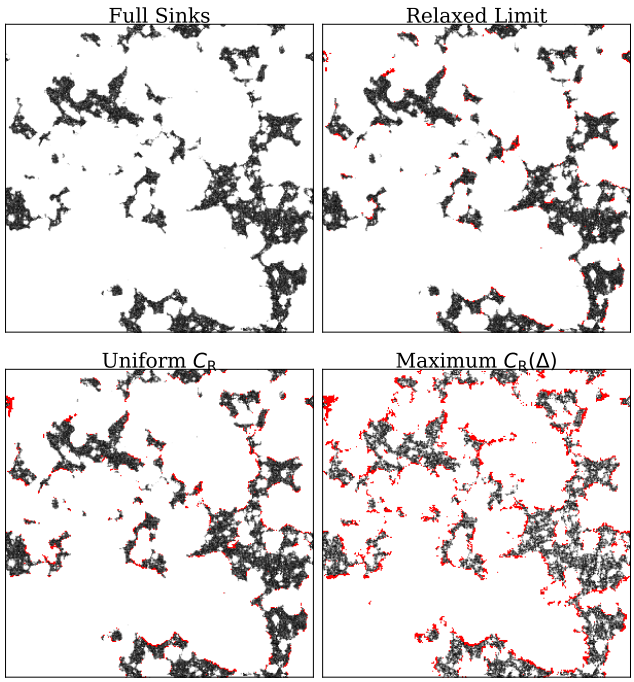

Figure 5.6: Visualization of neutral islands at 10% volume neutral fraction for our sinks models, assuming our fiducial source scenario. To aid comparison, the red shading highlights neutral regions that are ionized in the Full Sinks model. The Full Sinks, Relaxed Limit and Uniform C_R models have visually similar island morphologies, while the Maximum $C_R(\Delta)$ case has more extended and more fragmented islands.

the impact of sinks becomes larger (smaller) when fainter (brighter) sources dominate the photon budget.

5.3.5 Neutral Islands

So far our focus has been the morphology of ionized bubbles during the bulk of reionization. However, a lot of progress toward understanding reionization is being made with the growing number of $z > 5$ QSO absorption spectra, which may be probing the final phases of reionization when the mostly ionized IGM was punctuated by islands of neutral

gas.[8] Here we will briefly explore the morphology of these "neutral islands". Neutral islands have been the focus of a number of recent studies (e.g. [244, 245, 246, 227, 204]) owing to their importance for late-reionization observables.

In Figure 5.6, we illustrate the distribution of neutral gas at 10% volume neutral fraction using slices through our simulations. The red shading in each panel corresponds to neutral regions that are ionized in the Full Sinks model, i.e. to highlight differences in the neutral island morphology with that model. We see that the neutral islands in the Relaxed Limit and Uniform C_R models differ very little from the Full Sinks case, while there are substantial differences with the Maximum $C_R(\Delta)$ model. In that model the neutral structures are more extended – as illustrated in red – but also appear to be a lighter shading of gray. This lighter shading indicates that the neutral islands are more porous, i.e. they contain a larger number of small ionized bubbles inside of them.

We quantify the morphology with the neutral island size distribution (NISD), defined analogously to the IBSD. Late in reionization, the NISD is sensitive to the definition of a "neutral" cell, since most of the cells with neutral gas are partially ionized, especially in models with high opacity. We define a cell to be part of an island if $x_{\rm HI} > 0.01$. This choice is motivated by the fact that a sightline intersecting a partially neutral cell must pass within 1 Mpc/h of an ionization front. Gas this close to I-fronts typically has a low photo-ionization rate [104] and/or is un-relaxed [131, 74] and is thus likely to be opaque to both LyC and Lyα photons.

[8] These probes include Lyα/β forest statistics from QSO spectra [36, 38, 15, 30, 39, 24], the mean free path [12, 13, 14], and the LAE-forest connection [240, 241, 242, 243].

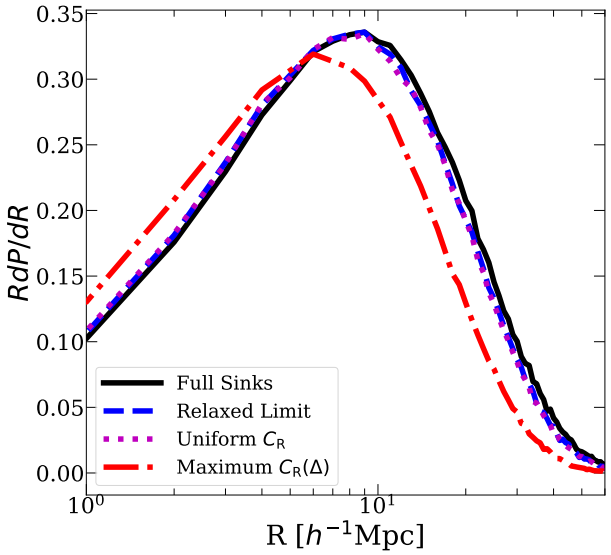

Figure 5.7: Neutral island size distribution defined such that any cell with $x_{\rm HI} > 0.01$ is part of an island. We include all the sinks models in Figure 5.5 and adopt our fiducial source model. The Maximum $C_R(\Delta)$ model has smaller islands, while the NISDs for the other three models are all very similar.

Figure 5.7 shows the NISD at 10% volume neutral fraction for our sinks models (which occurs at $z \approx 5.5$ for all models except the Maximum $C_R(\Delta)$ case, which is shown at $z \approx 6.0$). The Maximum $C_R(\Delta)$ model has the smallest islands while the other models are all very similar. The average island sizes for the Relaxed Limit, Full Sinks, Uniform C_R and Maximum $C_R(\Delta)$ models are 7.5 h^{-1}Mpc, 7.9 h^{-1}Mpc, 7.4 h^{-1}Mpc, and 5.8 h^{-1}Mpc, respectively. In spite of the Maximum $C_R(\Delta)$ model having more spatially extended neutral structures, the large abundance of small ionized bubbles within these structures break them up and shift the NISD towards smaller sizes. We see that even the approximation of a fully pressure-smoothed IGM is likely acceptable for capturing the morphology of neutral islands. On the other hand, ignoring pressure smoothing effects leads to a $\approx 20\%$ under-estimate of the mean island size in our fiducial source model.

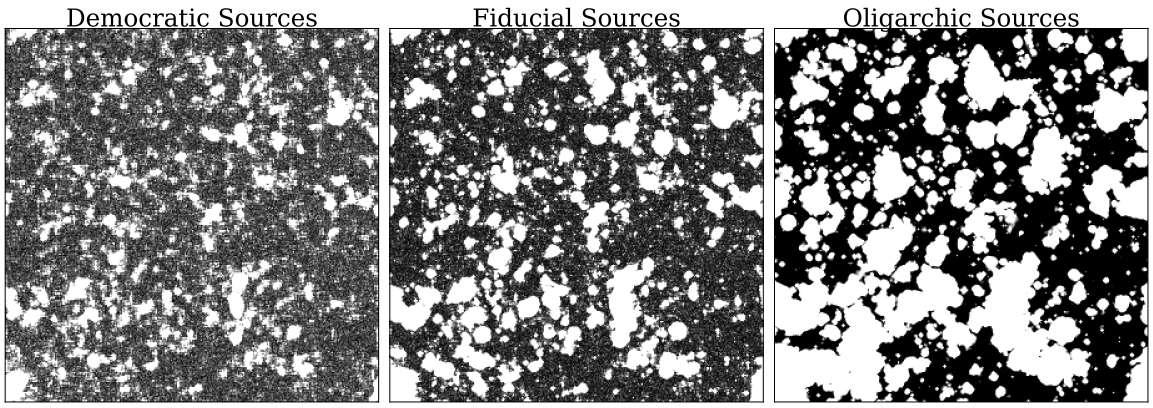

Figure 5.8: Ionization maps at 50% volume ionized for the Democratic Sources (left), Fiducial (middle) and Oligarchic Sources (right) models, all assuming the Full Sinks model. From left to right, the contribution to the photon budget from the brightest, most massive halos increases. Reionization by more massive, highly biased sources leads to ionized bubbles being larger and fewer in number.

5.4 Interplay Between Sources and Sinks

5.4.1 Source Models

In this section, we will generalize our analysis to include different models for the sources. Most previous studies of morphology have varied the source and sinks properties one at a time, while keeping the other fixed (e.g. [177, 226, 225, 227, 204, 236]). Our use of efficient RT simulations with sink dynamics included allows us to explore the relationship between the sources and sinks as it pertains to morphology. We consider three models for the sources:

- Democratic Sources: This model differs from our fiducial model in that it assigns all halos the same ionizing emissivity independent of their luminosity, i.e. $\beta = 0$ (see §5.2.4). At $z = 6$, 50% of the ionizing emissivity is produced by halos in the mass range $10^9 < M/[\mathrm{h}^{-1}M_\odot] < 1.8 \times 10^9$ ($-12.6 > M_{\mathrm{UV}} > -13.4$). This model

was introduced in [10] in an attempt to find a model that better recovers the short mean free path at $z = 6$ reported by [13]. This kind of picture would require a steep dependence of $f_{\rm esc}$ and/or the ionizing efficiency $\xi_{\rm ion}$ on luminosity, specifically, $f_{\rm esc}\xi_{\rm ion} \propto L_{\rm UV}^{-1}$ (corresponding to roughly $f_{\rm esc}\xi_{\rm ion} \propto M^{-1.4}$ over most of the mass range at $z = 6$). The sources driving reionization in this model are almost entirely below current detection limits, in contrast to the Oligarchic Sources model described below.

- Fiducial Sources: Our fiducial scenario with $M_{\rm min} = 10^9\ h^{-1}M_\odot$ and with the emissivity of each halo proportional to its UV luminosity (i.e. $\beta = 1$). At $z = 6$, halos with masses in the range $10^9 < M/[{\rm h}^{-1}M_\odot] < 1.8 \times 10^{10}$ ($-12.6 < M_{\rm UV} < -16.9$) contribute 50% of the ionizing emissivity. Of our three source models, this one is most similar to parameterizations commonly used in simulations, e.g. those that assume the emissivity to be proportional to halo mass [225, 127, 130, 247].

- Oligarchic Sources: In this model, bright and massive sources – the "oligarchs" – dominate reionization. We adopt $M_{\rm min} = 2 \times 10^{10}\ h^{-1}M_\odot$ with $\beta = 1$, corresponding to a limiting magnitude of $M_{\rm UV}^{\rm max}(z = 6) \approx -17$, roughly the limit of current observations at $5 < z < 10$ [248, 249]. Thus it assumes that the sources responsible for reionization have, for the most part, already been observed. This model is qualitatively similar to that proposed by [231] (see also [40, 250]). It also serves to contrast starkly with the Democratic Sources model.

To make some contact with previous works exploring how the source properties affect morphology, Figure 5.8 shows ionization maps at 50% volume ionized ($z \sim 7$) for

our Democratic Sources (left), Fiducial Sources (middle) and Oligarchic Sources (right), all assuming the Full Sinks model. The differences are clearly visible in the ionization fields; in the models driven by brighter sources, the ionized bubbles are larger and fewer in number. This is because the most massive, rare sources produce a larger fraction of the photons in the Fiducial and Oligarchic Sources models. This familiar result has been observed in many previous studies (e.g. [177, 227, 222, 236]). Now we turn our attention to the interplay between the sources and sinks.

5.4.2 Results

Figure 5.9 shows $\Delta_{21}(k)$ at 20%, 50%, and 80% ionized, in the same format as the bottom panel of Figure 5.5, for all combinations of source and sinks models. The top and bottom rows show results for the Democratic Sources and Oligarchic Sources models, while the results for the Fiducial Sources model (same as Figure 5.5) are shown by the thin lines in the bottom row. Note that models sharing the same sinks prescription have similar reionization histories and the same emissivity histories as those shown in Fig. 5.1. In the Democratic Sources case, the differences between sinks models are smaller at 20% ionized but somewhat larger at 50% and 80% ionized than in the Fiducial Sources case. The suppression of Δ_{21} at $k = 0.1\ h\mathrm{Mpc}^{-1}$ in the latter half of reionization relative to the Full Sinks case has increased from $30 - 60\%$ for the Fiducial Sources case to $70 - 80\%$. In addition, there are now $\approx 40\%$ differences between the Relaxed Limit, Full Sinks, and Uniform C_R models at 50% ionized. The Uniform C_R model is $\approx 35\%$ below the Full Sinks and Relaxed Limit models at 80% ionized.

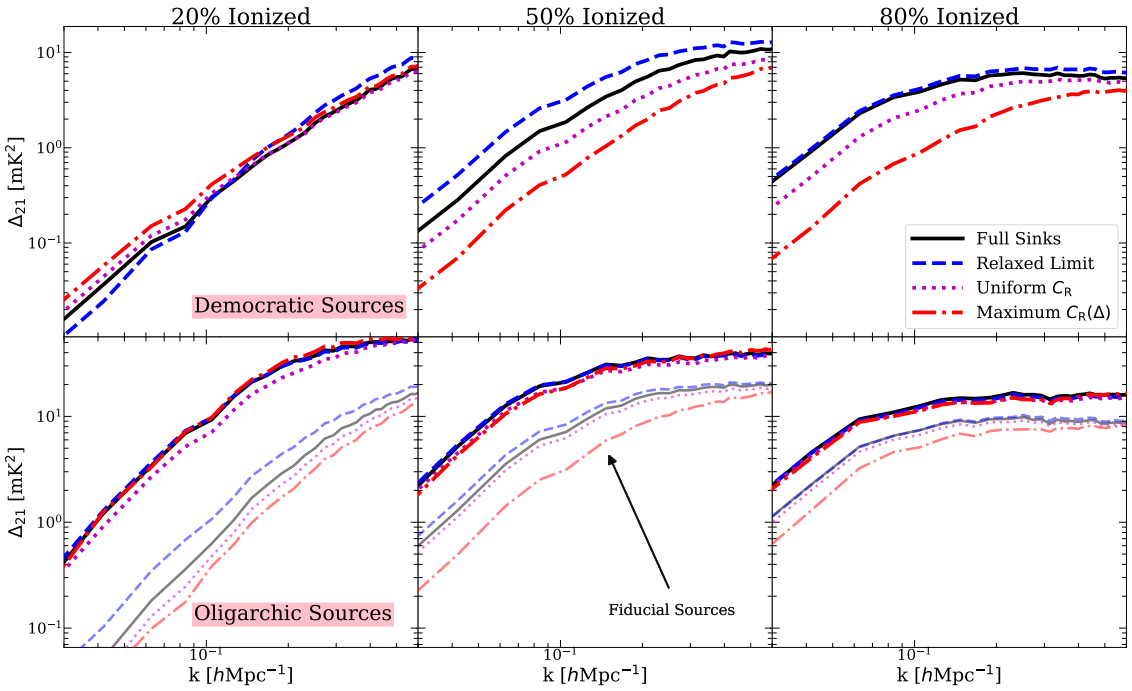

Figure 5.9: $\Delta_{21}(k)$ for all our sources and sinks models, illustrating the interplay between the sources and sinks of reionization. The top and bottom rows show results for the Democratic Sources and Oligarchic Sources models, respectively. The Fiducial Sources result is shown again by the thin curves in the bottom panel for comparison. The magnitude of the sinks' effect on morphology clearly depends on the nature of the sources. In the Democratic Sources scenario (top row), the differences between the sinks models are significantly larger than in the Oligarchic Sources scenario. Notably, in the former, the Uniform C_R model no longer matches so well the Full Sinks results, as it did for Fiducial Sources (compare to the thin curves in the bottom row). By contrast, in the Oligarchic Sources scenario, even the Maximum $C_R(\Delta)$ model matches the others well, especially at 50% and 80% ionization. We are led to conclude that in reionization scenarios driven by less (more) biased sources, the sinks become more (less) important for shaping morphology.

It is interesting that for the Democratic Sources model (top row) the Full Sinks and Uniform C_R models have appreciably different Δ_{21}. In particular, the Full Sinks model has *more* large-scale power, which is indicative of larger ionized bubbles. Recall from our discussion in §5.3.2 that the Full Sinks model should be expected to favor the growth of larger bubbles more than the Uniform C_R case owing to lower (higher) clumping factors in over-dense (under-dense) regions in the former. It seems that the these differences, which had little effect on morphology in our Fiducial Sources model, do become important in the limit that very faint, low-bias sources drive reionization. We caution that this effect may be exaggerated due to our probable over-estimation of the impact of un-relaxed gas, discussed in §5.2.3. However, it may also be a slight under-estimate due to the effects of using sub-resolution sources, as discussed in §5.2.4. In our tests using the Democratic Sources + Uniform C_R combination, fixing the positions of the sources (see last paragraph of §5.2.4) can reduce power at $k = 0.1\ h\mathrm{Mpc}^{-1}$ by up to 20%, while the Full Sinks model does not change appreciably. This reduction in power was as large as a factor of 2 in our tests using the Democratic Sources + Maximum $C_R(\Delta)$ combination. We note that these differences would work in the direction of strengthening our conclusions in these scenarios, and that for the other source models we found differences of 10% or less[9].

By contrast, in the Oligarchic Sources case, the differences are 15% or less between the Full Sinks, Relaxed Limit, and Uniform C_R models in all of the panels. More strikingly, at 50% and 80% ionized even the Maximum $C_R(\Delta)$ model is very similar to the Uniform

[9]Indeed, the Oligarchic Sources model does not use sub-resolution sources.

C_R case[10]. The insensitivity of morphology to the sinks in the Oligarchic Sources model contrasts the much stronger dependence seen in the Democratic Sources model.

Why is morphology sensitive to the sinks in models driven by fainter sources, but not in the Oligarchic Sources scenario? In §5.3, we saw that sinks limit the sizes of large ionized bubbles. However, it is harder for them to do so in the Oligarchic Sources scenario for two reasons. Nearly all the emissivity is concentrated in highly biased regions, strongly favoring the growth of the largest ionized bubbles. Second, these bubbles grow fast enough to escape the over-densities in which they are born before recombinations begin having a significant impact. This mitigates the "disadvantage" those bubbles have of inhabiting over-dense regions. In these ways, sources in the Oligarchic Sources model "win out" over the sinks in terms of shaping morphology. In the Democratic Sources model, by contrast, the sources are less biased than in Fiducial Sources and the sinks can more easily slow the growth of the largest bubbles. In other words, the sinks are unable to tax the rich enough to affect morphology when the source bias is very high, and become more effective at taxing them when the source bias is reduced.

This result has implications for forthcoming efforts to model reionization and interpret observations. Most straightforwardly, it demonstrates that studying the sinks and sources one at a time can produce biased results. For example, studying the sinks in a scenario with only highly biased sources would lead to the incorrect conclusion that they

[10]In the Oligarchic Sources scenario, the earlier ionization history in the Maximum $C_R(\Delta)$ model may obscure morphological differences that would be present if it had the same reionization history as the other sinks models. This is because the bias of the sources evolves strongly with redshift in the Oligarchic Sources model due to its high $M_{\rm min}$. To check this, we ran a Relaxed Limit simulation with an accelerated reionization history similar to the Maximum $C_R(\Delta)$ one. We found evidence for mild suppression (at most 20% at $k = 0.1$ hMpc^{-1}) at 50% ionized, and no sign of suppression at 80% ionized. This is less than the effect seen in the Fiducial Sources case, confirming our statement in the text.

are unimportant for morphology. Another point is that very highly-biased source models may be relatively easy to rule out (or confirm) with forthcoming 21 cm observations from reionization. For example, an upper limit of e.g. $\Delta_{21}(k = 0.1\ \mathrm{hMpc}^{-1}) \leq 10\ \mathrm{mK}^2$ midway through reionization would strongly disfavor the Oligarchic Sources model (which has $\Delta_{21}(k = 0.1\ \mathrm{hMpc}^{-1}) \approx 20\ \mathrm{mK}^2$ at $x_{\mathrm{ion}}^{\mathrm{V}} = 0.5$), since any physically reasonable sinks model would be unable to push Δ_{21} much lower than this[11]. The tightest upper limit to date from HERA [46] is $\Delta_{21} \leq 946\ \mathrm{mK}^2$ at $z \sim 7.9$ and $k = 0.19\ h\mathrm{Mpc}^{-1}$, less than 2 dex away from reaching the prediction of our Oligarchic Sources model. Other probes that are sensitive to the existence of large ionized regions, such as the visbility of LAEs at $z > 6$ [252, 253, 150, 148], may also be able to identify large bubbles like those predicted by the Oligarchic Sources model.

5.5 Conclusion

At present, there is no consensus on how much of an effect the sinks had in shaping reionization's morphology and, relatedly, how important they are for interpreting its observables. We have attempted to address these questions using cosmological RT simulations of reionization. Our simulations include the sub-grid model for the ionizing photon opacity developed by [10], which is based on high-resolution, fully coupled radiative hydrodynamics simulations of the IGM. The model improves over previous efforts in several key ways: it includes the effects of self-shielding and hydrodynamic response to photo-heating, keeping

[11] This statement presumes that at fixed ionized fraction, only the sources and sinks appreciably impact morphology. Two other effects - redshift-space distortions [251] and spin temperature fluctuations [47] may also impact the observed signal significantly. However, both of these work to boost large-scale power, which would only strengthen our statement about upper limits.

track of their dependencies on the LyC intensity, the timing of (local) reionization, and the environmental density. Our main conclusions can be summarized as follows:

- The sinks decrease the sizes of the largest ionized bubbles during reionization. We explored this effect in our detailed sub-grid model (Full Sinks), and in three other models representative of the ways that sinks have been implemented in previous studies: (1) A model that assumes a pressure-smoothed IGM (Relaxed Limit); (2) A simple clumping factor without dynamics or spatial in-homogeneity, tuned to have the same photon budget as our fiducial model (Uniform C_R); (3) An in-homogeneous clumping model from [225] that neglects pressure smoothing, thus representing a kind of upper limit on the effects of sinks (Maximum $C_R(\Delta)$).

- For our fiducial source model, which assumes the same escape fraction and ionizing efficiency for all sources, the Full Sinks model has up to $\sim 10-20\%$ smaller mean bubble sizes compared to the Relaxed Limit model in the first half of reionization. These differences mostly disappear in the second half.

- By contrast, the Maximum $C_R(\Delta)$ model underestimates bubble sizes by $\approx 40\%$ (compared to the Full Sinks model). Ignoring the dynamical effects of pressure smoothing and photoevaporation can over-estimate significantly the sinks' effects on morphology.

- We were able to reproduce a very similar morphology to our Full Sinks model using a uniform constant sub-grid clumping factor (the Uniform C_R model). Hence, under typical assumptions about reionization's source population, with regards to morphology, it appears that the detailed dynamics and spatial in-homogeneity of the sinks

can be adequately modeled in an average sense with a sub-grid clumping factor. This is a useful result for scenarios where either (1) the ionizing photon budget is fixed by a model (as in this work) or by some empirical constraint, or (2) the budget is free to vary, as in a parameter space study. To apply this result to a reionization simulation, one may simply re-scale the recombination rates at $T_{\rm ref} = 10,000$ K by a uniform sub-grid clumping factor, $C_{\rm R}$, tuned to match the given total ionizing photon budget. Note, however, that the Full Sinks and Uniform $C_{\rm R}$ models exhibit significant differences in $\Gamma_{\rm HI}$ (Fig. 5.1), which could render predictions for, e.g., the Lyα forest quite different. As such, we emphasize that this conclusion should only be taken to apply to the structure of ionized and neutral regions, and not other physical properties of the ionized IGM, such as $\Gamma_{\rm HI}$ or the mean free path.

- Differences in bubbles sizes between our models are manifest in the predicted power spectrum of the red-shifted 21cm background. The Maximum $C_{\rm R}(\Delta)$ under-estimates the large-scale 21 cm power by $30-60\%$ throughout reionization compared to our Full Sinks model for our fiducial source prescription. The Relaxed Limit model over-estimates power somewhat early in reionization, but becomes similar to both the Full Sinks and Uniform $C_{\rm R}$ cases in reionization's latter half.

- The morphology of neutral islands near the end of reionization is very similar in all of the models except the Maximum $C_{\rm R}(\Delta)$ case, which produces smaller islands. The islands in that model are 20% too small on average, highlighting again the importance of including the effects of pressure smoothing.

- The strength of the sinks' effect on morphology is sensitive to the properties of the sources that drove reionization. In a model where reionization was driven entirely by bright ($M_{\rm UV} < -17$), highly biased galaxies, the sinks suppress the 21 cm power at the $10-15\%$ level at a fixed ionized fraction throughout reionization, even in the Maximum $C_{\rm R}(\Delta)$ case. By contrast, when faint ($M_{\rm UV} \sim -13$), low-bias galaxies drove reionization, the large-scale 21 cm power can be suppressed by up to 80%, and the morphology in the Full Sinks and Uniform $C_{\rm R}$ models differ significantly. This result highlights the need to study the effects of sinks and sources together instead of separately. Moreover, the insensitivity of morphology to sinks in highly biased source models makes such models easier targets for forthcoming 21 cm experiments like HERA and SKA, and other probes sensitive to the presence of very large ionized bubbles.

Our Full Sinks model can be improved on in several ways. First, in future iterations we plan to address the caveats discussed in §5.2.3, namely the possible under-counting of rare, massive sinks and double-counting of absorptions in self-shielded systems. These issues can be addressed with sub-grid simulations in larger volumes and by explicitly modeling the evolution of the residual H I fraction in self-shielded systems. A notable uncertainty in our results is that simulations upon which our sub-grid model is based do not include galaxy formation processes, which may affect significantly the structure and state of sinks near massive halos.

Given the interplay between sources and sinks pointed out here, future studies should also move beyond simplistic source parameterizations. Source models should ideally

incorporate physically motivated prescriptions for effects such as feedback from reionization [254, 255, 217, 256, 257, 258, 144], bursty star formation [259, 260, 261], galaxy formation histories [262, 263, 264], and for $f_{\rm esc}$ [265, 266, 267, 268, 269], all of which play important roles in setting the abundance and bias of the sources.

Chapter 6

Supplemental Unpublished Material

6.1 Numerical solution of the 1D RT Equation in a static density IGM

6.1.1 The RT equation

The 1D time-dependent RT equation in spherical coordinates, ignoring scattering, has the form

$$\frac{1}{c}\frac{\partial I_\nu}{\partial t} + \frac{1}{r^2}\frac{\partial (r^2 I_\nu)}{\partial r} + \kappa_\nu(r) I = j_\nu(r) \tag{6.1}$$

where I_ν is the radiation intensity at frequency ν, $\kappa_\nu(r)$ is the absorption coefficient of the gas along the line of sight and $j_\nu(r)$ is the source function. In our case, $j_\nu(r)$ is a delta function at the origin (a point source) and so we can solve Eq. 1 assuming $j_\nu = 0$ and the appropriate boundary conditions. If we further assume that the speed of light is infinite,

the first term on the LHS drops out as well. Writing Eq. 1 as a finite difference on a spatial grid gives

$$\frac{1}{r_i^2 \Delta r_i}\left[r_i^2 I_\nu(r_i) - r_{i-1}^2 I_\nu(r_{i-1})\right] + \kappa_\nu(r_i) I_\nu(r_i) = 0 \tag{6.2}$$

where $\Delta r_i \equiv r_i - r_{i-1}$. The use of indices i and $i-1$ in the first term on the LHS of Eq. 2 makes this a *backwards-difference* approximation of Eq. 1. A *forwards-difference* approximation would have had indices $i+1$ and i instead. Solving for $I_\nu(r_i)$ gives

$$I_\nu(r_i) = \left(\frac{1}{\Delta r_i} + \kappa_\nu(r_i)\right)^{-1} \left(\frac{r_{i-1}}{r_i}\right)^2 \frac{1}{\Delta r_i} I_\nu(r_{i-1}) \tag{6.3}$$

Eq. 3 can be solved at all points on the grid in sequence starting from $r_0 \equiv R_0$. The boundary condition is

$$I_\nu(R_0) = \frac{L}{16\pi^2 R_0^2}\phi_\nu \tag{6.4}$$

where L is the luminosity of the ionizing source at the center and ϕ_ν is the spectrum of the ionizing radiation, normalized so that

$$\int_{\nu_{\min}}^{\nu_{\max}} d\nu \phi_\nu = 1 \tag{6.5}$$

where $\nu_{\min}$ and $\nu_{\max}$ are the minimum and maximum frequencies emitted by the source. The absorption coefficient κ_ν is given by

$$\kappa_\nu = \sum \kappa_\nu^i = \sum n_i \sigma_\nu^i \tag{6.6}$$

where n_i is the number density of species i and σ_ν^i is the absorption cross-section of species i. In the case of HI, $\sigma_\nu^{\rm HI} \approx \sigma_0 \left(\frac{\nu}{\nu_0}\right)^{-2.75}$ at $\nu > 13.6$ eV$/h_p = \nu_0$ and 0 otherwise (with $\sigma_0 = 6.3 \times 10^{-18}$ cm^{-2}). The exact form is taken from [270].

6.1.2 Chemistry Equations

Once we have solved for I_ν, we need to solve for the ionization state of the gas. The photo-ionization rate of species i in a thin shell with thickness Δr and intensity I_ν is

$$\Gamma_i = \int_{\nu_{\min}}^{\nu_{\max}} d\nu \sigma_\nu^i \frac{c u_\nu}{h_p \nu} \tag{6.7}$$

where $u_\nu = \frac{4\pi}{c} I_\nu$ is the spectral energy density and h_p is Planck's constant. The ionization states of H and He are then given by the following set of differential equations:

$$\frac{dn_{\rm HII}}{dt} = n_{\rm HI}\Gamma_{\rm HI} - \alpha_{\rm HII}(T) n_e n_{\rm HII} \tag{6.8}$$

$$\frac{dn_{\rm HeII}}{dt} = n_{\rm HeI}\Gamma_{\rm HeI} - \alpha_{\rm HeII}(T) n_e n_{\rm HeII} - n_{\rm HeII}\Gamma_{\rm HeII} + \alpha_{\rm HeIII}(T) n_e n_{\rm HeIII} \tag{6.9}$$

$$\frac{dn_{\rm HeIII}}{dt} = n_{\rm HeII}\Gamma_{\rm HeII} - \alpha_{\rm HeIII}(T) n_e n_{\rm HeIII} \tag{6.10}$$

$$n_{\rm HI} = n_{\rm H} - n_{\rm HII} \tag{6.11}$$

$$n_{\rm HeI} = n_{\rm He} - n_{\rm HeII} - n_{\rm HeIII} \tag{6.12}$$

$$n_e = n_{\rm HII} + n_{\rm HeII} + 2n_{\rm HeIII} \tag{6.13}$$

Eq. 8-10 are the ionization equations for HII, HeII, and HeIII, and Eq. 11-12 are the "closing conditions" that ensure conservation of H and He, and Eq. 13 specifies the number density of electrons. The α_i terms are the temperature-dependent recombination rates of each ionized state. We use this set of equations to solve for the ionization state in mostly neutral gas, where the abundances of the ionized states are very small. As an example, the backwards-difference form of Eq. 8 is

$$\frac{n_{\rm HII}(t_i) - n_{\rm HII}(t_{i-1})}{\Delta t_i} = [n_{\rm H} - n_{\rm HII}(t_i)]\Gamma_{\rm HI} - \alpha_{\rm HII}(T) n_e(t_i) n_{\rm HII}(t_i) \tag{6.14}$$

where $\Delta t \equiv t_i - t_{i-1}$. Solving Eq. 14 is in prinicple tricky, since $n_e(t_i)$ depends on the updated ionization states of HI, HeI, and HeII, which would render Eq. 8-10 a coupled set

of quadratic equations. To get around this, we initially take n_e to be it's previous value (at $t = t_{i-1}$) initially, which makes Eq. 14 easy to solve:

$$n_{\rm HII}(t_i) = \left[\frac{1}{\Delta t_i} + \Gamma_{\rm HI} + \alpha_{\rm HII}(T) n_e(t_{i-1})\right]^{-1} \left(\frac{n_{\rm HII}(t_{i-1})}{\Delta t_{i-1}} + n_{\rm H}\Gamma_{\rm HI}\right) \tag{6.15}$$

After solving Eq. 8-13 in this manner, we solve them again for the same time step, but using the updated value of n_e from the previous solution. Over several iterations n_e will converge to it's "present" value and Eq. 15 will be consistent with the full backwards-difference solution. Eq. 8-13 are appropriate when the number densities of the ionized states are small, but when densities of neutral states are small, as in highly ionized gas, it is more numerically sound to write the differential equations in terms of the neutral ionization states. For example, the equation for H would become

$$\frac{dn_{\rm HI}}{dt} = -n_{\rm HI}\Gamma_{\rm HI} + \alpha_{\rm HII}(T) n_e n_{\rm HII} \tag{6.16}$$

and would be solved in a manner analogous to Eq. 14 and 15. In the case of He, we have 3 possible ionization states and hence must pick two to solve for in this manner. Usually one of the three ionization states of He dominates, so we solve the other two using the backwards difference approach and use the closing condition to get the third. Based on the relative abundances of each ionization states, we optimally choose which set of equations to solve at each grid point.

6.1.3 Temperature

The equation for the temperature of an expanding IGM (ignoring evolution in the density contrast Δ) is

$$\frac{dT}{dt} = \frac{2}{3k_{\rm B}n_{tot}}(\mathcal{H} - \Lambda) - 2H(z)T - \frac{T}{n_e}\frac{dn_e}{dt} \tag{6.17}$$

Here, $\mathcal{H}$ and Λ are the heating and cooling functions respectively, $H(z)$ is the Hubble parameter, and $n_{\rm tot}$ is the total number density of the gas. The backwards different solution of this equation is straightforward if we ignore the fact that Λ depends on temperature:

$$T(t_i) = \left[\frac{1}{\Delta t_i} + 2H(z) + \frac{1}{n_e}\frac{dn_e}{dt}\right]^{-1}\left[\frac{T(t_{i-1})}{\Delta t_i} + \frac{2}{3k_{\rm B}n_{tot}}(\mathcal{H} - \Lambda)\right] \tag{6.18}$$

Sufficiently far from I-fronts and over long time scales, the main sources of cooling is the expansion of the universe, which is described by the $H(z)$ term. The main source of heating is photo-ionizational heating, which is given by

$$\mathcal{H}^i_{pi} = \int_{\nu_0}^{\nu_{\rm max}} d\nu\sigma^i_\nu(h\nu - h\nu_0)\frac{cu_\nu}{h\nu} \tag{6.19}$$

where ν_0 is the ionization edge of species i ($13.6/h_p$ eV for HI). The cooling mechanism over short timescales (and outside of I-fronts) is Compton cooling off the CMB:

$$\Lambda_{\rm compton} = C(z)n_e(T - T_{\rm CMB}) \tag{6.20}$$

where $T_{\rm CMB} = 2.7(1+z)$ K, and

$$C(z) = 5.6072 \text{ erg /K/ s } \times 10^{-36}(1+z)^4 \tag{6.21}$$

Inside ionization fronts, the dominant cooling channel is collisional ionization. The collisional ionization cooling rates are given by

$$\Lambda^i_{ci} = {\rm CIC}_i(T)n_e n_i \tag{6.22}$$

for temperatures 10^4 K $\leq T \leq 10^9$ K and 0 otherwise, where the coefficients CIC_i The are given by

$$\mathrm{CIC_{HI}} = 13.60 \text{ eV } \times 21.11 \text{ cm }^3/\text{ s } \times T^{-1.5} e^{-\lambda_{\mathrm{HI}}/2} \frac{\lambda_{\mathrm{HI}}^{-1.089}}{(1+(\lambda_{\mathrm{HI}}/0.354)^{0.874})^{1.101}} \tag{6.23}$$

$$\mathrm{CIC_{HeI}} = 24.59 \text{ eV } \times 32.38 \text{ cm }^3/\text{ s } \times T^{-1.5} e^{-\lambda_{\mathrm{HeI}}/2} \frac{\lambda_{\mathrm{HeI}}^{-1.146}}{(1+(\lambda_{\mathrm{HeI}}/0.416)^{0.987})^{1.056}} \tag{6.24}$$

$$\mathrm{CIC_{HeII}} = 54.42 \text{ eV } \times 19.95 \text{ cm }^3/\text{ s } \times T^{-1.5} e^{-\lambda_{\mathrm{HeII}}/2} \frac{\lambda_{\mathrm{HeII}}^{-1.089}}{(1+(\lambda_{\mathrm{HeII}}/0.553)^{0.735})^{1.275}} \tag{6.25}$$

where $\lambda_i \equiv 2E_i/k_{\mathrm{B}}T$, and E_i is the ionization energy of species i. Here n_i is the neutral state of the respective species (e.g. HI). At high densities, recombination cooling is important. The recombination cooling rates are given by

$$\Lambda_{rc}^{i} = \mathrm{RC}_i(T) n_e n_i \tag{6.26}$$

where now n_i refers to the ionized state of each species. The recombination cooling coefficients are given by

$$\mathrm{RC_{HII}^{A}} = 1.778 \times 10^{-29} \text{ erg } \text{ cm }^3/\text{ s } \times T \frac{\lambda_{\mathrm{HII}}^{1.965}}{(1+(\lambda_{\mathrm{HII}}/0.541)^{0.502})^{2.697}} \tag{6.27}$$

$$\mathrm{RC_{HII}^{B}} = 3.435 \times 10^{-30} \text{ erg } \text{ cm }^3/\text{ s } \times T \frac{\lambda_{\mathrm{HII}}^{1.970}}{(1+(\lambda_{\mathrm{HII}}/2.250)^{0.376})^{3.720}} \tag{6.28}$$

$$\mathrm{RC_{HeII}^{A}} = k_{\mathrm{B}} T \alpha_{\mathrm{HeII}}^{\mathrm{A}} \tag{6.29}$$

$$\mathrm{RC_{HeII}^{B}} = k_{\mathrm{B}} T \alpha_{\mathrm{HeII}}^{\mathrm{B}} \tag{6.30}$$

$$\mathrm{RC_{HeIII}^{A}} = 8\mathrm{RC_{HII}^{A}} \tag{6.31}$$

$$\mathrm{RC_{HeIII}^{B}} = 8\mathrm{RC_{HII}^{B}} \tag{6.32}$$

where the A and B superscripts refer to case A and B recombination rates.

6.2 Recent improvements to the IGM opacity sub-grid model

6.2.1 Multi-frequency Radiative Transfer

Multi-frequency RT model

The radiative hydrodynamics simulations of [74] assumed a power law spectrum of the form $J_\nu \propto \nu^{-\alpha}$, where $\alpha = 1.5$, discretized into 5 frequency bins between 1 and 4 Ry. Unfortunately, because these authors did not anticipate the subsequent application to a multi-frequency sub-grid model, they did not save the IGM opacities in each frequency bin. However, they did save the frequency-averaged absorption coefficient, $\langle\kappa_\nu\rangle_{\alpha=1.5}$, where the subscript denotes that the average is weighted by the spectrum $J_\nu \propto \nu^{-1.5}$, and the Lyman Continuum value, κ_{912}, which we use to calibrate an approximate multi-frequency treatment of the opacity as follows. First, we assume that the frequency dependence of κ is described by a power law in the photo-ionization cross-section,

$$\kappa_\nu = \kappa_{912} \left(\frac{\sigma_\nu}{\sigma_{912}}\right)^{\beta_{\rm N}-1} \tag{6.33}$$

This form follows from the frequency-dependent version of equation (5) of [178],

$$\kappa_\nu = \int dN_{\rm HI}\, \frac{\partial^2 N}{\partial N_{\rm HI}\partial r} \left(1 - e^{-N_{\rm HI}\sigma_\nu}\right), \tag{6.34}$$

with the additional assumption of a power-law H I column density distribution, $\partial^2 N/\partial N_{\rm HI}\partial r \propto N_{\rm HI}^{-\beta_{\rm N}}$, where $N_{\rm HI}$ is the H I column, and restricting $1 < \beta_{\rm N} < 2$. [178] showed that equation (6.34) provides an excellent approximation to the full κ_ν in the simulations of [74]. With a power-law spectrum of the form $J_\nu \propto \nu^{-\alpha}$ between 1 and 4 Ry, we can find $\beta_{\rm N}$ using

$$\frac{\langle\kappa_\nu\rangle_{\alpha=1.5}}{\kappa_{912}} = \frac{\alpha[1 - 4^{-\alpha-2.75(\beta_{\rm N}-1)}]}{[\alpha + 2.75(\beta_{\rm N}-1)](1-4^{-\alpha})}, \tag{6.35}$$

where we have used the approximation that $\sigma_\nu = \sigma_{912}(\nu/\nu_{912})^{-2.75}$. For $\alpha = 1.5$, the left hand side of equation (6.35) can be calculated for each RT cell of our reionization simulations, since our sub-grid model keeps track of the evolution of both $\langle\kappa_\nu\rangle_{\alpha=1.5}$ and κ_{912}, yielding a solution for $\beta_{\rm N}$. Once $\beta_{\rm N}$ has been estimated in this manner, κ_ν is calculated for each frequency bin using equation (6.33).

Multi-frequency generalization for $\Gamma_{\rm HI}$ (Eq. 5.1)

If the I-front in cell i is infinitely sharp and travels along one axis, then ray j intersecting cell i will travel a distance $x^i_{\rm ion}\Delta s^{ij}$ (recall Δs^{ij} is the total path length of ray j through cell i) before reaching neutral gas. The number of photons absorbed over this distance is

$$N^i_{\rm abs} = \sum_{j=1}^{N_{\rm rays}} \sum_\nu N^{ij}_{0,\nu} \left(1 - \exp\left[\frac{-x^i_{\rm ion}\Delta s^{ij}}{\lambda^i_\nu}\right]\right) \tag{6.36}$$

where the outer sum runs over all rays j intersecting cell i and the inner sum runs over all frequency bins characterizing ray j. Here, $N^{ij}_{0,\nu}$ is the number of photons in ray j at frequency ν and λ^i_ν is the frequency-dependent mean free path in cell i. During a time step Δt, $\Gamma_{\rm HI}$ behind the I-front is

$$\Gamma^i_{\rm HI} = \frac{\text{\# of photons absorbed per time}}{\text{\# of HI atoms in ionized gas}} = \frac{N^i_{\rm abs}/\Delta t}{n^\Gamma_{\rm HI} x^i_{\rm ion} V_{\rm cell}} \tag{6.37}$$

where $x^i_{\rm ion}V_{\rm cell}$ is the ionized volume of cell i and

$$n^\Gamma_{\rm HI} \equiv \frac{\langle\Gamma_{\rm HI} n_{\rm HI}\rangle_{\rm V}}{\langle\Gamma_{\rm HI}\rangle_{\rm V}} \tag{6.38}$$

is the $\Gamma_{\rm HI}$-weighted HI number density (the V sub-script denotes a volume average). In §C.3, we show that the frequency-averaged MFP in our sub-grid simulations is given by

$$\overline{\lambda}^{-1} = \frac{\langle n_{\rm HI}\Gamma_{\rm HI}\rangle_{\rm V}}{F_\gamma} = \frac{1}{F_\gamma}\int_{\nu_{\rm HI}}^{4\nu_{\rm HI}} d\nu \frac{I_\nu}{h\nu}\lambda_\nu^{-1} \tag{6.39}$$

where I_ν and F_γ are the specific intensity and ionizing photon flux at the source planes in the sub-grid simulations, respectively. Using this result, we can write

$$\frac{n_{\rm HI}^{\Gamma,i}}{F_\gamma} = \frac{1}{\langle\Gamma_{\rm HI}\rangle_{\rm V}}\int_{\nu_{\rm HI}}^{4\nu_{\rm HI}} d\nu \frac{1}{F_\gamma}\frac{I_\nu}{h\nu}\lambda_\nu^{-1} \approx \frac{\langle\lambda_\nu^{-1}\rangle_\nu^i}{\langle\Gamma_{\rm HI}\rangle_{\rm V}} \tag{6.40}$$

where $\langle\lambda_\nu^{-1}\rangle_\nu^i$ is the opacity averaged over the spectrum incident on cell i. In our monochromatic treatment, which assumed the same $\alpha = 1.5$ spectrum used in our sub-grid simulations, Eq. 6.40 is exact. In our multi-frequency treatment, the spectral shape can vary from cell to cell and differ from a power law. For each cell, we assume that Eq. 6.40 would hold for a hypothetical sub-grid simulation run sharing the same spectrum incident on the cell. This is an approximation, since we determine the frequency dependence of λ_ν entirely from our $\alpha = 1.5$ simulations using Eq. 6.33 (see next section). Eq. 6.40 also ignores spectral hardening taking place over distances smaller than the cell size. Substituting Eq. 6.36 and 6.40 to Eq. 6.38 yields

$$\Gamma_{\rm HI}^i = \frac{\sum_{j=1}^{N_{\rm rays}}\sum_\nu N_{0,\nu}^{ij}\left(1-\exp\left[\frac{-x_{\rm ion}^i\Delta s^{ij}}{\lambda_\nu^i}\right]\right)}{\langle(\lambda_\nu^{-1})_\nu F_\gamma/\langle\Gamma_{\rm HI}\rangle_{\rm V})x_{\rm ion}^i V_{\rm cell}\Delta t} \tag{6.41}$$

The ratio $F_\gamma/\langle\Gamma_{\rm HI}\rangle_{\rm V}$ can be simplified as long as $F_\gamma\langle\sigma_{\rm HI}\rangle_\nu^i \approx \langle\Gamma_{\rm HI}\rangle_{\rm V}$, where $\langle\sigma_{\rm HI}\rangle_\nu^i$ is the HI cross-section averaged over the spectrum incident on cell i. Under this approximation,

$$\Gamma_{\rm HI}^i = \frac{\langle\sigma_{\rm HI}\rangle_\nu^i\sum_{j=1}^{N_{\rm rays}}\sum_\nu N_{0,\nu}^{ij}\left(1-\exp\left[\frac{-x_{\rm ion}^i\Delta s^{ij}}{\lambda_\nu^i}\right]\right)}{\langle\lambda_\nu^{-1}\rangle_\nu^i x_{\rm ion}^i V_{\rm cell}\Delta t} \tag{6.42}$$

If we define $\langle\lambda_\nu\rangle_\nu \equiv \langle\lambda_\nu^{-1}\rangle_\nu^{-1}$, then Eq. 6.42 can be written in a form similar to Eq. 1 of [10],

$$\Gamma_{\rm HI}^i = \frac{\langle\lambda_\nu\rangle_\nu^i\langle\sigma_{\rm HI}\rangle_\nu^i\sum_{j=1}^{N_{\rm rays}}\sum_\nu N_{0,\nu}^{ij}\left(1-\exp\left[\frac{-x_{\rm ion}^i\Delta s^{ij}}{\lambda_\nu^i}\right]\right)}{x_{\rm ion}^i V_{\rm cell}\Delta t} \tag{6.43}$$

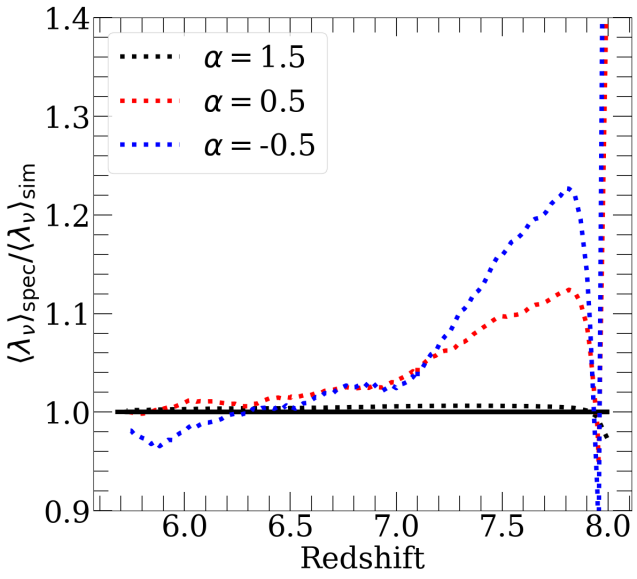

Figure 6.1: Direct test of our multi-frequency procedure described in §6.2.1. We have run small-scale simulations with $\alpha = 1.5$, 0.5, and -0.5, and used the procedure in that section to estimate $\langle\lambda_{nu}\rangle_{spec}$ using only the $\alpha = 1.5$ results. Here we show the ratio between $\langle\lambda_{nu}\rangle_{spec}$ and the true value extracted from each simulation. The extremely good agreement in the $\alpha = 1.5$ case validates our assumption that the column density distribution is well-described by a power law. The other cases differ by at most 20% (and usually much better).

Frequency Dependence of κ & IGM Filtering

In this appendix, we explain in more detail and provide validation of our multi-frequency RT treatment described in §6.2.1. To validate the procedure, we test it using a set of small-volume hydro/RT simulations similar to the ones used to calibrate our sub-grid model. We have run three simulations in 0.512 h^{-1}Mpc boxes with $N = 512^3$ gas/RT cells, each with $\Gamma_{HI} = 3 \times 10^{-13}$, $z_{reion} = 8$, and with the box-scale mean density equal to the cosmic mean. Our simulations have different power law spectra with indices $\alpha = 1.5$ (the value used in our sub-grid simulations), 0.5, and -0.5.

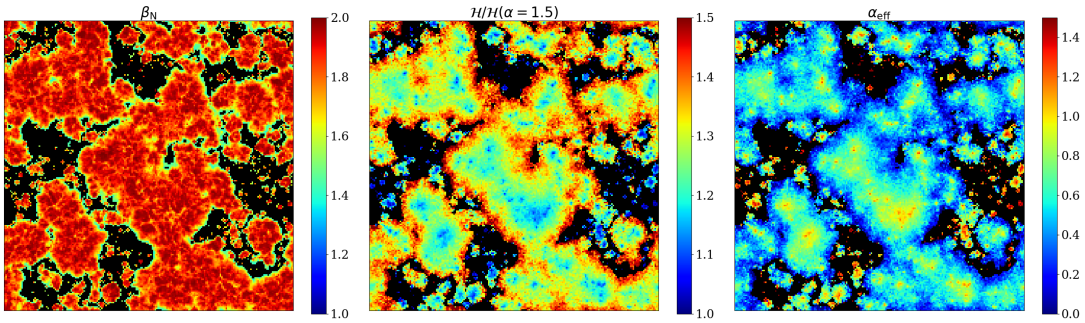

Figure 6.2: Visualization of the effect of IGM filtering at $z = 6$ in one of our reionization models. Left: β_N estimated using Eq. 6.35. We find $\beta_N \approx 1.7 - 1.9$ in most ionized gas, with smaller values (≈ 1.5) close to I-fronts. Middle: ratio of the IGM heating rate with the value expected for an $\alpha = 1.5$ spectrum. IGM heating rates are enhanced by as much as a factor of 1.5 close to ionization fronts, where the effect of IGM filtering is greatest. Right: spectral index ($\alpha_{\rm eff}$) that would reproduce the heating rates shown in the middle panel. We see that $\alpha_{\rm eff}$ can be as small as -0.5 close to ionization fronts.

Figure 6.1 shows the ratio of $\langle\lambda_\nu\rangle_{\rm spec}$ for each case, computed using the $\alpha = 1.5$ simulation results for each case, with the true value measured in the simulation. We find extremely good agreement for $\alpha = 1.5$, suggesting that our approximation of the column density distribution as a power law is a good one. For $\alpha = 0.5$ (-0.5), the reconstructed $\langle\lambda_\nu\rangle_{\rm spec}$ differs from the truth by at most 10% (20%), with the agreement improving significantly $\Delta z = 1$ after the gas is ionized. This disagreement likely owes to differences in the self-shielding properties of the gas in simulations with different α, which are are unable to correct for with our present approach. Given that $\langle\lambda_\nu\rangle_{\rm spec}$ for the $\alpha = 1.5$ and -0.5 simulations are different by almost a factor of 3, this level of agreement is acceptable.

In Figure 6.2, we visualize the effect of IGM filtering in our models on the properties of the IGM at $z = 6$. The left panel shows a slice of β_N, calculated using Eq. 6.35. We

find $\beta_{\rm N} \approx 1.7 - 1.9$ in highly ionized gas, consistent with the findings of [136] [1]. We find lower values ($\beta_{\rm N} \approx 1.5$) in the most recently ionized gas close to I-fronts, consistent with the results of [178]. In the middle panel, we show the enhancement in the IGM heating rate $\mathcal{H}$ relative to the heating rate expected for an $\alpha = 1.5$ spectrum. We see that near ionization fronts, where the effects of IGM filtering are the greatest, $\mathcal{H}$ can be up to a factor of 1.5 higher than it's value close to bright sources where minimal heating has occurred. The right panel shows the results of computing the spectral index in each RT cell - $\alpha_{\rm eff}$ - that would reproduce the heating rates seen in the middle panel. We see that $\alpha_{\rm eff}$ gets very small (≈ -0.5) near the I-fronts, where most of the radiation has traveled a couple mean free paths through the IGM. The average $\alpha_{\rm eff}$ is ~ 0.5, much lower than the value assumed for the sources. These visualizations illustrate the importance of using multi-frequency RT when modeling the Lyα forest.

6.2.2 Recombination Radiation

We have also added an approximate treatment of recombination radiation to our sub-grid model. To do this, we assume all ionized cells are is in photo-ionizational equilibrium and that the effects of self-shielded gas can be ignored, such that the recombination rate can be calculated directly from the MFP[2]. Assuming that a fraction $f_{\rm esc}^{\rm rec}$ of ionizing recombination photons escape from the dense, ionized clumps in which they are produced, the effective recombination coefficient is

$$\alpha(T) = f_{\rm esc}^{\rm rec}\alpha_{\rm A}(T) + (1 - f_{\rm esc}^{\rm rec})\alpha_{\rm B}(T) \tag{6.44}$$

[1] They found $\beta_{\rm N} \approx 1.8$ for optically thin systems.

[2] This is definitely not true in our sub-grid model, since self-shielded neutral regions play a significant role in setting the opacity in recently ionized gas [178]. However, this approximation is likely acceptable for the largely qualitative aims of this work.

Under the assumption of photo-ionizational equilibrium, and ignoring self-shielding systems, $\kappa \propto \alpha(T)$. Since our sub-grid simulations assume the case B recombination coefficient, κ must be re-scaled according to

$$\kappa = \kappa_{\rm B} \frac{\alpha(T)}{\alpha_{\rm B}(T)} \tag{6.45}$$

where $\lambda_{\rm B}$ is the MFP inferred from the sub-grid simulations. The production rate of ionizing recombination photons in cell i is given by

$$\dot{n}_{\gamma}^{\rm rec,i} = x_{\rm ion}^{\rm i} f_{\rm esc}^{\rm rad} \frac{\Gamma_{\rm HI}^{\rm i}}{\langle \sigma_{\rm HI} \rangle_{\nu}} \left(\langle \kappa_{\rm A}^{i} \rangle_{\nu} - \langle \kappa_{\rm B}^{i} \rangle_{\nu} \right) (1 + \chi) \tag{6.46}$$

where $\kappa_{\rm A}$ is the case A ($f_{\rm esc}^{\rm rec} = 1$) absorption coefficient.

The spectrum of ionizing recombination photons is likely softer than that of stellar sources. The energy of a recombination photon is given by

$$E_{\rm rec} = 13.6 \text{ eV} + \frac{1}{2} m_{\rm e} v^2 \tag{6.47}$$

where $m_{\rm p}$ is the electron mass and v is the relative velocity between the recombining electron and proton. The average energy is given by taking $\frac{1}{2} m_{\rm e} v^2 = \frac{3}{2} kT$, where T is the gas temperature. For 10^4 K gas this extra term is 1.3 eV, yielding an average energy of 14.9 eV and an HI cross-section of 4.93×10^{-18} cm^2, much higher than the $\langle \sigma_{\rm HI} \rangle = 2.55 \times 10^{-18}$ cm^2 for an $\alpha = 1.5$ spectrum. In our models which track multi-frequency radiation, we will deposit all recombination photons into the lowest energy bin (14.44 eV).

6.3 Forward-modeling the Lyα forest in RT simulations

6.3.1 Forest Model

Another key recent improvement is that we now model the $5 < z < 6$ Lyα forest using skewers traced through our simulation volume. The mean Lyα forest flux in particular provides the most important empirical anchor for calibrating our simulations.

We have traced 4,000 skewers, each of length 50 h^{-1}Mpc, in random directions and starting at random locations through the hydrodynamic simulation (using periodic boundary conditions). We compute the Lyα transmission along the skewers using the [271] approximation to the Voigt profile. RT cells with ionized fraction $x_{\rm ion} > 0.5$ are taken to be ionized, but we find that the statistical properties of our mock Lyα forests are not sensitive to the particular choice of $x_{\rm ion}$ threshold. The neutral hydrogen densities in the ionized cells are re-scaled under assumption of photoionization equilibrium with the case-A recombination coefficient, which is appropriate for the low-density regions that set the forest transmission at these redshifts. The photoionization rates and temperatures for this re-scaling are taken from the RT grid.

As described in chapters 3 and 5, the IGM temperatures on our RT grid are computed using the model of [135], which is based in part on the model of [272]. We note that the temperatures do not come into play for the RT itself, since the LyC opacities are obtained from the sub-grid model mentioned in the last section. We use the temperatures only for modeling the Lyα forest and for computing the IGM thermal history. We use the flux-based method described in [135] to estimate I-front speeds and then compute $T_{\rm reion}$ using

their equation (3), which assumes an incident spectral index of $\alpha = 1.5$.[3] The subsequent temperature evolution in ionized gas follows equation (6) of [135], with the exception that the equilibrium photo-heating rate is now computed using the discrete 5-bin radiation spectrum in each cell.

We note that the resolution of our hydro simulation ($N_{\rm gas} = 2048^3$) is much higher than that of our RT grid ($N_{\rm rt} = 200^3$). One issue with the approach outlined so far is that is misses the effects of temperature variations on scales smaller than our coarse-grained RT cells, $\Delta x = 1h^{-1}$Mpc. Although a given cell should be nearly isothermal (with temperature $\approx T_{\rm reion}$) shortly after it has been reionized, well after that the densities lower (higher) than the local mean should have lower (higher) temperatures than the value calculated for the RT cell. But the procedure outlined thus far would assign a single temperature to all of the hydro cells intersecting the RT cell. This over-estimate of the temperatures in small-scale under-densities leads to an over-estimate of the forest transmission by $\approx 10 - 15\%$. We correct for this effect by evaluating the analytic solution to the IGM temperature equation of [206] on a grid of (z, $z_{\rm reion}$, Δ) values, where Δ is gas density in units of the cosmic mean. For each z and $z_{\rm reion}$, we evaluate γ by fitting densities with $\Delta < 1$ (the regime that sets the forest transmission) to a power law. We then assign a local value of γ to each RT cell by interpolating in z and $z_{\rm reion}$. Finally, the temperature of each hydro cell is given by

$$T_{\rm hydro} = T_{\rm RT} \left(\frac{\Delta_{\rm hydro}}{\Delta_{\rm RT}} \right)^{\gamma(z, z_{\rm reion})-1}, \tag{6.48}$$

where $T_{\rm RT}$ and $\Delta_{\rm RT}$ are the temperature and density of the coarse-grained RT cell, $\Delta_{\rm hydro}$ is the density along the hydro skewer through the cell, and $\gamma(z, z_{\rm reion})$ represents the slope of

[3] Because [135] found that that $T_{\rm reion}$ is relatively insensitive to the spectral index for $\alpha < 1.5$, we do not take into account the effects of IGM filtering, i.e. decreases in α caused by absorptions in the intervening gas.

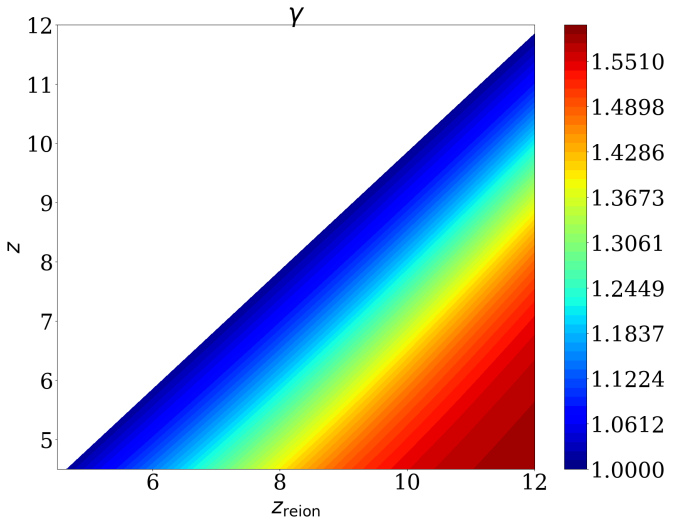

Figure 6.3: Power law index of the temperature-density relation, $\gamma(z, z_{\rm re})$, used to correct for scatter in the temperature-density relation when mapping our coarse-grained RT temperatures onto the high-resolution density grid for our Lyα forest calculations. $\gamma - 1$ approaches it's limiting value of 3/5 when $z << z_{\rm reion}$, while when $z = z_{\rm reion}$, $\gamma - 1 = 0$ (for iso-thermal gas).

the local temperature-density relation. Appendix 6.3.2 discusses this correction in further detail and its effect on the global temperature-density relation.

Finally, it is well known that achieving numerical convergence in large-volume simulations of the high-z Lyα forest is difficult (see e.g.[273, 79]). For Eulerian codes, this difficulty owes to the transmission at $z > 5$ being set by the most under-dense ($\Delta < 0.5$) voids, which become less dense, thus more transmissive, at higher spatial resolution. The appendix of [79] describes a convergence test for the same hydrodynamic simulation used in this work. We apply the correction factors provided in their Table 1A to correct for the resolution effects in our Lyα forest fluxes. These corrections were successfully applied by [79] to obtain forest measurements of $\Gamma_{\rm HI}$.

6.3.2 Correcting for the IGM Temperature-Density Relation

In this section, we provide more details about how we model the temperature-density relation in the IGM in our Lyα forest calculation (see §6.3.1). As discussed there, mismatch between the hydro and RT cell sizes introduces unwanted scatter in the temperature-density relation on scales smaller than the RT cell size. As explained in §6.3.1, we correct for this by constructing a model for the temperature-density power law index γ using the results of [206]. We have fit the [206] solution to a power law at densities $\Delta \leq 1$, which is the range of densities that sets the Lyα forest transmission at these redshifts. Each cell RT cell is then assigned a value of γ based on the the current redshift and the redshift at which the cell was half ionized ($z_{\rm reion}$).

Figure 6.3 shows γ vs. z vs. $z_{\rm reion}$ for $5 < z, z_{\rm reion} < 12$. Note that the upper left corner of the plot is empty because $z \leq z_{\rm reion}$ for a cell to be considered ionized. At $z = z_{\rm reion}$, $\gamma = 1$, consistent with the flat temperature-density relation expected in freshly ionized gas. As we approach $z << z_{\rm reion}$, γ steadily grows towards its asymptotic value of 5/3, expected for gas which has reached approximate thermal equilibrium. Note that the [206] solution includes only photo-heating, cosmic expansion cooling, and Compton cooling. At $\Delta < 1$ other processes, such as recombination cooling, are sub-dominant to these, so this approximation is valid in the regime of interest here.

In Figure 6.4, we show the effect of applying this correction to our $N = 2048^3$ density field. The left panel shows the temperature-density relation for the coarse-grained temperature and density fields from our fiducial RT simulations at $z = 5.2$. At the highest densities, which ionize the earliest, the gas has had ample time to cool and relax to a tight

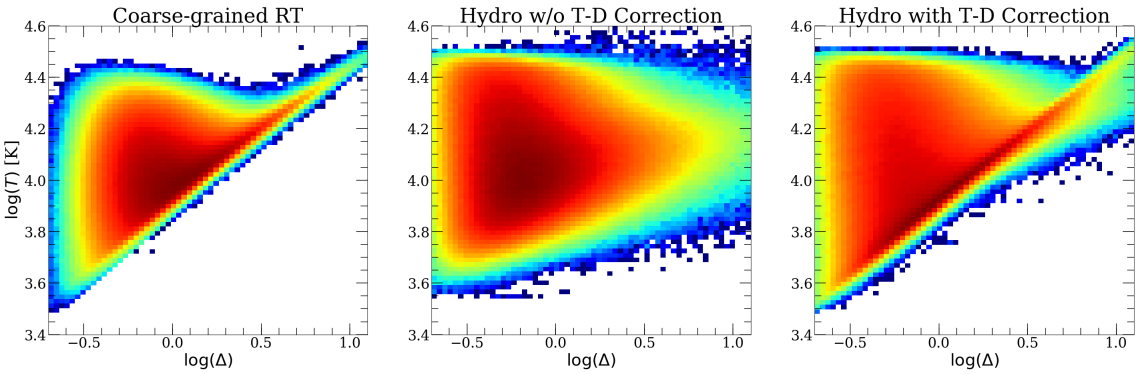

Figure 6.4: The temperature-density relation in our in our Lyα forest calculation before and after the correction described in this section. Left: the T-D relation in our coarse-grained RT simulation for one of our models at $z = 5.6$. Right: T-D relation on the high-resolution density grid using a straight mapping of the coarse-grained RT temperatures. Right: T-D relation on the high-res density grid after applying our correction. We see that this procedure approximately restores the T-D relation seen in the RT simulation itself, albeit with some extra scatter.

power law. At lower densities, the cooling timescales are longer and gas is more likely to have ionized very recently, resulting in large scatter. The middle panel shows this relation after the RT temperatures have been mapped to the high-resolution density field used for the forest calculation. We see that the tight power law at high densities vanishes due density fluctuations below the scale of the RT cell. As the right panel shows, applying our correction approximately recovers the shape seen in the left panel.

Chapter 7

Conclusions

In this thesis, I have made significant progress towards the addressing goals outlined in the introduction. I have shown that the sinks can be modelled accurately with high resolution hydro/RT simulations, and that their dynamics and effects can be accounted for in large-scale reionization simulations. I have developed a modeling framework that includes these effects and have used it to study several existing and forthcoming reionization observables. These studies have yielding a number of interesting and relevant conclusions. Along the way, I have made a number of key improvements to the original modeling framework.

In the future, I plan to continue to develop this framework to include a better subgrid opacity model, faster radiative transfer, and a more realistic treatment of the sources of reionization. In addition to continuing to address key open questions in the field, I intend to develop my modeling framework into a versatile tool for use by the reionization community. With key improvements and optimizations, my radiative transfer code will eventually become fast enough to enable large parameter inference studies that will make

use of a wealth of forthcoming observational data. With improved modeling of reionization's sources, this will lead to competitive constraints on the properties of the first galaxies.

Bibliography

[1] Planck Collaboration, N. Aghanim, Y. Akrami, M. Ashdown, J. Aumont, C. Baccigalupi, M. Ballardini, A. J. Banday, R. B. Barreiro, N. Bartolo, S. Basak, R. Battye, K. Benabed, J. P. Bernard, M. Bersanelli, P. Bielewicz, J. J. Bock, J. R. Bond, J. Borrill, F. R. Bouchet, F. Boulanger, M. Bucher, C. Burigana, R. C. Butler, E. Calabrese, J. F. Cardoso, J. Carron, A. Challinor, H. C. Chiang, J. Chluba, L. P. L. Colombo, C. Combet, D. Contreras, B. P. Crill, F. Cuttaia, P. de Bernardis, G. de Zotti, J. Delabrouille, J. M. Delouis, E. Di Valentino, J. M. Diego, O. Doré, M. Douspis, A. Ducout, X. Dupac, S. Dusini, G. Efstathiou, F. Elsner, T. A. Enßlin, H. K. Eriksen, Y. Fantaye, M. Farhang, J. Fergusson, R. Fernandez-Cobos, F. Finelli, F. Forastieri, M. Frailis, E. Franceschi, A. Frolov, S. Galeotta, S. Galli, K. Ganga, R. T. Génova-Santos, M. Gerbino, T. Ghosh, J. González-Nuevo, K. M. Górski, S. Gratton, A. Gruppuso, J. E. Gudmundsson, J. Hamann, W. Hand ley, D. Herranz, E. Hivon, Z. Huang, A. H. Jaffe, W. C. Jones, A. Karakci, E. Keihänen, R. Keskitalo, K. Kiiveri, J. Kim, T. S. Kisner, L. Knox, N. Krachmalnicoff, M. Kunz, H. Kurki-Suonio, G. Lagache, J. M. Lamarre, A. Lasenby, M. Lattanzi, C. R. Lawrence, M. Le Jeune, P. Lemos, J. Lesgourgues, F. Levrier, A. Lewis, M. Liguori, P. B. Lilje, M. Lilley, V. Lindholm, M. López-Caniego, P. M. Lubin, Y. Z. Ma, J. F. Macías-Pérez, G. Maggio, D. Maino, N. Mandolesi, A. Mangilli, A. Marcos-Caballero, M. Maris, P. G. Martin, M. Martinelli, E. Martínez-González, S. Matarrese, N. Mauri, J. D. McEwen, P. R. Meinhold, A. Melchiorri, A. Mennella, M. Migliaccio, M. Millea, S. Mitra, M. A. Miville-Deschênes, D. Molinari, L. Montier, G. Morgante, A. Moss, P. Natoli, H. U. Nørgaard-Nielsen, L. Pagano, D. Paoletti, B. Partridge, G. Patanchon, H. V. Peiris, F. Perrotta, V. Pettorino, F. Piacentini, L. Polastri, G. Polenta, J. L. Puget, J. P. Rachen, M. Reinecke, M. Remazeilles, A. Renzi, G. Rocha, C. Rosset, G. Roudier, J. A. Rubiño-Martín, B. Ruiz-Granados, L. Salvati, M. Sandri, M. Savelainen, D. Scott, E. P. S. Shellard, C. Sirignano, G. Sirri, L. D. Spencer, R. Sunyaev, A. S. Suur-Uski, J. A. Tauber, D. Tavagnacco, M. Tenti, L. Toffolatti, M. Tomasi, T. Trombetti, L. Valenziano, J. Valiviita, B. Van Tent, L. Vibert, P. Vielva, F. Villa, N. Vittorio, B. D. Wand elt, I. K. Wehus, M. White, S. D. M. White, A. Zacchei, and A. Zonca, "Planck 2018 results. VI. Cosmological parameters," *arXiv e-prints*, p. arXiv:1807.06209, Jul 2018.

[2] B. A. Reid, W. J. Percival, D. J. Eisenstein, L. Verde, D. N. Spergel, R. A. Skibba,

N. A. Bahcall, T. Budavari, J. A. Frieman, M. Fukugita, J. R. Gott, J. E. Gunn, v. Ivezic, G. R. Knapp, R. G. Kron, R. H. Lupton, T. A. McKay, A. Meiksin, R. C. Nichol, A. C. Pope, D. J. Schlegel, D. P. Schneider, C. Stoughton, M. A. Strauss, A. S. Szalay, M. Tegmark, M. S. Vogeley, D. H. Weinberg, D. G. York, and I. Zehavi, "Cosmological constraints from the clustering of the Sloan Digital Sky Survey DR7 luminous red galaxies," *Monthly Notices of the Royal Astronomical Society*, vol. 404, pp. 60–85, 04 2010.

[3] M. A. Troxel, N. MacCrann, J. Zuntz, T. F. Eifler, E. Krause, S. Dodelson, D. Gruen, J. Blazek, O. Friedrich, S. Samuroff, J. Prat, L. F. Secco, C. Davis, A. Ferté, J. DeRose, A. Alarcon, A. Amara, E. Baxter, M. R. Becker, G. M. Bernstein, S. L. Bridle, R. Cawthon, C. Chang, A. Choi, J. De Vicente, A. Drlica-Wagner, J. Elvin-Poole, J. Frieman, M. Gatti, W. G. Hartley, K. Honscheid, B. Hoyle, E. M. Huff, D. Huterer, B. Jain, M. Jarvis, T. Kacprzak, D. Kirk, N. Kokron, C. Krawiec, O. Lahav, A. R. Liddle, J. Peacock, M. M. Rau, A. Refregier, R. P. Rollins, E. Rozo, E. S. Rykoff, C. Sánchez, I. Sevilla-Noarbe, E. Sheldon, A. Stebbins, T. N. Varga, P. Vielzeuf, M. Wang, R. H. Wechsler, B. Yanny, T. M. C. Abbott, F. B. Abdalla, S. Allam, J. Annis, K. Bechtol, A. Benoit-Lévy, E. Bertin, D. Brooks, E. Buckley-Geer, D. L. Burke, A. Carnero Rosell, M. Carrasco Kind, J. Carretero, F. J. Castander, M. Crocce, C. E. Cunha, C. B. D'Andrea, L. N. da Costa, D. L. DePoy, S. Desai, H. T. Diehl, J. P. Dietrich, P. Doel, E. Fernandez, B. Flaugher, P. Fosalba, J. García-Bellido, E. Gaztanaga, D. W. Gerdes, T. Giannantonio, D. A. Goldstein, R. A. Gruendl, J. Gschwend, G. Gutierrez, D. J. James, T. Jeltema, M. W. G. Johnson, M. D. Johnson, S. Kent, K. Kuehn, S. Kuhlmann, N. Kuropatkin, T. S. Li, M. Lima, H. Lin, M. A. G. Maia, M. March, J. L. Marshall, P. Martini, P. Melchior, F. Menanteau, R. Miquel, J. J. Mohr, E. Neilsen, R. C. Nichol, B. Nord, D. Petravick, A. A. Plazas, A. K. Romer, A. Roodman, M. Sako, E. Sanchez, V. Scarpine, R. Schindler, M. Schubnell, M. Smith, R. C. Smith, M. Soares-Santos, F. Sobreira, E. Suchyta, M. E. C. Swanson, G. Tarle, D. Thomas, D. L. Tucker, V. Vikram, A. R. Walker, J. Weller, Y. Zhang, and DES Collaboration, "Dark Energy Survey Year 1 results: Cosmological constraints from cosmic shear," *Phys. Rev. D*, vol. 98, p. 043528, Aug. 2018.

[4] M. Viel, J. Weller, and M. G. Haehnelt, "Constraints on the primordial power spectrum from high-resolution Lyman α forest spectra and WMAP," *Monthly Notices of the Royal Astronomical Society*, vol. 355, pp. L23–L28, Dec. 2004.

[5] S. Chabanier, M. Millea, and N. Palanque-Delabrouille, "Matter power spectrum: from Ly α forest to CMB scales," *Monthly Notices of the Royal Astronomical Society*, vol. 489, pp. 2247–2253, Oct. 2019.

[6] N. Sabti, J. B. Muñoz, and D. Blas, "New Roads to the Small-Scale Universe: Measurements of the Clustering of Matter with the High-Redshift UV Galaxy Luminosity Function," *arXiv e-prints*, p. arXiv:2110.13161, Oct. 2021.

[7] D. Gilman, A. Benson, J. Bovy, S. Birrer, T. Treu, and A. Nierenberg, "The primordial matter power spectrum on sub-galactic scales," *arXiv e-prints*, p. arXiv:2112.03293, Dec. 2021.

[8] V. Iršič, M. Viel, M. G. Haehnelt, J. S. Bolton, S. Cristiani, G. D. Becker, V. D'Odorico, G. Cupani, T.-S. Kim, T. A. M. Berg, S. López, S. Ellison, L. Christensen, K. D. Denney, and G. Worseck, "New constraints on the free-streaming of warm dark matter from intermediate and small scale Lyman-α forest data," *Phys. Rev. D*, vol. 96, p. 023522, July 2017.

[9] V. Iršič, H. Xiao, and M. McQuinn, "Early Structure Formation Constraints on the Ultra-Light Axion in the Post-Inflation Scenario," *arXiv e-prints*, p. arXiv:1911.11150, Nov 2019.

[10] C. Cain, A. D'Aloisio, N. Gangolli, and G. D. Becker, "A Short Mean Free Path at z = 6 Favors Late and Rapid Reionization by Faint Galaxies," *The Astrophysical Journal Letters*, vol. 917, p. L37, Aug. 2021.

[11] A. Mesinger and S. Furlanetto, "Efficient Simulations of Early Structure Formation and Reionization," *The Astrophysical Journal*, vol. 669, pp. 663–675, Nov. 2007.

[12] G. Worseck, J. X. Prochaska, J. M. O'Meara, G. D. Becker, S. L. Ellison, S. Lopez, A. Meiksin, B. Ménard, M. T. Murphy, and M. Fumagalli, "The Giant Gemini GMOS survey of z_{em} ¿ 4.4 quasars - I. Measuring the mean free path across cosmic time," *Monthly Notices of the Royal Astronomical Society*, vol. 445, pp. 1745–1760, Dec. 2014.

[13] G. D. Becker, A. D'Aloisio, H. M. Christenson, Y. Zhu, G. Worseck, and J. S. Bolton, "The mean free path of ionizing photons at 5 ¡ z ¡ 6: evidence for rapid evolution near reionization," *arXiv e-prints*, p. arXiv:2103.16610, Mar. 2021.

[14] S. E. I. Bosman, "Constraints on the mean free path of ionising photons at $z \sim 6$ using limits on individual free paths," *arXiv e-prints*, p. arXiv:2108.12446, Aug. 2021.

[15] I. D. McGreer, A. Mesinger, and V. D'Odorico, "Model-independent evidence in favour of an end to reionization by z $\approx$ 6," *Monthly Notices of the Royal Astronomical Society*, vol. 447, pp. 499–505, Feb. 2015.

[16] B. Greig, A. Mesinger, Z. Haiman, and R. A. Simcoe, "Are we witnessing the epoch of reionization at z=7.1 from the spectrum of J1120+0641?," *Monthly Notices of the Royal Astronomical Society*, vol. 466, pp. 4239–4249, 12 2016.

[17] B. Greig, A. Mesinger, and E. Bañados, "Constraints on reionization from the z = 7.5 QSO ULASJ1342+0928," *Monthly Notices of the Royal Astronomical Society*, vol. 484, pp. 5094–5101, Apr. 2019.

[18] F. B. Davies, J. F. Hennawi, E. Bañados, Z. Lukić, R. Decarli, X. Fan, E. P. Farina, C. Mazzucchelli, H.-W. Rix, B. P. Venemans, F. Walter, F. Wang, and J. Yang, "Quantitative constraints on the reionization history from the IGM damping wing signature in two quasars at z ¿ 7," *The Astrophysical Journal*, vol. 864, p. 142, sep 2018.

[19] C. A. Mason, T. Treu, S. de Barros, M. Dijkstra, A. Fontana, A. Mesinger, L. Pentericci, M. Trenti, and E. Vanzella, "Beacons into the Cosmic Dark Ages: Boosted Transmission of Lyα from UV Bright Galaxies at z ¿ 7," *The Astrophysical Journal Letters*, vol. 857, p. L11, Apr. 2018.

[20] C. A. Mason, A. Fontana, T. Treu, K. B. Schmidt, A. Hoag, L. Abramson, R. Amorin, M. Bradač, L. Guaita, T. Jones, A. Henry, M. A. Malkan, L. Pentericci, M. Trenti, and E. Vanzella, "Inferences on the timeline of reionization at z $\sim$ 8 from the KMOS Lens-Amplified Spectroscopic Survey," *Monthly Notices of the Royal Astronomical Society*, vol. 485, pp. 3947–3969, 03 2019.

[21] F. Wang, F. B. Davies, J. Yang, J. F. Hennawi, X. Fan, A. J. Barth, L. Jiang, X.-B. Wu, D. M. Mudd, E. Bañados, F. Bian, R. Decarli, A.-C. Eilers, E. P. Farina, B. Venemans, F. Walter, and M. Yue, "A Significantly Neutral Intergalactic Medium Around the Luminous z = 7 Quasar J0252-0503," *The Astrophysical Journal*, vol. 896, p. 23, June 2020.

[22] J. Yang, F. Wang, X. Fan, J. F. Hennawi, F. B. Davies, M. Yue, E. Banados, X.-B. Wu, B. Venemans, A. J. Barth, F. Bian, K. Boutsia, R. Decarli, E. P. Farina, R. Green, L. Jiang, J.-T. Li, C. Mazzucchelli, and F. Walter, "Pōniuā'ena: A Luminous z = 7.5 Quasar Hosting a 1.5 Billion Solar Mass Black Hole," *The Astrophysical Journal Letters*, vol. 897, p. L14, July 2020.

[23] B. Greig, A. Mesinger, F. B. Davies, F. Wang, J. Yang, and J. F. Hennawi, "IGM damping wing constraints on reionization from covariance reconstruction of two z ¿ 7 QSOs," *Monthly Notices of the Royal Astronomical Society*, vol. 512, pp. 5390–5403, June 2022.

[24] Y. Zhu, G. D. Becker, S. E. I. Bosman, L. C. Keating, V. D'Odorico, R. L. Davies, H. M. Christenson, E. Bañados, F. Bian, M. Bischetti, H. Chen, F. B. Davies, A.-C. Eilers, X. Fan, P. Gaikwad, B. Greig, M. G. Haehnelt, G. Kulkarni, S. Lai, A. Pallottini, Y. Qin, E. V. Ryan-Weber, F. Walter, F. Wang, and J. Yang, "Long Dark Gaps in the Lyβ Forest at z ¡ 6: Evidence of Ultra-late Reionization from XQR-30 Spectra," *The Astrophysical Journal*, vol. 932, p. 76, June 2022.

[25] L. Y. A. Yung *et al.*, "Semi-analytic forecasts for Roman – the beginning of a new era of deep-wide galaxy surveys," *arXiv e-prints*, p. arXiv:2210.04902, Oct. 2022.

[26] The HERA Collaboration, "Improved Constraints on the 21 cm EoR Power Spectrum and the X-Ray Heating of the IGM with HERA Phase I Observations," *arXiv e-prints*, p. arXiv:2210.04912, Oct. 2022.

[27] Z.-Y. Zheng *et al.*, "First Results from the Lyman Alpha Galaxies in the Epoch of Reionization (LAGER) Survey: Cosmological Reionization at z $\sim$ 7," *The Astrophysical Journal Letters*, vol. 842, p. L22, June 2017.

[28] K. N. Abazajian *et al.*, "CMB-S4 Science Book, First Edition," *arXiv e-prints*, p. arXiv:1610.02743, Oct. 2016.

[29] P. Ade *et al.*, "The Simons Observatory: science goals and forecasts," *Journal of Cosmology and Astroparticle Physics*, vol. 2019, p. 056, Feb. 2019.

[30] S. E. I. Bosman, F. B. Davies, G. D. Becker, L. C. Keating, R. L. Davies, Y. Zhu, A.-C. Eilers, V. D'Odorico, F. Bian, M. Bischetti, S. V. Cristiani, X. Fan, E. P. Farina, M. G. Haehnelt, G. Kulkarni, A. Mesinger, R. A. Meyer, M. Onoue, A. Pallottini, Y. Qin, E. Ryan-Weber, J.-T. Schindler, F. Walter, F. Wang, and J. Yang, "Hydrogen reionisation ends by $z = 5.3$: Lyman-α optical depth measured by the XQR-30 sample," *arXiv e-prints*, p. arXiv:2108.03699, Aug. 2021.

[31] N. Kashikawa, K. Shimasaku, M. A. Malkan, M. Doi, Y. Matsuda, M. Ouchi, Y. Taniguchi, C. Ly, T. Nagao, M. Iye, K. Motohara, T. Murayama, K. Murozono, K. Nariai, K. Ohta, S. Okamura, T. Sasaki, Y. Shioya, and M. Umemura, "The End of the Reionization Epoch Probed by Lyα Emitters at z = 6.5 in the Subaru Deep Field," *The Astrophysical Journal*, vol. 648, pp. 7–22, Sept. 2006.

[32] Y. Ono, M. Ouchi, B. Mobasher, M. Dickinson, K. Penner, K. Shimasaku, B. J. Weiner, J. S. Kartaltepe, K. Nakajima, H. Nayyeri, D. Stern, N. Kashikawa, and H. Spinrad, "SPECTROSCOPIC CONFIRMATION OF THREEz-DROPOUT GALAXIES ATz= 6.844-7.213: DEMOGRAPHICS OF lyα EMISSION INz$\sim$ 7 GALAXIES," *The Astrophysical Journal*, vol. 744, p. 83, dec 2011.

[33] M. A. Schenker, D. P. Stark, R. S. Ellis, B. E. Robertson, J. S. Dunlop, R. J. McLure, J.-P. Kneib, and J. Richard, "Keck Spectroscopy of Faint 3 < z < 8 Lyman Break Galaxies: Evidence for a Declining Fraction of Emission Line Sources in the Redshift Range 6 < z < 8," *The Astrophysical Journal*, vol. 744, p. 179, Jan. 2012.

[34] A. Mesinger, A. Aykutalp, E. Vanzella, L. Pentericci, A. Ferrara, and M. Dijkstra, "Can the intergalactic medium cause a rapid drop in Lyα emission at z > 6?," *Monthly Notices of the Royal Astronomical Society*, vol. 446, pp. 566–577, Jan 2015.

[35] M. Ouchi, Y. Harikane, T. Shibuya, K. Shimasaku, Y. Taniguchi, A. Konno, M. Kobayashi, M. Kajisawa, T. Nagao, Y. Ono, A. K. Inoue, M. Umemura, M. Mori, K. Hasegawa, R. Higuchi, Y. Komiyama, Y. Matsuda, K. Nakajima, T. Saito, and S.-Y. Wang, "Systematic Identification of LAEs for Visible Exploration and Reionization Research Using Subaru HSC (SILVERRUSH). I. Program strategy and clustering properties of $\sim$2000 Lyα emitters at z = 6-7 over the 0.3-0.5 Gpc^2 survey area," *Publications of the Astronomical Society of Japan*, vol. 70, p. S13, Jan. 2018.

[36] X. Fan, M. A. Strauss, R. H. Becker, R. L. White, J. E. Gunn, G. R. Knapp, G. T. Richards, D. P. Schneider, J. Brinkmann, and M. Fukugita, "Constraining the Evolution of the Ionizing Background and the Epoch of Reionization with z˜6 Quasars. II. A Sample of 19 Quasars," *Astronomical Journal*, vol. 132, pp. 117–136, Jul 2006.

[37] D. J. Mortlock, S. J. Warren, B. P. Venemans, M. Patel, P. C. Hewett, R. G. McMahon, C. Simpson, T. Theuns, E. A. Gonzáles-Solares, A. Adamson, S. Dye, N. C. Hambly, P. Hirst, M. J. Irwin, E. Kuiper, A. Lawrence, and H. J. A. Röttgering, "A luminous quasar at a redshift of z = 7.085," *Nature*, vol. 474, pp. 616–619, June 2011.

[38] G. D. Becker, J. S. Bolton, P. Madau, M. Pettini, E. V. Ryan-Weber, and B. P. Venemans, "Evidence of patchy hydrogen reionization from an extreme Lyα trough below redshift six," *Monthly Notices of the Royal Astronomical Society*, vol. 447, pp. 3402–3419, Mar. 2015.

[39] Y. Zhu, G. D. Becker, S. E. I. Bosman, L. C. Keating, H. M. Christenson, E. Bañados, F. Bian, F. B. Davies, V. D'Odorico, A.-C. Eilers, X. Fan, M. G. Haehnelt, G. Kulkarni, A. Pallottini, Y. Qin, F. Wang, and J. Yang, "Chasing the Tail of Cosmic Reionization with Dark Gap Statistics in the Lyα Forest over 5 ¡ z ¡ 6," *The Astrophysical Journal*, vol. 923, p. 223, Dec. 2021.

[40] R. P. Naidu, J. Matthee, P. A. Oesch, C. Conroy, D. Sobral, G. Pezzulli, M. Hayes, D. Erb, R. Amorín, M. Gronke, D. Schaerer, S. Tacchella, J. Kerutt, A. Paulino-Afonso, J. Calhau, M. Llerena, and H. Röttgering, "The synchrony of production and escape: half the bright Lyα emitters at z = 2 have Lyman continuum escape fractions =50," *Monthly Notices of the Royal Astronomical Society*, vol. 510, pp. 4582–4607, Mar. 2022.

[41] N. Leethochawalit *et al.*, "Early results from GLASS-JWST. X: Rest-frame UV-optical properties of galaxies at $7 < z < 9$," *arXiv e-prints*, p. arXiv:2207.11135, July 2022.

[42] S. L. Finkelstein *et al.*, "A Long Time Ago in a Galaxy Far, Far Away: A Candidate z ~12 Galaxy in Early JWST CEERS Imaging," *arXiv e-prints*, p. arXiv:2207.12474, July 2022.

[43] G. Sun *et al.*, "LIMFAST. II. Line Intensity Mapping as a Probe of High-Redshift Galaxy Formation," *arXiv e-prints*, p. arXiv:2206.14186, June 2022.

[44] A. Fasano *et al.*, "CONCERTO: a breakthrough in wide field-of-view spectroscopy at millimeter wavelengths," in *Millimeter, Submillimeter, and Far-Infrared Detectors and Instrumentation for Astronomy XI* (J. Zmuidzinas and J.-R. Gao, eds.), vol. 12190 of *Society of Photo-Optical Instrumentation Engineers (SPIE) Conference Series*, p. 121900Q, Aug. 2022.

[45] G. Mellema, L. V. E. Koopmans, F. A. Abdalla, G. Bernardi, B. Ciardi, S. Daiboo, A. G. de Bruyn, K. K. Datta, H. Falcke, A. Ferrara, I. T. Iliev, F. Iocco, V. Jelić, H. Jensen, R. Joseph, P. Labroupoulos, A. Meiksin, A. Mesinger, A. R. Offringa, V. N. Pandey, J. R. Pritchard, M. G. Santos, D. J. Schwarz, B. Semelin, H. Vedantham, S. Yatawatta, and S. Zaroubi, "Reionization and the Cosmic Dawn with the Square Kilometre Array," *Experimental Astronomy*, vol. 36, pp. 235–318, Aug. 2013.

[46] Z. Abdurashidova, J. E. Aguirre, P. Alexander, Z. S. Ali, Y. Balfour, A. P. Beardsley, G. Bernardi, T. S. Billings, J. D. Bowman, R. F. Bradley, P. Bull, J. Burba, S. Carey, C. L. Carilli, C. Cheng, D. R. DeBoer, M. Dexter, E. de Lera Acedo, T. Dibblee-Barkman, J. S. Dillon, J. Ely, A. Ewall-Wice, N. Fagnoni, R. Fritz, S. R. Furlanetto, K. Gale-Sides, B. Glendenning, D. Gorthi, B. Greig, J. Grobbelaar, Z. Halday, B. J. Hazelton, J. N. Hewitt, J. Hickish, D. C. Jacobs, A. Julius, N. S. Kern,

J. Kerrigan, P. Kittiwisit, S. A. Kohn, M. Kolopanis, A. Lanman, P. La Plante, T. Lekalake, D. Lewis, A. Liu, D. MacMahon, L. Malan, C. Malgas, M. Maree, Z. E. Martinot, E. Matsetela, A. Mesinger, M. Molewa, M. F. Morales, T. Mosiane, S. G. Murray, A. R. Neben, B. Nikolic, C. D. Nunhokee, A. R. Parsons, N. Patra, R. Pascua, S. Pieterse, J. C. Pober, N. Razavi-Ghods, J. Ringuette, J. Robnett, K. Rosie, P. Sims, S. Singh, C. Smith, A. Syce, N. Thyagarajan, P. K. G. Williams, H. Zheng, and HERA Collaboration, "First Results from HERA Phase I: Upper Limits on the Epoch of Reionization 21 cm Power Spectrum," *The Astrophysical Journal*, vol. 925, p. 221, Feb. 2022.

[47] Z. Abdurashidova, J. E. Aguirre, P. Alexander, Z. S. Ali, Y. Balfour, R. Barkana, A. P. Beardsley, G. Bernardi, T. S. Billings, J. D. Bowman, R. F. Bradley, P. Bull, J. Burba, S. Carey, C. L. Carilli, C. Cheng, D. R. DeBoer, M. Dexter, E. de Lera Acedo, J. S. Dillon, J. Ely, A. Ewall-Wice, N. Fagnoni, A. Fialkov, R. Fritz, S. R. Furlanetto, K. Gale-Sides, B. Glendenning, D. Gorthi, B. Greig, J. Grobbelaar, Z. Halday, B. J. Hazelton, S. Heimersheim, J. N. Hewitt, J. Hickish, D. C. Jacobs, A. Julius, N. S. Kern, J. Kerrigan, P. Kittiwisit, S. A. Kohn, M. Kolopanis, A. Lanman, P. La Plante, T. Lekalake, D. Lewis, A. Liu, Y.-Z. Ma, D. MacMahon, L. Malan, C. Malgas, M. Maree, Z. E. Martinot, E. Matsetela, A. Mesinger, J. Mirocha, M. Molewa, M. F. Morales, T. Mosiane, J. B. Muñoz, S. G. Murray, A. R. Neben, B. Nikolic, C. D. Nunhokee, A. R. Parsons, N. Patra, S. Pieterse, J. C. Pober, Y. Qin, N. Razavi-Ghods, I. Reis, J. Ringuette, J. Robnett, K. Rosie, M. G. Santos, S. Sikder, P. Sims, C. Smith, A. Syce, N. Thyagarajan, P. K. G. Williams, and H. Zheng, "HERA Phase I Limits on the Cosmic 21 cm Signal: Constraints on Astrophysics and Cosmology during the Epoch of Reionization," *The Astrophysical Journal*, vol. 924, p. 51, Jan. 2022.

[48] I. D. McGreer, S. Eftekharzadeh, A. D. Myers, and X. Fan, "A Constraint on Quasar Clustering at z = 5 from a Binary Quasar," *Astronomical Journal*, vol. 151, p. 61, Mar. 2016.

[49] S. E. I. Bosman, X. Fan, L. Jiang, S. Reed, Y. Matsuoka, G. Becker, and M. Haehnelt, "New constraints on Lyman-α opacity with a sample of 62 quasarsat $z \geq 5.7$," *Monthly Notices of the Royal Astronomical Society*, vol. 479, pp. 1055–1076, Sept. 2018.

[50] A.-C. Eilers, F. B. Davies, and J. F. Hennawi, "The Opacity of the Intergalactic Medium Measured along Quasar Sightlines at z$\sim$6," *The Astrophysical Journal*, vol. 864, p. 53, Sep 2018.

[51] G. Becker, A. D'Aloisio, F. B. Davies, J. F. Hennawi, and R. A. Simcoe, "Studying the Reionization Epoch with QSO Absorption Lines," *Bulletin of the American Astronomical Society*, vol. 51, p. 440, May 2019.

[52] L. Pentericci, E. Vanzella, A. Fontana, M. Castellano, T. Treu, A. Mesinger, M. Dijkstra, A. Grazian, M. Bradač, C. Conselice, S. Cristiani, J. Dunlop, A. Galametz, M. Giavalisco, E. Giallongo, A. Koekemoer, R. McLure, R. Maiolino, D. Paris, and P. Santini, "NEW OBSERVATIONS OFz$\sim$ 7 GALAXIES: EVIDENCE FOR a PATCHY REIONIZATION," *The Astrophysical Journal*, vol. 793, p. 113, sep 2014.

[53] A. K. Inoue, K. Hasegawa, T. Ishiyama, H. Yajima, I. Shimizu, M. Umemura, A. Konno, Y. Harikane, T. Shibuya, M. Ouchi, K. Shimasaku, Y. Ono, H. Kusakabe, R. Higuchi, and C.-H. Lee, "SILVERRUSH. VI. A simulation of Lyα emitters in the reionization epoch and a comparison with Subaru Hyper Suprime-Cam survey early data," *Publications of the Astronomical Society of Japan*, vol. 70, p. 55, June 2018.

[54] L. H. Weinberger, M. G. Haehnelt, and G. Kulkarni, "Modelling the observed luminosity function and clustering evolution of Lyα emitters: growing evidence for late reionization," *Monthly Notices of the Royal Astronomical Society*, vol. 485, pp. 1350–1366, 02 2019.

[55] S. R. Furlanetto, S. P. Oh, and F. H. Briggs, "Cosmology at low frequencies: The 21 cm transition and the high-redshift Universe," *Physics Reports*, vol. 433, pp. 181–301, Oct. 2006.

[56] D. Tseliakhovich and C. Hirata, "Relative velocity of dark matter and baryonic fluids and the formation of the first structures," *Phys. Rev. D*, vol. 82, p. 083520, Oct 2010.

[57] U. Maio, L. V. E. Koopmans, and B. Ciardi, "The impact of primordial supersonic flows on early structure formation, reionization and the lowest-mass dwarf galaxies," *Monthly Notices of the Royal Astronomical Society: Letters*, vol. 412, pp. L40–L44, 03 2011.

[58] T. H. Greif, S. D. M. White, R. S. Klessen, and V. Springel, "The Delay of Population III Star Formation by Supersonic Streaming Velocities," *Apj*, vol. 736, p. 147, Aug 2011.

[59] A. T. P. Schauer, S. C. O. Glover, R. S. Klessen, and D. Ceverino, "The influence of streaming velocities on the formation of the first stars," *Monthly Notices of the Royal Astronomical Society*, vol. 484, pp. 3510–3521, Apr. 2019.

[60] S. Naoz, N. Yoshida, and N. Y. Gnedin, "Simulations of Early Baryonic Structure Formation with Stream Velocity. I. Halo Abundance," *The Astrophysical Journal*, vol. 747, p. 128, Mar 2012.

[61] T. L. Tanaka and M. Li, "The formation of massive black holes in $z \sim 30$ dark matter haloes with large baryonic streaming velocities," *Monthly Notices of the Royal Astronomical Society*, vol. 439, pp. 1092–1100, Mar 2014.

[62] J. A. Blazek, J. E. McEwen, and C. M. Hirata, "Streaming Velocities and the Baryon Acoustic Oscillation Scale," *Phys. Rev. Lett.*, vol. 116, p. 121303, Mar 2016.

[63] C. M. Hirata, "Small-scale structure and the Lyman-α forest baryon acoustic oscillation feature," *MNRAS*, vol. 474, pp. 2173–2193, Feb 2018.

[64] J. J. Givans and C. M. Hirata, "Redshift-space streaming velocity effects on the Lyman-α forest baryon acoustic oscillation scale," *Phys. Rev. D*, vol. 102, no. 2, p. 023515, 2020.

[65] S. Naoz and R. Narayan, "GLOBULAR CLUSTERS AND DARK SATELLITE GALAXIES THROUGH THE STREAM VELOCITY," *The Astrophysical Journal*, vol. 791, p. L8, jul 2014.

[66] Y. S. Chiou, S. Naoz, B. Burkhart, F. Marinacci, and M. Vogelsberger, "The supersonic project: Shining light on SIGOs—a new formation channel for globular clusters," *The Astrophysical Journal*, vol. 878, p. L23, jun 2019.

[67] N. Dalal, U.-L. Pen, and U. Seljak, "Large-scale BAO signatures of the smallest galaxies," *Journal of Cosmology and Astroparticle Physics*, vol. 2010, p. 007, Nov 2010.

[68] A. Fialkov, R. Barkana, D. Tseliakhovich, and C. M. Hirata, "Impact of the relative motion between the dark matter and baryons on the first stars: semi-analytical modelling," *Monthly Notices of the Royal Astronomical Society*, vol. 424, pp. 1335–1345, Aug 2012.

[69] M. McQuinn and R. M. O'Leary, "THE IMPACT OF THE SUPERSONIC BARYON-DARK MATTER VELOCITY DIFFERENCE ON THEz∼ 20 21 cm BACKGROUND," *The Astrophysical Journal*, vol. 760, p. 3, oct 2012.

[70] Y. Ali-Haimoud, P. D. Meerburg, and S. Yuan, "New light on 21 cm intensity fluctuations from the dark ages," *Phys. Rev. D*, vol. 89, p. 083506, Apr 2014.

[71] A. Cohen, A. Fialkov, and R. Barkana, "The 21-cm BAO signature of enriched low-mass galaxies during cosmic reionization," *Monthly Notices of the Royal Astronomical Society: Letters*, vol. 459, pp. L90–L94, 03 2016.

[72] J. B. Muñoz, "Robust velocity-induced acoustic oscillations at cosmic dawn," *Phys. Rev. D*, vol. 100, p. 063538, Sept. 2019.

[73] R. M. O'Leary and M. McQuinn, "THE FORMATION OF THE FIRST COSMIC STRUCTURES AND THE PHYSICS OF THEz∼ 20 UNIVERSE," *The Astrophysical Journal*, vol. 760, p. 4, oct 2012.

[74] A. D'Aloisio, M. McQuinn, H. Trac, C. Cain, and A. Mesinger, "Hydrodynamic response of the intergalactic medium to reionization," *The Astrophysical Journal*, vol. 898, p. 149, aug 2020.

[75] J. M. Bittner and A. Loeb, "The imprint of the relative velocity between baryons and dark matter on the 21-cm signal from reionization," *arXiv e-prints*, p. arXiv:1110.4659, Oct 2011.

[76] H. Trac and U.-L. Pen, "A moving frame algorithm for high Mach number hydrodynamics," *New Astronomy*, vol. 9, pp. 443–465, July 2004.

[77] H. Trac and R. Cen, "Radiative transfer simulations of cosmic reionization. i. methodology and initial results," *The Astrophysical Journal*, vol. 671, pp. 1–13, dec 2007.

[78] J. Towns, T. Cockerill, M. Dahan, I. Foster, K. Gaither, A. Grimshaw, V. Hazlewood, S. Lathrop, D. Lifka, G. D. Peterson, R. Roskies, J. Scott, and N. Wilkins-Diehr, "Xsede: Accelerating scientific discovery," *Computing in Science & Engineering*, vol. 16, pp. 62–74, sep 2014.

[79] A. D'Aloisio, M. McQuinn, F. B. Davies, and S. R. Furlanetto, "Large fluctuations in the high-redshift metagalactic ionizing background," *Monthly Notices of the Royal Astronomical Society*, vol. 473, pp. 560–575, Jan 2018.

[80] K. Ahn and B. D. Smith, "Formation of First Galaxies inside Density Peaks and Voids under the Influence of Dark Matter-Baryon Streaming Velocity. I. Initial Condition and Simulation Scheme," *The Astrophysical Journal*, vol. 869, p. 76, Dec. 2018.

[81] T. Padmanabhan, *Structure Formation in the Universe, by T. Padmanabhan, pp. 499. ISBN 0521424860. Cambridge, UK: Cambridge University Press, June 1993.* May 1993.

[82] K. Ahn, "How the Density Environment Changes the Influence of the Dark Matter-Baryon Streaming Velocity on Cosmological Structure Formation," *The Astrophysical Journal*, vol. 830, p. 68, Oct. 2016.

[83] D. Tseliakhovich, R. Barkana, and C. M. Hirata, "Suppression and spatial variation of early galaxies and minihaloes," *Monthly Notices of the Royal Astronomical Society*, vol. 418, pp. 906–915, Dec. 2011.

[84] A. Fialkov, "Supersonic relative velocity between dark matter and baryons: A review," *International Journal of Modern Physics D*, vol. 23, p. 1430017, Jul 2014.

[85] J. D. Emberson, R. M. Thomas, and M. A. Alvarez, "THE OPACITY OF THE INTERGALACTIC MEDIUM DURING REIONIZATION: RESOLVING SMALL-SCALE STRUCTURE," *The Astrophysical Journal*, vol. 763, p. 146, jan 2013.

[86] M. McQuinn and A. D'Aloisio, "The observable 21cm signal from reionization may be perturbative," *JCAP*, vol. 2018, p. 016, Oct 2018.

[87] J. R. Pritchard and A. Loeb, "21 cm cosmology in the 21st century," *Reports on Progress in Physics*, vol. 75, p. 086901, jul 2012.

[88] H. Jensen, K. K. Datta, G. Mellema, E. Chapman, F. B. Abdalla, I. T. Iliev, Y. Mao, M. G. Santos, P. R. Shapiro, S. Zaroubi, G. Bernardi, M. A. Brentjens, A. G. de Bruyn, B. Ciardi, G. J. A. Harker, V. Jelić, S. Kazemi, L. V. E. Koopmans, P. Labropoulos, O. Martinez, A. R. Offringa, V. N. Pand ey, J. Schaye, R. M. Thomas, V. Veligatla, H. Vedantham, and S. Yatawatta, "Probing reionization with LOFAR using 21-cm redshift space distortions," *Monthly Notices of the Royal Astronomical Society*, vol. 435, pp. 460–474, Oct. 2013.

[89] H. Jensen, S. Majumdar, G. Mellema, A. Lidz, I. T. Iliev, and K. L. Dixon, "The wedge bias in reionization 21-cm power spectrum measurements," *Monthly Notices of the Royal Astronomical Society*, vol. 456, pp. 66–70, Feb. 2016.

[90] S. A. Wouthuysen, "On the excitation mechanism of the 21-cm (radio-frequency) interstellar hydrogen emission line.," *Astronomical Journal*, vol. 57, pp. 31–32, Jan. 1952.

[91] P. Madau, A. Meiksin, and M. J. Rees, "21 Centimeter Tomography of the Intergalactic Medium at High Redshift," *The Astrophysical Journal*, vol. 475, pp. 429–444, Feb. 1997.

[92] J. R. Pritchard and S. R. Furlanetto, "21-cm fluctuations from inhomogeneous X-ray heating before reionization," *Monthly Notices of the Royal Astronomical Society*, vol. 376, pp. 1680–1694, 03 2007.

[93] S. K. Giri, A. D'Aloisio, G. Mellema, E. Komatsu, R. Ghara, and S. Majumdar, "Position-dependent power spectra of the 21-cm signal from the epoch of reionization," *Journal of Cosmology and Astro-Particle Physics*, vol. 2019, p. 058, Feb 2019.

[94] S. Furlanetto, C. L. Carilli, J. Mirocha, J. Aguirre, Y. Ali-Haimoud, M. Alvarez, A. Beardsley, G. Becker, J. D. Bowman, P. Breysse, V. Bromm, P. Bull, J. Burns, I. P. Carucci, T.-C. Chang, X. Chen, H. Chiang, J. Cohn, F. Davies, D. DeBoer, J. Dillon, O. Doré, C. Dvorkin, A. Fialkov, N. Gnedin, B. Hazelton, D. Jacobs, K. Karkare, S. Kohn, L. Koopmans, E. Kovetz, P. La Plante, A. Lidz, A. Liu, Y.-Z. Ma, Y. Mao, K. Masui, M. McQuinn, A. Mesinger, J. Munoz, S. Murray, A. Parsons, J. Pober, B. Saliwanchik, J. Sievers, E. Switzer, N. Thyagarajan, H. Trac, E. Visbal, and M. Zaldarriaga, "Astro2020 Science White Paper: Insights Into the Epoch of Reionization with the Highly-Redshifted 21-cm Line," *arXiv e-prints*, p. arXiv:1903.06204, Mar 2019.

[95] L. Koopmans, R. Barkana, M. Bentum, G. Bernardi, A.-J. Boonstra, J. Bowman, J. Burns, X. Chen, A. Datta, H. Falcke, A. Fialkov, B. Gehlot, L. Gurvits, V. Jelić, M. Klein-Wolt, L. Koopmans, J. Lazio, D. Meerburg, G. Mellema, F. Mertens, A. Mesinger, A. Offringa, J. Pritchard, B. Semelin, R. Subrahmanyan, J. Silk, C. Trott, H. Vedantham, L. Verde, S. Zaroubi, and P. Zarka, "Peering into the Dark (Ages) with Low-Frequency Space Interferometers," *arXiv e-prints*, p. arXiv:1908.04296, Aug 2019.

[96] A. Parsons, J. E. Aguirre, A. P. Beardsley, G. Bernardi, J. D. Bowman, P. Bull, C. L. Carilli, W.-M. Dai, D. R. DeBoer, J. S. Dillon, A. Ewall-Wice, S. R. Furlanetto, B. K. Gehlot, D. Gorthi, B. Greig, B. J. Hazelton, J. N. Hewitt, D. C. Jacobs, N. S. Kern, P. Kittiwisit, M. Kolopanis, P. La Plante, A. Liu, Y.-Z. Ma, M. Mdlalose, J. Mirocha, S. G. Murray, C. D. Nunhokee, J. C. Pober, P. H. Sims, and N. a. Thyagarajan, "A Roadmap for Astrophysics and Cosmology with High-Redshift 21 cm Intensity Mapping," in *Bulletin of the American Astronomical Society*, vol. 51, p. 241, Sep 2019.

[97] P. Madau, F. Haardt, and M. J. Rees, "Radiative Transfer in a Clumpy Universe. III. The Nature of Cosmological Ionizing Sources," *The Astrophysical Journal*, vol. 514, pp. 648–659, Apr. 1999.

[98] B. Ciardi, F. Stoehr, and S. D. M. White, "Simulating intergalactic medium reionization," *Monthly Notices of the Royal Astronomical Society*, vol. 343, pp. 1101–1109, 08 2003.

[99] S. R. Furlanetto, M. Zaldarriaga, and L. Hernquist, "The Growth of H II Regions During Reionization," *The Astrophysical Journal*, vol. 613, pp. 1–15, Sept. 2004.

[100] A. Mesinger, S. Furlanetto, and R. Cen, "21CMFAST: a fast, seminumerical simulation of the high-redshift 21-cm signal," *Monthly Notices of the Royal Astronomical Society*, vol. 411, pp. 955–972, Feb. 2011.

[101] N. Y. Gnedin, A. V. Kravtsov, and D. H. Rudd, "Implementing the DC Mode in Cosmological Simulations with Supercomoving Variables," *The Astrophysical Journal Supplement*, vol. 194, p. 46, June 2011.

[102] A. Mesinger and S. Furlanetto, "The inhomogeneous ionizing background following reionization," *Monthly Notices of the Royal Astronomical Society*, vol. 400, pp. 1461–1471, 12 2009.

[103] X. Wu, M. McQuinn, R. Kannan, A. D'Aloisio, S. Bird, F. Marinacci, R. Davé, and L. Hernquist, "Imprints of temperature fluctuations on the z $\sim$ 5 Lyman-α forest: a view from radiation-hydrodynamic simulations of reionization," *Monthly Notices of the Royal Astronomical Society*, vol. 490, pp. 3177–3195, 10 2019.

[104] F. Nasir and A. D'Aloisio, "Observing the tail of reionization: neutral islands in the z = 5.5 lyman-α forest," *Monthly Notices of the Royal Astronomical Society*, vol. 494, p. 3080–3094, Apr 2020.

[105] B. E. Robertson, R. S. Ellis, S. R. Furlanetto, and J. S. Dunlop, "Cosmic Reionization and Early Star-forming Galaxies: A Joint Analysis of New Constraints from Planck and the Hubble Space Telescope," *The Astrophysical Journal Letters*, vol. 802, p. L19, Apr 2015.

[106] G. Sun and S. R. Furlanetto, "Constraints on the star formation efficiency of galaxies during the epoch of reionization," *Monthly Notices of the Royal Astronomical Society*, vol. 460, pp. 417–433, July 2016.

[107] R. Barkana and A. Loeb, "In the beginning: the first sources of light and the reionization of the universe," *Physics Reports*, vol. 349, pp. 125–238, July 2001.

[108] R. H. Mebane, J. Mirocha, and S. R. Furlanetto, "The Persistence of Population III Star Formation," *Monthly Notices of the Royal Astronomical Society*, vol. 479, pp. 4544–4559, Oct. 2018.

[109] A. Fialkov, R. Barkana, A. Pinhas, and E. Visbal, "Complete history of the observable 21 cm signal from the first stars during the pre-reionization era," *Monthly Notices of the Royal Astronomical Society*, vol. 437, pp. L36–L40, Jan 2014.

[110] S. R. Furlanetto, J. Mirocha, R. H. Mebane, and G. Sun, "A minimalist feedback-regulated model for galaxy formation during the epoch of reionization," *Monthly Notices of the Royal Astronomical Society*, vol. 472, pp. 1576–1592, Dec. 2017.

[111] E. Visbal, G. L. Bryan, and Z. Haiman, "Self-consistent semianalytic modeling of feedback during primordial star formation and reionization," *The Astrophysical Journal*, vol. 897, p. 95, jul 2020.

[112] H. Trac, R. Cen, and P. Mansfield, "SCORCH I: The Galaxy-Halo Connection in the First Billion Years," *The Astrophysical Journal*, vol. 813, p. 54, Nov 2015.

[113] M. Trenti and M. Stiavelli, "Formation Rates of Population III Stars and Chemical Enrichment of Halos during the Reionization Era," *The Astrophysical Journal*, vol. 694, pp. 879–892, Apr. 2009.

[114] E. Visbal, Z. Haiman, and G. L. Bryan, "Self-consistent semi-analytic models of the first stars," *Monthly Notices of the Royal Astronomical Society*, vol. 475, pp. 5246–5256, Apr. 2018.

[115] A. Fialkov, R. Barkana, and E. Visbal, "The observable signature of late heating of the Universe during cosmic reionization," *Nature*, vol. 506, pp. 197–199, Feb. 2014.

[116] C. A. Watkinson and J. R. Pritchard, "The impact of spin-temperature fluctuations on the 21-cm moments," *Monthly Notices of the Royal Astronomical Society*, vol. 454, pp. 1416–1431, Dec. 2015.

[117] J. C. Pober, Z. S. Ali, A. R. Parsons, M. McQuinn, J. E. Aguirre, G. Bernardi, R. F. Bradley, C. L. Carilli, C. Cheng, D. R. DeBoer, M. R. Dexter, S. R. Furlanetto, J. Grobbelaar, J. Horrell, D. C. Jacobs, P. J. Klima, S. A. Kohn, A. Liu, D. H. E. MacMahon, M. Maree, A. Mesinger, D. F. Moore, N. Razavi-Ghods, I. I. Stefan, W. P. Walbrugh, A. Walker, and H. Zheng, "PAPER-64 Constraints On Reionization. II. The Temperature of the z =8.4 Intergalactic Medium," *The Astrophysical Journal*, vol. 809, p. 62, Aug. 2015.

[118] T. Venumadhav, L. Dai, A. Kaurov, and M. Zaldarriaga, "Heating of the intergalactic medium by the cosmic microwave background during cosmic dawn," *Phys. Rev. D*, vol. 98, p. 103513, Nov. 2018.

[119] R. Ghara and G. Mellema, "Impact of Ly α heating on the global 21-cm signal from the Cosmic Dawn," *Monthly Notices of the Royal Astronomical Society*, vol. 492, pp. 634–644, Feb. 2020.

[120] L. V. E. Koopmans, J. Pritchard, G. Mellema, F. Abdalla, J. Aguirre, K. Ahn, R. Barkana, I. van Bemmel, G. Bernardi, A. Bonaldi, F. Briggs, A. G. de Bruyn, T. C. Chang, E. Chapman, X. Chen, B. Ciardi, K. K. Datta, P. Dayal, A. Ferrara, A. Fialkov, F. Fiore, K. Ichiki, I. T. Illiev, S. Inoue, V. Jelić, M. Jones, J. Lazio, U. Maio, S. Majumdar, K. J. Mack, A. Mesinger, M. F. Morales, A. Parsons, U. L. Pen, M. Santos, R. Schneider, B. Semelin, R. S. de Souza, R. Subrahmanyan, T. Takeuchi,

C. Trott, H. Vedantham, J. Wagg, R. Webster, and S. Wyithe, "The cosmic dawn and epoch of reionization with the square kilometre array," Apr 2015.

[121] D. R. DeBoer, A. R. Parsons, J. E. Aguirre, P. Alexander, Z. S. Ali, A. P. Beardsley, G. Bernardi, J. D. Bowman, R. F. Bradley, C. L. Carilli, C. Cheng, E. de Lera Acedo, J. S. Dillon, A. Ewall-Wice, G. Fadana, N. Fagnoni, R. Fritz, S. R. Furlanetto, B. Glendenning, B. Greig, J. Grobbelaar, B. J. Hazelton, J. N. Hewitt, J. Hickish, D. C. Jacobs, A. Julius, M. Kariseb, S. A. Kohn, T. Lekalake, A. Liu, A. Loots, D. MacMahon, L. Malan, C. Malgas, M. Maree, Z. Martinot, N. Mathison, E. Matsetela, A. Mesinger, M. F. Morales, A. R. Neben, N. Patra, S. Pieterse, J. C. Pober, N. Razavi-Ghods, J. Ringuette, J. Robnett, K. Rosie, R. Sell, C. Smith, A. Syce, M. Tegmark, N. Thyagarajan, P. K. G. Williams, and H. Zheng, "Hydrogen Epoch of Reionization Array (HERA)," *Publications of the Astronomical Society of the Pacific*, vol. 129, p. 045001, Apr 2017.

[122] C. M. Trott and J. C. Pober, "The status of 21cm interferometric experiments," *arXiv e-prints*, p. arXiv:1909.12491, Sep 2019.

[123] B. Greig, A. Mesinger, and L. V. E. Koopmans, "Reionization and cosmic dawn astrophysics from the Square Kilometre Array: impact of observing strategies," *Monthly Notices of the Royal Astronomical Society*, vol. 491, pp. 1398–1407, Jan. 2020.

[124] A. E. Lanman, J. C. Pober, N. S. Kern, E. de Lera Acedo, D. R. DeBoer, and N. Fagnoni, "Quantifying eor delay spectrum contamination from diffuse radio emission," *Monthly Notices of the Royal Astronomical Society*, vol. 494, p. 3712–3727, Apr 2020.

[125] F. Schmidt, "Effect of relative velocity and density perturbations between baryons and dark matter on the clustering of galaxies," *Phys. Rev. D*, vol. 94, p. 063508, Sept. 2016.

[126] G. Kulkarni, L. C. Keating, M. G. Haehnelt, S. E. I. Bosman, E. Puchwein, J. Chardin, and D. Aubert, "Large Ly α opacity fluctuations and low CMB τ in models of late reionization with large islands of neutral hydrogen extending to z $<$ 5.5," *Monthly Notices of the Royal Astronomical Society*, vol. 485, pp. L24–L28, May 2019.

[127] L. C. Keating, L. H. Weinberger, G. Kulkarni, M. G. Haehnelt, J. Chardin, and D. Aubert, "Long troughs in the Lyman-α forest below redshift 6 due to islands of neutral hydrogen," *Monthly Notices of the Royal Astronomical Society*, vol. 491, pp. 1736–1745, Jan. 2020.

[128] Y. Qin, A. Mesinger, S. E. I. Bosman, and M. Viel, "Reionization and galaxy inference from the high-redshift Lyα forest," *Monthly Notices of the Royal Astronomical Society*, vol. 506, pp. 2390–2407, 06 2021.

[129] S. L. Finkelstein, A. D'Aloisio, J.-P. Paardekooper, J. Ryan, Russell, P. Behroozi, K. Finlator, R. Livermore, P. R. Upton Sanderbeck, C. Dalla Vecchia, and S. Khochfar, "Conditions for Reionizing the Universe with a Low Galaxy Ionizing Photon Escape Fraction," *The Astrophysical Journal*, vol. 879, p. 36, July 2019.

[130] L. C. Keating, G. Kulkarni, M. G. Haehnelt, J. Chardin, and D. Aubert, "Constraining the second half of reionization with the Ly β forest," *Monthly Notices of the Royal Astronomical Society*, vol. 497, pp. 906–915, Sept. 2020.

[131] H. Park, P. R. Shapiro, J.-h. Choi, N. Yoshida, S. Hirano, and K. Ahn, "The Hydrodynamic Feedback of Cosmic Reionization on Small-scale Structures and Its Impact on Photon Consumption During the Epoch of Reionization," *ApJ*, vol. 831, p. 86, Nov 2016.

[132] I. T. Iliev, G. Mellema, K. Ahn, P. R. Shapiro, Y. Mao, and U.-L. Pen, "Simulating cosmic reionization: how large a volume is large enough?," *Monthly Notices of the Royal Astronomical Society*, vol. 439, pp. 725–743, Mar. 2014.

[133] X. Wu, M. McQuinn, and D. Eisenstein, "On the accuracy of common moment-based radiative transfer methods for simulating reionization," *Journal of Cosmology and Astroparticle Physics*, vol. 2021, p. 042, Feb. 2021.

[134] T. Abel and B. D. Wandelt, "Adaptive ray tracing for radiative transfer around point sources," *Monthly Notices of the Royal Astronomical Society*, vol. 330, pp. L53–L56, Mar. 2002.

[135] A. D'Aloisio, M. McQuinn, O. Maupin, F. B. Davies, H. Trac, S. Fuller, and P. R. Upton Sanderbeck, "Heating of the Intergalactic Medium by Hydrogen Reionization," *The Astrophysical Journal*, vol. 874, p. 154, Apr. 2019.

[136] M. McQuinn, S. P. Oh, and C.-A. Faucher-Giguère, "ON LYMAN-LIMIT SYSTEMS AND THE EVOLUTION OF THE INTERGALACTIC IONIZING BACKGROUND," *The Astrophysical Journal*, vol. 743, p. 82, nov 2011.

[137] K. Ahn, I. T. Iliev, P. R. Shapiro, and C. Srisawat, "Non-linear bias of cosmological halo formation in the early universe," *Monthly Notices of the Royal Astronomical Society*, vol. 450, pp. 1486–1502, June 2015.

[138] G. D. Becker and J. S. Bolton, "New measurements of the ionizing ultraviolet background over 2 ¡ z ¡ 5 and implications for hydrogen reionization," *Monthly Notices of the Royal Astronomical Society*, vol. 436, pp. 1023–1039, Dec. 2013.

[139] G. D. Becker, J. S. Bolton, M. G. Haehnelt, and W. L. W. Sargent, "Detection of extended He II reionization in the temperature evolution of the intergalactic medium," *Monthly Notices of the Royal Astronomical Society*, vol. 410, pp. 1096–1112, Jan. 2011.

[140] M. Walther, J. Oñorbe, J. F. Hennawi, and Z. Lukić, "New Constraints on IGM Thermal Evolution from the Lyα Forest Power Spectrum," *The Astrophysical Journal*, vol. 872, p. 13, Feb. 2019.

[141] E. Boera, G. D. Becker, J. S. Bolton, and F. Nasir, "Revealing Reionization with the Thermal History of the Intergalactic Medium: New Constraints from the Lyα Flux Power Spectrum," *The Astrophysical Journal*, vol. 872, p. 101, Feb. 2019.

[142] P. Gaikwad, M. Rauch, M. G. Haehnelt, E. Puchwein, J. S. Bolton, L. C. Keating, G. Kulkarni, V. Iršič, E. Bañados, G. D. Becker, E. Boera, F. S. Zahedy, H.-W. Chen, R. F. Carswell, J. Chardin, and A. Rorai, "Probing the thermal state of the intergalactic medium at z ¿ 5 with the transmission spikes in high-resolution Ly α forest spectra," *Monthly Notices of the Royal Astronomical Society*, vol. 494, pp. 5091–5109, June 2020.

[143] J. X. Prochaska, G. Worseck, and J. M. O'Meara, "A Direct Measurement of the Intergalactic Medium Opacity to H I Ionizing Photons," *The Astrophysical Journal Letters*, vol. 705, pp. L113–L117, Nov. 2009.

[144] P. Ocvirk, J. S. W. Lewis, N. Gillet, J. Chardin, D. Aubert, N. Deparis, and E. Thelie, "Lyman-alpha opacities at z=4-6 require low mass, radiatively-suppressed galaxies to drive cosmic reionization," *arXiv e-prints*, p. arXiv:2105.01663, May 2021.

[145] F. B. Davies, S. E. I. Bosman, S. R. Furlanetto, G. D. Becker, and A. D'Aloisio, "The Predicament of Absorption-Dominated Reionization: Increased Demands on Ionizing Sources," *arXiv e-prints*, p. arXiv:2105.10518, May 2021.

[146] R. J. Bouwens, R. Smit, I. Labbé, M. Franx, J. Caruana, P. Oesch, M. Stefanon, and N. Rasappu, "The Lyman-Continuum Photon Production Efficiency ξ_{ion} of z ˜ 4-5 Galaxies from IRAC-based Hα Measurements: Implications for the Escape Fraction and Cosmic Reionization," *The Astrophysical Journal*, vol. 831, p. 176, Nov. 2016.

[147] D. P. Stark, R. S. Ellis, S. Charlot, J. Chevallard, M. Tang, S. Belli, A. Zitrin, R. Mainali, J. Gutkin, A. Vidal-García, R. Bouwens, and P. Oesch, "Lyα and C III] emission in z = 7-9 Galaxies: accelerated reionization around luminous star-forming systems?," *Monthly Notices of the Royal Astronomical Society*, vol. 464, pp. 469–479, Jan. 2017.

[148] R. Endsley, D. P. Stark, S. Charlot, J. Chevallard, B. Robertson, R. J. Bouwens, and M. Stefanon, "MMT spectroscopy of Lyman-alpha at z = 7: evidence for accelerated reionization around massive galaxies," *Monthly Notices of the Royal Astronomical Society*, vol. 502, pp. 6044–6063, Apr. 2021.

[149] M. Castellano, L. Pentericci, E. Vanzella, F. Marchi, A. Fontana, P. Dayal, A. Ferrara, A. Hutter, S. Carniani, S. Cristiani, M. Dickinson, S. Gallerani, E. Giallongo, M. Giavalisco, A. Grazian, R. Maiolino, E. Merlin, D. Paris, S. Pilo, and P. Santini, "Spectroscopic Investigation of a Reionized Galaxy Overdensity at z = 7," *The Astrophysical Journal Letters*, vol. 863, p. L3, Aug. 2018.

[150] V. Tilvi, S. Malhotra, J. E. Rhoads, A. Coughlin, Z. Zheng, S. L. Finkelstein, S. Veilleux, B. Mobasher, J. Wang, R. Probst, R. Swaters, P. Hibon, B. Joshi, J. Zabl, T. Jiang, J. Pharo, and H. Yang, "Onset of Cosmic Reionization: Evidence of an Ionized Bubble Merely 680 Myr after the Big Bang," *The Astrophysical Journal Letters*, vol. 891, p. L10, Mar. 2020.

[151] A. Loeb and M. Zaldarriaga, "Small-scale power spectrum of cold dark matter," *Phys. Rev. D*, vol. 71, p. 103520, May 2005.

[152] S. Profumo, K. Sigurdson, and M. Kamionkowski, "What Mass Are the Smallest Protohalos?," *Phys. Rev. Lett.*, vol. 97, p. 031301, July 2006.

[153] E. Bertschinger, "Effects of cold dark matter decoupling and pair annihilation on cosmological perturbations," *Phys. Rev. D*, vol. 74, p. 063509, Sept. 2006.

[154] J. Diemand, M. Kuhlen, and P. Madau, "Early Supersymmetric Cold Dark Matter Substructure," *The Astrophysical Journal*, vol. 649, pp. 1–13, Sept. 2006.

[155] M. Viel, G. D. Becker, J. S. Bolton, and M. G. Haehnelt, "Warm dark matter as a solution to the small scale crisis: New constraints from high redshift Lyman-α forest data," *Phys. Rev. D*, vol. 88, p. 043502, Aug. 2013.

[156] N. Palanque-Delabrouille, C. Yèche, A. Borde, J.-M. Le Goff, G. Rossi, M. Viel, É. Aubourg, S. Bailey, J. Bautista, M. Blomqvist, A. Bolton, J. S. Bolton, N. G. Busca, B. Carithers, R. A. C. Croft, K. S. Dawson, T. Delubac, A. Font-Ribera, S. Ho, D. Kirkby, K.-G. Lee, D. Margala, J. Miralda-Escudé, D. Muna, A. D. Myers, P. Noterdaeme, I. Pâris, P. Petitjean, M. M. Pieri, J. Rich, E. Rollinde, N. P. Ross, D. J. Schlegel, D. P. Schneider, A. Slosar, and D. H. Weinberg, "The one-dimensional Lyα forest power spectrum from BOSS," *Astronomy & Astrophysics*, vol. 559, p. A85, Nov. 2013.

[157] V. Iršič, M. Viel, M. G. Haehnelt, J. S. Bolton, and G. D. Becker, "First Constraints on Fuzzy Dark Matter from Lyman-α Forest Data and Hydrodynamical Simulations," *Phys. Rev. Lett.*, vol. 119, p. 031302, July 2017.

[158] J. Baur, N. Palanque-Delabrouille, C. Yèche, A. Boyarsky, O. Ruchayskiy, É. Armengaud, and J. Lesgourgues, "Constraints from Ly-α forests on non-thermal dark matter including resonantly-produced sterile neutrinos," *Journal of Cosmology and Astroparticle Physics*, vol. 2017, p. 013, Dec. 2017.

[159] R. Murgia, V. Iršič, and M. Viel, "Novel constraints on noncold, nonthermal dark matter from Lyman-α forest data," *Phys. Rev. D*, vol. 98, p. 083540, Oct. 2018.

[160] D. Gilman, S. Birrer, T. Treu, A. Nierenberg, and A. Benson, "Probing dark matter structure down to 10^7 solar masses: flux ratio statistics in gravitational lenses with line-of-sight haloes," *Monthly Notices of the Royal Astronomical Society*, vol. 487, pp. 5721–5738, Aug. 2019.

[161] Q. He, R. Li, C. S. Frenk, J. Nightingale, S. Cole, N. C. Amorisco, R. Massey, A. Robertson, A. Etherington, A. Amvrosiadis, and X. Cao, "Galaxy-galaxy strong lens perturbations: line-of-sight haloes versus lens subhaloes," *Monthly Notices of the Royal Astronomical Society*, vol. 512, pp. 5862–5873, June 2022.

[162] J. H. Wise, V. G. Demchenko, M. T. Halicek, M. L. Norman, M. J. Turk, T. Abel, and B. D. Smith, "The birth of a galaxy - III. Propelling reionization with the faintest galaxies," *Monthly Notices of the Royal Astronomical Society*, vol. 442, pp. 2560–2579, Aug. 2014.

[163] M. L. Norman, P. Chen, J. H. Wise, and H. Xu, "Fully Coupled Simulation of Cosmic Reionization. III. Stochastic Early Reionization by the Smallest Galaxies," *The Astrophysical Journal*, vol. 867, p. 27, Nov. 2018.

[164] P. R. Shapiro, M. L. Giroux, and A. Babul, "Reionization in a Cold Dark Matter Universe: The Feedback of Galaxy Formation on the Intergalactic Medium," *The Astrophysical Journal*, vol. 427, p. 25, May 1994.

[165] A. A. Thoul and D. H. Weinberg, "Hydrodynamic Simulations of Galaxy Formation. II. Photoionization and the Formation of Low-Mass Galaxies," *The Astrophysical Journal*, vol. 465, p. 608, July 1996.

[166] M. Hoeft, G. Yepes, S. Gottlöber, and V. Springel, "Dwarf galaxies in voids: suppressing star formation with photoheating," *Monthly Notices of the Royal Astronomical Society*, vol. 371, pp. 401–414, Sept. 2006.

[167] T. Okamoto, L. Gao, and T. Theuns, "Mass loss of galaxies due to an ultraviolet background," *Monthly Notices of the Royal Astronomical Society*, vol. 390, pp. 920–928, Nov. 2008.

[168] E. Sobacchi and A. Mesinger, "The depletion of gas in high-redshift dwarf galaxies from an inhomogeneous reionization.," *Monthly Notices of the Royal Astronomical Society*, vol. 432, pp. L51–L55, May 2013.

[169] Y. Noh and M. McQuinn, "A physical understanding of how reionization suppresses accretion on to dwarf haloes," *Monthly Notices of the Royal Astronomical Society*, vol. 444, pp. 503–514, Oct. 2014.

[170] F. C. van den Bosch, G. Ogiya, O. Hahn, and A. Burkert, "Disruption of dark matter substructure: fact or fiction?," *Monthly Notices of the Royal Astronomical Society*, vol. 474, pp. 3043–3066, Mar. 2018.

[171] T. E. Collett, "The Population of Galaxy-Galaxy Strong Lenses in Forthcoming Optical Imaging Surveys," *The Astrophysical Journal*, vol. 811, p. 20, Sept. 2015.

[172] E. Ripamonti, M. Mapelli, and S. Zaroubi, "Radiation from early black holes - I. Effects on the neutral intergalactic medium," *Monthly Notices of the Royal Astronomical Society*, vol. 387, pp. 158–172, June 2008.

[173] M. Jeon, A. H. Pawlik, V. Bromm, and M. Milosavljević, "Radiative feedback from high-mass X-ray binaries on the formation of the first galaxies and early reionization," *Monthly Notices of the Royal Astronomical Society*, vol. 440, pp. 3778–3796, June 2014.

[174] P. R. Shapiro, I. T. Iliev, and A. C. Raga, "Photoevaporation of cosmological minihaloes during reionization," *Monthly Notices of the Royal Astronomical Society*, vol. 348, pp. 753–782, 03 2004.

[175] I. T. Iliev, P. R. Shapiro, and A. C. Raga, "Minihalo photoevaporation during cosmic reionization: evaporation times and photon consumption rates," *Monthly Notices of the Royal Astronomical Society*, vol. 361, pp. 405–414, 08 2005.

[176] I. T. Iliev, E. Scannapieco, and P. R. Shapiro, "The Impact of Small-Scale Structure on Cosmological Ionization Fronts and Reionization," *The Astrophysical Journal*, vol. 624, pp. 491–504, May 2005.

[177] M. McQuinn, A. Lidz, O. Zahn, S. Dutta, L. Hernquist, and M. Zaldarriaga, "The morphology of HII regions during reionization," *Monthly Notices of the Royal Astronomical Society*, vol. 377, pp. 1043–1063, May 2007.

[178] F. Nasir, C. Cain, A. D'Aloisio, N. Gangolli, and M. McQuinn, "Hydrodynamic Response of the Intergalactic Medium to Reionization. II. Physical Characteristics and Dynamics of Ionizing Photon Sinks," *The Astrophysical Journal*, vol. 923, p. 161, Dec. 2021.

[179] J. Preskill, M. B. Wise, and F. Wilczek, "Cosmology of the invisible axion," *Physics Letters B*, vol. 120, pp. 127–132, Jan. 1983.

[180] G. Efstathiou and J. R. Bond, "Isocurvature cold dark matter fluctuations," *Monthly Notices of the Royal Astronomical Society*, vol. 218, pp. 103–121, 01 1986.

[181] C. Hogan and M. Rees, "Axion miniclusters," *Physics Letters B*, vol. 205, no. 2, pp. 228–230, 1988.

[182] L. Dai and J. Miralda-Escudé, "Gravitational Lensing Signatures of Axion Dark Matter Minihalos in Highly Magnified Stars," *The Astrophysical Journal*, vol. 159, p. 49, Feb. 2020.

[183] H. Xiao, I. Williams, and M. McQuinn, "Simulations of axion minihalos," *Phys. Rev. D*, vol. 104, p. 023515, July 2021.

[184] N. Afshordi, P. McDonald, and D. N. Spergel, "Primordial Black Holes as Dark Matter: The Power Spectrum and Evaporation of Early Structures," *The Astrophysical Journal Letters*, vol. 594, pp. L71–L74, Sept. 2003.

[185] P. H. Frampton, M. Kawasaki, F. Takahashi, and T. T. Yanagida, "Primordial black holes as all dark matter," *Journal of Cosmology and Astroparticle Physics*, vol. 2010, p. 023, Apr. 2010.

[186] K. M. Belotsky, A. E. Dmitriev, E. A. Esipova, V. A. Gani, A. V. Grobov, M. Y. Khlopov, A. A. Kirillov, S. G. Rubin, and I. V. Svadkovsky, "Signatures of primordial black hole dark matter," *Modern Physics Letters A*, vol. 29, p. 1440005, Nov. 2014.

[187] S. Bird, I. Cholis, J. B. Muñoz, Y. Ali-Haïmoud, M. Kamionkowski, E. D. Kovetz, A. Raccanelli, and A. G. Riess, "Did LIGO Detect Dark Matter?," *Phys. Rev. Lett.*, vol. 116, p. 201301, May 2016.

[188] S. Clesse and J. García-Bellido, "The clustering of massive Primordial Black Holes as Dark Matter: Measuring their mass distribution with advanced LIGO," *Physics of the Dark Universe*, vol. 15, pp. 142–147, Mar. 2017.

[189] A. Lewis, A. Challinor, and A. Lasenby, "Efficient Computation of Cosmic Microwave Background Anisotropies in Closed Friedmann-Robertson-Walker Models," *The Astrophysical Journal*, vol. 538, pp. 473–476, Aug 2000.

[190] P. Bode, J. P. Ostriker, and N. Turok, "Halo Formation in Warm Dark Matter Models," *The Astrophysical Journal*, vol. 556, pp. 93–107, July 2001.

[191] M. Viel, J. Lesgourgues, M. G. Haehnelt, S. Matarrese, and A. Riotto, "Constraining warm dark matter candidates including sterile neutrinos and light gravitinos with WMAP and the Lyman-α forest," *Phys. Rev. D*, vol. 71, p. 063534, Mar. 2005.

[192] A. Rahmati, A. H. Pawlik, M. Raičević, and J. Schaye, "On the evolution of the H I column density distribution in cosmological simulations," *Monthly Notices of the Royal Astronomical Society*, vol. 430, pp. 2427–2445, Apr. 2013.

[193] J. Chardin, M. G. Haehnelt, D. Aubert, and E. Puchwein, "Calibrating cosmological radiative transfer simulations with Lyα forest data: evidence for large spatial UV background fluctuations at z $\sim$ 5.6-5.8 due to rare bright sources," *Monthly Notices of the Royal Astronomical Society*, vol. 453, pp. 2943–2964, Nov. 2015.

[194] J. Miralda-Escudé and M. J. Rees, "Reionization and thermal evolution of a photoionized intergalactic medium.," *Monthly Notices of the Royal Astronomical Society*, vol. 266, pp. 343–352, Jan. 1994.

[195] C. Zeng and C. M. Hirata, "Nonequilibrium Temperature Evolution of Ionization Fronts during the Epoch of Reionization," *The Astrophysical Journal*, vol. 906, p. 124, Jan. 2021.

[196] H. J. Mo and S. D. M. White, "An analytic model for the spatial clustering of dark matter haloes," *Monthly Notices of the Royal Astronomical Society*, vol. 282, pp. 347–361, Sept. 1996.

[197] F. B. Davies and S. R. Furlanetto, "Large fluctuations in the hydrogen-ionizing background and mean free path following the epoch of reionization," *Monthly Notices of the Royal Astronomical Society*, vol. 460, pp. 1328–1339, Aug 2016.

[198] Y. Feng, S. Bird, L. Anderson, A. Font-Ribera, and C. Pedersen, "Mp-gadget/mp-gadget: A tag for getting a doi," Oct. 2018.

[199] W. A. Watson, I. T. Iliev, A. D'Aloisio, A. Knebe, P. R. Shapiro, and G. Yepes, "The halo mass function through the cosmic ages," *Monthly Notices of the Royal Astronomical Society*, vol. 433, pp. 1230–1245, Aug. 2013.

[200] P. Villanueva-Domingo, N. Y. Gnedin, and O. Mena, "Warm Dark Matter and Cosmic Reionization," *The Astrophysical Journal*, vol. 852, p. 139, Jan. 2018.

[201] I. P. Carucci and P.-S. Corasaniti, "Cosmic reionization history and dark matter scenarios," *Phys. Rev. D*, vol. 99, p. 023518, Jan. 2019.

[202] M. Romanello, N. Menci, and M. Castellano, "The Epoch of Reionization in Warm Dark Matter Scenarios," *Universe*, vol. 7, p. 365, Sept. 2021.

[203] S. K. Giri, G. Mellema, and R. Ghara, "Optimal identification of H II regions during reionization in 21-cm observations," *Monthly Notices of the Royal Astronomical Society*, vol. 479, pp. 5596–5611, Oct. 2018.

[204] P.-J. Wu, Y. Xu, X. Zhang, and X. Chen, "Effects of Small-scale Absorption Systems on Neutral Islands during the Late Epoch of Reionization," *The Astrophysical Journal*, vol. 927, p. 5, Mar. 2022.

[205] A. Mesinger, "Was reionization complete by z ~5-6?," *Monthly Notices of the Royal Astronomical Society*, vol. 407, pp. 1328–1337, Sept. 2010.

[206] M. McQuinn and P. R. Upton Sanderbeck, "On the intergalactic temperature-density relation," *Monthly Notices of the Royal Astronomical Society*, vol. 456, pp. 47–54, Feb. 2016.

[207] E. Garaldi, R. Kannan, A. Smith, V. Springel, R. Pakmor, M. Vogelsberger, and L. Hernquist, "The THESAN project: properties of the intergalactic medium and its connection to reionization-era galaxies," *Monthly Notices of the Royal Astronomical Society*, vol. 512, pp. 4909–4933, June 2022.

[208] J. S. W. Lewis, P. Ocvirk, J. G. Sorce, Y. Dubois, D. Aubert, L. Conaboy, P. R. Shapiro, T. Dawoodbhoy, R. Teyssier, G. Yepes, S. Gottlöber, Y. Rasera, K. Ahn, I. T. Iliev, H. Park, and É. Thélie, "The short ionizing photon mean free path at z=6 in Cosmic Dawn III, a new fully-coupled radiation-hydrodynamical simulation of the Epoch of Reionization," *arXiv e-prints*, p. arXiv:2202.05869, Feb. 2022.

[209] J. Tinker, A. V. Kravtsov, A. Klypin, K. Abazajian, M. Warren, G. Yepes, S. Gottlöber, and D. E. Holz, "Toward a Halo Mass Function for Precision Cosmology: The Limits of Universality," *The Astrophysical Journal*, vol. 688, pp. 709–728, Dec. 2008.

[210] W. Hu, J. Wang, Z.-Y. Zheng, S. Malhotra, J. E. Rhoads, L. Infante, L. F. Barrientos, H. Yang, C. Jiang, W. Kang, L. A. Perez, I. Wold, P. Hibon, L. Jiang, A. A. Khostovan, F. Valdes, A. R. Walker, G. Galaz, A. Coughlin, S. Harish, X. Kong, J. Pharo, and X. Zheng, "The Lyα Luminosity Function and Cosmic Reionization at z $\sim$ 7.0: A Tale of Two LAGER Fields," *The Astrophysical Journal*, vol. 886, p. 90, Dec. 2019.

[211] Y. Qin, A. Mesinger, S. E. I. Bosman, and M. Viel, "Reionization and galaxy inference from the high-redshift Ly α forest," *Monthly Notices of the Royal Astronomical Society*, vol. 506, pp. 2390–2407, Sept. 2021.

[212] O. Doré, J. Bock, M. Ashby, P. Capak, A. Cooray, R. de Putter, T. Eifler, N. Flagey, Y. Gong, S. Habib, K. Heitmann, C. Hirata, W.-S. Jeong, R. Katti, P. Korngut, E. Krause, D.-H. Lee, D. Masters, P. Mauskopf, G. Melnick, B. Mennesson, H. Nguyen, K. Öberg, A. Pullen, A. Raccanelli, R. Smith, Y.-S. Song, V. Tolls, S. Unwin, T. Venumadhav, M. Viero, M. Werner, and M. Zemcov, "Cosmology with the SPHEREX All-Sky Spectral Survey," *arXiv e-prints*, p. arXiv:1412.4872, Dec. 2014.

[213] S. R. Furlanetto and S. P. Oh, "Taxing the rich: recombinations and bubble growth during reionization," *Monthly Notices of the Royal Astronomical Society*, vol. 363, pp. 1031–1048, 11 2005.

[214] I. T. Iliev, E. Scannapieco, and P. R. Shapiro, "The Impact of Small-Scale Structure on Cosmological Ionization Fronts and Reionization," *The Astrophysical Journal*, vol. 624, pp. 491–504, May 2005.

[215] M. A. Alvarez and T. Abel, "The Effect of Absorption Systems on Cosmic Reionization," *The Astrophysical Journal*, vol. 747, p. 126, Mar. 2012.

[216] E. Sobacchi and A. Mesinger, "Inhomogeneous recombinations during cosmic reionization," *Monthly Notices of the Royal Astronomical Society*, vol. 440, pp. 1662–1673, May 2014.

[217] N. Y. Gnedin, "Effect of Reionization on Structure Formation in the Universe," *The Astrophysical Journal*, vol. 542, pp. 535–541, Oct. 2000.

[218] S. Naoz and R. Barkana, "The formation and gas content of high-redshift galaxies and minihaloes," *Monthly Notices of the Royal Astronomical Society*, vol. 377, pp. 667–676, May 2007.

[219] H. D. Kaur, N. Gillet, and A. Mesinger, "Minimum size of 21-cm simulations," *Monthly Notices of the Royal Astronomical Society*, vol. 495, pp. 2354–2362, June 2020.

[220] N. Y. Gnedin, "Cosmic Reionization on Computers. I. Design and Calibration of Simulations," *The Astrophysical Journal*, vol. 793, p. 29, Sept. 2014.

[221] P. Ocvirk, N. Gillet, P. R. Shapiro, D. Aubert, I. T. Iliev, R. Teyssier, G. Yepes, J.-H. Choi, D. Sullivan, A. Knebe, S. Gottlöber, A. D'Aloisio, H. Park, Y. Hoffman, and T. Stranex, "Cosmic Dawn (CoDa): the First Radiation-Hydrodynamics Simulation of Reionization and Galaxy Formation in the Local Universe," *Monthly Notices of the Royal Astronomical Society*, vol. 463, pp. 1462–1485, Dec. 2016.

[222] R. Kannan, E. Garaldi, A. Smith, R. Pakmor, V. Springel, M. Vogelsberger, and L. Hernquist, "Introducing the THESAN project: radiation-magnetohydrodynamic simulations of the epoch of reionization," *Monthly Notices of the Royal Astronomical Society*, vol. 511, pp. 4005–4030, Apr. 2022.

[223] T. R. Choudhury, A. Paranjape, and S. E. I. Bosman, "Studying the Lyman α optical depth fluctuations at z $\sim$ 5.5 using fast semi-numerical methods," *Monthly Notices of the Royal Astronomical Society*, vol. 501, pp. 5782–5796, Mar. 2021.

[224] S. Gazagnes, L. V. E. Koopmans, and M. H. F. Wilkinson, "Inferring the properties of the sources of reionization using the morphological spectra of the ionized regions," *Monthly Notices of the Royal Astronomical Society*, vol. 502, pp. 1816–1842, Apr. 2021.

[225] Y. Mao, J. Koda, P. R. Shapiro, I. T. Iliev, G. Mellema, H. Park, K. Ahn, and M. Bianco, "The impact of inhomogeneous subgrid clumping on cosmic reionization," *Monthly Notices of the Royal Astronomical Society*, vol. 491, pp. 1600–1621, Jan. 2020.

[226] H. Shukla, G. Mellema, I. T. Iliev, and P. R. Shapiro, "The effects of Lyman-limit systems on the evolution and observability of the epoch of reionization," *Monthly Notices of the Royal Astronomical Society*, vol. 458, pp. 135–150, May 2016.

[227] S. K. Giri, G. Mellema, T. Aldheimer, K. L. Dixon, and I. T. Iliev, "Neutral island statistics during reionization from 21-cm tomography," *Monthly Notices of the Royal Astronomical Society*, vol. 489, pp. 1590–1605, Oct. 2019.

[228] F. B. Davies and S. R. Furlanetto, "Improved treatments of the ionizing photon mean free path in seminumerical simulations of reionization," *Monthly Notices of the Royal Astronomical Society*, vol. 514, pp. 1302–1314, July 2022.

[229] H. Trac, N. Chen, I. Holst, M. A. Alvarez, and R. Cen, "AMBER: A Semi-numerical Abundance Matching Box for the Epoch of Reionization," *The Astrophysical Journal*, vol. 927, p. 186, Mar. 2022.

[230] E. Garaldi, R. Kannan, A. Smith, V. Springel, R. Pakmor, M. Vogelsberger, and L. Hernquist, "The THESAN project: properties of the intergalactic medium and its connection to reionization-era galaxies," *Monthly Notices of the Royal Astronomical Society*, Feb. 2022.

[231] R. P. Naidu, S. Tacchella, C. A. Mason, S. Bose, P. A. Oesch, and C. Conroy, "Rapid Reionization by the Oligarchs: The Case for Massive, UV-bright, Star-forming Galaxies with High Escape Fractions," *The Astrophysical Journal*, vol. 892, p. 109, Apr. 2020.

[232] J. S. W. Lewis, P. Ocvirk, D. Aubert, J. G. Sorce, P. R. Shapiro, N. Deparis, T. Dawoodbhoy, R. Teyssier, G. Yepes, S. Gottlöber, K. Ahn, I. T. Iliev, and J. Chardin, "Galactic ionizing photon budget during the epoch of reionization in the Cosmic Dawn II simulation," *Monthly Notices of the Royal Astronomical Society*, vol. 496, pp. 4342–4357, Aug. 2020.

[233] K. M. Gorski, B. D. Wandelt, F. K. Hansen, E. Hivon, and A. J. Banday, "The HEALPix Primer," *arXiv e-prints*, pp. astro–ph/9905275, May 1999.

[234] A. P. Calverley, G. D. Becker, M. G. Haehnelt, and J. S. Bolton, "Measurements of the ultraviolet background at 4.6 ¡ z ¡ 6.4 using the quasar proximity effect*," *Monthly Notices of the Royal Astronomical Society*, vol. 412, pp. 2543–2562, 04 2011.

[235] J. S. B. Wyithe and J. S. Bolton, "Near-zone sizes and the rest-frame extreme ultraviolet spectral index of the highest redshift quasars," *Monthly Notices of the Royal Astronomical Society*, vol. 412, pp. 1926–1936, 04 2011.

[236] N. Chen, H. Trac, S. Mukherjee, and R. Cen, "Patchy Kinetic Sunyaev-Zel'dovich Effect with Controlled Reionization History and Morphology," *arXiv e-prints*, p. arXiv:2203.04337, Mar. 2022.

[237] A. R. Parsons, D. C. Backer, G. S. Foster, M. C. H. Wright, R. F. Bradley, N. E. Gugliucci, C. R. Parashare, E. E. Benoit, J. E. Aguirre, D. C. Jacobs, C. L. Carilli, D. Herne, M. J. Lynch, J. R. Manley, and D. J. Werthimer, "The Precision Array for Probing the Epoch of Re-ionization: Eight Station Results," *Astronomical Journal*, vol. 139, pp. 1468–1480, Apr. 2010.

[238] S. J. Tingay, R. Goeke, J. D. Bowman, D. Emrich, S. M. Ord, D. A. Mitchell, M. F. Morales, T. Booler, B. Crosse, R. B. Wayth, C. J. Lonsdale, S. Tremblay, D. Pallot, T. Colegate, A. Wicenec, N. Kudryavtseva, W. Arcus, D. Barnes, G. Bernardi, F. Briggs, S. Burns, J. D. Bunton, R. J. Cappallo, B. E. Corey, A. Deshpande, L. Desouza, B. M. Gaensler, L. J. Greenhill, P. J. Hall, B. J. Hazelton, D. Herne, J. N. Hewitt, M. Johnston-Hollitt, D. L. Kaplan, J. C. Kasper, B. B. Kincaid, R. Koenig, E. Kratzenberg, M. J. Lynch, B. Mckinley, S. R. Mcwhirter, E. Morgan, D. Oberoi, J. Pathikulangara, T. Prabu, R. A. Remillard, A. E. E. Rogers, A. Roshi, J. E. Salah, R. J. Sault, N. Udaya-Shankar, F. Schlagenhaufer, K. S. Srivani, J. Stevens, R. Subrahmanyan, M. Waterson, R. L. Webster, A. R. Whitney, A. Williams, C. L. Williams, and J. S. B. Wyithe, "The Murchison Widefield Array: The Square Kilometre Array Precursor at Low Radio Frequencies," *Publications of the Astronomical Society of Australia*, vol. 30, p. e007, Jan. 2013.

[239] S. Yatawatta, A. G. de Bruyn, M. A. Brentjens, P. Labropoulos, V. N. Pandey, S. Kazemi, S. Zaroubi, L. V. E. Koopmans, A. R. Offringa, V. Jelić, O. Martinez Rubi, V. Veligatla, S. J. Wijnholds, W. N. Brouw, G. Bernardi, B. Ciardi, S. Daiboo, G. Harker, G. Mellema, J. Schaye, R. Thomas, H. Vedantham, E. Chapman, F. B. Abdalla, A. Alexov, J. Anderson, I. M. Avruch, F. Batejat, M. E. Bell, M. R. Bell, M. Bentum, P. Best, A. Bonafede, J. Bregman, F. Breitling, R. H. van de Brink, J. W. Broderick, M. Brüggen, J. Conway, F. de Gasperin, E. de Geus, S. Duscha, H. Falcke, R. A. Fallows, C. Ferrari, W. Frieswijk, M. A. Garrett, J. M. Griessmeier, A. W. Gunst, T. E. Hassall, J. W. T. Hessels, M. Hoeft, M. Iacobelli, E. Juette, A. Karastergiou, V. I. Kondratiev, M. Kramer, M. Kuniyoshi, G. Kuper, J. van Leeuwen, P. Maat, G. Mann, J. P. McKean, M. Mevius, J. D. Mol, H. Munk, R. Nijboer, J. E. Noordam, M. J. Norden, E. Orru, H. Paas, M. Pandey-Pommier, R. Pizzo, A. G. Polatidis, W. Reich, H. J. A. Röttgering, J. Sluman, O. Smirnov, B. Stappers, M. Steinmetz, M. Tagger, Y. Tang, C. Tasse, S. ter Veen, R. Vermeulen, R. J. van Weeren, M. Wise,

O. Wucknitz, and P. Zarka, "Initial deep LOFAR observations of epoch of reionization windows. I. The north celestial pole," *Astronomy and Astrophysics*, vol. 550, p. A136, Feb. 2013.

[240] G. D. Becker, F. B. Davies, S. R. Furlanetto, M. A. Malkan, E. Boera, and C. Douglass, "Evidence for Large-scale Fluctuations in the Metagalactic Ionizing Background Near Redshift Six," *The Astrophysical Journal*, vol. 863, p. 92, Aug 2018.

[241] R. A. Meyer, K. Kakiichi, S. E. I. Bosman, R. S. Ellis, N. Laporte, B. E. Robertson, E. V. Ryan-Weber, K. Mawatari, and A. Zitrin, "The role of galaxies and AGN in reionizing the IGM - III. IGM-galaxy cross-correlations at z $\sim$ 6 from eight quasar fields with DEIMOS and MUSE," *Monthly Notices of the Royal Astronomical Society*, vol. 494, pp. 1560–1578, May 2020.

[242] H. M. Christenson, G. D. Becker, S. R. Furlanetto, F. B. Davies, M. A. Malkan, Y. Zhu, E. Boera, and A. Trapp, "Constraints on the End of Reionization from the Density Fields Surrounding Two Highly Opaque Quasar Sightlines," *The Astrophysical Journal*, vol. 923, p. 87, Dec. 2021.

[243] R. Ishimoto, N. Kashikawa, D. Kashino, K. Ito, Y. Liang, Z. Cai, T. Yoshioka, K. Okoshi, T. Misawa, M. Onoue, Y. Takeda, and H. Uchiyama, "The physical origin for spatially large scatter of IGM opacity at the end of reionization: the IGM Lyα opacity-galaxy density relation," *arXiv e-prints*, p. arXiv:2207.05098, July 2022.

[244] Y. Xu, B. Yue, M. Su, Z. Fan, and X. Chen, "An Analytical Model of the Large Neutral Regions during the Late Stage of Reionization," *The Astrophysical Journal*, vol. 781, p. 97, Feb. 2014.

[245] M. Malloy and A. Lidz, "How to Search for Islands of Neutral Hydrogen in the z ~5.5 IGM," *The Astrophysical Journal*, vol. 799, p. 179, Feb. 2015.

[246] Y. Xu, B. Yue, and X. Chen, "The Neutral Islands during the Late Epoch of Reionization," *IAU Symp.*, vol. 333, pp. 64–67, 2017.

[247] M. Bianco, I. T. Iliev, K. Ahn, S. K. Giri, Y. Mao, H. Park, and P. R. Shapiro, "The impact of inhomogeneous subgrid clumping on cosmic reionization - II. Modelling stochasticity," *Monthly Notices of the Royal Astronomical Society*, vol. 504, pp. 2443–2460, June 2021.

[248] S. L. Finkelstein, "Observational Searches for Star-Forming Galaxies at z ¿ 6," *Publications of the Astronomical Society of Australia*, vol. 33, p. e037, Aug. 2016.

[249] R. J. Bouwens, P. A. Oesch, M. Stefanon, G. Illingworth, I. Labbé, N. Reddy, H. Atek, M. Montes, R. Naidu, T. Nanayakkara, E. Nelson, and S. Wilkins, "New Determinations of the UV Luminosity Functions from z 9 to 2 Show a Remarkable Consistency with Halo Growth and a Constant Star Formation Efficiency," *Astronomical Journal*, vol. 162, p. 47, Aug. 2021.

[250] J. Matthee, R. P. Naidu, G. Pezzulli, M. Gronke, D. Sobral, P. A. Oesch, M. Hayes, D. Erb, D. Schaerer, R. Amorín, S. Tacchella, A. Paulino-Afonso, M. Llerena, J. Calhau, and H. Röttgering, "(Re)Solving Reionization with Lyα: How Bright Lyα Emitters account for the z = 2 - 8 Cosmic Ionizing Background," *Monthly Notices of the Royal Astronomical Society*, Mar. 2022.

[251] H. E. Ross, S. K. Giri, G. Mellema, K. L. Dixon, R. Ghara, and I. T. Iliev, "Redshift-space distortions in simulations of the 21-cm signal from the cosmic dawn," *Monthly Notices of the Royal Astronomical Society*, vol. 506, pp. 3717–3733, Sept. 2021.

[252] E. Vanzella, L. Pentericci, A. Fontana, A. Grazian, M. Castellano, K. Boutsia, S. Cristiani, M. Dickinson, S. Gallozzi, E. Giallongo, M. Giavalisco, R. Maiolino, A. Moorwood, D. Paris, and P. Santini, "Spectroscopic Confirmation of Two Lyman Break Galaxies at Redshift Beyond 7," *The Astrophysical Journal Letters*, vol. 730, p. L35, Apr. 2011.

[253] I. Jung, S. L. Finkelstein, M. Dickinson, T. A. Hutchison, R. L. Larson, C. Papovich, L. Pentericci, A. N. Straughn, Y. Guo, S. Malhotra, J. Rhoads, M. Song, V. Tilvi, and I. Wold, "Texas Spectroscopic Search for Lyα Emission at the End of Reionization. III. The Lyα Equivalent-width Distribution and Ionized Structures at z ¿ 7," *The Astrophysical Journal*, vol. 904, p. 144, Dec. 2020.

[254] P. R. Shapiro, M. L. Giroux, and A. Babul, "Reionization in a Cold Dark Matter Universe: The Feedback of Galaxy Formation on the Intergalactic Medium," *The Astrophysical Journal*, vol. 427, p. 25, May 1994.

[255] A. A. Thoul and D. H. Weinberg, "Hydrodynamic simulations of galaxy formation. II. photoionization and the formation of low-mass galaxies," *The Astrophysical Journal*, vol. 465, p. 608, jul 1996.

[256] M. Hoeft, G. Yepes, S. Gottlöber, and V. Springel, "Dwarf galaxies in voids: suppressing star formation with photoheating," *Monthly Notices of the Royal Astronomical Society*, vol. 371, pp. 401–414, Sept. 2006.

[257] K. Finlator, R. Davé , and F. Özel, "GALACTIC OUTFLOWS AND PHOTOIONIZATION HEATING IN THE REIONIZATION EPOCH," *The Astrophysical Journal*, vol. 743, p. 169, dec 2011.

[258] X. Wu, R. Kannan, F. Marinacci, M. Vogelsberger, and L. Hernquist, "Simulating the effect of photoheating feedback during reionization," *Monthly Notices of the Royal Astronomical Society*, vol. 488, pp. 419–437, Sept. 2019.

[259] D. R. Weisz, B. D. Johnson, L. C. Johnson, E. D. Skillman, J. C. Lee, R. C. Kennicutt, D. Calzetti, L. van Zee, M. S. Bothwell, J. J. Dalcanton, D. A. Dale, and B. F. Williams, "MODELING THE EFFECTS OF STAR FORMATION HISTORIES ON hα AND ULTRAVIOLET FLUXES IN NEARBY DWARF GALAXIES," *The Astrophysical Journal*, vol. 744, p. 44, dec 2011.

[260] N. Emami, B. Siana, D. R. Weisz, B. D. Johnson, X. Ma, and K. El-Badry, "A Closer Look at Bursty Star Formation with L $_{H\alpha}$ and L $_{UV}$ Distributions," *The Astrophysical Journal*, vol. 881, p. 71, Aug. 2019.

[261] S. R. Furlanetto and J. Mirocha, "Bursty star formation during the Cosmic Dawn driven by delayed stellar feedback," *Monthly Notices of the Royal Astronomical Society*, vol. 511, pp. 3895–3909, Apr. 2022.

[262] J. S. Bullock, A. V. Kravtsov, and D. H. Weinberg, "Reionization and the Abundance of Galactic Satellites," *The Astrophysical Journal*, vol. 539, pp. 517–521, Aug. 2000.

[263] R. S. Somerville and R. Davé, "Physical Models of Galaxy Formation in a Cosmological Framework," *Annual Review of Astron and Astrophysis*, vol. 53, pp. 51–113, Aug. 2015.

[264] J. Mirocha, P. L. Plante, and A. Liu, "The importance of galaxy formation histories in models of reionization," *Monthly Notices of the Royal Astronomical Society*, vol. 507, pp. 3872–3887, sep 2021.

[265] M. Kuhlen and C.-A. Faucher-Giguère, "Concordance models of reionization: implications for faint galaxies and escape fraction evolution," *Monthly Notices of the Royal Astronomical Society*, vol. 423, pp. 862–876, 05 2012.

[266] K. S. S. Barrow, B. E. Robertson, R. S. Ellis, K. Nakajima, A. Saxena, D. P. Stark, and M. Tang, "The Lyman Continuum Escape Survey: Connecting Time-dependent [O III] and [O II] Line Emission with Lyman Continuum Escape Fraction in Simulations of Galaxy Formation," *The Astrophysical Journal Letters*, vol. 902, p. L39, Oct. 2020.

[267] M. Maji, A. Verhamme, J. Rosdahl, T. Garel, J. Blaizot, V. Mauerhofer, M. Pittavino, M.-P. Victoria Feser, M. Chuniaud, T. Kimm, H. Katz, and M. Haehnelt, "Predicting Lyman-continuum emission of galaxies using their physical and Lyman-alpha emission properties," *Astronomy and Astrophysics*, vol. 663, p. A66, July 2022.

[268] R. Marques-Chaves, D. Schaerer, R. O. Amorín, H. Atek, S. Borthakur, J. Chisholm, V. Fernández, S. R. Flury, M. Giavalisco, A. Grazian, M. J. Hayes, T. M. Heckman, A. Henry, Y. I. Izotov, A. E. Jaskot, Z. Ji, S. R. McCandliss, M. S. Oey, G. Östlin, S. Ravindranath, M. J. Rutkowski, A. Saldana-Lopez, H. Teplitz, T. X. Thuan, A. Verhamme, B. Wang, G. Worseck, and X. Xu, "No correlation of the Lyman continuum escape fraction with spectral hardness," *Astronomy and Astrophysics*, vol. 663, p. L1, July 2022.

[269] J. Y. C. Yeh, A. Smith, R. Kannan, E. Garaldi, M. Vogelsberger, J. Borrow, R. Pakmor, V. Springel, and L. Hernquist, "The THESAN project: ionizing escape fractions of reionization-era galaxies," *arXiv e-prints*, p. arXiv:2205.02238, May 2022.

[270] L. Hui and N. Y. Gnedin, "Equation of state of the photoionized intergalactic medium," *Monthly Notices of the Royal Astronomical Society*, vol. 292, pp. 27–42, Nov. 1997.

[271] T. Tepper-García, "Voigt profile fitting to quasar absorption lines: an analytic approximation to the Voigt-Hjerting function," *Monthly Notices of the Royal Astronomical Society*, vol. 369, pp. 2025–2035, July 2006.

[272] P. R. Upton Sanderbeck, A. D'Aloisio, and M. J. McQuinn, "Models of the thermal evolution of the intergalactic medium after reionization," *Monthly Notices of the Royal Astronomical Society*, vol. 460, pp. 1885–1897, Aug. 2016.

[273] J. S. Bolton and G. D. Becker, "Resolving the high redshift Lyα forest in smoothed particle hydrodynamics simulations," *Monthly Notices of the Royal Astronomical Society: Letters*, vol. 398, pp. L26–L30, 09 2009.

[274] N. Y. Gnedin, "Cosmological Reionization by Stellar Sources," *The Astrophysical Journal*, vol. 535, pp. 530–554, Jun 2000.

[275] M. L. Giroux and P. R. Shapiro, "The Reionization of the Intergalactic Medium and Its Observational Consequences," *The Astrophysical Journal Supplement*, vol. 102, p. 191, Feb. 1996.

[276] V. Iršič, M. Viel, M. G. Haehnelt, J. S. Bolton, S. Cristiani, G. D. Becker, V. D'Odorico, G. Cupani, T.-S. Kim, T. A. M. Berg, S. López, S. Ellison, L. Christensen, K. D. Denney, and G. Worseck, "New constraints on the free-streaming of warm dark matter from intermediate and small scale Lyman-α forest data," *Phys. Rev. D*, vol. 96, p. 023522, July 2017.

[277] J. Chardin, G. Kulkarni, and M. G. Haehnelt, "Self-shielding of hydrogen in the IGM during the epoch of reionization," *MNRAS*, vol. 478, pp. 1065–1076, Jul 2018.

Appendix A

Appendix for Chapter 2

A.1 Bias Factor Derivation

We provide here the derivation for the sinks contribution to b_{x_i,v^2} in Equation 2.16. Assuming x_i^r and $C_{\rm R}^r$ satisfy Equation 2.13, we can write a differential equation for $\delta_{x_i}^r$ with the simple form

$$\dot{\delta}_{x_i}^r + A(t)\delta_{x_i}^r = B(t)\delta_{C_{\rm R}}^r \tag{A.1}$$

where

$$A(t) \equiv \frac{\langle \dot{x_i} \rangle}{\langle x_i \rangle} + \alpha_B n_e \langle C_{\rm R} \rangle \qquad\qquad B(t) \equiv -\alpha_B n_e \langle C_{\rm R} \rangle \tag{A.2}$$

are functions only of the IGM mean values of x_i and $C_{\rm R}$ for which the solution to Equation 2.13 is known already. The fluctuation $\delta_{C_{\rm R}}^r$ is given by the average of local fluctuations over the distribution of $z_{\rm re}$ and $v_{\rm bc}$ within the patch, analogous to Equation 2.14. Assuming the right-hand-side of Equation A.1 is a function of time only and not of $\delta_{x_i}^r$ (which will be justified momentarily), the solution is

$$\delta_{x_i}^r(t) = D(t) \int_{t(z_0)}^{t} dt' F(t') \delta_{C_{\rm R}}^r(t') \tag{A.3}$$

where

$$D(t) \equiv e^{-\int_{t(z_0)}^{t} dt' A(t')} \qquad F(t) \equiv B(t') e^{\int_{t(z_0)}^{t} dt' A(t')} \tag{A.4}$$

where z_0 is the redshift at which Reionization starts. Finally, we may write to first order in $\delta^r_{v^2} \equiv (v^2_{\rm bc} - \sigma^2_{bc})/\sigma^2_{bc}$,

$$\delta^r_{C_{\rm R}} = \frac{\sigma^2_{bc}}{\langle C_{\rm R} \rangle} \left\langle \frac{\partial C_{\rm R}}{\partial v^2_{\rm bc}}\Big|_{v_{\rm bc}=\sigma_{bc}} \right\rangle \delta^r_{v^2} + \text{ matter terms} \tag{A.5}$$

where the partial derivative is averaged as in Equation 2.14. Equation A.5 is the statement that $v_{\rm bc}$ is a biased tracer of $C_{\rm R}$. Combining Equations A.3 and A.5 yields

$$\delta^r_{x_i} = b^r_{x_i,v^2} \delta^r_{v^2} \tag{A.6}$$

where $b^r_{x_i,v^2}$ is the scale-dependent ionized fraction bias factor. Provided r is large enough that spatial fluctuations in $\mathcal{P}_{z_{\rm re}}(x_i(t))$ are unimportant, we may write the scale-independent bias factor (Equation 2.16) as

$$b_{x_i,v^2}(t) = \lim_{r\to\infty} b^r_{x_i,v^2}(t) = \frac{\sigma^2_{bc} D(t)}{\langle C_{\rm R} \rangle} \int_{t(z_0)}^{t} dt' F(t') S(t') \tag{A.7}$$

where

$$S(t) \equiv \int_{z_0}^{z(t)} dz_{\rm re} \mathcal{P}_{z_{\rm re}}(x_i(t)) \frac{\partial C_{\rm R}}{\partial v^2_{\rm bc}}\Big|_{v_{\rm bc}=\sigma_{bc}} (z_{\rm re}, t) \tag{A.8}$$

Note that $\mathcal{P}_{v_{\rm bc}}$ was absorbed in the definition of $\delta^r_{v^2}$.

A.2 Test of Initial Conditions

We tested the initial conditions prescription used in this work by comparing the simulated matter power spectrum at very high redshifts to the expectation from linear

Simulation	$z_{\rm init}$	N	L (Mpc/h)	$v_{\rm bc}$ (km/s)
Fiducial	1080	256^3	0.256	0
Fiducial + $v_{\rm bc}$	1080	256^3	0.256	30
High Res	1080	512^3	0.256	0
High Res + $v_{\rm bc}$	1080	512^3	0.256	30
Low z	300	256^3	0.256	0

Table A.1: List of simulations run to test the accuracy of the initial conditions setup used in this work. Here, $z_{\rm init}$ is the initialization redshift of the simulation.

theory (LT). We did this primarily to verify that $v_{\rm bc}$ is implemented correctly in our simulations, but also to confirm that starting from $z = 1080$ produces correct results. To do this, we ran a set of hydro-only test simulations down to $z = 30$, which are listed in Table A.1. These simulations were initialized at $z_{\rm start}$, which is either 1080 (as in our production runs) or at $z = 300$ (as in D20).

The matter power spectrum for the tests starting from $z = 1080$ are shown in Figure A.1 at redshifts 270, 145, 68, and 45. The top (bottom) set of curves show the DM (baryon) power spectrum. The solid blue (black) curves are the LT predictions evolved from redshift 1080 CAMB TFs using the LT approximation from [73] and employed in their initial conditions code CICsASS. Runs with and without v_{bc} have indistinguishable DM power spectra, while the baryon power spectrum is suppressed significantly in the cases with v_{bc}. In all cases, the simulations agree well with the LT expectation until $z = 45$ when non-linear effects begin to become important. The higher resolution runs do a better job at small scales, as expected. Importantly, the simulations with v_{bc} reproduce the CICsASS prediction very well at scales that are captured by the simulations. These results demonstrate that $v_{\rm bc}$ is implemented correctly in our simulations.

We also checked how our results are affected by using different starting redshifts. In Figure A.2, we plot the Fiducial (cyan dashed), High res (magenta dotted), Low z(red dashed) power spectra. We compare these to the CICsASS LT expectation without $v_{\rm bc}$ (black solid curve). We see that the simulations initialized at $z = 1080$ (Fiducial and High Res) agree well the LT approximation. The one started from the $z = 300$ CAMB TF deviates slightly from the other two initially. However, after some time has passed, the relative difference decreases, indicating that the slight difference in initial conditions does not affect the results significantly at much later times. This is important for us because it indicates that we can reasonably compare our results to the simulations in D20 (which were initialized in the same was as the Low z run). It also demonstrates that initializing simulations at $z = 1080$ does not introduce significant shot noise, as has been suggested by many previous authors (e.g. [73]).

A.3 Effects of Resolution and Box Size

We also assessed the sensitivity of our clumping factor results to numerical resolution and box size. This is important because $v_{\rm bc}$ impacts small-scale gas structures appreciably but leaves the larger structures unaffected. This suggests that too-small boxes would fail to capture the large-scale structures, producing an over-estimate of the $v_{\rm bc}$ effect. Conversely, large boxes with poor resolution would fail to resolve the structures that are

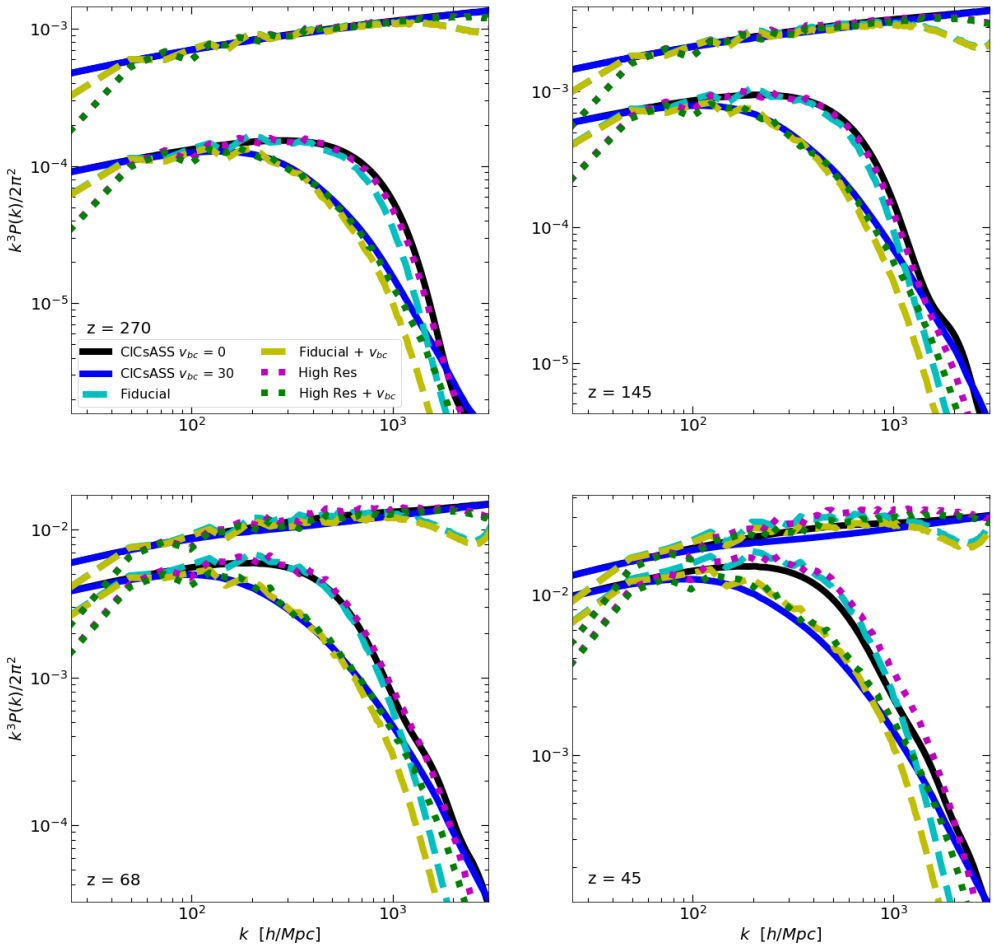

Figure A.1: Power spectra of baryons (bottom curves) and DM (top curves) for Fiducial (cyan dashed), Fiducial + $v_{\rm bc}$ (yellow dashed), High Res (magenta dotted), High Res + $v_{\rm bc}$ (greed dotted) at redshifts 270, 145, 68, and 45 compared to the LT expectation from CICsASS. The blue (black) solid curves are the CICsASS LT approximation with(out) $v_{\rm bc}$. All the DM curves are indistinguishable, and the simulations with and without $v_{\rm bc}$ agree well with their respective LT predictions, especially when the resolution is increased.

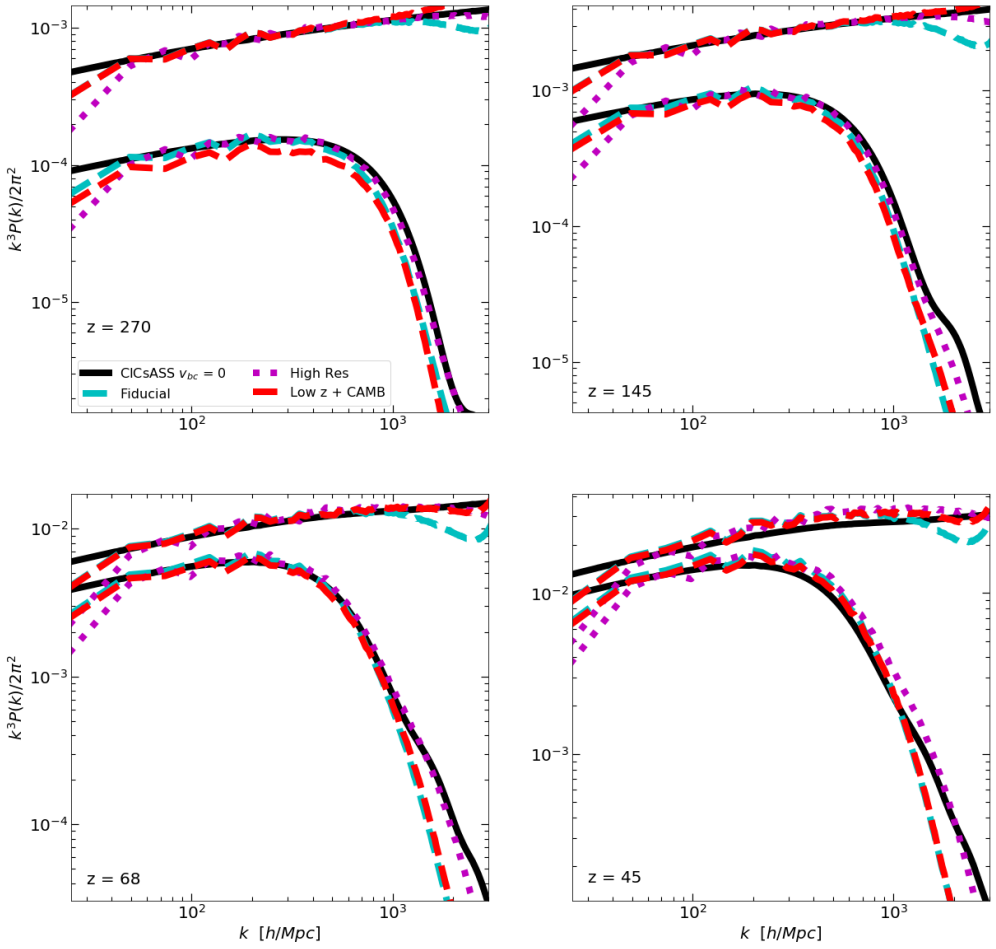

Figure A.2: Baryon and CDM power spectra showing how our results vary with different initialization schemes. The simulations shown are Fiducial (cyan dashed), High Res (magenta dotted), and Low z + CAMB (red dashed). The Low z run deviates slightly from the others initially, but all three converge at lower redshifts. This implies that starting from $z = 1080$ and 300 give very similar results especially at low redshifts.

most affected, leading to an under-estimate. We quantified these differences by running a set of simulations with $N = 512$ and $L = 256$ kpc, which gives 8 times the resolution and 1/64th the volume of our fiducial runs. We ran simulations with $v_{\rm bc} = 0, 65$ km/s and $\Gamma_{-12} = 0.3, 9.2$ for $z_{\rm re} = 6$. We compared these results to our full box-size run with $v_{\rm bc} = 65$ km/s, $z_{\rm re} = 6$, and $\Gamma_{-12} = 0.3$. We see a maximum suppression in $C_{\rm R}$ relative to the no-$v_{\rm bc}$ case with the same parameters of $\sim 25\%(35\%)$ for $\Gamma_{-12} = 0.3(9.2)$, significantly more than the 15% we got for the fiducial case. We ran a similar set of tests at $z_{\rm re} = 12$, but this time varying the resolution and box size one at a time. We found that increasing box size at fixed resolution reduces the relative v_{bc} effect after about $\Delta t \sim 5$ Myr, while increased resolution boosts the effect considerably for $\Delta t < 10$ Myr but not much after this. These results are consistent with the picture that small structures that are affected by v_{bc} dominate the recombination rate early, but after relaxation is complete the recombination rate is set by larger structures that are not appreciably affected by v_{bc}.

In Figure A.3, we plot the number of hydrogen recombinations per hydrogen atom since $z_{\rm re}$ for the convergence tests at $z_{re} = 6$ alongside our production runs (the fiducial case) with $(z_{re}, \Gamma_{-12}) = (6, 0.3)$, all for $v_{bc} = 0$ (65 km/s). The difference between the runs with and without v_{bc} increases for smaller box size/higher resolution and increasing Γ_{-12}, suggesting that the systems that are resolved in those simulations are more strongly impacted by $v_{\rm bc}$. In addition, the number of recombinations is higher at later times in fiducial case, suggesting that large structures not captured in the smaller simulations contribute a large fraction of the recombinations. This result confirms our suspicion that box sizes that

are too small to capture a representative sample of absorbing systems will over-estimate the importance of $v_{\rm bc}$. However, it may be that some of the difference comes from the additional resolution these boxes, in which case our fiducial runs may slightly under-estimate $v_{\rm bc}$'s importance in patches that have been recently ionized.

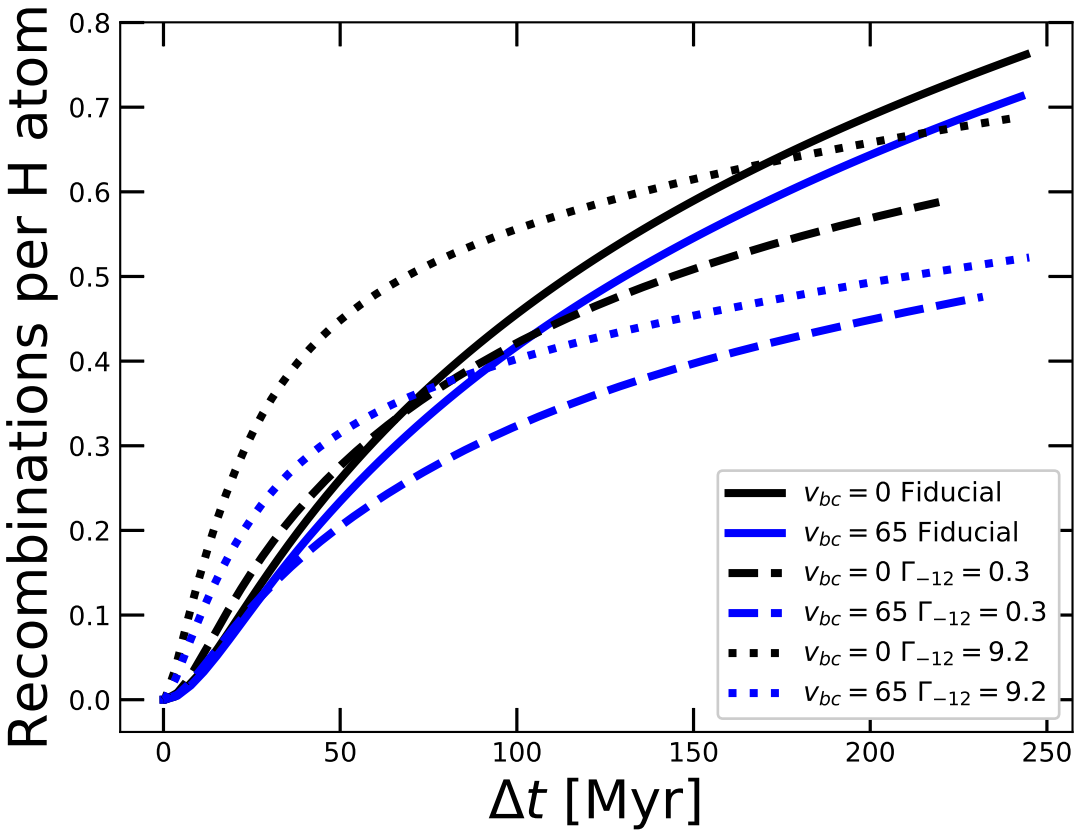

Figure A.3: Number of recombinations per hydrogen atom for our convergence runs (dotted/dashed curves) and our fiducial $z_{\rm re} = 6$, $\Gamma_{-12} = 0.3$ run ((solid curves). The difference due to $v_{\rm bc}$ is much larger in the smaller boxes, especially the high Γ_{-12} case. This is likely due to a combination of the lack of large systems and better resolution of small ones, both of which enhance the importance of $v_{\rm bc}$.

Appendix B

Appendix for Chapter 4

B.1 Self-Shielding Implementation

We account for self-shielding by using the results of [178] to model $\Gamma_{\rm HI}(n_{\rm H})$ at high densities. We find that the form $\frac{\Gamma_{\rm HI}}{\langle\Gamma_{\rm HI}\rangle} = F(n_{\rm H})\exp[-(n_{\rm H}/n_0)^6]$ where $F(n_{\rm H})$ is given by (as in [192, 277])

$$F(n_{\rm H}) = (1-f)\left(1+\left[\frac{n_{\rm H}}{n_0}\right]^{\beta}\right)^{\alpha_1} + f\left(1+\frac{n_{\rm H}}{n_0}\right)^{\alpha_2} \tag{B.1}$$

fits well the median $\Gamma_{\rm HI}(n_{\rm HI})$ of Ref [178] in relaxed gas for $(n_0/{\rm cm}^{-3}, \beta, \alpha_1, \alpha_2, f) = (0.015, 2, -3, -1, 0.01)$ for $\Gamma_{-12} = 0.3$. We additionally found that their result for $\Gamma_{-12} = 3.0$ can be reproduced by assuming the same parameters with $n_0 \propto \Gamma_{\rm HI}^{2/3}$, so we adopted this scaling to account for evolution of $\Gamma_{\rm HI}$. We used the same self-shielding prescription in the post-processing MFP calculation for both the relaxed and un-relaxed simulations.

B.2 Numerical Convergence

We tested the numerical convergence of the MFP estimation (Eq. 4.1) in our simulations in different DM cosmologies in the relaxed and un-relaxed limits. The test simulations were run in a box with $L = 2h^{-1}$Mpc, with no DC mode. In the relaxed limit, our fiducial $\Gamma_{\rm HI}$ history was applied. Figure B.1 shows the MFP in the relaxed (top row) and un-relaxed (bottom row) limits for different resolution choices, indicated in the legend. (Note that we did not run a case with $N = 2048^3$ in the un-relaxed $m_X = 1$ keV scenario, so only four curves appear in that panel.) The left, middle, and right columns show convergence tests for CDM, $m_X = 3$ keV, and $m_X = 1$ keV, respectively. We see that in the relaxed limit, our choice of $N = 1024^3$ is more than sufficient for numerical convergence for all three DM models.

In contrast, convergence is extremely difficult in the un-relaxed limit, which has already been noted in [85] and [74]. Recall that the un-relaxed production run resolutions for our CDM and $m_X = 3$ keV simulations are both $N = 2048^3$, while our $m_X = 1$ keV simulations were run with $N = 1024^3$. The key takeaway from the bottom row of Figure B.1 is that the degree of convergence appears to improve as m_X decreases. For example, at $z = 6$, the main redshift of interest for this work, the percent differences between adjacent curves for CDM, starting at the lowest resolutions, are 37%, 32%, 27%, and 23%. For $m_X = 3$ keV, they are 21%, 14%, 13%, and 12%. For $m_X = 1$ keV, they are 5%, 2%, and 1%. Hence, even with $N = 1024^3$, our production run with $m_X = 1$ keV is likely better converged than our CDM run (which was run with $N = 2048^3$), justifying our use of a lower resolution for the former. This feature owes to the intrinsic lack of small-scale power in the

WDM cosmology with $m_X = 1$ keV. Another takeaway here is that our main results likely underestimate the LyC opacity in the CDM model, and therefore underestimate the differences in MFP between the WDM and CDM models. Note, however, that our simulations do not include the effect of pre-heating the IGM by the first X-ray sources. This heating would raise the Jeans filtering mass, smoothing out the smallest structures present in the CDM cosmology. Ref [74] found that this could lead to as much as a factor of 2 decrease in the IGM clumping factor, which would act in the direction of diminishing differences in the MFP between the CDM and WDM models in the un-relaxed limit.

B.3 Testing the relaxation ansatz (Eq. 4.3)

In this section we examine the accuracy of the simple relaxation ansatz given by equation 4.3. To test this, we ran a hydrodynamic simulation in a CDM cosmology with $N = 512^3$ which was flash re-ionized at $z_{\rm re} = 6.5$ using our fiducial $\Gamma_{\rm HI}$ prescription. For comparison, we then ran $N = 512^3$ relaxed and un-relaxed limit runs, and plugged these into equation 4.3 for several values of $t_{\rm relax}$. The left panel in Figure B.2 shows the MFP for the simulation with $z_{\rm re} = 6.5$ (red dashed), the relaxed and un-relaxed limits (black dashed and black solid respectively) and the results of evaluating equation 4.3 for $t_{\rm relax} = 50$, 150, and 250 Myr (dotted curves). The right panel shows the fractional difference with the $z_{\rm re} = 6.5$ simulation for each value of $t_{\rm relax}$. We see that for our fiducial choice of $t_{\rm relax} = 150$ Myr, the ansatz reproduces the simulation result to within at most 10% at $4.5 < z < 6.5$. Higher (lower) values of $t_{\rm relax}$ produce MFPs that are distinctly too short (long) compared to the

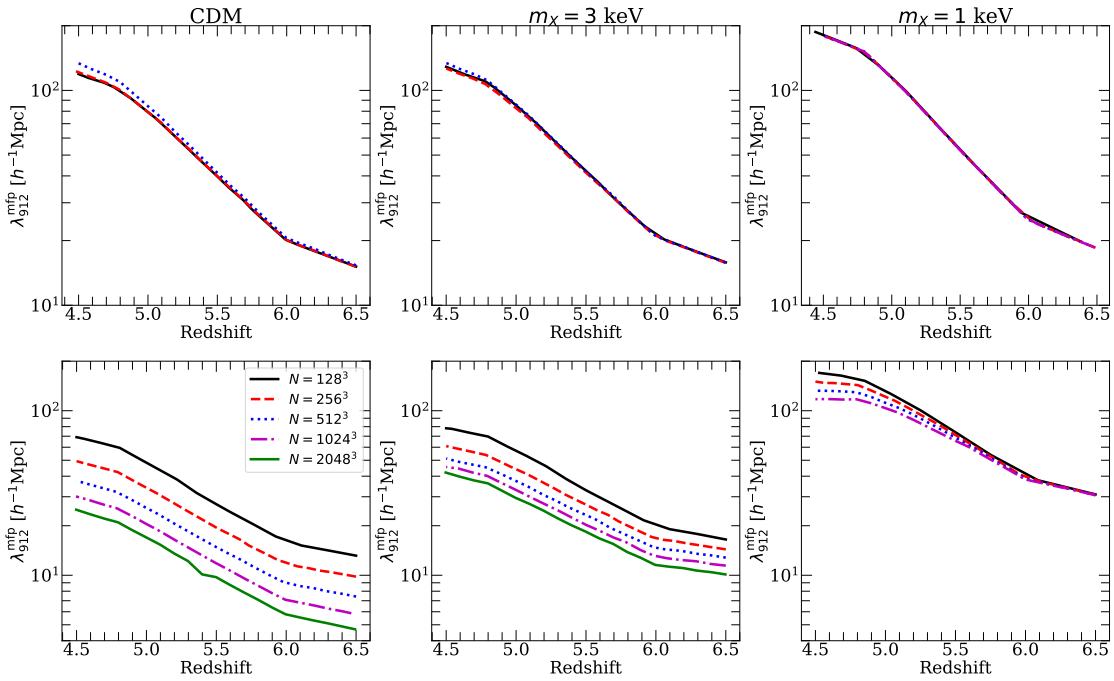

Figure B.1: Numerical convergence test for our simulation suite. We show the MFP in ionized gas in the mean-density volume for each of our three DM scenarios (from left to right, CDM, $m_X = 3$ keV and $m_X = 1$ keV), in the relaxed and un-relaxed limits (top and bottom rows respectively). We tested several resolution levels, the highest in each panel corresponding to the production resolution for that combination of DM model and relaxation state. The top row shows that our production run resolution of $N = 1024^3$ is more than sufficient for convergence in the relaxed limit. The bottom row shows that convergence requirements are less stringent in cosmologies with a larger free streaming scale (lower m_X). The lack of convergence in the CDM run highlights the importance of small-scale power in setting the MFP in the un-relaxed limit. Given that our WDM runs are better converged than our CDM runs, our main results likely underestimate differences in the global MFP between these two cosmologies. We emphasize, however, that our runs do not include any pre-heating by X-ray sources, which would diminish these differences as well.

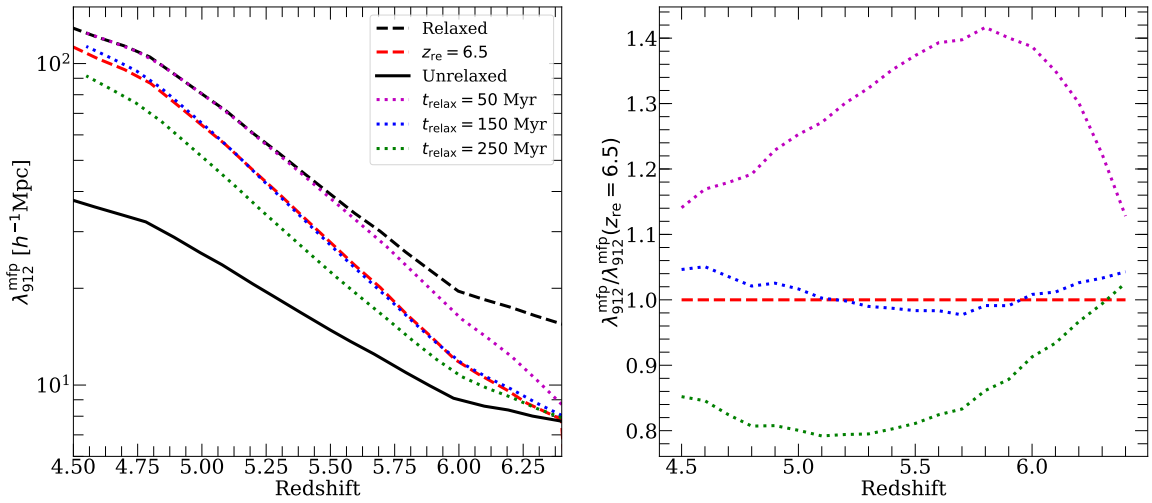

Figure B.2: Test of the relaxation ansatz (Eq. 4.3). **Left**: MFP for our simulation with $z_{\rm re} = 6.5$ (red dashed), the corresponding relaxed and un-relaxed limits (black dashed and solid, respectively) and the result of equation 4.3 for several values of $t_{\rm relax}$ (dotted curves). **Right**: ratio between the MFP from the $z_{\rm re} = 6.5$ simulation and the results of equation 4.3. We see agreement to within at least 10% between equation 4.3 and the simulation for $t_{\rm relax} = 150$ Myr, while the other choices of $t_{\rm relax}$ significantly under or overshoot the simulation result.

simulation. This test validates both our simple relaxation ansatz and our our fiducial choice of $t_{\rm relax} = 150$ Myr.

Appendix C

Appendix for Chapter 5

C.1 Numerical Convergence

Here we describe some additional parameters in our code and demonstrate convergence of the ionization field in our simulations. The first parameter is $N_{\rm iter}$, the number of times Eq. 5.1 is iterated with the equation for $\overline{\lambda}$ (Eq. 3.2 or 5.4) during each time step. Our fiducial value is $N_{\rm iter} = 5$. Our initial guess for $\Gamma_{\rm HI}$ assumes $\overline{\lambda} >> \Delta x_{\rm cell}$, where $\Delta x_{\rm cell}$ is the cell size, in which limit Eq. 5.1 is independent of $\overline{\lambda}$. Thus in general, convergence takes longest when $\overline{\lambda} < \Delta x_{\rm cell}$ - that is, in optically thick cells. To test convergence of $N_{\rm iter}$, we ran simulations with $N_{\rm iter}$ = 1, 3, 5, and 10 on a coarse-grained ($N = 150^3$; $\Delta x_{\rm cell} = 2\ h^{-1}$Mpc) version of our reionization volume using the Democratic Sources and Maximum $C_{\rm R}(\Delta)$ models. This is the most extreme combination of source and sinks scenarios since it has the shortest $\overline{\lambda}$ on average. In Fig. C.1 we show $\Delta_{21}(k)$ vs. wavenumber at 30% and 70% ionized for our tests, re-scaled so that the two sets of curves can be distinguished. At $k = 0.1\ h{\rm Mpc}^{-1}$, the $N_{\rm iter} = 5$ and 10 cases are $\approx 10\%$ apart at 30% ionized

and 35% apart at 70% ionized. This is considerably less than the factor of several difference between the Maximum $C_R(\Delta)$ and Full Sinks models the top row of Figure 5.9. We have checked convergence for different combinations of sinks and source models and found better convergence in all cases. Moreover, this result is conservative because the condition $\overline{\lambda} < \Delta x_{\rm cell}$ is more likely to occur for $\Delta x_{\rm cell} = 2\ h^{-1}$Mpc than for our fiducial $\Delta x_{\rm cell} = 1\ h^{-1}$Mpc.

Next we checked for convergence in the angular resolution of the radiation field. This is adjustable in our code through two parameters that control how rays are merged. The first, $l_{\rm hpx}$, is the order of the HealPix sphere onto which rays are binned when they are merged. Our fiducial $l_{\rm hpx} = 0$ corresponds to keeping track of 12 directions. The other parameter is $N_{\rm ex}$ - the number of rays per cell that are "exempt" from being merged. Before rays merged, they are sorted in order of their photon counts, and the top $N_{\rm ex}N^3$ rays are not considered for merging[1]. Using the same coarse-grained setup, we checked all combinations of $l_{\rm hpx} = 0$ and 1 (which corresponds to tracking 48 directions) and $N_{\rm ex} = 16$ (our fiducial choice) and 44. We found that Δ_{21} for these tests (not shown) to be indistinguishable for all combinations of these parameters on scales of interest, despite the amount of noise in the radiation field decreasing considerably for higher resolution runs.

C.2 Derivation of Eq. 5.1 (for $\Gamma_{\rm HI}$)

Here we will derive Eq. 5.1 for $\Gamma_{\rm HI}$. Consider cell i with ionized fraction $x_{\rm ion}^i$ and volume $V_{\rm cell}$. If the I-front in cell i is infinitely sharp and travels along one axis, then ray j

[1]We found that this procedure considerably reduces noise in the radiation field, particularly around the brightest sources.

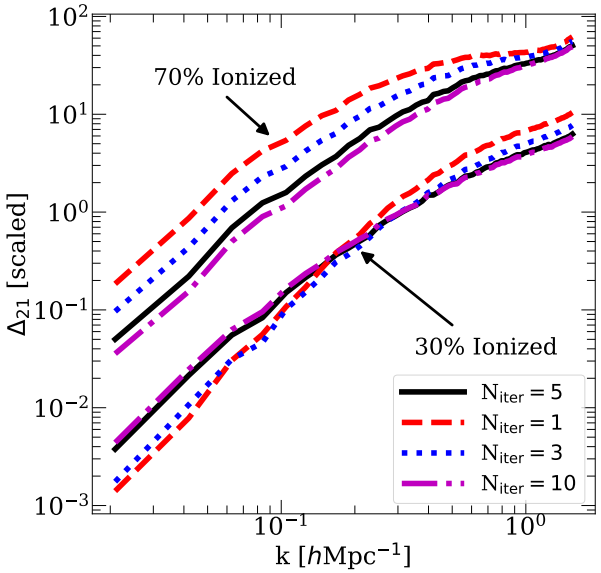

Figure C.1: $\Delta_{21}(k)$ at 30% and 70% ionized (see annotations) for four values of $N_{\rm iter}$ (see legend). This test uses the Democratic Sources and Maximum $C_{\rm R}(\Delta)$ models (the combination with the shortest $\overline{\lambda}$) in a coarse-grained version of the original simulation volume with 2 h^{-1}Mpc cells. Our fiducial value of $N_{\rm iter} = 5$ is within 10% or the $N_{\rm iter} = 10$ case at 30% ionized and within 35% at 70% ionized at all k. This is relatively small compared to the differences seen in the top row of Figure 5.9. Moreover, all the other combinations of models that we checked displayed significantly better convergence.

intersecting cell i will travel a distance $x^i_{\rm ion}\Delta s^{ij}$ (recall Δs^{ij} is the total path length of ray j through cell i) before reaching neutral gas. The number of photons absorbed over this distance is

$$N^i_{\rm abs} = \sum_{j=1}^{N_{\rm rays}} N^{ij}_0 \left(1 - \exp\left[\frac{-x^i_{\rm ion}\Delta s^{ij}}{\overline{\lambda}^i}\right]\right) \tag{C.1}$$

where N^{ij}_0 is the number of photons in ray j entering cell i and $\overline{\lambda}$ is the mean free path in cell i behind the I-front. During a time step Δt, $\Gamma_{\rm HI}$ behind the I-front is

$$\Gamma^i_{\rm HI} = \frac{\text{\# of photons absorbed per time}}{\text{\# of HI atoms in ionized gas}} = \frac{N^i_{\rm abs}/\Delta t}{n^\Gamma_{\rm HI} x^i_{\rm ion} V_{\rm cell}} \tag{C.2}$$

where $x^i_{\rm ion}V_{\rm cell}$ is the ionized volume of cell i and

$$n^\Gamma_{\rm HI} \equiv \frac{\langle \Gamma_{\rm HI} n_{\rm HI}\rangle_{\rm V}}{\langle \Gamma_{\rm HI}\rangle_{\rm V}} \tag{C.3}$$

is the $\Gamma_{\rm HI}$-weighted HI number density (the V sub-script denotes a volume average). Eq. 5.2 relates the numerator of Eq. C.3 to our definition for $\overline{\lambda}$ for the small-volume simulations (derived in the next section). Combining Eqs. 5.2, C.3, and C.1 yields

$$\Gamma^i_{\rm HI} = \sum_{j=1}^{N_{\rm rays}} \frac{N^{ij}_0 \left(1 - \exp\left[-x^i_{\rm ion}\Delta s^{ij}/\overline{\lambda}^i\right]\right)}{(\overline{\lambda}^{-1} F_\gamma/\langle \Gamma_{\rm HI}\rangle_{\rm V}) x^i_{\rm ion} V_{\rm cell}\Delta t} \tag{C.4}$$

where $F_\gamma \equiv \Gamma^0_{\rm HI}\overline{\sigma}^{-1}_{\rm HI}$ is the ionizing flux at the source planes in the small-volume simulations and $\Gamma^0_{\rm HI}$ is the photo-ionization rate at the source planes. Because the domain size (32 h^{-1}kpc) is much less than $\overline{\lambda}$ in all our small-volume simulations, F_γ usually attenuates very little over the domain width except around self-shielded systems, which (typically) occupy a small fraction of the volume. Thus, $\langle \Gamma_{\rm HI}\rangle_{\rm V} \approx \Gamma^0_{\rm HI}$, which gives

$$\Gamma^i_{\rm HI} \approx \sum_{j=1}^{N_{\rm rays}} \frac{N^{ij}_0 \left(1 - \exp\left[-x^i_{\rm ion}\Delta s^{ij}/\overline{\lambda}^i\right]\right)}{(\overline{\lambda}\overline{\sigma}_{\rm HI})^{-1} x^i_{\rm ion} V_{\rm cell}\Delta t} \tag{C.5}$$

which is equivalent to Eq. 5.1.

Note that Eq. C.2 and Eq. C.5 together imply that $n_{\rm HI}^{\Gamma} \approx (\overline{\lambda}\overline{\sigma}_{\rm HI})^{-1}$ should be true in our small-volume simulations. Figure C.2 tests this equality for simulations with $\Gamma_{-12} = 3.0$ (blue curves), 0.3 (red) and 0.03 (black) for $z_{\rm re} = 8$ and $\delta/\sigma = 0$ (mean density). The top panel plots both quantities vs. time since ionization, while the bottom panel shows their ratio. In the simulations with $\Gamma_{-12} = 3.0$ and 0.3 the equality holds to within a few percent even during the first few Myr when self-shielding is most important. However in the 0.03 case, they do not agree to within 10% until $\approx$ 10 Myr after ionization. In that case, $n_{\rm HI}^{\Gamma} > (\overline{\lambda}\overline{\sigma}_{\rm HI})^{-1}$, Eq. 5.1 under-estimates the number of absorptions in ionized gas because it over-estimates $\Gamma_{\rm HI}$, and therefore the converged value of $\overline{\lambda}$ (Eq. 3.2). This works in the direction of making the opacity too low in recently ionized gas with low $\Gamma_{\rm HI}$ in our reionization simulations. However, the double-counting issue described in §5.2.3 likely still renders the total opacity in these regions an over-estimate. The test and photon budget comparison described in that section includes the effect discussed here, so our statements there should still hold.

C.3 Derivation of Eq. 5.2 (for $\overline{\lambda}$)

In this section we derive our estimator for the frequency-averaged mean free path in our small-volume simulations, $\overline{\lambda}$ (Eq. 5.2). Let I_ν be the specific intensity at the source planes. The ionizing flux along one direction of our box is,

$$F_\gamma = \int_{\nu_{\rm HI}}^{4\nu_{\rm HI}} \frac{I_\nu}{h_p \nu}\, d\nu, \tag{C.6}$$

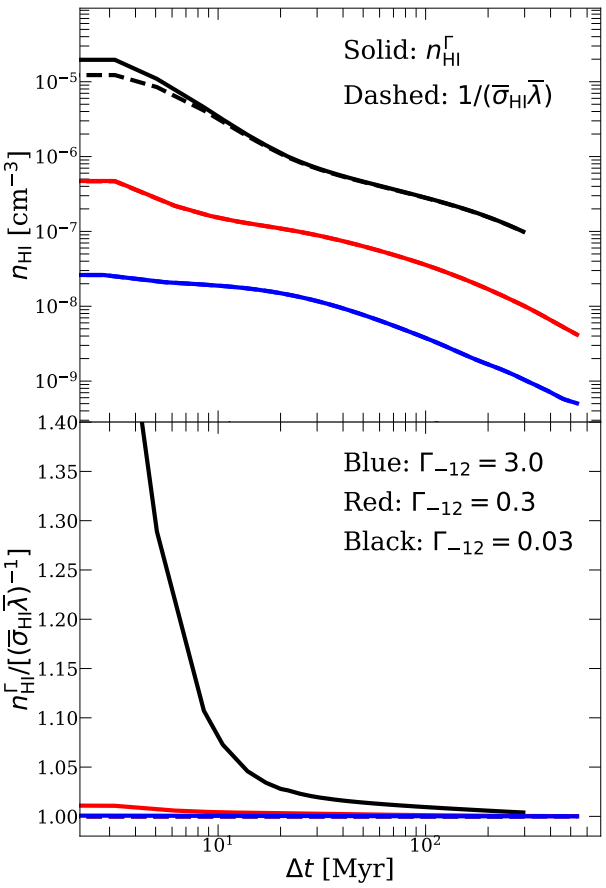

Figure C.2: Test of the relation $n_{\rm HI}^{\Gamma} = (\overline{\lambda}\overline{\sigma}_{\rm HI})^{-1}$, as required by Eq. 5.1. **Top**: $n_{\rm HI}^{\Gamma}$ (solid) and $(\overline{\lambda}\overline{\sigma}_{\rm HI})^{-1}$ (dashed) vs. time since ionization for small-volume simulations with $\Gamma_{-12} = 3.0$ (blue), 0.3 (red), and 0.03 (black), assuming $z_{\rm re} = 8$ and $\delta/\sigma = 0$. **Bottom**: the ratio between these two quantities for each case. For $\Gamma_{-12} = 3.0$ and 0.3 the equality holds within a few percent at all times, but for 0.03 agreement to within 10% is not reached until $\Delta t \approx 10$ Myr. This works in the direction of under-estimating the absorption rate in recently ionized cells with low $\Gamma_{\rm HI}$ in our reionization simulations.

where h_p is Planck's constant and $h_p\nu_{\rm HI}$ is the ionization potential of hydrogen. Assuming the radiation streams along the x_1 direction, the photoionization rate at location $\mathbf{x} = (x_1, x_2, x_3)$ along a ray is

$$\Gamma_{\rm HI}(\mathbf{x}) = \int_{\nu_{\rm HI}}^{4\nu_{\rm HI}} \frac{\sigma_\nu}{h\nu} I_\nu e^{-\int_0^{x_1} dx' n_{\rm HI}(x', x_2, x_3)\sigma_\nu} \, d\nu, \tag{C.7}$$

where $n_{\rm HI}(\mathbf{x})$ is the proper hydrogen number density and σ_ν is its photoionization cross section. We can write

$$n_{\rm HI}(\mathbf{x}) \; \Gamma_{\rm HI}(\mathbf{x}) = \int_{\nu_{\rm HI}}^{4\nu_{\rm HI}} d\nu \frac{I_\nu}{h\nu} \; n_{\rm HI}(\mathbf{x})\sigma_\nu \; e^{-\int_0^{x_1} dx' n_{\rm HI}(x', x_2, x_3)\sigma_\nu} =$$

$$- \int_{\nu_{\rm HI}}^{4\nu_{\rm HI}} d\nu \frac{I_\nu}{h\nu} \frac{\partial}{\partial x_1} e^{-\int_0^{x_1} dx' n_{\rm HI}(x', x_2, x_3)\sigma_\nu} \tag{C.8}$$

Integrating over the domain volume $V_d = L_d^3$, we obtain

$$V_d \langle n_{\rm HI}\Gamma_{\rm HI}\rangle_{V_d} =$$

$$\int_{\nu_{\rm HI}}^{4\nu_{\rm HI}} d\nu \frac{I_\nu}{h\nu} \int_0^{L_d} dx_2 dx_3 \; \left(1 - e^{-\int_0^{L_d} dx' n_{\rm HI}(x', x_2, x_3)\sigma_\nu}\right) \tag{C.9}$$

where $\langle \ldots \rangle_{V_d}$ denotes an average over the domain volume. We define the effective optical depth through

$$e^{-\tau_{\rm eff}} \equiv \langle e^{-\int_0^{L_d} dx' n_{\rm HI}(x', x_2, x_3)\sigma_\nu} \rangle_{A_d} =$$

$$A_d^{-1} \int_0^{L_d} dx_2 dx_3 \; e^{-\int_0^{L_d} dx' n_{\rm HI}(x', x_2, x_3)\sigma_\nu} \tag{C.10}$$

where $A_d = L_d^2$ and $\langle \ldots \rangle_{A_d}$ denotes an average over the transverse plane. Plugging this into equation C.9 yields

$$L_d \langle n_{\rm HI}\Gamma_{\rm HI}\rangle_{V_d} = \int_{\nu_{\rm HI}}^{4\nu_{\rm HI}} d\nu \frac{I_\nu}{h\nu} (1 - e^{-\tau_{\rm eff}}). \tag{C.11}$$

The mean free path is defined to be $\overline{\lambda} = L_d/\tau_{\rm eff}$. Assuming that $\lambda \gg L_d$ (recall that $L_d = 32h^{-1}$ kpc), we can expand the exponential in equation C.11 to first order, yielding

$$\overline{\lambda}^{-1} \equiv \langle \lambda^{-1} \rangle_\nu = \frac{\langle n_{\rm HI} \Gamma_{\rm HI} \rangle_{V_d}}{F_\gamma}, \tag{C.12}$$

where we have used that $\langle \lambda^{-1} \rangle_\nu = (1/F_\gamma) \int_{\nu_{\rm HI}}^{4\nu_{\rm HI}} d\nu \frac{I_\nu}{h\nu} \lambda^{-1}$. The RHS of Eq. C.12 is the volume-averaged absorption rate divided by the incident flux, and is equivalent to the volume averaged absorption coefficient. Note that Eq. C.12 counts *all* absorptions within ionized regions, not just those balanced by recombinations.

C.4 Test of Eq. 3 (to account for evolving $\Gamma_{\rm HI}$)

In this section we will show how Eq. 3.2 accounts for the sensitivity of $\overline{\lambda}$ to the history of $\Gamma_{\rm HI}$ in our RT cells. Figure C.3 shows $\overline{\lambda}$ for several tests of Eq. 3.2 in small-volume simulations with evolving $\Gamma_{\rm HI}$. In the top panel, we show the mean free path for a fiducial box size/resolution simulation with $\Gamma_{-12}(z) = 0.3 + (3.0 - 0.3)\frac{8-z}{3}$ (dashed blue curve) alongside two approximations based on constant-$\Gamma_{\rm HI}$ simulations. The solid green curve is a direct power law interpolation between $\Gamma_{-12} = 3.0$ (red dashed curve) and 0.3 (black dashed curve) simulations. The magenta dotted curve is the result of evaluating Eq. 3.2 with $\xi = 0.6$ and $t_{\rm relax} = 100$ Myr (close to our fiducial values for these parameters). We see that the direct interpolation over-estimates $\overline{\lambda}$ by 10-15%, while Eq. 3.2 agrees with the evolving $\Gamma_{\rm HI}$ simulation to within a few percent.

We also ran several tests (in smaller boxes) in which we increased $\Gamma_{\rm HI}$ impulsively by $1-2$ orders of magnitude midway through the simulation. These tests represent a

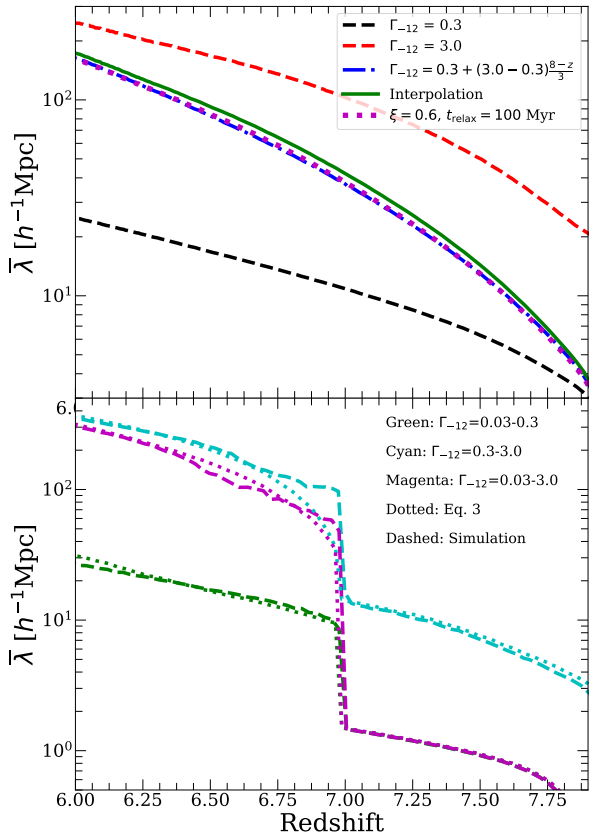

Figure C.3: Tests of Eq. 3.2 using small-volume simulations with evolving $\Gamma_{\rm HI}$. **Top**: Test with $\Gamma_{\rm HI}(z) = 0.3 + (3.0 - 0.3)\frac{8-z}{3}$ (blue dot-dashed) alongside a direct interpolation between simulations with constant $\Gamma_{\rm HI}$ (green solid) and the result of evaluating Eq. 3.2 with $\xi = 0.6$ and $t_{\rm relax} = 100$ Myr (magenta dotted). The interpolation over-estimates $\overline{\lambda}$ by 10-15% while Eq. 3.2 produces agreement to within a few percent. **Bottom**: Tests in smaller (0.256 h^{-1}Mpc) volumes in which we impulsively increased $\Gamma_{\rm HI}$ by $1-2$ orders of magnitude at $z = 7$. The dashed curves are the simulation results and the dotted curves are Eq. 3.2. The model agrees reasonably well even in these extreme cases, although the values of ξ and $t_{\rm relax}$ vary between fits (and from our fiducial values).

Starting Γ_{-12}	**Ending** Γ_{-12}	$\boldsymbol{\xi}$	$\boldsymbol{t}_{\rm relax}$ [Myr]
0.03	0.3	0.8	700
0.3	3.0	0.33	100
0.03	3.0	0.67	300

Table C.1: Best-fit parameters for our "impulsive-$\Gamma_{\rm HI}$" tests of Eq. 3.2, shown in Figure C.3.

"maximum stress test" of Eq. 3.2, since in reality $\Gamma_{\rm HI}$ will evolve more gradually. The bottom panel of Fig. C.3 shows the result of three tests, with $\Gamma_{\rm HI}$ impulsively jumping between the values quoted in the legend at $z = 7$. The dashed lines show the simulation results and the dotted lines the result of Eq. 3.2 (evaluated using a suite of similar simulations with constant Γ_{-12}). Though the values of ξ and $t_{\rm relax}$ that gave these fits, given in Table C.1, are somewhat different from each other (and our fiducial model), the goodness of the fits demonstrates the ability of Eq. 3.2 to capture $\overline{\lambda}$ in a variety of environments accurately. The variation may be due in part to the smaller box sizes of these tests and the fact that ξ and $t_{\rm relax}$ are partially degenerate, but we also do expect that ξ and $t_{\rm relax}$ should in general depend on $\Gamma_{\rm HI}$ (and, in principle, over-density and $z_{\rm reion}$). Future work will be required to address the environmental dependence of ξ and $t_{\rm relax}$ in more detail.